THE UNIVERSITY OF
WARWICK

AUTHOR: **Catherine Louise Fleck** DEGREE: **Ph.D.**

TITLE: **Magnetism in the complex cobaltates $\mathbf{Y}_{1-x}\mathbf{Sr}_x\mathbf{CoO}_{3-\delta}$ $(0.7 \leq x \leq 0.95)$ and $\mathbf{Ca_3Co_2O_6}$**

DATE OF DEPOSIT: .....

I agree that this thesis shall be available in accordance with the regulations governing the University of Warwick theses.

I agree that the summary of this thesis may be submitted for publication.

I **agree** that the thesis may be photocopied (single copies for study purposes only).

Theses with no restriction on photocopying will also be made available to the British Library for microfilming. The British Library may supply copies to individuals or libraries. subject to a statement from them that the copy is supplied for non-publishing purposes. All copies supplied by the British Library will carry the following statement:

> "Attention is drawn to the fact that the copyright of this thesis rests with its author. This copy of the thesis has been supplied on the condition that anyone who consults it is understood to recognise that its copyright rests with its author and that no quotation from the thesis and no information derived from it may be published without the author's written consent."

AUTHOR'S SIGNATURE: .....

USER'S DECLARATION

1. I undertake not to quote or make use of any information from this thesis without making acknowledgement to the author.
2. I further undertake to allow no-one else to use this thesis while it is in my care.

DATE SIGNATURE ADDRESS

.....

.....

.....

.....

.....

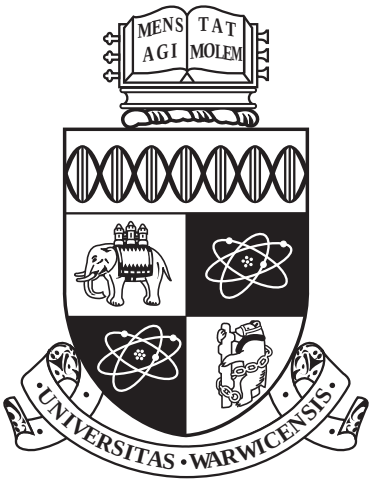

Magnetism in the complex cobaltates $\mathbf{Y_{1-x}Sr_xCoO_{3-\delta}}$ $\mathbf{(0.7 \leq x \leq 0.95)}$ and $\mathbf{Ca_3Co_2O_6}$

by

Catherine Louise Fleck

Thesis

Submitted to the University of Warwick

for the degree of

Doctor of Philosophy

Department of Physics

October 2011

THE UNIVERSITY OF WARWICK

Contents

List of Tables

List of Figures

Acknowledgments

Completing this Ph.D has been a collaborative process and I'd like to thank the following people for their help and support. First and foremost, I would like to express my thanks to my supervisor Martin Lees for being willing to answer my every question, however daft, and his continuous support and patience. I am very grateful to Oleg Petrenko for all his constructive criticism and being 'paper chief'. Thanks to Geetha Balakrishnan for supervising all the crystal growths, both successful and unsuccessful, and Don Paul for his general advice on all things neutron scattering. Many thanks to Tom Orton, for technical and moral support. Also thanks to the rest of the superconductivity and magnetism group, especially Andrew Crichton, Dan O'Flynn and Thomas Hayes, for their help and company over the last four years, I wish them all the best of luck for the future.

Thanks to all my contacts and collaborators for their assistance in the preparing the work contained in this thesis. Firstly to Stephano Agrestini, for all his efforts in teaching me FULLPROF and allowing me to collaborate with him on the $Ca_3Co_2O_6$ project, and also our collaborators Claudio Mazzoli and Alessandro Bombardi. Thanks to Aziz Daoud-Aladine for his help with interpreting and refining the $Y_{1-x}Sr_xCoO_{3-\delta}$ data. Also thanks to Dean Keeble for his doomed efforts in trying to solve the crystal structure of $Y_{1-x}Sr_xCoO_{3-\delta}$, and to Dan Baker and the rest of the crystallography group for their help with using the X-ray equipment and interpreting the results.

Special thanks to all the instrument scientists I have worked with for their patience and dedication; Clemens Ritter on D1B, Garry McIntyre, Bachir Ouladdiaf and Silvia Capelli on D10, Pascale Deen and Tom Fennell on D7, Phillppe Bourges on 2T1, Laurent Chapon on GEM, Aziz Daoud-Aladine on HRPD and Caroline Curfs on ID31.

Finally thanks to my Mum and Dad, the rest of my family, Francis and all of my friends for their love and support during the last four years, and for constantly reminding me that the best things in life need no qualification.

Declarations

The experimental work presented in this thesis was all carried out between October 2007 and June 2011 in the University of Warwick Physics Department, at the ISIS facility at the Rutherford-Appleton Laboratories (RAL) in Oxfordshire, the Institute Laue Langevin (ILL) in Grenoble and at the Laboratoire Leon Brillouin (LLB) in Saclay, Paris. All the $Y_{1-x}Sr_xCoO_{3-\delta}$ samples studied were prepared by myself under the guidance of Dr. Geetha Balakrishnan. The polycrystalline $Ca_3Co_2O_6$ samples were either prepared by Dr. S. Agrestini or myself, and the $Ca_3Co_2O_6$ single crystal used in chapter 9 was prepared by Dr. S. Agrestini prior to the start of my Ph.D.

The EDAX and TGA measurements were made by myself with assistance from Steve York and Dave Hammond respectively. The magnetic and physical properties measurements at Warwick were carried out by myself under the supervision of Dr. Martin Lees. The X-ray diffraction data was collected either solely by myself or by myself under the supervision of Dr. Dan Baker or Dr. Dean Keeble. The Rietveld refinement of the single crystal X-ray data included in chapter 5 was performed by Dr. Dean Keeble in collaboration with myself.

All experiments at large scale facilities were performed with the assistance of an instrument scientist, and in all cases I was either the sole experimentalist or a leading member of the experimental team. The Rietveld refinement of the neutron powder diffraction data from $Ca_3Co_2O_6$ presented in chapter 8 was analysed in collaboration with Dr. S. Agrestini. I am also grateful for the input of Dr. Aziz Daoud-Aladine when analysing $Y_{1-x}Sr_xCoO_{3-\delta}$ neutron diffraction data. The remaining neutron data presented was analysed by myself with input from instrument scientists and the academic staff in the group, particularly Dr. Oleg Petrenko.

No part of this thesis has been submitted for examination at any other institution. Sections of the work described in this thesis have been published in the following journal articles:

- C. L. Fleck, M. R. Lees, S. Agrestini, G. J. McIntyre and O. A. Petrenko *EPL* **90** (2010) 67006.
- C. L. Fleck, G. Balakrishnan and M. R. Lees *J. Mater. Chem.* **21** (2011)

1212.

- S. Agrestini, C. L. Fleck, L. C. Chapon, C. Mazzoli, A. Bombardi, M. R. Lees and O. A. Petrenko *Phys. Rev. Lett.* **106** (2011) 197204.

The work described in this thesis has also been presented in talks and posters at the following conferences:

- Time and magnetic field dependent behaviour in the spin chain material $Ca_3Co_2O_6$, *Condensed Matter and Materials Physics Conference*, University of Warwick (14th-16th December 2010) *Talk*.

- Interplay between orbital, spin and charge degrees of freedom in single crystals of the cobaltate $Y_{0.15}Sr_{0.85}CoO_{3-\delta}$, *The New Generation in Strongly Correlated Electron Systems Conference*, Playa Blanca, Canary Islands (20th-26th June 2010) *Talk*.

- Field-driven magnetisation steps in geometrically frustrated $Ca_3Co_2O_6$: A neutron diffraction study, *The New Generation in Strongly Correlated Electron Systems Conference*, Playa Blanca, Canary Islands (20th-26th June 2010) *Poster*.

- Observations of the low-temperature magnetic ordering in $Ca_3Co_2O_6$, *Condensed Matter and Materials Physics Conference*, University of Warwick (15th-17th December 2009) *Poster*.

Abstract

The magnetic phases in the complex cobaltates $Y_{1-x}Sr_xCoO_{3-\delta}$ ($0.7 \leq x \leq 0.95$) and $Ca_3Co_2O_6$ have been investigated by susceptibility, heat capacity, X-ray and neutron scattering techniques. These measurements have shown that the superstructure ordering in the perovskite cobaltate $Y_{1-x}Sr_xCoO_{3-\delta}$ which evolves as a function of temperature heavily influences the ferrimagnetic behaviour of this material. Neutron scattering has also been used to probe the unusual time and magnetic field dependent behaviour of the spin-chain compound $Ca_3Co_2O_6$, and to further our understanding of the magnetic phase diagram of this system.

Both polycrystalline and single crystal samples have been used in this study. High quality single crystals of the *A*-site (Sr/Y) and oxygen vacancy ordered form of the perovskite $Y_{1-x}Sr_xCoO_{3-\delta}$ have been produced using the floating zone technique and characterised using EDAX and TGA. The single crystals produced were large enough to perform polarised and inelastic neutron scattering experiments on this compound for the first time, revealing anisotropic quasi-elastic scattering above the magnetic transition temperature. In addition, diffraction experiments on these samples found evidence of coincident structural and magnetic transitions in $Y_{1-x}Sr_xCoO_{3-\delta}$ at both 370 and 280 K.

Neutron diffraction measurements were also performed on the geometrically frustrated compound $Ca_3Co_2O_6$. The low temperature magnetisation process was found to be accompanied by clearly visible steps in the intensity of the ferromagnetic and antiferromagnetic Bragg peaks. Detailed measurements have shown that the presence of short-range correlations cannot account for the reduction in intensity of the antiferromagnetic Bragg peaks at low temperatures. Instead, the origin of this drop in intensity was found to be a slow time-dependent magnetic transition from one long-range ordered antiferromagnetic state to another. This transition occurs over a timescale of hours and is never complete.

The experimental work detailed in this thesis provides new information about the phase diagrams of $Y_{1-x}Sr_xCoO_{3-\delta}$ and $Ca_3Co_2O_6$ and contributes to our overall understanding of the physics of these complex cobaltate compounds.

Part I

Introduction

Chapter 1

Cobaltates: Introduction

This thesis details studies of the magnetic behaviour of two cobaltate compounds $Y_{1-x}Sr_xCoO_{3-\delta}$ and $Ca_3Co_2O_6$, both of which have a complex relationship between their structural and magnetic properties. The word Cobalt is derived from the German Kobold [1], a mischievous goblin or sprite in Germanic mythology [2]. Kobalds were thought to frequent underground places such as mines, and their spitefulness was blamed for the difficultly of extracting metals from certain ores. This was particularly true of the cobalt ores Cobaltite and Smaltite, both of which release poisonous arsenic fumes on smelting [1]. When in 1735, Swedish chemist Georg Brant discovered a new metal he named it 'Cobalt Rex' after the infamous sprite [3]. Compounds containing cobalt ions such as the two discussed in this thesis are currently of interest to researchers both from a scientific perspective, several new kinds of physics and magnetic phenomena have been discovered in the cobaltates, and for their potential applications in solid state devices.

1.1 Applications of Cobaltate Compounds

Cobalt oxides and ores had been used to colour jewellery, glass and pottery long before the pure metal was discovered. The pigment called 'Cobalt Blue' was used extensively on Chinese blue and white porcelain from the 9th century (see figure 1.1) and other cobalt pigments such as Smalt have also been found on Egyptian pottery and Iranian glass beads dating to 2500 BC [1]. Cobalt metal is used as a catalyst in petroleum production and chemical synthesis. The cobalt isostope Co-60

Figure 1.1: A Ming dynasty blue and white plate. Taken from reference [4].

also has medical applications in radiotherapy and is commonly used as a source of γ-radiation [1]. Additionally, Li_xCoO_2 is the most common material for electrodes in lithium-ion batteries, widely used to power portable electronic devices such as laptop computers [5].

The technological importance of cobalt and its oxides has served to motivate much of the scientific research into cobaltates over the last few years. The high catalytic activity of cobaltates means one of the most developed of these applications is as cathodes in solid oxide fuel cells. Currently, the key problems with these devices are thermal stability, material degradation and high thermal expansion, and these issues provide one focus for materials research into cobaltates [6]. The same property of high catalytic activity means cobaltates can be used as gas sensors, and $LaCoO_3$ has been used to measure the concentration of ammonia by oxidising NH_3 to NO_x [7].

The high oxygen diffusion in many cobaltates has spawned research into uses as membranes for gas separation. The main contribution to oxygen transport in ceramics come from diffusion across grain boundaries, and so grain size becomes very important in manufacturing these materials [6]. One of the most dramatic properties of cobaltates is their anomalously high thermopower. This property has already been used to manufacture a thermocouple from the cobaltate $La_{1-x}Sr_xCoO_3$ [8], and research continues into practical applications of this effect. Inherent problems with stability and durability of new materials means there is a constant search for new systems with good physical and electronic properties.

1.2 Magnetism in the Cobaltates

Cobalt metal is an itinerant ferromagnet, where the electrons at the Fermi surface split such that there are more electrons with spin-up than with spin-down. Cobalt compounds, especially cobaltates, are more likely to be insulators where the magnetic moments are localised, but many still exhibit ferromagnetic behaviour due to the spin on the cobalt ions. All ferromagnets have a spontaneous magnetisation in the absence of an applied magnetic field and a ferromagnetic component to the magnetisation is essential for all permanent magnets. Ferromagnetism is uniquely important for technology as it is the only magnetic mechanism strong enough to have an effect on everyday life. It is integral to modern innovations such as credit cards and hard drives. Although cobalt itself is a relatively strong ferromagnet, it is more commonly used as a constituent in permanent magnetic alloys such as 'Alnico' (aluminium-nickel-cobalt) [1].

Not all cobalt compounds are ferromagnetic, and many cobaltates display other kinds of magnetic behaviour. Along with many other transition metal oxides, cobaltates have strong electron correlations which give rise not only to a myriad of

different magnetic behaviour but superconductivity [9, 10], metal-insulator transitions [11] and substantial magnetoresistance [12]. Interest in the whole transition metal oxide class of strongly correlated electron systems can be traced back to the discovery of high temperature superconductivity in $La_{2-x}Ba_xCuO_4$ [13] and $YBa_2Cu_3O_7$ in 1987 [14]. $La_{2-x}Ba_xCuO_4$ has a perovskite structure with a transition metal element in the middle of an oxygen face-centred cube with a rare-earth in each of the corners, shown in figure 1.2. This structure is very important in materials which have strongly correlated electrons such as the cuprates, manganites and cobaltates.

1.3 Perovskite Cobaltates

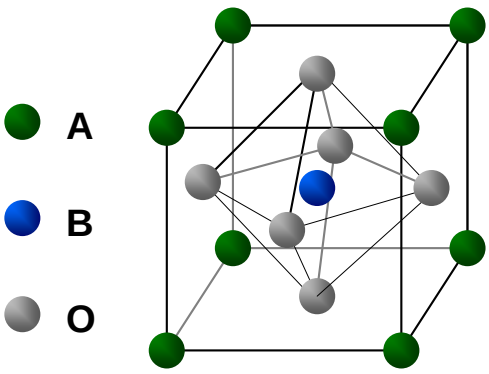

Figure 1.2: The perovskite crystal structure ABO_3, where A is a rare earth, B is a transition metal and O is oxygen. The oxygen ions form octahedra surrounding the B transition metal ion.

Perovskite cobaltates tend to be oxygen deficient, and this means the CoO_6 octahedra are often distorted, forming structures with lower crystal symmetry than a simple perovskite. Due to the oxygen deficiency, some of the polyhedra can form pyramidal complexes, which are also typical of the layered cobaltates $LnMCo_2O_{5+\delta}$ (where *Ln* stands for a lanthanide, lanthanum or yttrium and M is one of the alkali-earth elements). The extent of the structural distortion in the perovskite cobaltates changes quite markedly with temperature and often non-monotomically, a feature which first attracted researchers to this family of compounds [6].

Typically, the perovskite-structured cobaltates have the chemical formula $LnCoO_3$. The parent compound of this series of perovskite cobaltates is $LaCoO_3$. This material has been well studied because of the discovery of a spin state transition at a temperature of around 100 K [15, 16]. The spin state transition in $LaCoO_3$ is from the non-magnetic low spin to the paramagnetic state (either intermediate or high spin) state [17]). There is also some discussion of a further spin state transition at the higher temperature of 500 K [18]. Spin state transitions have been detected in other cobaltate compounds, but all at much higher temperatures than 100 K [6]. The

addition of a spin state degree of freedom in the cobaltates increases the possibility of unusual magnetic behaviour compared to the cuprates and manganites, which both have charge and orbital degrees of freedom but usually only a single possible spin state in perovskite compounds. The theory of spin state transitions is discussed in more depth in Section 2.1.2.

The intermediate spin state Co^{3+} ion in $LaCoO_3$ is Jahn-Teller active, this means it is associated with a lattice distortion. This is a very similar situation to that found in the manganites, and the classic compound $LaMnO_3$. An enormous research effort has been directed at the manganites because of the colossal magnetoresistance effect they exhibit, which has potential applications in read-write magnetic memory devices [19]. Cobaltates have a smaller magnetoresistance than manganites although they exhibit much of the same behaviour, such as charge and orbital ordering. However, in cobaltates the Jahn-Teller distortions are predominately dynamic rather than the static distortions found in manganites [6].

Experiments have shown the most promising cobaltates for practical applications are the substituted systems with a general formula $Ln_{1-x}M_xCoO_3$. The introduction of a bivalent alkali-earth ion can lead to the formation of Co^{4+} ions. In high concentrations, the introduction of alkali-earth atoms can lead to magnetic phase separation of ferromagnetic and non-ferromagnetic regions. When the percolation threshold is reached, the clustering manifests itself as a metal-insulator transition coupled to a paramagnet-to-ferromagnet transition [20]. $Y_{1-x}Sr_xCoO_{3-\delta}$ is an example of this family of doped-perovskite cobaltates. The structural and magnetic properties of this compound have an unusual sensitivity to oxygen concentration which results in a complex superstructure [21], a metal-to-insulator transition [11] and significant magnetoresistance. $Y_{1-x}Sr_xCoO_{3-\delta}$ is also a room-temperature ferromagnet [22]. The source of this ferromagnetic signal is the matter of some debate, and clustering [23], ferrimagnetism [24] and spin canting [25] have all been discussed in the context of this compound. The structure and magnetism respectively have been studied in this thesis using magnetometry, X-ray and neutron scattering on powders and single crystals, discussed in chapters 5 and 6. A literature review discussing the details of the research into $Y_{1-x}Sr_xCoO_{3-\delta}$ is included in this thesis as chapter 4.

1.4 Low-Dimensional Cobaltates

Not all the cobaltates of scientific interest have a 3D perovskite crystal structure. Layered cobaltates of the $LnMCo_2O_{5+\delta}$ type can show some of the most dramatic manifestations of the interplay of the spin, charge and orbital degrees of freedom. The key feature of this class of materials is the CoO_2 plane. Various cuprates, man-

ganites and ruthenates have this layered structure and features of their behaviour include striped structural ordering in the cuprates [26] and unconventional superconductivity in Sr_2RuO_4 [27]. Unconventional superconductivity has also manifest itself in the cobaltates in the layered compound $Na_xCoO_2 \cdot {}_yH_2O$ [9]. Superconductivity only appears in this compound on the intercalation of water, and it is hoped that understanding this unusual behaviour may provide some insight into the mechanisms of superconductivity in other layered transition metal oxides [6].

Such is the richness of the physics of the cobaltate family of materials, both quasi-2D layered systems and quasi-1D systems display interesting phase diagrams. One of the most important and most studied of the quasi-1D cobaltates is $Ca_3Co_2O_6$. Not only is this compound quasi-1D but the strong anisotropy of the magnetic interactions and crystal fields means the spins are Ising-like, exciting much interest from researchers [28]. Doped Ca_3CoXO_6 (X =Rh [29], Ir [30], Fe [31] and Mn [32, 33]), versions of this compound are also 1D magnetic materials and have also generated significant recent scientific interest. The research literature on $Ca_3Co_2O_6$ is summarised in chapter 7.

$Ca_3Co_2O_6$ itself is a bulk antiferromagnet below 25 K [34, 35, 36]. However, the feature of its magnetic behaviour that has caused the most interest is the appearance of regularly-spaced steps in the magnetisation on the application of a magnetic field [37], and our research into this phenomenon and the behaviour of $Ca_3Co_2O_6$ as a function of magnetic field is presented in chapter 9. The appearance of these steps varies with sweep rate [38], and this time dependent behaviour has led to some researchers describing the system as glassy [39]. Our neutron scattering investigations into the temperature and time dependence of the magnetic behaviour in $Ca_3Co_2O_6$ are described in chapter 8.

1.5 Discussion

Strongly correlated electron systems such as the cobaltates, ruthenates, manganites and cuprates have complex phase diagrams and showcase a plethora of interesting phenomena. These materials have provided condensed matter researchers with a rich playground over the past 25 years, and have dramatically changed our view of interactions in solids. Despite all this research, the microscopic mechanisms operating in many of these compounds are still poorly understood. Competing magnetic phases in these materials often lead to spatial inhomogeneity on a nanometre scale and there may be several coexisting magnetic phases within a single sample. Many of these materials exhibit giant responses to small perturbations, such as changes in temperature and doping, and behaviour such as superconductivity and ferromagnetism may be considered to be emergent phenomena [40].

The interplay of the charge, orbital and spin degrees of freedom in the cobaltates means these systems are particularly sensitive to environmental conditions and doping levels. These different degrees of freedom are defined in chapter 2 which also outlines the other theoretical considerations relevant to the study of $Y_{1-x}Sr_xCoO_{3-\delta}$ and $Ca_3Co_2O_6$. Understanding these complex systems requires detailed and systematic measurement, and the techniques employed to carry out the measurements in this thesis are outlined in chapter 3. The experimental work on the compounds $Y_{1-x}Sr_xCoO_{3-\delta}$ and $Ca_3Co_2O_6$ on which this thesis is based is described in chapters 5, 6, 8 and 9. Finally, the broader implications of the research described in this thesis are discussed in chapter 10.

Chapter 2

Theory

Cobalt is a transition metal element with a $3d$ electronic structure (Sc-Zn). These $3d$ transition metals, and in particular their oxides, are one of the most important groups of elements in the study of magnetism. The wide variety of different electronic interactions possible in these materials will be discussed in this chapter. Section 2.1 covers the theory of magnetism, beginning with a description of the behaviour of isolated magnetic moments and mean field theory and then discussing the exchange interactions between magnetic atoms and the crystal field environments they inhabit. The formalism for describing crystalline solids in terms of crystal and magnetic structures will be outlined in section 2.2. Section 2.3 outlines some of the phase transitions most likely to be found in the cobaltates, as the study of phase transitions is central to research into bulk magnetic materials. Finally, the role of quantized excitations in this class of materials is introduced in section 2.5.

2.1 Magnetism in Solids

2.1.1 Magnetic Moments

The magnetic moment μ on an atom is associated with its total angular momentum $\mathbf{J}$. For a single atom with only one electron, $\mathbf{J}$ is given by equation 2.1, where the quantum number $\mathbf{L}$ describes the orbital angular momentum and $\mathbf{S}$ is the quantum number associated with the intrinsic spin on the electron.

$$\mathbf{J} = \mathbf{L} + \mathbf{S} \tag{2.1}$$

For a material with a linear magnetic response in a small applied magnetic field, the relationship between the magnetic moment μ and total angular momentum $\mathbf{J}$ is given by:

$$\mu = g_J \mu_B \sqrt{J(J+1)} \tag{2.2}$$

In this equation, μ_B is the Bohr magneton, $\mu_B = e\hbar/2m_e$, and g_J is the Landé g-factor, which can be expressed in terms of the quantum numbers J, L and S as follows:

$$g_J = \frac{3}{2} + \frac{S(S+1) - L(L+1)}{2J(J+1)} \tag{2.3}$$

The magnetic susceptibility χ, the magnetic response of a material to an external stimulus, can be expressed in terms of the magnetic moment per unit volume, known as the magnetisation M, and the magnetic field strength H. The magnetic flux density B is related to the magnetic field strength H by $B = \mu_0(H + M)$. As above, for a material with a linear magnetic susceptibility in a small magnetic field the following expression is true (μ_0 and k_B are the permeability of free space and Boltzmann constants respectively):

$$\chi = \frac{M}{H} \approx \frac{\mu_0 M}{B} = \frac{\mu_0 \mu^2}{3k_B T} \tag{2.4}$$

In fact, equation 2.4 is a statement of Curie's law, which states that magnetic susceptibility of a material is proportional to the inverse of the temperature. A system in which Curie's law is valid, where the moments tend to align with any applied magnetic field, is known as paramagnetic. The magnetic moments associated with unpaired electrons in paramagnetic systems can be considered independent and are therefore randomly aligned in zero magnetic field. Applying a magnetic field causes the spins to align parallel to the field direction, depending on the strength of the applied field, until in a high enough field all the moments are aligned and the magnetisation becomes saturated. An example of a paramagnet in a small applied magnetic field is illustrated in figure 2.1.

The other kind of magnetic order which may occur when a magnetic field is applied is diamagnetism. Diamagnetism is usually a weak effect, and most materials are diamagnetic to some degree. Unlike paramagnetism, the magnetic response of diamagnets is also largely temperature independent, and equation 2.4 is no longer valid in these materials. The magnetic moments in a diamagnetic material tend to oppose any applied magnetic field, and this is illustrated in figure 2.1.

In most systems, the orbital angular momentum L and intrinsic spin S in-

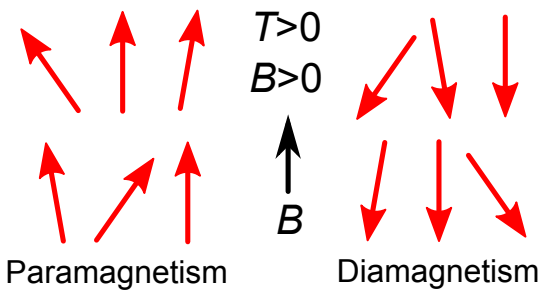

Figure 2.1: Paramagnetic and diamagnetic materials at finite temperatures in a small applied magnetic field. Both systems require an applied field to produce a finite magnetisation.

teract, albeit weakly, splitting into a number of levels with different J known as the fine structure. The total angular momentum **J**, given in equation 2.1, is conserved through this process. The values of S, L and J for a particular atom which minimise the energy can be estimated using Hund's rules, which give an empirical prediction of the ground state of an ion.

Hund's Rules

(1) Maximise S
(2) Maximise L
(3) If the shell is less than half full $J = \mid L - S \mid$
If the shell is more than half full $J = \mid L + S \mid$

It is also necessary to consider how the magnetic moments on neighbouring atoms interact with each other. This is via an exchange interaction, which will be discussed in detail in section 2.1.3. These interactions can result in a variety of different kinds of long-range magnetic order such as ferromagnetism, ferrimagnetism, antiferromagnetism, spiral order, helical order and spin glasses. Some of these are illustrated in figure 2.2. Ferromagnetic systems have a Curie temperature T_c below which ferromagnetism onsets. It is related to the susceptibility by the Curie-Weiss law:

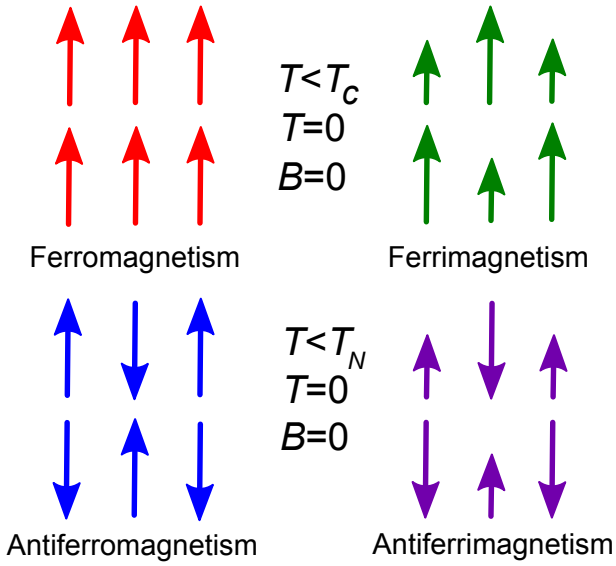

Figure 2.2: Some possible types of long-range magnetic order. Ferromagnetism, ferrimagnetism, antiferromagnetism and antiferrimagnetism are all varieties of spontenous magnetic ordering in zero applied field.

$$\chi \propto \frac{1}{T - T_c} \tag{2.5}$$

Cobalt metal is an itinerant ferromagnet, it has a spontaneous magnetisation without an applied magnetic field due to the splitting of the electron energy bands at the Fermi level. The Curie temperature for cobalt metal $T_c = 1394$ K with magnetic moment of $\mu = 1.715\ \mu_B/f.u.$

In an antiferromagnet, the critical temperature is known as the Néel temper-

ature T_N, and in this case $T_c = -\Theta$ in equation 2.5. We therefore expect $\Theta = -T_N$. Below T_N, the magnetic moments lie antiparallel to their nearest neighbours. In a crystal lattice the situation is further complicated as these are several possible ways of arranging an equal number of antiparallel spins on a cubic lattice, discussed in section 2.2.2.

2.1.2 Crystal Fields

The d orbitals in $3d$ compounds have a pronounced angular dependence as shown in figure 2.3. The five d orbitals can be grouped into the two e_g orbitals which point along the crystallographic axes and the t_{2g} orbitals which point between the crystallographic axes. The local environment can split these two groups of orbitals in energy. If the environment is octahedral, as in a perovskite where a transition metal ion is surrounded by 6 oxygens at the centre of each face of the cube, the t_{2g} levels will be lowered and the e_g levels will be raised in energy. The reverse is true in a tetrahedral configuration [42]. This raising or lowering of the energy levels is known as crystal field splitting.

Cobalt can exist in several oxidation states (valencies), the most common being Co^{2+} and Co^{3+}, with Co^{4+} also possible. These give electronic configurations of $3d^7$, $3d^6$ and $3d^5$ respectively. Using Hund's rules, these give ground state configurations of ${}^4F_{9/2}$, ${}^5D_4$ and ${}^6S_{5/2}$ for these three cobalt oxidation states. Hund's rules maximise the value of the quantum number S, however in $3d$ transition metals crystal field effects compete with the Coulomb pairing energy allowing other possible configurations. The case predicted by Hund's rules is known as high spin (HS) because S is maximised and the crystal field energy is lower than the pairing energy. When the crystal field energy is much greater than the pairing energy then the electrons doubly occupy the lower energy states (t_{2g} in an octahedral environment) before they start to fill the higher energy states. This leads to a lower value of S and is know as the low spin (LS) case. An intermediate spin (IS) state is also possible for Co^{3+} and Co^{4+} (see also section 2.3.4).

For $3d$ ions the crystal field interaction is much stronger than the spin-orbit interaction and this interaction becomes unimportant, an effect known as orbital quenching. In this case Hund's third rule is no longer applicable and the ground state is that where the quantum number $\mathbf{L} = 0$ and $\mathbf{J} = \mathbf{S}$. These results have shown much better agreement with experiment than the predictions of Hund's rules for these atoms [42]. However, the spin-orbit interaction can never entirely be ignored, and some states with non-zero angular momentum may be mixed in, so an assumption of $\mathbf{L} = 0$ must always be considered an approximation.

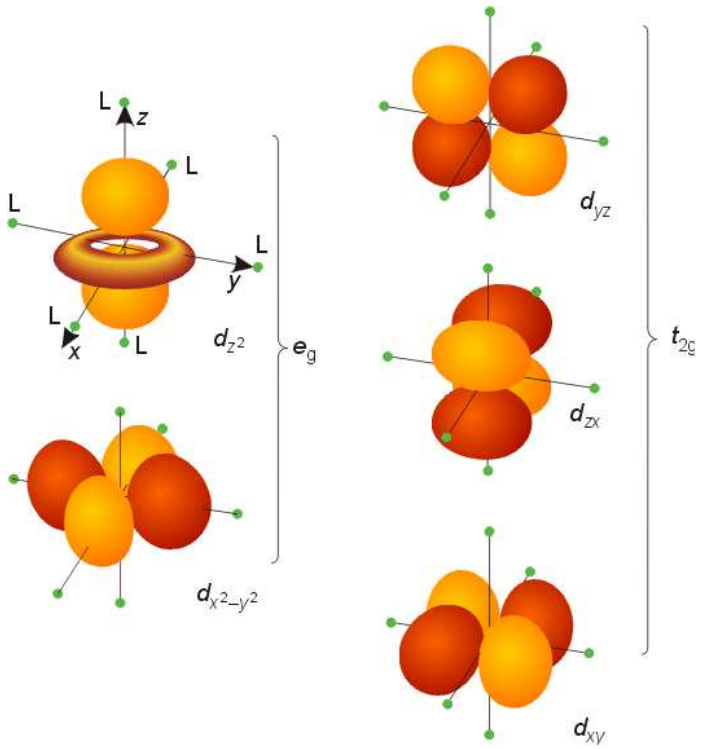

Figure 2.3: The angular distribution of the d orbitals. The e_g orbitals are the d_{z^2} and $d_{x^2-y^2}$ levels which lie along the crystallographic axes and the t_{2g} orbitals are the d_{xy}, d_{xz} and d_{yz} levels which lie between the crystallographic axes. Figure taken from reference [41].

2.1.3 Exchange Interactions

Exchange interactions are the mechanism for the formation of long-range magnetic order, and describe the interplay between the electrons on neighbouring magnetic ions. For the exchange mechanism to be direct the electron orbitals of neighbouring atoms must overlap, which is rare in real systems.

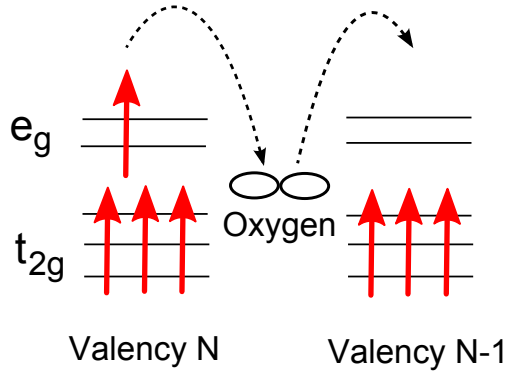

Figure 2.4: Double exchange in mixed valency materials.

In most magnetic materials, the exchange mechanism is indirect. The indirect exchange interaction mediated by a non-magnetic ion is know as superexchange, as it extends beyond the orbital ligands of the magnetic atoms. The classic example is two transition metal ions separated by an oxygen atom. The arrangement of the overlapping half-filled d orbitals and the p orbitals of the oxygen ions favours long-range antiferromagnetic ordering according to the first Goodenough-Kanamori rule. The second of these rules states that ferromagnetic ordering may also occur in such systems where the d orbitals are full and empty respectively [43].

Ferromagnetic ordering in mixed valency materials such as $Y_{1-x}Sr_xCoO_{3-\delta}$ is more likely to be mediated by double exchange. This occurs in materials where the magnetic ions have mixed valency. This is because having neighbouring atoms of different valency allows electron hopping between the atoms. Ferromagnetic alignment is therefore favourable because hopping can only occur between ferromagnetically aligned spins [42], as shown in figure 2.4.

Charge ordering in mixed valency materials promotes ferromagnetism due to double exchange as charge ordering means ions of different valency alternate. This is another phenomenon frequently found in the colossal magnetoresistive manganites. An example of charge ordering for mixed valency Mn^{3+}/Mn^{4+} is shown in figure 2.5. The Mn^{3+} and Mn^{4+} ions alternate in a square lattice with manganese ions with different charges as nearest neighbours. The nearest neighbours can then ferromagnetically align via the double exchange interaction.

Additionally the anisotropy and, depending on the system, the degeneracy of the d electron orbitals in such transition metal oxides mean the different orbitals can also order. This orbital ordering is also illustrated in figure 2.5 for the Mn^{3+} ions. The orbital ordering scheme can either favour ferromagnetism or antiferromagnetism depending on whether the orientation of the orbitals gives rise to double exchange or superexchange, and several orbital ordering configurations are possible. The

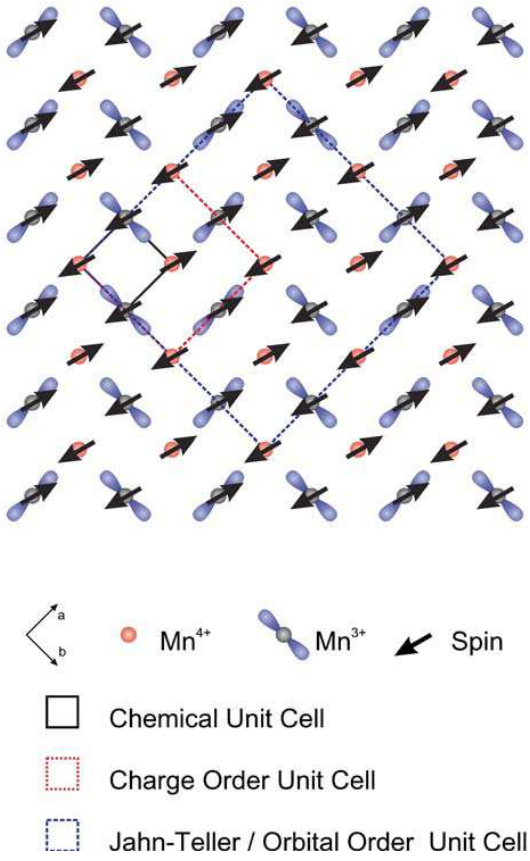

Figure 2.5: Charge and orbital ordering in the manganites. Figure taken from reference [44]).

ordering scheme depicted in the figure is the CE-type orbital ordering (see figure 2.6) commonly found in the manganites, where the Mn^{3+} and Mn^{4+} ions alternate and charge and orbital ordering coexist. The complex superstructure in $Y_{1-x}Sr_xCoO_{3-\delta}$ has led to recent suggestions that orbital ordering may also occur in this compound [45].

2.2 Structures of Solids

2.2.1 Space Group Symmetry

Crystalline materials are defined by their fully ordered, periodic structure known as the crystal lattice. The formalism for describing these structures involves defining the unit cell of the lattice, which is the smallest parallelepiped which will fully replicate the lattice, filling all space, using only appropriate translation operations [46]. The vectors defining the sides of this parallelepiped are the lattice parameters and their relationship to each other defines the 7 crystal systems; cubic, tetragonal, orthorhombic, monoclinic, triclinic, trigonal and hexagonal. These crystal systems can then be either primitive (P), face-centred (F), body-centred (I) or side-centred (A, B or C), giving the 14 Bravais lattices.

The overall symmetry of a crystal structure is described by a combination of the translational and point symmetry of the atoms, known as the space group. There are four point symmetry operators: rotation, mirror planes, centre symmetry and rotoinversion. The number of rotational axes is denoted by a number between 1 and 6, and the number of mirror planes by the letter m such that a system with 4 rotational axes and 2 mirror planes will have the point group $4mm$. A centrosymmetric structure has inversion symmetry, denoted $\bar{1}$, rotoinversion symmetry is therefore the combination of a rotation and inversion operation such that the notation $\bar{2}$ is a two-fold rotation plus inversion symmetry. The situation is somewhat complicated by the frequent combination of these symmetry elements, such as the combination of a 2-fold rotational axis normal to a mirror plane, which would be written $2/m$. The combination of the 32 possible point groups and the 14 Bravais lattices gives 61 of the 230 possible space groups [47].

The other 169 space groups are given by the addition of translational symmetry given by screw axis and glide planes. Screw axis are the combination of rotation and translation operations, with notation n_m where n is the order of the rotation and m is the translation as a fraction of the lattice vector $1/m$. Glide planes are the combination of a reflection in a given plane and a translation parallel to it, denoted a, b or c depending on the direction of the translation [47]. The combination of the space group and the Wyckoff positions of the atoms within the unit cell should entirely describe the crystal structure of a material.

A structure whose periodicity does not match the periodicity of the crystal lattice is known as incommensurate. Incommensurability is usually associated with a phase transition, and may only be present across a small temperature range (see section 2.3). A system whose incommensurability is a finite fraction of the crystal lattice is known as modulated, and involves a periodic distortion [48]. This distortion will give rise to satellite reflections which could also be described by a unit cell of lower symmetry, so called superstructure, where the original unit cell is the parent structure [49]. Such commensurate and incommensurate structural modulations are often associated with Jahn-Teller lattice distortions (section 2.3.2) and charge and orbital ordering (see figure 2.5) and have been intensely studied in the context of the combination of ferroelectricity and antiferromagnetism in the manganites [50]. Such structural modulations are discussed in the context of the cobaltate $Y_{1-x}Sr_xCoO_{3-\delta}$ in chapter 5 of this thesis.

2.2.2 Magnetic Structures

The arrangements of spins in a crystal lattice can be described by defining its magnetic structure. As with a crystal structure, a space group must be given and symmetry operators defined in order to generate atoms at all symmetry equivalent positions in the magnetic unit cell. There are 1651 magnetic space groups, the extra number compared to the crystallographic space groups being due to the need for a time reversal operator. Obviously, the magnitude and direction of the spin on each magnetic atom site must be specified. As magnetism is a dynamic process involving spin waves (see section 2.5.2) the magnetic structure is a static approximation of the configuration of magnetic moments in the lattice. Magnetic structures may also be described using group theory [51].

The key parameter when defining a magnetic structure is the propagation vector. This parameter describes the relationship between the unit cell of the magnetic structure and the unit cell of the crystal structure. In a commensurate magnetic structure, the magnetic and crystallographic unit cells are the same and the propagation vector is (0,0,0). The magnetic unit cell may also be larger than the crystallographic unit cell, such as in the case of a single antiferromagnetic spin per crystallographic unit cell, where the magnetic unit cell will be doubled. Additionally the magnetic unit cell can be completely incommensurate, and the propagation vector may have no relationship to the lattice parameter in any direction. This would imply a spin density wave propagating through the lattice in the direction of the incommensuration, and at least one of the terms in the propagation vector would be non-integer. This is the case in $Ca_3Co_2O_6$ and will be discussed in detail in chapter 7.

The magnetic structure describes the arrangement of spins on a lattice. This

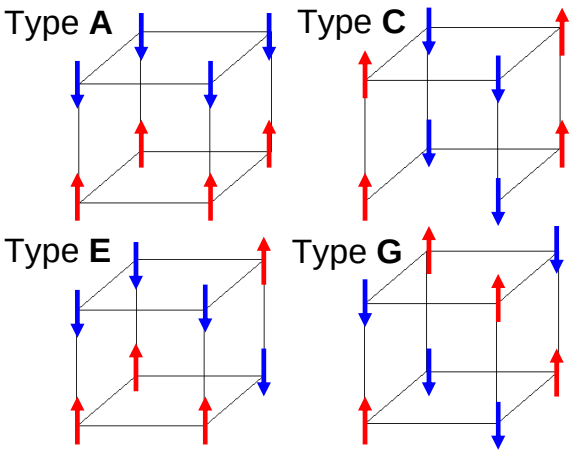

Figure 2.6: The four types of antiferromagnetic order which can occur on simple cubic lattices. In perovskite structures, G-type ordering is common because nearest neighbour superexchange interactions are mediated by the oxygen octahedra. Adapted from reference [42].

is especially important for antiferromagnetic materials, as there are several ways of arranging an equal number of up and down spins on a lattice. The four types of antiferromagnetic order possible for a simple cubic structure are shown in figure 2.6. In perovskite structures such as that of $Y_{1-x}Sr_xCoO_{3-\delta}$, G-type antiferromagnetism is common because superexchange interactions mediated by the oxygen atoms force all nearest neighbour spins to be antiferromagnetically aligned. An exception is $LaMnO_3$, whose magnetic ordering scheme is A-type [42]. Ferrimagnetic and antiferrimagnetic structures may have even more complex configurations, as the unequal magnetic moments on different crystallographic sites arrange to form long-range magnetic order in the lattice.

2.2.3 Dimensionality

The magnetic interactions in a solid may be described using one of several microscopic models. The choice of model depends on the dimensionality of the magnetic order. This is distinct from the dimensionality of the crystal lattice, which may be 1, 2 or 3D depending on the atom positions. The dimensionality of the magnetic structure describes how the spins are correlated within the lattice. 3D magnetic correlations can be described using the nearest-neighbour Heisenberg model, equation 2.6, where J is the nearest neighbour exchange integral and the spins $\mathbf{S_i}$ and $\mathbf{S_j}$ are 3D vectors. The dimensionality of the lattice for the 3D nearest neighbour Heisenberg model may be 1, 2 or 3D.

$$H = -\sum_{ij} J_{ij}\mathbf{S_i}\cdot\mathbf{S_j} \tag{2.6}$$

If the dimensionality of the magnetic order is 1D, as with the spin chains in $Ca_3Co_2O_6$, the appropriate magnetic model is the Ising model. In this model we only consider the z component of the spin in equation 2.6 and the spins can only align exactly parallel or antiparallel with the z axis. For a system with perfectly

Ising spins on a 1D lattice, it can be shown that the critical temperature $T_c = 0$ and there is no phase transition to long-range order [42].

2.3 Phase Transitions

2.3.1 Orders of Phase Transitions

Phase transitions can be structural, magnetic, superconducting or ferroelectric, to name a few. The nature of phase transitions can be studied using Landau theory. Landau theory states that the free energy can be written as a function of the order parameter of the system, and this function can be expressed as a Taylor expansion:

$$F(\xi) = a + a_0(T) + a_2(T)\xi^2 + a_3(T)\xi^4 \tag{2.7}$$

If $a_3(T)$ is positive, the phase transition is known as second-order, and the order parameter goes continuously to zero at the transition temperature (T_0), shown in the left panel of figure 2.7 [46]. First-order phase transitions occur when the coefficient $a_3(T)$ is negative. First-order phase transitions involve a latent heat, and there is a discontinuity in the order parameter at the transition temperature, shown in the right panel of figure 2.7. An example of a first-order phase transition is the ferroelectric transition in $BaTiO_3$ as a function of temperature [46]. Most of the phase transitions discussed in this thesis are second-order.

2.3.2 Structural Transitions

The perovskite ABO_3 structure, described in the introduction and shown in figure 1.2, is cubic with space group $Pm\bar{3}m$. Although many systems have this structure, even more common are its derivatives which are related to the $Pm\bar{3}m$ structure by

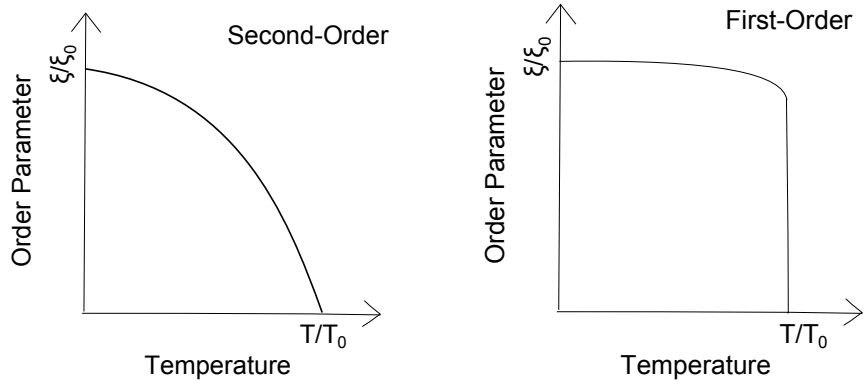

Figure 2.7: Orders of phase transitions (adapted from reference [46]). First-order transitions are discontinuous at the phase boundary, whereas for second-order phase transitions the order parameter goes continuously to zero.

the suppression of one or more symmetry operators. This structural phase transition to a lower or higher symmetry state may take place as a function of temperature, pressure or chemical doping. The loss of symmetry can be due to; tilting of the polyhedra surrounding the B cations, displacement of B cations from the centre of the structure or distortion of the polyhedra due to the Jahn-Teller effect [52]. Increased covalency of A-O or B-O bonds, incomplete occupancy of one or more the lattice sites or ordering of the atoms on either the A or B sites, such as in the (A'A")BO_3 or A(B'B")O_3 double perovskites, can also result in change in structural symmetry [53].

The most common type of distortion in a perovskite lattice is the tilting of the BO_6 octahedra. The rotation of successive layers in the same direction is known as an *in-phase* tilt, denoted by a positive superscript (a^+ is a rotation about the x axis), the rotation of successive layers in opposing directions is known as an *anti-phase* tilt, denoted by a negative superscript (b^- is a rotation about the y axis which has a different magnitude to the rotation about x) [53]. The notation for an axis with no tilting is a^0. The tilting from the simple perovskite structure which leads to the $R\bar{3}c$ space group of $Ca_3Co_2O_6$ is $a^-a^-a^-$ and the $I4/mmm$ space group proposed for $Y_{1-x}Sr_xCoO_{3-\delta}$ is formed through an $a^0b^+b^+$ tilt. This tilt leads to so called tilt peaks in the X-ray or neutron diffraction pattern, small peaks to the side of one of the main Bragg peaks belonging to the simple perovskite phase, the side on which the peaks appear depending on the phase of the distortion.

The loss of centrosymmetry of a perovskite due to the displacement of the B cation from the centre of the structure is common in ferroelectric materials, as the induction of a dipole moment in the unit cell means a net polarization is generated. The classic example of this is $BaTiO_3$. These displacive phase transitions are often associated with the distortion of the octahedra in perovskites [52], which in turn can also be driven by electronic interactions such as the Jahn-Teller effect. This effect occurs when the local crystal field environment causes it to be energetically favourable for the perovskite ocathedra to distort. This distortion results in the splitting of the levels of the d orbital, and can be either static or dynamic in nature. This type of lattice distortion is common in the manganites, and can also be coupled to an octahedral tilt.

From empirical evidence and group theory considerations, a sequence of structural phase transitions for a perovskite might be $Pm\bar{3}m$ to $I4/mcm$ to $Cmcm$ to $Pnma$, seen in $SrTiO_3$, $SrRuO_3$ and $CaTiO_3$ [53]. In terms of crystal systems, this is cubic to tetragonal to octahedral to (pseudo)monoclinic. The number of transitions and distortions possible in perovskites can make it difficult to assign a space group, and mistakes and incorrect space group assignment are prevalent in the literature.

It should be noted that at finite temperatures, some thermal expansion of the lattice parameter is expected, as the thermal motion of the atoms means they have a greater average separation when the temperature is increased. For solids, the coefficient of thermal expansion α has lattice, magnetic, electronic and Schottky contributions, as expressed below:

$$\alpha = \alpha_{lattice} + \alpha_{magnetic} + \alpha_{Schottky} + \alpha_{electronic} \tag{2.8}$$

The lattice contribution may be affected by the crystalline anisotropy of the material, and identifying structural transitions from changes in the thermal expansion of the lattice parameter is non-trivial.

2.3.3 Magnetic Phase Transitions

Magnetic phase transitions come in many forms, and like structural phase transitions can also be induced as a function of temperature, pressure, composition, or applied magnetic field. Some classic examples include the paramagnetic-to-ferromagnetic transition and the superconducting phase transition. The experimental signature of a paramagnetic-to-ferromagnetic phase transition is a spontaneous magnetisation which can manifest itself as the opening up of the hysteresis loop in a measurement of the magnetisation as a function of applied magnetic field strength. This effect is due to the increasing alignment of the domains in the sample as the applied field is increased. At some applied magnetic field, a ferromagnet will reach a saturation magnetisation M_s when the whole sample consists of a single domain aligned with the applied field.

The magnetic phase diagram for a material such as $Y_{1-x}Sr_xCoO_{3-\delta}$ or $Ca_3Co_2O_6$ in which several magnetic phase transitions occur may be very complex, with mixed phase regions possible, particularly when the sample is only partially ordered, such as a frustrated system or a spin glass (section 2.4). A complete phase diagram as a function of temperature, composition and magnetic field for a material of interest is one of the goals of solid state science.

2.3.4 Spin State Transitions

The fact the electrons in cobalt atoms can exist in three different spin states depending on the crystal field environment has already been discussed in section 2.1.2. This should be emphasised, as spin state transitions are not usually possible in perovskite manganites or cuprates, although they are possible in compounds containing Fe^{2+} [42]. Figure 2.8 illustrates the possible spin states for each of the three cobalt valencies.

In a perovskite, it would be expected that the cobalt valency is Co^{3+}, as it

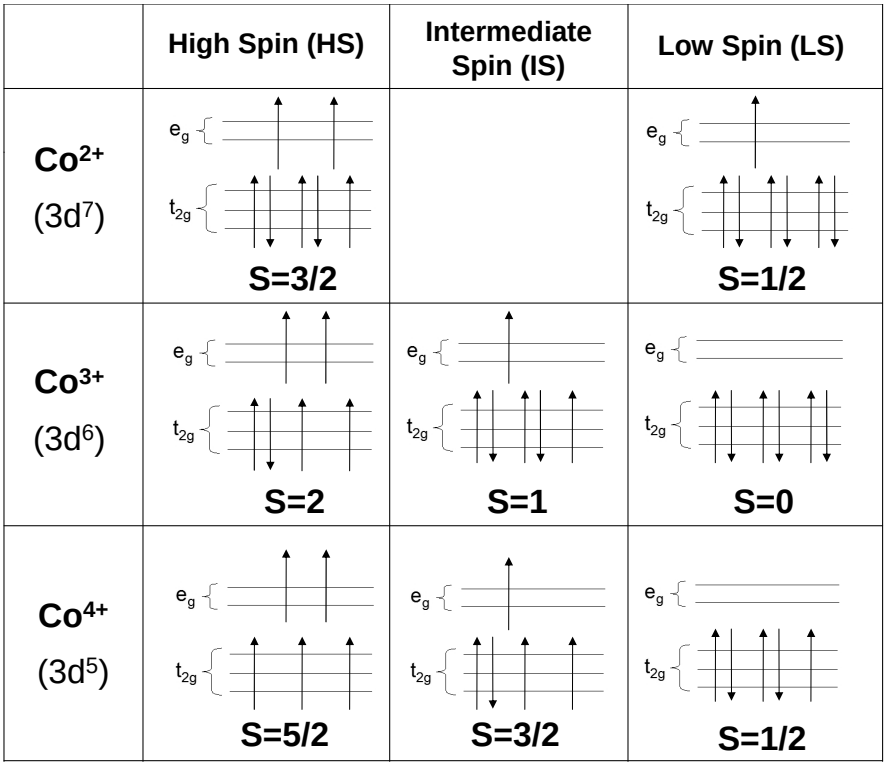

Figure 2.8: The electronic configuration for Co^{2+}, Co^{3+} and Co^{4+} in an octahedral environment in the high spin (HS), intermediate spin (IS) and low spin (IS) cases [57].

is in an environment surrounded by six oxygen atoms at the centre of a face-centred unit cell (oxygen has valency O^{2-}). The classic material which exhibits a spin state transition, $LaCoO_3$, is a rhombohedrally-distorted perovskite, so looking at figure 2.8 and assuming orbital quenching, $\mu = 2\sqrt{S(S+1)}\ \mu_B$ and the expected sizes of the moments for the possible spin states are $\mu = 0\ \mu_B$ for LS, $\mu = 2.83\ \mu_B$ for IS and $\mu = 4.90\ \mu_B$ for HS.

Cobalt atoms have different ionic radii in different spin states [6]. For Co^{3+}, the ionic radii are 0.545 Å, 0.560 Å and 0.610 Å for LS, IS and HS respectively. This means a spin state transition is accompanied by a corresponding change in the lattice parameter, with an expansion coinciding with a transition to a higher spin state. Other experimental evidence of spin state transitions comes from polarised neutron scattering [15] and NMR measurements [54]. As with other structural and magnetic transitions, the temperature at which a spin state transition occurs may be altered by pressure, illumination and composition, and the transition is shifted to a higher temperature when lanthanum is replaced by a larger lanthanide ion [6].

2.4 Novel Magnetic Behaviour

2.4.1 Frustration

In some magnetic systems, competing interactions mean there is no unique ground state. The term for a system with such degenerate ground states is frustrated. Probably the most common example is geometric frustration arising from triangular arrangements of spins which are antiferromagnetically coupled [55], shown in figure 2.9.

The effects of frustration mean some frustrated magnets will never reach a long-range ordered state. Spin-liquids are frustrated systems which have a high degree of correlation, but still retain fluctuations at the lowest temperatures [56]. Spin-ice materials are 3D spin-liquids where Ising spins sit on the apexes of corner-sharing tetrahedra, the so called pyrochlore lattice with chemical formula $A_2B_2O_7$. These systems have caused particular interest because of the discovery of 'magnetic monopoles', a semi-infinite string of spins with a magnetic charge, in spin-ice [56].

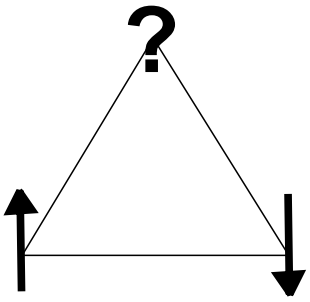

Figure 2.9: Antiferromagnetic nearest neighbour interactions on a 2D triangular lattice. It is not possible to orientate the three spins in such a way that the antiferromagnetic interactions between the three spins are satisfied [42].

2.4.2 Glassiness

Frustration can also be induced by site or bond-randomness, such as in the manganese substituted alloy $Cu_{1-x}Mn_x$ [42]. These materials are also known as dilute spin glasses because of the disorder such a substitution causes. Spin glasses are disordered magnetic systems which nevertheless exhibit a distinct magnetic transition at some well-defined temperature. Below the transition, the spins are frozen in a metastable magnetic state. The randomness may be chemical, such as the site or bond randomness discussed above, or due to competing interactions or magnetic anisotropy [42].

At temperatures well above the transition, the moments in a spin glass will be independent and uncorrelated. However, as the transition is approached the spins can become locally correlated, forming clusters. The magnetic ground state of such a material would be 'glassy' and usually displays time dependent behaviour. This would be signaled by a divergence in the dc-susceptibility and a sharp peak in the ac-susceptibility at the transition temperature. This behaviour has been seen in the perovskite $La_{1-x}Sr_xCoO_3$, where a model of short-range clustered ferromagnetism and intrinsic phase separation has been proposed [57].

2.4.3 Time Dependent Magnetic Behaviour

Although all transitions in real systems are to some extent time dependent, notably compounds in a 'glassy' regime, some correlated electron systems change state over much longer timescales. For magnetic systems, the measured value of τ can vary from 10^{-12} seconds to geological timescales.

The simplest mathematical description of a perturbed system returning to equilibrium is an exponential decay or Arrhenius equation, used to describe the dynamics of an activated process, typically a chemical reaction. This assumes that an energy barrier hinders the forward progress of a transition to a new state, and is given in equation 2.9 where E_a is the activation energy, T is the temperature and k is the rate coefficient:

$$k = Ae^{-\frac{E_a}{k_B T}} \tag{2.9}$$

This equation was recently used to describe the long-time variation of the magnetic structure in $CeIr_3Si_2$ [58]. In this material, there is a transition between magnetic phases at 1 K as a function of time with an activation energy $E_a/\mathrm{k}_B = 4$ K.

If a system has a range of activation energies, it may be necessary to use a stretched exponential to describe the time dependence. The stretched exponential can be used to provide a phenomenological description of relaxation in disordered systems. Traditionally, it has been used to describe the discharge of a capacitor, where it is known as the Kohlrausch function. The stretched exponential is defined

in equation 2.10,

$$P(t) = P_{eq} + [P(0) - P_{eq}]e^{-(t/\tau))^{\beta}} \tag{2.10}$$

where P is some order parameter with $P(0)$ and P_{eq} the initial and equilibrium values of the order parameter respectively, and τ is the characteristic relaxation time. The parameter β can take values satisfying $0 \leq \beta \leq 1$.

Time dependence plays a crucial role in the behaviour of many magnetic systems. An example of a family of magnetic materials where this is the case would be the systems of ferromagnetic nanoparticles known as superparamagnets. The magnetisation in these systems can flip direction, and the energy at which this happens is known as the activation energy, and the time dependence of this behaviour changes as a function of temperature. The magnetic particles cease to fluctuate and become 'locked-in' to some energy minima at some defined temperature [42]. A discussion of the role of time dependence in the magnetic behaviour of the compound $Ca_3Co_2O_6$ forms the core of chapter 8 of this thesis.

2.5 Excitations

2.5.1 Phonons

Lattice vibrations, quantized as phonons, are characterised by their dispersion relation which express the angular frequency $\omega(k)$ as a function of wavevector k (or energy $\hbar\omega$ and momentum $\hbar q$). The dispersion relation for 1D phonons is given in equation 2.11 [47], where m is the mass of the atoms and J is the force constant:

$$\omega(k) = \sqrt{\frac{2J}{m}(1 - \cos(ka))} \tag{2.11}$$

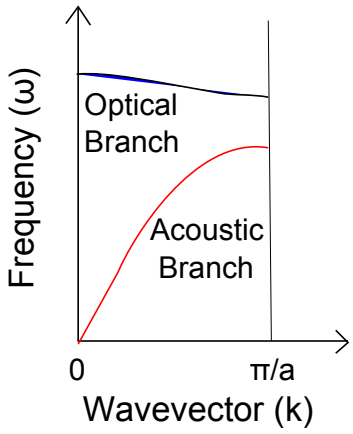

Figure 2.10: The phonon dispersion relation in the first Brillouin zone for a diatomic lattice.

Where there is more than one atom per cell, the dispersion relation has multiple branches, and in a diatomic lattice the optical branch is formed when atoms move together in-phase and the acoustic branch when the vibrations are out-of-phase. The key characteristics of these two branches are shown in figure 2.10, the acoustic phonons are gapless and the optical phonons are flatter and gapped at $k = 0$. Generally, for N atoms per unit cell there will be three acoustic branches, of which one will be longitudinal and two will be transverse, and $3N - 3$ optical branches.

Phonons are an important factor in measurements of the specific heat, and various models are used to describe their contribution. The empirical Dulong-Petit law states that the specific heat of a material is a constant 3R per mole of atoms as a function of temperature, where R is the gas constant. It was later shown that this is only valid in the high temperature limit, as the low temperature behaviour of the specific heat is a quantum phenomenon. The phonon contribution to the specific heat at constant volume (C_v) at low temperatures can then be modelled using equation 2.12:

$$C_v = \frac{12}{5}\pi^4 N k_B \left(\frac{T}{\theta_D}\right)^3 \tag{2.12}$$

Where N is the number of atoms, k_B is the Boltzmann constant, T is the temperature and θ_D is the Debye temperature. The Debye temperature can be expressed as a function of β as $\theta_D = \left(\frac{12}{5}\pi^4 p\mathrm{R}/\beta\right)^{1/3}$ where p is the number of atoms in each molecule and β is the quantity measured.

The Debye model is derived from the assumption of the propagation of an acoustic wave through an isotropic solid, and the Debye temperature is therefore temperature at which all the vibration modes are excited. The model predicts the heat capacity to vary as T^3, but the other contributions must be considered in any real measurement. A derivation of the electronic contribution to the specific heat for a free electron gas is given in reference [46], and it is predicted to vary as $C_v \propto T$. The combination of electronic and phonon contributions will therefore give a low temperature heat capacity as a function of temperature according to equation 2.13.

$$C_v(T) = \gamma T + \beta T^3 \tag{2.13}$$

There may also be Schottky and magnetic contributions, and the latter of these will be discussed in the next section.

2.5.2 Magnons

While lattice vibrations are quantised as phonons, fluctuations of the magnetic structure are quantised as magnons. Magnon spin waves can be described by a dispersion relation, given in equation 2.14 for a linear ferromagnetic chain, in the same vein as phonon lattice vibrations:

$$\hbar\omega(k) = 4\mathbf{JS}(1 - \cos(ka)) \tag{2.14}$$

It can be shown that for an isotropic ferromagnet these spin waves are gapless at $q = 0$ [42], although gaps may appear due to anisotropy. For ferromagnets, equation 2.14 can be simplified to $\omega(k) \propto q^2$ in the low q region. For antiferromagnets, the dispersion relation for a spin wave on a linear antiferromagnetic chain is

$\omega(k) \propto |\sin(qa)|$, where a is the separation between spins [59]. This means for antiferromagnets in the low q region, $\omega(k) \propto q$, where the constant of proportionality is the spin wave speed.

Magnon vibrations will contribute to the heat capacity just as the phonons do. Bloch derived the reduction in the spontaneous magnetisation at low temperature due to the thermal excitation of ferromagnetic magnon modes to be $\Delta M \propto T^{3/2}$ which implies the heat capacity is also proportional to $T^{3/2}$. For antiferromagnetic magnons, $C_v \propto T^3$, so antiferromagnetic spin waves can be difficult to distinguish from ordinary phonon modes in a heat capacity measurement.

2.6 Discussion

Both $Y_{1-x}Sr_xCoO_{3-\delta}$ and $Ca_3Co_2O_6$ are complex magnetic system in which many competing physical processes act in combination. The magnetic moments in these compounds are influenced by the crystal field environments, the neighbouring atoms and the shape of the d electron orbitals. These in turn may be altered as a function of temperature, pressure, chemical composition or applied magnetic field, resulting in a phase transition. Magnetic and structural phase transitions between the different states in these systems will be investigated as part of this thesis and the precise nature of the magnetic state in each regime will be studied. Various experimental methods will be used to make these investigations, including susceptibility and heat capacity measurements to examine the macroscopic properties of these two cobaltates and neutron scattering to probe the microscopic behaviour of the magnetic moments. Both powder and single crystal samples of $Ca_3Co_2O_6$ and $Y_{1-x}Sr_xCoO_{3-\delta}$ will be employed. The next chapter details the experimental techniques utilised in these studies.

Chapter 3

Experimental Techniques

This chapter details the four key experimental techniques which have been part of this study of the magnetic phases in $Y_{1-x}Sr_xCoO_{3-\delta}$ and $Ca_3Co_2O_6$; sample preparation, laboratory measurements of their physical and magnetic properties, X-ray diffraction and neutron scattering. These techniques are described in sections 3.1, 3.2, 3.3 and 3.4 respectively. Both polycrystalline and single crystal samples were used in this investigation, and the precise composition of each of the $Y_{1-x}Sr_xCoO_{3-\delta}$ samples was characterised using EDAX, TGA and X-ray diffraction. A substantial portion of this thesis concerns the diffraction, spin-polarised and inelastic neutron scattering measurements used to study the magnetic properties of $Y_{1-x}Sr_xCoO_{3-\delta}$ and $Ca_3Co_2O_6$, and the theoretical considerations behind these techniques are discussed in the latter part of this chapter.

3.1 Sample Preparation and Characterisation

3.1.1 Crystal Growth Techniques

The advantage of using single crystals in the study of strongly correlated electron systems is clear. Not only can the magnetocrystalline anisotropy of a material be measured but the uncertainty associated with the powder average is also eliminated. Single crystals of both $Y_{1-x}Sr_xCoO_{3-\delta}$ and $Ca_3Co_2O_6$ were investigated as part of work included in this thesis, and the preparation of the $Y_{1-x}Sr_xCoO_{3-\delta}$ single crystals using the floating zone technique forms a portion of the experimental work. $Ca_3Co_2O_6$ single crystals were prepared using a flux method by another researcher prior to the start of the work described [154].

Flux Growth

Flux growth is a solution method for growing single crystals where the appropriate reactants are dissolved in a solvent or flux to make a homogeneous solution and

then cooled slowly to promote spontaneous nucleation. The main advantages of this method are that the equipment required is simple, the timescale for the preparation of samples is relatively short, both congruently and incongruently melting materials can be grown and only small amounts of starting materials are needed.

The disadvantages of the flux growth method mean that it is not always the first choice of technique for the production of single crystals. The crystals formed using flux growth are usually small, and unsuitable for experiments requiring large sample volume. Furthermore, using this method can make the crystals difficult to extract from the crucible or flux, risking contamination, which means the outcome of such a growth can be unpredictable and several attempts may be required to successfully produce crystals.

The Floating Zone Method

In 1953 Siemens were granted a patent for the floating zone method for producing large single crystals of silicon. However, this technique has only been used for the growth of single crystals of magnetic materials and superconductors since the 1980's. Figure 3.1 shows a photograph and diagram of a two mirror NEC image furnace used for the production of single crystals using the floating zone method. A polycrystalline feed rod is suspended in the furnace above a polycrystalline or single crystal seed. The light from two halogen bulbs is focused onto the feed rod using two ellipsoidal mirrors. When the tip of the feed rod melts a molten zone is formed between the feed and seed rods, held by surface tension. The polycrystalline feed rod is slowly drawn through the molten zone and solidifies on the seed rod. The feed and seed rods are counter-rotated to ensure homogeneity of composition and temperature. Small adjustments to the rate of shaft movement, the shaft rotation speed and the power to the bulbs help to maintain the zone over the timeline of the growth, anywhere between hours and weeks.

The floating zone method ensures the solid crystal forms without contamination. The facilities at Warwick allow growth in an atmosphere of air, oxygen, nitrogen or argon up to 9 bars, according the compound, and the floating zone method has been found particularly useful for the growth of crystals of oxide materials. Suitable polycrystalline rods are produced by compacting the precursor powder into a waterproof membrane (a balloon!) and applying isostatic pressure. The rod is then sintered to preserve the shape. The seed may be the same composition or a different composition with the same lattice structure. The crystals produced are usually much larger than those made by a flux growth method, with a diameter of around 1 cm and lengths of several cm. This size makes them useful for experiments requiring a large volume, such as neutron scattering.

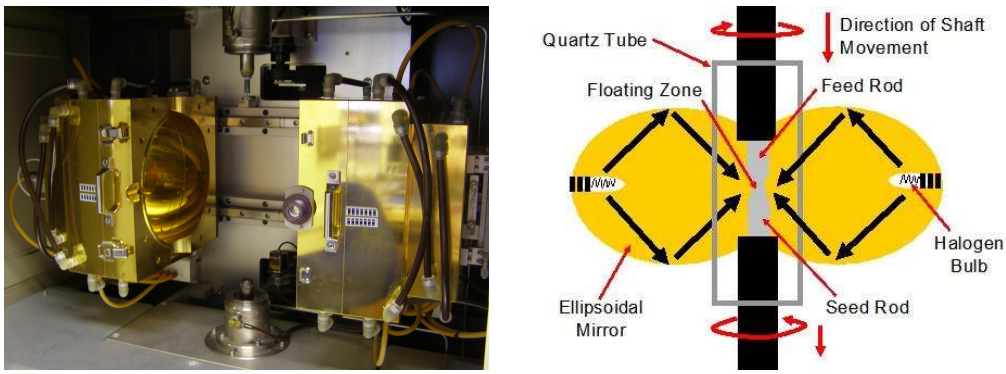

Figure 3.1: The key features of a floating zone image furnace. Ellipsoidal mirrors are used to form a molten floating zone which the polycrystalline feed rod is slowly drawn through.

3.1.2 Energy Dispersive Analysis using X-rays

EDAX (Energy Dispersive Analysis using X-rays) measurements to determine the final stoichiometry of the polycrystalline and single crystal samples were made using a JEOL 6100 scanning electron microscope with optional energy analysis. The beam of electrons interacts with the sample and an electron from an inner atomic shell may be excited to an outer shell. A higher energy electron then fills the hole and energy is given off in the form of an X-ray. The energy of that X-ray will be characteristic of the energy difference between the two energy levels, and so characteristic of the electronic structure of the element involved. From the resulting energy spectrum, peaks can be identified which are associated with particular elements. An example of the energy spectrum from a sample of Ca_3CoMnO_6 is shown in figure 3.2. The peaks corresponding to each of the elements are labelled, and their relative sizes can be used to calculate the population of these species in the sample.

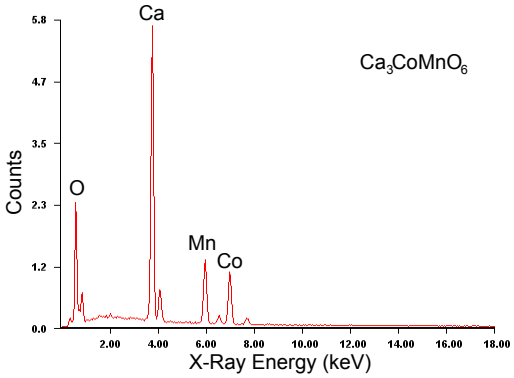

Figure 3.2: The EDAX spectrum of Ca_3CoMnO_6 taken on JEOL 6100 scanning electron microscope with optional energy analysis. The Kα peaks for the elements present are labelled.

The accuracy of EDAX as an analysis technique is known to be limited by several factors. Light elements are more difficult to detect as windows in front of the detector absorb low energy X-rays. Incorrect settings can alter the relative intensi-

ties of the peaks. Peaks may also overlap. Most importantly for the bulk samples studied in this thesis, EDAX is surface sensitive technique, and imperfections on the surface of a sample such as roughness or impurities can adversely affect the measurement.

3.1.3 Thermogravimetic Analysis

The oxygen content of perovskite cobalt oxides can be evaluated using a variety of methods. The two most commonly used of these are thermogravimetric analysis (TGA) and iodometric titration [60]. Both of these are redox processes where the cobalt species are reduced to those of lower valency, in the case of TGA to cobalt metal and in the case of iodometric titration to Co^{2+}. Thermogravimetric analysis involves heating the sample in a reducing atmosphere (3.5 % H_2 in Ar) and equation 3.1 shows the reduction process for a $Ln\mathrm{CoO}_{3-\delta}$ perovskite. Assuming the reduction is complete, the oxygen content can be derived from precise measurement of the change in mass.

$$Ln\mathrm{CoO}_{3-\delta}(s) + \mathrm{H}_2(\mathrm{g}) \rightarrow Ln\mathrm{O}(\mathrm{s}) + \mathrm{Co}(\mathrm{s}) + (3-\delta)\mathrm{H}_2\mathrm{O}(\mathrm{g}) \tag{3.1}$$

TGA measurements are often carried out in conjunction with heat flow measurements such as differential thermal analysis (DTA) and differential scanning calorimetry (DSC). This is because it allows differentiation between thermal processes involving no change in mass (e.g. melting) and those where the mass changes. The main advantages of TGA for oxygen content analysis are its relative simplicity and the extra thermal information gained during the measurement. Studies [60, 61] have shown that TGA and titration methods give the same result, but TGA is less precise, with the results showing greater scatter.

3.2 Physical and Magnetic Properties Measurements

3.2.1 dc-Susceptibility

dc-susceptibility measurements were made using a SQuID (Superconducting Quantum Interference Device) magnetometer, part of Quantum Design's Magnetic Property Measurement System (MPMS) [62]. The magnetometer consists of a second-order gradiometer (counter-wound pick-up coils) connected to two parallel Josephson junctions in a superconducting ring. The sample is mounted in a non-magnetic sample holder on a sample rod, shown in figure 3.3, and moved through the gradiometer so that a current is induced in the coils by electromagnetic induction. The SQuID then functions as an extremely sensitive current to voltage converter, outputting the change in magnetic flux measured by the pick-up coils as a dipole voltage re-

sponse. When calibrated to a sample of known mass and magnetic susceptibility, this response can be fitted to obtain the magnetic moment of the sample in electromagnetic units (emu). The sensitivity of the SQuID means signals of $5\text{x}10^{-8}$ emu can be measured with this system.

A superconducting magnet is incorporated into the MPMS system, enabling measurements to be made in applied magnetic fields (μ_0H) of up to 7 T, with a field uniformity of 0.01% over 4 cm. Magnetisation measurements can be made as a function of both temperature and applied magnetic field over a temperature range of 2 to 400 K. Temperatures up to 800 K can be achieved by using an optional furnace insert, but the sample must be mounted in an alumina sample holder to withstand the higher temperatures, which increases distortion of the dipole signal and therefore the background noise on the measurement.

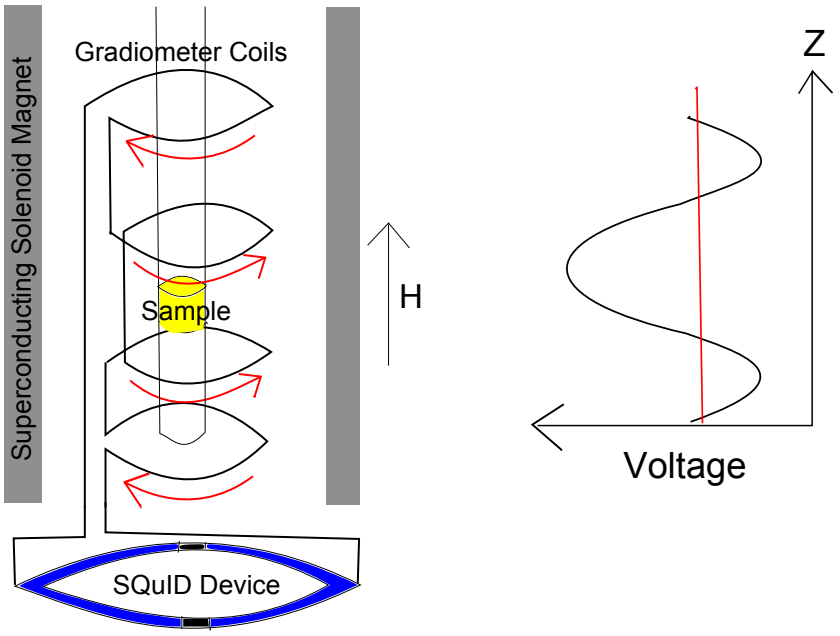

Figure 3.3: Schematic diagram of the MPMS system, showing the sample rod inside the pick-up coils connected to the SQuID device. The dipole voltage response recorded by the SQuID is shown on the right of the figure.

3.2.2 ac-Susceptibility

An ac-susceptibility option available for use with the MPMS was also utilised. While dc-susceptibility measurements record the equilibrium value for the magnetisation, ac-measurements yield information about the magnetisation dynamics in a material. A small ac drive field H_{ac} with frequency ω is applied to the sample in addition to any larger applied dc field, inducing a time dependent moment. The quantity measured $M_{ac} = (dM/dH) \cdot H_{ac} \sin(\omega t)$ is sensitive to the susceptibility $\chi = dM/dH$,

and features will be observed in the data where there are changes in the slope of the magnetisation. This means small changes in the magnetisation behaviour can be detected. When the sample response lags behind the driving field, and a phase shift is introduced into the equation above. This means the ac-susceptibility can be interpreted as having two components, the real χ' and imaginary χ'' parts, which probe dM/dH and dissipative processes in the sample respectively. For example, the irreversibly in spin-glasses leads to a non-zero χ'' which has a frequency dependence [63].

3.2.3 Specific Heat

Specific heat measurements were performed using a two-tau relaxation method in a Quantum Design Physical Properties Measurement System (PPMS). The sample is mounted on a stage which is suspended in the centre of the puck [64] to provide a controlled heat leak to the sample. The sample is attached to the stage using Apiezon H or N grease to ensure good thermal contact. The puck is then inserted into the PPMS, which is equipped with a 9 T magnet and capable of a temperature range of 1.9 to 400 K [64]. The heat capacity at a particular temperature is measured by inducing a small increase in temperature, around 2 % of the temperature of the sample, and recording the differences in temperature between the sample, sample stage and puck on warming and cooling.

The two-tau model for measuring heat capacity assumes the sample is not in good thermal contact with its surroundings [65]. Two time constants are taken from the relaxation times between the sample and sample stage and the sample stage and puck. This is then compared to a model involving perfect thermal contact between the sample and stage to give the relaxation model. An addenda measurement of the heat capacity of the sample stage and the heat capacity of the grease is also subtracted from the measured signal to give the sample heat capacity [65].

As discussed in section 2.5, there are may be phonon, electronic, Schottky and magnetic contributions to the heat capacity. In order to deconvolve these contributions, a phonon blank measurement is often made of a compound with the same crystal structure and molecular weight as the system of interest, but with no magnetic ordering. The phonon and electronic contributions of the two systems should then be the same, and then the phonon blank measurement can be subtracted to give the magnetic contribution to the heat capacity. The difference between the molecular weights of the sample and phonon blank may also be corrected for.

Heat capacity can also provide quantitative information about the entropy (S) of the system, the relationship between the two is given in equation 3.2.

$$C_V = T\left(\frac{dS}{dT}\right)_V \tag{3.2}$$

This can then be compared with expected entropy per mole of a saturated paramagnetic substance with total angular momentum J, $S = R\ln(2J+1)$, where R is the molar gas constant and C_v is the heat capacity at constant volume [66].

3.3 X-ray Scattering

3.3.1 Diffraction

Diffraction of X-rays, neutrons and electrons is the most important method of studying the crystal and magnetic structure of materials. The wavevectors $\mathbf{k}$ and $\mathbf{k}'$ of the incoming and outgoing beams in the diffraction experiment respectively are defined in figure 3.4. The scattering vector is then $\Delta\mathbf{k} = \mathbf{k}' - \mathbf{k}$ [46]. For elastic scattering the magnitudes of $\mathbf{k}$ and $\mathbf{k}'$ are equal, and for the special case of Bragg diffraction $\Delta\mathbf{k} = G$, where G a reciprocal lattice vector of the crystal structure under investigation. Diffraction is coherent elastic scattering from a crystal structure and is governed by Bragg's law, $n\lambda = 2d\sin\theta$, where n is the order of the reflection, λ is the wavelength of the incoming radiation, d is the lattice spacing and θ is the incident angle of the radiation. When the energy of scattered beam is allowed to change, the magnitudes of $\mathbf{k}$ and $\mathbf{k}'$ are not constrained to be equal and this is known as spectroscopy, discussed in detail later in the chapter.

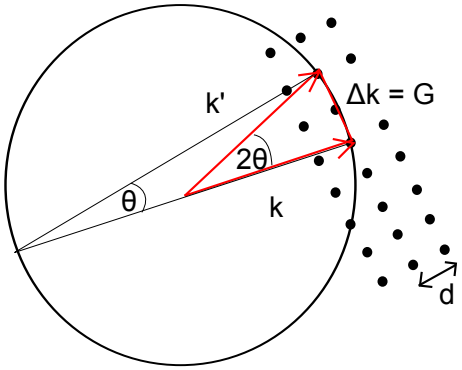

Figure 3.4: The Ewald sphere construction where **k** and **k'** are the wavevectors of the incoming and outgoing beams respectively. $\Delta\mathbf{k} = \mathbf{k}' - \mathbf{k} = G$, where G is a reciprocal lattice vector of the sample, d is the lattice spacing, θ is the incident angle of the wavevector and the Bragg condition is $\lambda = 2d\sin\theta$ (n =1).

3.3.2 Powder X-ray Diffraction

Powder X-ray diffraction is an extremely versatile technique which was used in this thesis both to assess the composition of compounds of interest by matching recorded patterns to those in a large database and for detailed analysis of the material structure. Rietveld refinement, described in section 3.3.5, was used to analyse the crystal structure and subtle structural changes in a material. However, this kind of analysis is non-trivial, as when we make a diffraction measurement no phase information is

incorporated into the measurement of the intensity $I = |F(hkl)|^2$. This is known as the phase problem. Many methods and assumptions are used to try and deal with this problem, for example in most crystalline materials we can assume centrosymmetry and the associated reduction in degrees of freedom that can be made from this assumption is known as Friedel's law.

Powder diffractometers may be set up in several geometries. In a traditional Debye-Scherrer geometry, the detector moves in a circle around the sample. More common in modern diffractometers is the Bragg-Brentano geometry, where the detector and sample are moved so that the detector is always at an angle of 2θ and the sample surface is always an angle of θ to the incident X-ray beam. In Bragg-Brentano geometry there is a sensitivity to errors in the sample height which are corrected by the addition of an offset. The X-ray sources used for the powder diffraction experiments described in this thesis were all copper-based, and some were monochromated to improve the resolution.

3.3.3 Laue Diffraction

The Laue method is used to determine the orientation of single crystals and align them along particular directions. The beam is not monchromated, so a range of wavelengths, a white beam, is used. This means many diffraction events happen simultaneously and a whole plane of reciprocal space can be probed in a single measurement. The recorded images can then be compared to those predicted from the knowledge of the crystal structure of the material, this was done using the OrientExpress software package.

The X-ray Laue camera used in this work is operated in backscatter geometry, and the incident X-ray is fired through the centre of the scintillator screen and then backscattered towards the screen by the crystal. The peak emission of the (terbium-doped gadolinium oxysulfide) scintillator screen is at 500 nm, which matches the quantum efficiency response of the charge-coupled device (CCD) used to detect the diffracted X-rays.

The Laue system is remotely controlled from a computer, which means multiple images can be recorded in sequence. The voltage and current of the X-ray tube can be altered, although there is an overall limit on the output power. The exposure times and number of images recorded can also be manipulated. The computer system is also used to remotely control a triple-axis xyz goniometer which allows both rotation and translation about the three axes.

3.3.4 Single Crystal X-ray Diffraction

Monochromated X-rays can be used to improve the resolution of powder and single crystal diffraction experiments. As part of this thesis they were used to map the intensities of the single crystal Bragg peaks using a single crystal diffractometer. A significant percentage of the Ewald sphere can be collected by collecting multiple frames using a large area CCD detector. A kappa-geometry goniometer moves the sample so that the majority of reciprocal space can be accessed. The parameters for a run, including the step size and X-ray voltage are optimised for a particular sample by performing a pre-experiment. Measurements at temperatures from 77 to 400 K are possible through use of a cryo-jet and either molybdenum or copper X-ray sources can be used.

Figure 3.5: An Oxford Diffraction CCD single crystal diffractometer. The figure shows the sample on a four-circle goniometer, the cryo-jet, X-ray source, CCD and beam stop.

Post-experiment outlier rejection is performed by selecting a particular Laue group under which to perform the integration. This means any reflections which break the Laue symmetry are discarded. A correction for X-ray absorption by the sample is also implemented post-experiment by fitting using a Gaussian-grid method and adjusting for the shape of the sample.

3.3.5 Rietveld Refinement

Various methods have been developed to account for the phase problem discussed in section 3.3.2. One of these is the Rietveld method, an algorithm for fitting diffraction patterns which minimises the difference between the experimental data and a model based on the profile information, crystallographic parameters and atom positions. The space group, lattice parameters, Wyckoff positions and Debye-Waller factors (isotropic thermal parameters, B) are all specified in the model. The atomic form factor (discussed in section 3.4.3) is internally accounted for by specifying the element positioned on each lattice site. The background is fitted with either a polynomial or by specifying a series of interpolated points. Additional parameters can also be specified including; the peak broadening, detector zero error, absorption, preferred orientation or anisotropic temperature factors. The difference between the observed and calculated profiles is minimised based on a least-squares regression.

The profile functions used in this thesis are specified in table 3.1. The Gaussian function implies a normal distribution, and would be the expected peak shape

for a perfect crystal with a single long-range ordering or only instrumental line broadening. The Lorentzian function implies homogeneous broadening by some physical mechanism. The combination of the two broadening mechanisms is a Voigt function, approximated to a Pseudo-Voigt for computational purposes. More complicated functions are possible, including those that allow for asymmetric line broadening. Peak broadening may also be due to strain in the sample, which can also be incorporated in the refinement model.

Peak Shape	Function
Gaussian G(x)	$y = y_0 + \frac{A}{\omega\sqrt{\pi/2}} e^{-2\frac{(x-x_c)^2}{\omega^2}}$
Lorentzian L(x)	$y = y_0 + \frac{2A}{\pi} \frac{\mathrm{w}}{4(x-x_c)^2 + \mathrm{w}^2}$
Pseudo-Voigt	$y = (1-\eta)G(x) + (\eta)L(x)$

Table 3.1: The mathematical definitions of the Gaussian, Lorentzian, Pseudo-Voigt peak profile functions. The peaks are described by the offset y_0, peak area A, peak centre x_c, full width half maximum w and mixing coefficient η. The FWHM w is related to the Gaussian width ω by $\omega = \mathrm{w}/\sqrt{\ln(4)}$.

Rietveld refinement should not be used to determine the space group as the method imposes conditions which might not be valid for an unknown space group [53]. Rather, profile matching, simulated annealing or symmetry considerations should be used to determine a space group, and refinement can then be employed to get a full description of the details of the crystal structure.

3.4 Neutron Scattering

3.4.1 Properties of Neutrons

X-ray and neutron scattering serve as complementary techniques due to their different atomic scattering mechanisms. While X-rays respond according to the number of electrons in an atom and can have limited penetration into the bulk of a material, neutrons scatter from the nucleus and have a much higher penetrating capacity. This means neutrons are sensitive to different isotopes of a material and the scattering is not proportional to the atomic number, which means unlike X-rays, neutrons can be used to probe materials containing the lightest elements. Neutrons are a natural technique for the study of magnetism, as the neutron has spin-1/2 and will interact with the magnetic moments present in the compound. Additionally, neutrons can be used to study both magnetic and non-magnetic excitations in materials, as the energy of thermal neutrons is comparable to the energy of lattice vibrations and the neutron wavelength is comparable with typical interatomic distances in solids.

Peak Shape	Function
Profile Factor	$R_p = 100 \left(\frac{\sum_i \lvert y_i - y_{c,i} \rvert}{\sum_i y_i} \right)$
Weighted Profile Factor	$R_{wp} = 100 \left(\frac{\sum_i w_i \lvert y_i - y_{c,i} \rvert^2}{\sum_i w_i {y_i}^2} \right)^{1/2}$
Expected Weighted Profile Factor	$R_{exp} = 100 \left(\frac{n-p}{\sum_i w_i {y_i}^2} \right)^{1/2}$
Bragg Factor	$R_{Bragg} = 100 \left(\frac{\sum_i \lvert I_{Obs,i} - I_{Calc,i} \rvert}{\sum_i I_{Obs,i}} \right)$
Reduced Chi-Squared	$\chi^2 = \left(\frac{R_{wp}}{R_{exp}} \right)^2$

Table 3.2: The conventional agreement factors for any refinement, where w_i is the variance of the observation y_i and $y_{c,i}$ is the calculated value of y at the position i. I_{Obs} and I_{Calc} are the observed and calculated integrated peak intensities. Finally, $n - p$ is the number of degrees of freedom where n is the total number of points in the refinement and p is the number of refined parameters.

The quantity measured in a neutron scattering experiment is the cross-section σ, where the total scattering cross-section is the number of neutrons scattered in all directions per second per unit of incident neutron flux. The number of neutrons scattered per second into a solid angle $d\Omega$ per unit incident flux per solid angle $d\Omega$ is known as the differential cross section $d\sigma/d\Omega$, which is the quantity measured in a diffraction experiment. If there is an energy change, such as in a neutron spectroscopy experiment, the quantity measured is the double differential cross-section $d^2\sigma/d\Omega dE_f$, where the final energy of the scattered neutrons is between E_f and $E_f + dE_f$. The geometry of a neutron scattering experiment is illustrated in figure 3.6.

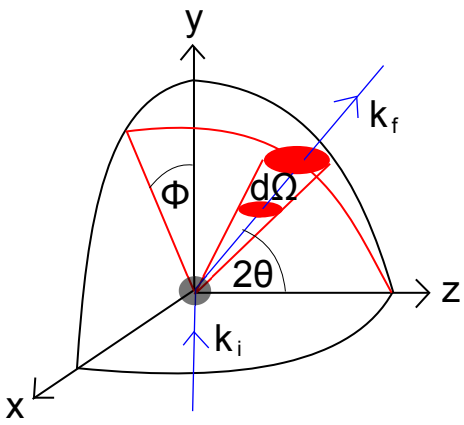

Figure 3.6: The geometry of a scattering experiment

The strength of the scattering from the nucleus of a particular element is described by the scattering length b, which is usually independent of wavelength but dependent on spin and isotope. This quantity is usually determined experimentally and recorded in look-up tables. The relationship between scattering length and the total scattering cross-section is given in equation 3.3.

$$\sigma_{Tot} = \frac{\text{Scattered flux}}{\text{Incident flux}} = 4\pi b^2 \tag{3.3}$$

The spherical wave ψ_f scattered by an isolated nucleus can be expressed in terms of the scattering length $\psi_f = -be^{ikr}/r$, where r is the the radius of the scattered wave. By convention the nomenclature for the neutron scattering vector $\mathbf{k_i} - \mathbf{k_f}$ is $\mathbf{Q}$, as opposed to the $\mathbf{\Delta k}$ used in the X-ray case. The differential and double differential cross-sections can then be expressed in terms of these quantities, and the differential cross-section as a function of b and is given in equation 3.4 (for a derivation see reference [67]).

$$\frac{d\sigma}{d\Omega} = \frac{d\sigma_{Coh}}{d\Omega} + \frac{d\sigma_{Incoh}}{d\Omega} = \sum_{j,j'} \langle b \rangle^2 e^{i\mathbf{Q}\cdot(r_j - r_{j'})} + \sum_j (\langle b^2 \rangle - \langle b \rangle^2) \tag{3.4}$$

This equation can be separated into the coherent and incoherent scattering terms, where the coherent scattering assumes an average value of b for each nucleus and gives information about interference effects, and the incoherent term gives the mean-square deviation of the scattering length from the average value. In a powder experiment, the recorded pattern will consist of two components, the Bragg peaks associated with the coherent scattering and an incoherent background.

3.4.2 Sources of Neutrons

For quantitative studies of condensed matter using neutrons, large fluxes are required. These can be generated using either a fission reactor or a spallation source. Of the sources used for the work in this thesis, the Institute Laue-Langevin (ILL) in Grenoble, France houses a reactor source, ISIS at the Rutherford-Appleton Laboratories in Oxfordshire is a spallation source and Orphee at the Laboratoire Leon Brillouin, Saclay, Paris, France is also a reactor source.

Both ILL and Orphee use uranium 235 as the fission fuel with heavy water at a temperature of 300 K as a moderator producing thermal neutrons, which are used for most of the instruments. Hot and cold neutrons are produced using 2400 K graphite and 25 K liquid hydrogen respectively. Water used as a coolant also serves as an additional moderator. Reflecting neutron guide tubes can be used to direct the neutron flux to the experimental halls where the instruments are installed.

Spallation occurs when high energy particles are accelerated into the nuclei of heavy atoms, igniting a chain reaction which results in the emission of a selection of nucleons including neutrons. At ISIS, protons are accelerated into a tungsten target. The high energy protons are produced in a linear accelerator (linac) and are accelerated to above the threshold energy for spallation in a synchrotron. The neutrons produced by the spallation process are moderated by 300 K water, 105 K liquid methane or 25 K liquid hydrogen before use on the beamlines.

Spallation and reactor neutron sources each have their own advantages and disadvantages. Reactor sources are intrinsically more reliable, partially because of their relative simplicity and partially because their components are usually manufactured with more inherent fail safes because of the safety implications of using a fission source. However, as the power levels needed to run a spallation source are far lower, the problem of cooling is much less critical. Time of flight at ISIS benefits from it being a pulsed source, giving a time structure to the beam, which is particularly advantageous when carrying out inelastic experiments as a complete data set can be collected in one measurement. In addition, higher resolution is possible when short pulses are used, such as at the spallation source ISIS, because of the high resolution over a wide **Q** range.

3.4.3 Neutron Diffraction

Neutron diffraction can be performed on both pulsed and continuous sources using fixed-angle or fixed-wavelength methods respectively. A fixed-wavelength powder diffractometer will have a pair of collimators to reduce the angular divergence of the incident and scattered beams. A crystal monochromator is sited before the sample to select a single wavelength. For a fixed-angle technique, a white beam of neutrons is incident on the sample. The wavelength is determined by measuring the time of flight

from source to detector. The resolution can therefore be improved by increasing the flight path of the neutrons, for example the HRPD powder diffractometer at ISIS is located approximately 100 m from the target.

Neutrons are detected by neutron capture, usually by the nuclei of ^{3}He, ^{10}B, ^{6}Li and ^{235}U, depending on the detector. Beam monitors for recording the incident flux detect neutrons by the ionisation of uranium hexafluoride UF_6. Most instruments use ^{3}He and BF_3 gas detectors, where the capture of a neutron causes an exothermic nuclear reaction and ionisation in the gas. This ionisation is collected by an anode wire at high voltage. In most modern instruments, many of these gas detectors are collected together in banks or modified gas detectors are used as proportional counters, both of which are built into large position sensitive arrays of detectors.

Like any other kind of diffraction, both powder and single crystal neutron diffraction obey Bragg's law, equation 3.5. However, corrections must be made in the process of taking both these measurements for preferred orientation in the case of powder diffractions and for absorption, extinction and multiple scattering in the case of single crystals. Absorption has already been discussed, as it is generally a larger effect for X-rays than for neutrons. Extinction is a problem for larger samples and is due to the reflection of some of the incident radiation by the surface of the sample so that the bulk of crystal has less probability of scattering. Multiple diffraction arises when more than one family of planes satisfies the Bragg condition.

$$\mathbf{Q} = \frac{4\pi \sin 2\theta}{\lambda} \tag{3.5}$$

The way an incident beam is scattered by the atoms in a unit cell is described by the structure factor, which is the Fourier transform of the unit cell. The measured intensity is then proportional to the square of the structure factor, $I = |F(hkl)|^2$. For neutron diffraction, there will be both nuclear F_N and magnetic components F_M, given in equation 3.6 [47, 68, 67] for phase angle $i\mathbf{Q} \cdot \mathbf{r_i}$.

$$|F_{hkl}|^2 = |F_N|^2 + |F_M|^2 = |\sum_j \bar{b_j} e^{i\mathbf{Q}\cdot\mathbf{r_j}} e^{-W_j}|^2 + |\sum_j p_j \mathbf{q_j} e^{i\mathbf{Q}\cdot\mathbf{r_j}} e^{-W_j}|^2 \tag{3.6}$$

The factor e^{-W_j} is the Debye-Waller temperature contribution and $\bar{b}$ is the mean nuclear scattering length. Analogously, p is the magnetic scattering length and $\mathbf{q}$ is the magnetic scattering vector, introduced because only the component of the moment perpendicular to the scattering vector will result in magnetic scattering. As with the nuclear structure factor, the magnetic structure factor gives the Fourier transform of the magnetisation distribution in the lattice. Unlike the nuclear scattering length, the magnetic scattering length p can be defined in terms of the properties

of the scattering nucleus:

$$p = \left(\frac{e^2\mu_n}{m_e c^2}\right) \mathbf{S} f_M(\mathbf{Q}) \tag{3.7}$$

Equation 3.7, where μ_n and $\mathbf{S}$ are the neutron magnetic moment and spin quantum number respectively, introduces the magnetic form factor $f_M(\mathbf{Q})$. This quantity describes how the magnetic scattering depends on $\mathbf{Q}$. It is necessary because the magnetisation distribution in a crystal is much more diffuse than the nuclear one and so scattering takes place across a much larger spatial volume. An analytical approximation to the magnetic form factor exists, and can be expressed in terms of functions which describe the distribution of spin and current densities, $\langle j_0(\mathbf{Q})\rangle$ and $\langle j_2(\mathbf{Q})\rangle$ [69], equation 3.8.

$$f_M(\mathbf{Q}) = \langle j_0(\mathbf{Q})\rangle + \left(1 - \frac{2}{g_J}\right) \langle j_2(\mathbf{Q})\rangle \tag{3.8}$$

These are available in look-up tables for particular elements. In $3d$ ions such as cobalt we can assume orbital quenching, so $g_J = g_S = 2$. The calculated form factor for Co^{3+} is shown in figure 3.7 and shows the strong $\mathbf{Q}$ dependence of this function, which explains the necessity of measuring magnetic Bragg peaks at low scattering angles.

3.4.4 Polarisation Analysis

The instrument D7 at the ILL, results from which are included in chapters 6 and 8, is equipped with xyz polarisation analysis. This is the only technique which allows the separation of nuclear and magnetic contributions to the scattering. The polarisation process requires a high flux, as there are high losses during the polarisation process. On D7, this high flux is achieved at the expense of Q resolution.

The polarisation process involves the addition of four key components. The incident neutron beam is first polarised using a Scharpf bender-type supermirror polariser. The polarisation direction is then manipulated using a Mezei-type flipper and a set of xyz field coils. The polarisation of the scattered beam is analysed by a large bank of supermirror analysers. A 20 Gauss guide field exists everywhere within D7 to maintain the polarisation of the beam. The polarisation of the detected neutron beam will be either spin flip (SF) or non-spin flip (NSF) with respect to the polarisation of the incident beam. For spin flip scattering in the z channel, a neutron will be polarised spin up, be flipped to spin down, rotated along the z axis and spin flipped in the sample by interaction with any magnetic moments parallel to the neutron spin. The analyser will then select only those neutrons with polarisation spin up, which have necessarily been scattered by a magnetic atom with a component of its spin along z. For a detailed description of the polarisation

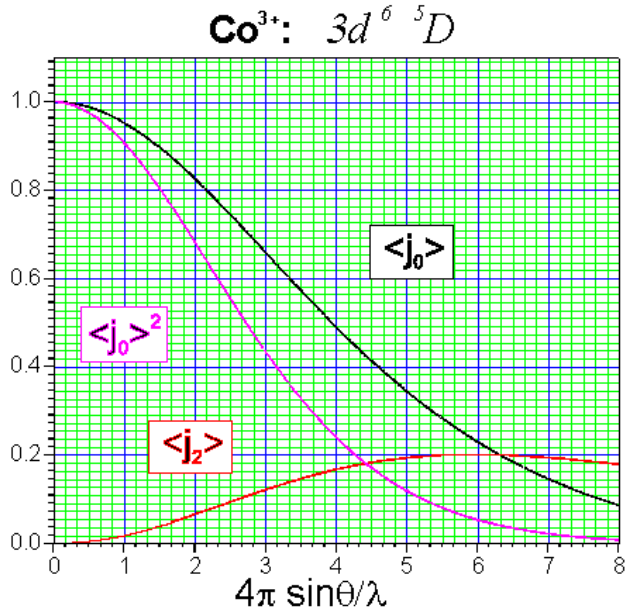

Figure 3.7: The calculated magnetic form factor for Co^{3+} where $f_M(\mathbf{Q}) = \langle j_0(\mathbf{Q})\rangle + \langle j_2(\mathbf{Q})\rangle$. Figure taken from reference [69].

analysis available on D7 see references [67] and [70].

The scattered neutrons from six different incident spin flip configurations are recorded to complete a single polarisation measurement. These are $\left(\frac{d\sigma}{d\Omega}\right)^{x}_{SF}$, $\left(\frac{d\sigma}{d\Omega}\right)^{y}_{SF}$, $\left(\frac{d\sigma}{d\Omega}\right)^{z}_{SF}$, $\left(\frac{d\sigma}{d\Omega}\right)^{x}_{NSF}$, $\left(\frac{d\sigma}{d\Omega}\right)^{y}_{NSF}$ and $\left(\frac{d\sigma}{d\Omega}\right)^{z}_{NSF}$ respectively. The dependence of each of these differential cross-sections on the coherent, magnetic and spin incoherent scattering components for a paramagnetic system can be derived from the spin-dependent scattering amplitudes, shown in references [68] and [70]. Dependence of the coherent, magnetic and spin incoherent scattering on these six individual measurements can then be easily calculated, and these are given in equations 3.9, 3.10 and 3.11 respectively.

$$\left(\frac{d\sigma}{d\Omega}\right)_{Coh} = \frac{1}{6}\left[2\left(\frac{d\sigma}{d\Omega}\right)^{xyz}_{NSF} - \left(\frac{d\sigma}{d\Omega}\right)^{xyz}_{SF}\right] \tag{3.9}$$

$$\left(\frac{d\sigma}{d\Omega}\right)_{Mag} = 2\left(\frac{d\sigma}{d\Omega}\right)^{x}_{SF} + 2\left(\frac{d\sigma}{d\Omega}\right)^{y}_{SF} - 4\left(\frac{d\sigma}{d\Omega}\right)^{z}_{SF} \tag{3.10}$$

$$\left(\frac{d\sigma}{d\Omega}\right)_{Incoh} = \frac{1}{2}\left(\frac{d\sigma}{d\Omega}\right)^{xyz}_{SF} - \left(\frac{d\sigma}{d\Omega}\right)_{Mag} \tag{3.11}$$

There are limitations to the applicability of the xyz polarisation technique and the above equations are only valid for magnetic materials with collinear magnetisation and a randomly ordered magnetic moment. This excludes ferromagnetic systems which by definition have spontaneously ordered spins and will depolarise the beam, which in itself can be used as a test for the presence of ferromagnetic correlations. Care must also be taken when measuring single crystals of antiferromagnetic materials, where then can be a possible change of sign of the moment direction if the crystal is not aligned such that the angle between **M** and **Q** is known.

3.4.5 Magnetic Refinement

Several methods exist for the quantitative analysis of neutron diffraction data from magnetic systems. The most accurate method is that of representational theory, which a detailed symmetry analysis of the system is carried out. The method involves a high level of group theory, and hence has not been used in this thesis. The formalism employed here is an extension of the process involved with the refinement of nuclear structures, where the magnetic structure, see 2.2.2, is also defined. Magnetic and nuclear structures are not usually refined simultaneously. Rather, the nuclear structure is refined at a temperature where the sample is paramagnetic or using X-ray data and then fixed during the refinement of the data taken in the magnetic regime.

3.4.6 Inelastic Neutron Scattering

Phonons and magnons in magnetic materials are studied by measuring the double differential cross-section using inelastic neutron scattering. On a reactor source, the instrument used is usually a triple-axis spectrometer and on a pulsed source a time-of-flight spectrometer is used which may employ a monochromated or white incident beam where the final energies of the neutrons are analysed.

A triple-axis spectrometer uses a monochromating crystal to select the incident energy of the beam, which will then have incident wavevector $\mathbf{k}_i$ and defines the first axis of rotation. The crystal is orientated on a second rotation axis so that the neutrons scatter off the Bragg plane of interest. An analyser crystal on a third rotation axis then selects the final wavevector $\mathbf{k}_f$. For coherent inelastic scattering from a single excitation, the neutron scattering vector is directly related to the wavevector transfer, stated in equation 3.12.

$$\mathbf{Q} = \mathbf{k_i} - \mathbf{k_f} \tag{3.12}$$

The relationship between $\mathbf{k}_i$, $\mathbf{k}_f$ and $\mathbf{Q}$ in a reciprocal lattice is illustrated in figure 3.8, where ϕ and ψ are angles that can be varied. During a measurement, either $\mathbf{k}_i$, $\mathbf{k}_f$ or both can be varied. The effect of modifying ϕ and ψ while keeping k_i and $\mathbf{Q}$ constant is to make a scan as a function of energy transfer. Conversely, the effect of keeping k_i and k_f the same while varying their direction, and therefore varying $\mathbf{Q}$, is to make a scan as a function of $\mathbf{Q}$ at constant energy transfer. Both these kinds of measurement can be made on a triple-axis spectrometer.

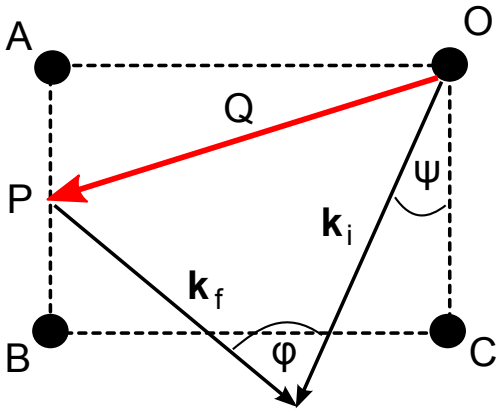

Figure 3.8: The relationship between Q, $\mathbf{k}_i$ and $\mathbf{k}_f$ in a reciprocal lattice for an inelastic neutron scattering experiment. ϕ and ψ are angles of the sample and analyser respectively that can be varied, and A, B and C are reciprocal lattice points with origin O, with P the point being probed. Adapted from reference [67].

3.5 Discussion

A range of techniques have been used to study the structure and magnetism in the complex cobaltates $Y_{1-x}Sr_xCoO_{3-\delta}$ and $Ca_3Co_2O_6$. Polycrystalline and single crystal samples have been prepared and characterised using EDAX, TGA and X-

ray diffraction. The physical and magnetic properties of the prepared samples have then been measured using magnetometry and heat capacity respectively. A variety of X-ray and neutron scattering measurements have also been made. The structure and magnetism in $Y_{1-x}Sr_xCoO_{3-\delta}$ are discussed in chapters 5 and 6 respectively. Chapters 8 and 9 then detail neutron scattering measurements on $Ca_3Co_2O_6$ measurements first made as a function of time and temperature and then as a function of applied magnetic field. The experimental work on each of these compounds is preceded by a literature review chapter.

Part II

$\mathbf{Y}_{1-x}\mathbf{Sr}_{x}\mathbf{CoO}_{3-\delta}$

Chapter 4

$Y_{1-x}Sr_xCoO_{3-\delta}$: Introduction

$Y_{1-x}Sr_xCoO_{3-\delta}$ is a member of the family of the doped perovskite cobaltates with general formula $Ln_{1-x}Sr_xCoO_{3-\delta}$, where Ln is a lanthanide ion. The archetype perovskite cobaltate is $LaCoO_3$ [71], which exhibits at least one spin state transition as a function of temperature. The initial attempts to control the properties of $LaCoO_3$ focused on doping with strontium, and the compound $La_{1-x}Sr_xCoO_3(0 < x < 0.5)$ has been found to be a spin glass in the region $0 < x < 0.18$ [72]. At higher doping ($0.18 \leq x \leq 0.5$) the behaviour has been characterised as that of a cluster glass, and intrinsic magnetic phase separation is believed to be the mechanism for the observed weak ferromagnetism in this system [57, 73].

Research has implied that $Y_{1-x}Sr_xCoO_{3-\delta}$ is also a weak room temperature ferromagnet. The source of the ferromagnetic signal in $Y_{1-x}Sr_xCoO_{3-\delta}$ is a matter of some debate. Early work [23] suggested magnetic phase separation, with ferromagnetic regions existing within a long-range ordered antiferromagnetic matrix was the mechanism for the observed weak ferromagnetism in $Y_{1-x}Sr_xCoO_{3-\delta}$ as well as $La_{1-x}Sr_xCoO_3$ ($0.18 \leq x \leq 0.5$). However, most reports [22, 25] have implied spin canting is responsible for the ferromagnetic signal, and papers contemporary with the work in this thesis have suggested ferrimagnetic order in $Y_{1-x}Sr_xCoO_{3-\delta}$ [24, 45].

4.1 $SrCoO_{3-\delta}$

The cobaltate $SrCoO_{3-\delta}$ has a cubic perovskite crystal structure with space group $Pm\bar{3}m$ [74]. The strontium ions sit on the A-site of the general perovskite cell with formula ABO_3, and the cobalt ions sit on the B-site (figure 1.2). The compound can form in such a way that it is oxygen deficient from the ABO_3 perovskite by a factor of δ resulting in oxygen vacancies in the structure.

The magnetic properties of $SrCoO_{3-\delta}$ have been studied for more than 50 years [75]. Early studies [75, 76] highlighted the features of the magnetic behaviour

of these materials that still dominate discussion today, ferromagnetic behaviour and the sensitivity to changes in oxygen concentration. Magnetisation measurements showed evidence of both ferromagnetic and antiferromagnetic behaviour depending on the preparation conditions, originally discussed in terms of double exchange which had only recently been postulated [77, 78]. The Curie temperature was found to vary with oxygen concentration, with an increase in oxygen content (and therefore an increase in the percentage Co^{4+}) leading to an observed increase in T_c. The T_c for $SrCoO_3$ was found to be 222 K [76].

Single crystals of $SrCoO_{3-\delta}$ have previously been prepared using the floating zone method [74, 80] and characterised using magnetic measurements and neutron diffraction [79]. The magnetocrystalline anisotropy of both oxygenated and oxygen deficient $SrCoO_{3-\delta}$ was measured. This anisotropy was found to be greatest for the fully oxygenated compound, whereas the most oxygen deficient compound, declared to be $SrCoO_{2.70}$, was virtually isotropic. By synthesizing the compound under high oxygen pressure, the oxygen deficiency was substantially reduced, which raised the T_c above room temperature [81]. The same research postulated the existence of a magnetovolume effect in this compound, a correlation between changes in the unit cell volume and the magnetic transition.

Instead of using complex synthesis conditions, the pure perovskite form of $SrCoO_{3-\delta}$ can be stabilised by doping with around 5% of rare earth (Sm^{3+}-Yb^{3+}) [82]. Examination of the different $Ln_{0.05}Sr_{0.95}CoO_{3-\delta}$ compounds revealed different phase behaviour depending on the ionic radius of the rare earth species. Only rare earth ions smaller than neodymium form phase pure perovskite structures. In fact, all these compounds were found to form tetragonal superstructures when stabilised in the perovskite form. The magnetic measurements showed the yttrium-doped form of $Ln_{0.05}Sr_{0.95}CoO_{3-\delta}$ had the lowest T_c (99 K) and χ of the compounds studied, and the dysprosium and holmium-doped forms had highest χ. This highlighted the importance of the magnetic coupling between the cobalt and the rare earth moments [82], as both holmium and dysprosium are magnetic ions, whereas yttrium is non-magnetic.

4.2 Crystal Structure of $Y_{1-x}Sr_xCoO_{3-\delta}$

The recent interest in yttrium-doped $SrCoO_{3-\delta}$ was ignited when a detailed structural study of $Sr_{0.7}Y_{0.3}CoO_{2.62}$ was published in 2003 [83]. The study focuses on the role of oxygen vacancies in determining the superstructure of this and similar perovskite compounds. For example the oxygen deficient compound $SrCoO_{2.5}$ adopts a brownmillerite (Ca_2FeAlO_5 [84]) type structure [85] with layers of CoO_6 octahedra and CoO_4 tetrahedra alternating along the a axis of the $Ima2$ space group.

$Sr_{0.7}Y_{0.3}CoO_{2.62}$ was found to have a similar structure, with oxygen vacancies occupying alternating layers of the tetragonal $I4/mmm$ crystal structure. Additional superstructure peaks indicating an orthorhombic distortion were also observed for some crystallites using electron microscopy, but as these peaks were not observed in the synchrotron or neutron diffraction patterns, they were not included in the structural analysis. It was suggested the driving force behind the formation of this structural phase may be the ordering of the Y^{3+} and Sr^{2+} ions on the A-site of the perovskite substructure.

Later structural studies of this compound investigated the complex arrangement of the atoms in $Y_{1-x}Sr_xCoO_{3-\delta}$ in more detail. A series of investigations used electron diffraction and X-ray diffraction to image a selection of superstructure peaks which have been assigned to a range of different space groups; some tetragonal ($I4/mmm$) [83, 86], some orthorhombic ($Cmcm$, $Cmma$) [21, 87, 88] and even monoclinic ($A2/m$) [89, 90]. The complication is due to the potential for A-site, oxygen vacancy [91, 92] and orbital ordering [45, 93], giving an unusual number of structural degrees of freedom. The largest and most complex superstructures have been reported in the solid solution range ($0.750 \leq x \leq 0.850$) [21] for the yttrium-doped compound. The details of the structure of $Y_{1-x}Sr_xCoO_{3-\delta}$ will be discussed in further detail in Chapter 5.

4.3 Magnetism in $Y_{1-x}Sr_xCoO_{3-\delta}$

It has been claimed that $Y_{1-x}Sr_xCoO_{3-\delta}$ has the highest ferromagnetic ordering temperature, $T_c = 335$ K for powder [22], 370 K for single crystals [94], of any of the perovskite cobaltates and much of the research on this compound has focused on understanding the competition between the ferromagnetic and the antiferromagnetic exchange interactions in the material [22]. Early neutron diffraction measurements characterised $Y_{1-x}Sr_xCoO_{3-\delta}$ as a G-type antiferromagnet (figure 2.6) and found no evidence for long-range ferromagnetic ordering [23]. However, laboratory magnetisation measurements on $Y_{1-x}Sr_xCoO_{3-\delta}$ have consistently detected a weak ferromagnetic signal, suggesting some short-range or weak ferromagnetic ordering [22, 23, 91] which is still of unknown origin. The nature of the magnetic order in $Y_{1-x}Sr_xCoO_{3-\delta}$ is highly dependent on oxygen stoichiometry, and a change in oxygen content of $\Delta\delta = 0.04$ can result in a change from an insulating antiferromagnet to a metallic ferromagnet [11].

The relationship between structure and magnetism in this compound has also been discussed in depth by a number of authors, and appears to be key to understanding the behaviour of this material. This is clear, as the valency of the cobalt impacts on the possible exchange mechanisms and therefore the magnetic ordering.

Three forms of $Y_{1-x}Sr_xCoO_{3-\delta}$ exist depending on the arrangement of the A-site (Y/Sr) ions and oxygen vacancies. The A-site and oxygen vacancy ordered form of the compound (AO/OO), with the complex superstructure, also has a $T_c = 335$ K, more than twice that of the fully (AD/OD) and partially (AD/OO) structurally disordered compounds ($T_c = 100 - 150$ K) [91, 92]. Knowledge of the structure and the different cobalt environments in the unit cell has also given insight into the magnetism of this compound, as it has been found that there is a correlation between the chemical coordination of the cobalt ions and the magnitude of the magnetic moment, and that cobalt atoms in different layers have moments differing by a factor $\sim$2 [25]. The most recent research has extended this concept to the orthorhombic structure, suggesting cobalt atoms with different chemical coordination each have different magnitudes for their magnetic moments [24]. This will be further discussed in Chapter 6.

The presence of cobalt sites with different magnetic moments means it is likely these cobalts have different spin states. It has been suggested that the four-fold coordinated cobalt ions are in a high spin state while the six-fold coordinated cobalt ions are in an intermediate spin state [95]. This allows for the possibility of spin state transitions which have been observed for $Y_{1-x}Sr_xCoO_{3-\delta}$ under high pressures ($\sim$ 10 GPa) [95], calcium substitution [96] and in high magnetic fields ($\sim$ 53 T) [97]. In the case of high pressures, it has been suggested this leads to a transition from G-type antiferromagnetism to a new antiferromagnetic phase with mixed ferromagnetic and antiferromagnetic nearest neighbour coupling [95].

4.4 Other Doped Strontium Cobaltates

Although the yttrium-doped compound is the most studied of the doped strontium cobaltates, larger lanthanide ions such as holmium [98, 99], erbium [89], dysprosium [100], cerium [101], europium [102] and gadolinium [103] have also been the subject of investigations. Unlike yttrium, many of these ions are magnetic, resulting in different Curie temperatures and measured magnitudes of their magnetisation. However, like $Y_{1-x}Sr_xCoO_{3-\delta}$, the formation of complex superstructures is believed to play a key role in the peculiar weak ferromagnetism recorded in all these compounds at doping levels close to $x = 0.2$. Other features of the magnetic behaviour of this family of materials discussed to date include glassiness [99], short-range charge ordering [104] and ferromagnetic clustering [102].

4.5 Discussion

In many cases doped systems such as $Y_{1-x}Sr_xCoO_{3-\delta}$ have properties that make them particularly suitable for applications compared to their undoped counterparts. Technologically relevant properties such as high thermopower [11] and increased oxygen diffusion [105] have been reported in $Y_{1-x}Sr_xCoO_{3-\delta}$ and have potential applications in solid oxide fuel cells [106] or as membranes for gas separation [105]. It is therefore most important to fully characterise the structural, magnetic and transport properties of this class of materials.

The doped strontium cobaltates have also been investigated in order to better understand the physics of these and similar systems. The magnetic ordering schemes in this class of materials can be very complex and they can have multiple magnetic phases in their phase diagrams. The following two chapters discuss the structure and magnetism respectively of the complex cobaltate $Y_{1-x}Sr_xCoO_{3-\delta}$. Chapter 5 outlines the procedure adopted for the preparation of powders and single crystals of $Y_{1-x}Sr_xCoO_{3-\delta}$. The composition and crystal structure of these samples were then analysed using Laue diffraction, EDAX, TGA, X-ray and neutron diffraction. The magnetic ordering in $Y_{1-x}Sr_xCoO_{3-\delta}$ is discussed in detail in chapter 6. This chapter is divided into four sections, focussing on magnetometry, powder neutron diffraction, single crystal neutron diffraction and inelastic neutron spectroscopy measurements respectively.

Chapter 5

$Y_{1-x}Sr_xCoO_{3-\delta}$: Crystal Growth and Structure

The initial aim of our experimental work on $Y_{1-x}Sr_xCoO_{3-\delta}$ was to produce large single crystals suitable for further study. $Y_{1-x}Sr_xCoO_{3-\delta}$ is a complex system and single crystals offer a significant advantage over polycrystalline samples in that they afford the opportunity to measure the magnetocrystalline anisotropy and make more precise measurements of the crystal and magnetic structures of the material. The only previous work on either the growth or properties of such single crystals consisted of a single brief conference report [94]. The synthesis procedure adopted and characterisation measurements used on these crystals are described in sections 5.1 and 5.2 of this chapter respectively. The process of characterising these crystals allowed us to understand in more detail the complex crystal structure of this compound, and powder and single crystals diffraction measurements, outlined in section 5.3, were made using both X-rays and neutrons. These measurements meant the suggested charge and orbital ordering in $Y_{1-x}Sr_xCoO_{3-\delta}$ could be probed and the formation of the complex superstructure as a function of temperature in this compound could be studied.

5.1 Sample Preparation

5.1.1 Powder Synthesis

As there are two different ions on the *A*-site of the ABO_3 perovskite unit cell of $Y_{1-x}Sr_xCoO_{3-\delta}$, it is possible for them to lie in an ordered arrangement, so called *A*-site ordering (AO). It is also possible for the oxygen vacancies to order (OO), and this means polycrystalline samples of $Y_{1-x}Sr_xCoO_{3-\delta}$ can be synthesized in three different forms: (i) *A*-site and oxygen vacancy disordered (AD/OD), (ii) *A*-site disordered and oxygen vacancy ordered (AD/OO) and (iii) *A*-site and oxygen

vacancy ordered (AO/OO) [91, 92]. *A*-site and oxygen vacancy disordered (AD/OD) $Y_{1-x}Sr_xCoO_{3-\delta}$ is a simple perovskite, the AD/OO material has a brownmillerite structure and fully ordered (AO/OO) $Y_{1-x}Sr_xCoO_{3-\delta}$ has a complex superstructure with tetragonal or lower symmetry [83]. It is not possible to prepare an AO/OD version of the compound. Samples of each of these three structural variants of $Y_{1-x}Sr_xCoO_{3-\delta}$ with $x = 0.85$ were prepared using an established solid state reaction process described below [91, 92].

High purity powders of $SrCO_3$ ($\geq$99.9 %), Y_2O_3 (99.99 %), and Co_3O_4 (99.9985 %) were mixed together in stoichiometric ratios and heated in an 0.5 bar (gauge pressure) oxygen atmosphere at 1100°C for 24 hrs. All three samples were then reground and sintered. The AD/OD and AD/OO samples were sintered in air at 1100°C for 24 hrs and then quenched in liquid nitrogen. The AO/OO sample was sintered in an 0.5 bar oxygen atmosphere at 1100°C for 24 hrs. To enhance the *A*-site ordering the AO/OO sample was then post-annealed at 900°C in a 0.5 bar argon atmosphere for 24 hrs. After quenching, the AD/OO sample was post-annealed in a reducing 3.5 % H_2 in Ar atmosphere at 300°C for 6 hrs to control the oxygen levels and the AD/OD sample was post-annealed at 500°C in O_2 for 2 hrs to ensure oxygen stoichiometry.

All three samples were measured using X-ray diffraction to investigate if they had formed the correct structural variants and were fully reacted. The AO/OO powder was then reground and isostatically pressed into rods. The rods were then further annealed for 24 hrs in an oxygen atmosphere at 600°C ready to be used in the preparation of single crystals.

5.1.2 Single Crystal Growth

At the time of undertaking this research, only one previous report [94] existed which described the preparation of single crystals of $Y_{1-x}Sr_xCoO_{3-\delta}$, and in this report $x = 0.75$. The relative brevity of this report and the absence of any detail about the preparation methods adopted led us to develop our growth strategy independently and across a range of compositions [107].

Single crystals of AO/OO $Y_{1-x}Sr_xCoO_{3-\delta}$, with $x = 0.92$, 0.85, 0.8, 0.75 and 0.7, were produced using the floating-zone technique in either a Nippon Electric Company (NEC) SC-N35HD two mirror image furnace or a Crystal Systems Incorporated (CSI) F-ZT-10000-H-IV-VPS four mirror infra-red image furnace. The growths were performed in an oxygen atmosphere of 3 bars with a small flow of gas. Initially the seed rod was a polycrystalline rod of the same composition as the feed rod but, for subsequent growths, a seed crystal obtained from the previous growths was used. For the first set of trials, growth speeds of 1-2 mm/h and a rotation rate of 25-30 rpm for both the feed and seed rods were used. For the later experiments,

the growth speeds were reduced to 0.5-1 mm/h as it was found that lower growth speeds improved the crystal quality. Crystal facets were visible during the growths. The as-grown crystals were annealed for 24 hrs at 900°C in an oxygen atmosphere in order to increase their oxygen content, and the resulting varieties of crystal are hereafter referred to as 'O_2-annealed' or 'as-grown', as appropriate.

The crystals obtained were around 8 mm in diameter and 30-40 mm in length. Figure 5.1 shows the as-grown crystal boules of $Y_{0.15}Sr_{0.85}CoO_{3-\delta}$ and $Y_{0.2}Sr_{0.8}CoO_{3-\delta}$. These are typical of the crystals grown. The exterior of the as-grown crystals were a dull grey and X-ray Laue diffraction later showed that this is due to a thin polycrystalline coating on the exterior of the crystals, the interior of the crystals were clearly shinier and a paler grey. When cutting through the boule, this polycrystalline coating can be easily distinguished and is usually no more than 0.5 mm thick, although it was observed that increased yttrium content resulted in a slightly thicker polycrystalline layer.

5.2 Sample Characterisation

5.2.1 Crystal Quality

The X-ray Laue method was used to investigate the crystal quality and to align the samples for other experiments. The quality of the X-ray Laue images taken was limited to some extent by the fluorescence of the cobalt in the samples. Neutron Laue experiments were performed on the OrientExpress Laue diffractometer [108] at the ILL, Grenoble. A Philips PW 1720 X-ray diffraction set with a CuKα source and a monochromating crystal mounted before the detector was used for the powder X-ray diffraction measurements.

An X-ray Laue image taken along the c axis of one of the $x = 0.85$ crystals is shown in figure 5.3 (centre). Clear diffraction patterns were visible from the cut

Figure 5.1: As-grown boules of $Y_{0.15}Sr_{0.85}CoO_{3-\delta}$ (left panel) and $Y_{0.2}Sr_{0.8}CoO_{3-\delta}$ (right panel) grown at speeds of 0.5-1 mm/hr using the floating-zone method.

ends of all the samples produced, indicating that there were indeed single crystals. However, there was evidence from some splitting of the spots that the boules with a higher yttrium content ($x \leq 0.75$) may contain several smaller crystal grains.

An example of one of the neutron Laue images collected on the OrientExpress neutron Laue diffractometer is shown in figure 5.3 (lower). These measurements confirmed that for $0.8 \leq x \leq 0.92$ the quality of the crystals was good, and suitable for further experiments. A 20 mm long, 8 mm diameter section was cut from one crystal boule and found to be a single grain (a later neutron diffraction measurement using a triple-axis spectrometer showed the mosaic spread of this crystal was $\sim 0.7^\circ$). A crystal of this volume and quality would be sufficient for experiments requiring large samples, such as inelastic neutron scattering. In contrast, neutron Laue data showed that the samples of a similar volume with $x \leq 0.75$ contained several crystal grains. These measurements support the conclusions made from X-ray Laue measurements, that the boules of $Y_{1-x}Sr_xCoO_{3-\delta}$ with $x = 0.92$, 0.85, and 0.8 are each made up of a large single crystal, while the boules with $x = 0.7$ and 0.75 consist of several smaller crystal grains.

X-ray diffraction measurements on powdered sections of each boule confirmed the as-grown crystals were the AO/OO variant of $Y_{1-x}Sr_xCoO_{3-\delta}$, with a peak at 11.5° characteristic of this phase [92] clearly visible in the diffraction patterns (see figure 5.2). There was no evidence of any additional peaks in the X-ray diffraction patterns, indicating that the crystals are single phase.

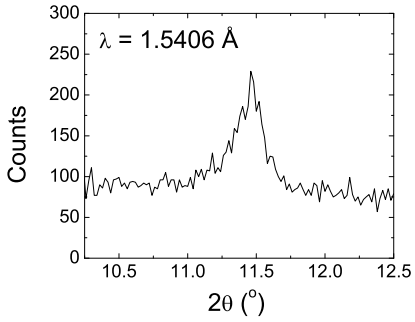

Figure 5.2: X-ray diffraction pattern showing the characteristic peak of the AO/OO phase as measured on a powdered piece of an $Y_{1-x}Sr_xCoO_{3-\delta}$ single crystal.

5.2.2 Y/Sr Ratio

Most studies of AO/OO $Y_{1-x}Sr_xCoO_{3-\delta}$ have focused on either the $x = 0.75$ or the $x = 0.67$ compound as these yttrium contents ensure exactly 1/4 or 1/3 respectively of the *A*-sites of the perovskite cell contain an yttrium ion. However, powder X-ray and neutron diffraction studies [21] have shown that all the compounds with $0.75 \leq x \leq 0.875$ have the same structural and magnetic behaviour. In this case, an $Y_{1-x}Sr_xCoO_{3-\delta}$ single crystal with $x = 0.85$ was chosen for a more in-depth study, as the quality of the crystal was good and this value of x is within the range necessary for observing a room temperature ferromagnetic response from the sample [22].

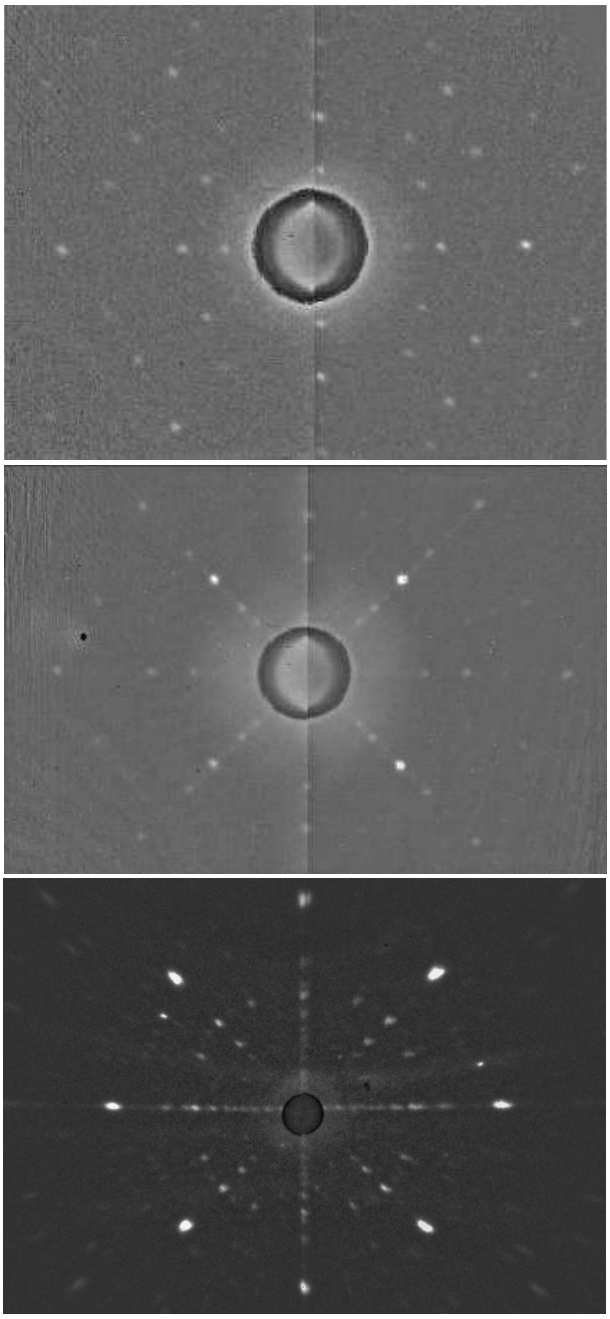

Figure 5.3: The top panel shows a typical X-ray Laue back-diffraction image obtained from a crystal of $Y_{0.15}Sr_{0.85}CoO_{3-\delta}$ with the crystal oriented so that the X-rays are directed parallel to the a axis of the $I4/mmm$ unit cell, and the middle panel shows a similar image with the crystal oriented so that the X-rays are directed parallel to the c axis. The X-ray images were taken on a low voltage setting to avoid excessive cobalt fluorescence. The lower panel shows a neutron Laue image with the crystal oriented so that the neutrons are directed parallel to the c axis of the $Y_{0.15}Sr_{0.85}CoO_{3-\delta}$ crystal.

The Y/Sr ratios in the crystals were obtained using EDAX measurements, described in section 3.1.2, and agree reasonably well with the initial stoichiometries (see table 5.1). It should be noted that the error in the experimentally determined value of x is the predominant source of error in calculating the oxygen content of each of the crystals. The results indicate that for compounds with $x \geq 0.75$ there is no significant or systematic loss of either strontium or yttrium during the crystal growth process. For compounds with lower strontium content than $x = 0.75$, the EDAX data shows that it is more difficult to introduce yttrium into the system, as both the $x = 0.75$ and $x = 0.7$ sample were found to have the same Y/Sr ratio.

Y/Sr Ratio		Oxygen Content	Cobalt Valency
Nominal Starting	EDAX	$(3-\delta)$	
0.15/0.85	0.17(1)/0.83(1)	2.59(1)	3.03(4)
0.20/0.80	0.22(1)/0.78(2)	2.61(1)	3.02(4)
0.25/0.75	0.26(1)/0.74(1)	2.57(2)	2.90(6)
0.30/0.70	0.26(1)/0.74(1)	2.53(2)	2.77(6)

Table 5.1: Values of x for $Y_{1-x}Sr_xCoO_{3-\delta}$ from both for the nominal starting stoichiometry and from the EDAX measurements. The oxygen content $3-\delta$ of various members of the as-grown $Y_{1-x}Sr_xCoO_{3-\delta}$ ($0.7 \leq x \leq 0.85$) series determined using TGA is also given. The cobalt valency has been calculated using charge balance by assuming valencies of Y^{3+}, Sr^{2+} and O^{2-} respectively.

5.2.3 Oxygen Content

Thermogravimetric analysis (TGA, described in section 3.1.3) was carried out using a Mettler-Toledo thermal analysis apparatus in order to evaluate the oxygen content of the crystals. Powdered samples of approximately 30 mg were heated from 30°C to 900°C at 10°C/min in alumina crucibles in a reducing 3% H_2/Ar atmosphere. An example of one of the reduction curves obtained using TGA is shown in figure 5.4. The stepwise form of the data with two intermediate plateaux is typical of the reduction curves for this family of cobalt oxides, and reflects the subsequent reduction of the cobalt from a valency of 3+, to 2+ then to cobalt metal [60, 86]. The reduction of $Y_{1-x}Sr_xCoO_{3-\delta}$ to a mixture of yttrium oxide, strontium oxide and cobalt metal is completed around 800°C. The change in mass gives us the oxygen lost during the process via conservation of the molar mass, expressed in equation 5.1.

$$\frac{M_{Initial}}{M_{Final}} = \frac{M_{Y_{1-x}Sr_xCoO_{3-\delta}}}{M_{SrO} + M_{Y_2O_3} + M_{Co}} \tag{5.1}$$

Table 5.2 shows the oxygen content of the AD/OD, AD/OO and AO/OO

powders as well as a comparison between the oxygen content of as-grown and O_2-annealed crystals as determined from the TGA measurements. From the value for δ found, and assuming the valencies of Sr, Y and O to be 2^+, 3^+ and 2^- respectively, the cobalt valencies were calculated and are given in both table 5.1 and table 5.2. The values in table 5.1 show a decrease in oxygen content for crystals with higher yttrium content, which is likely to be related to the decrease in quality of the $x = 0.75$ and $x = 0.7$ crystals compared to those with lower yttrium content.

The oxygen contents of the powders of the three different structural variants of $Y_{0.15}Sr_{0.85}CoO_{3-\delta}$ were also analysed. The results generally agree with those previously reported, with some small variation [91, 92]. For the AD/OD sample prepared using the same annealing conditions, the previous work had measured an oxygen content of 2.778, which is slightly higher than ours, probably due to the slightly higher hydrogen content of their reducing gas. The same report measured a value of δ for the AD/OO sample identical to ours, the difference in cobalt valence reported being due to the difference in yttrium content between their compound, where $x = 0.75$, and ours. Intuitively, the oxygen content of the AO/OO powder is lower than might be expected, 2.67 is stoichiometric, but the measurements were made prior to any oxygen annealing, so the difference is understandable [91, 92].

Table 5.1 shows an increase in oxygen content of $\delta = 0.04$ for the O_2-annealed crystal compared to the as-grown crystal. The cobalt valency was found to be very close to pure trivalent cobalt for the as-grown crystal, but for the annealed crystal these measurements imply the presence of a small amount of tetravalent cobalt. It has been shown [11] that a change in oxygen content of $\delta = 0.04$ is enough to turn $Y_{1-x}Sr_xCoO_{3-\delta}$ from an insulating antiferromagnet to a metallic ferromagnet, so this small difference in oxygen content could prove significant when studying the magnetic properties of these materials.

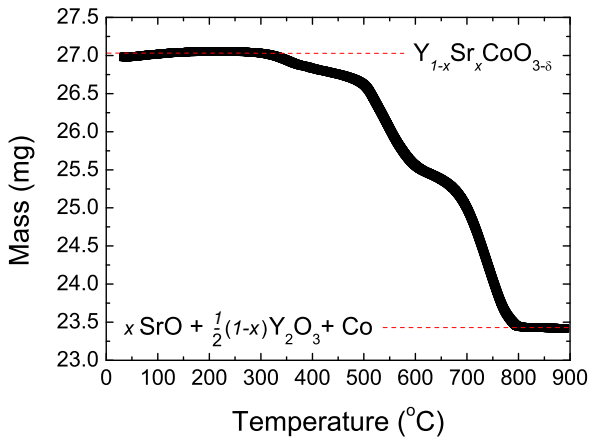

Figure 5.4: A typical TGA curve for the reduction of a powdered $Y_{0.15}Sr_{0.85}CoO_{3-\delta}$ crystal in a 3% H_2/Ar atmosphere. This particular measurement was for the O_2-annealed $Y_{0.15}Sr_{0.85}CoO_{3-\delta}$ crystal, but all the measurements for the crystals grown showed the same features.

Compound	Oxygen Content $(3-\delta)$	Co Valency
AD/OD Powder	2.70(1)	3.25(4)
AD/OO Powder	2.53(1)	2.91(4)
AO/OO Powder	2.50(1)*	2.85(4)*
'As-Grown' Crystal	2.59(1)*	3.03(4)*
'O_2-Annealed' Crystal	2.63(1)	3.11(4)

Table 5.2: The oxygen content $3-\delta$ of each of the forms of $Y_{0.15}Sr_{0.85}CoO_{3-\delta}$ ($0.7 \leq x \leq 0.85$) prepared. The cobalt valency has been calculated using charge balance. The values marked with a * correspond to those for the AO/OO powder prior to the final oxygen annealing.

5.3 Crystal Structure

5.3.1 Experimental Details: X-ray Diffraction and D1B and D10 Neutron Diffractometers

Preliminary measurements to confirm the published crystal structures of the three different $Y_{0.15}Sr_{0.85}CoO_{3-\delta}$ powders were made using both X-ray and neutron diffractometers. The X-ray diffraction measurements were made using a Panalytical X-Pert Pro MPD $K_{\alpha 1}$ machine [109] and the neutron measurements were made on the high intensity powder diffractometer D1B at the ILL in Grenoble. For the X-ray experiments, $Y_{1-x}Sr_xCoO_{3-\delta}$ powder was mounted in an aluminium sample holder which was spun at 4 s per revolution with a Nickel filter placed before the detector. The scan was made from $5-100^\circ$ at room temperature. The data was noisier than might be expected due to the cobalt fluorescence in the $CuK_{\alpha 1}$ range.

The instrument used for powder neutron diffraction measurements, D1B, is a two-axis spectrometer with a high neutron flux. At small angles where the magnetic peaks are expected, a high spatial resolution can be achieved. The incident wavelength is 2.52 Å. Large area detectors mean large sections of the diffraction pattern can be measured simultaneously, and so fast data collection is possible [110]. Samples of the three $Y_{1-x}Sr_xCoO_{3-\delta}$ powders were mounted in vanadium cans. The AD/OD and AD/OO samples filled the sample cans, and the AO/OO sample filled the can to a depth of 4 cm. Measurements to probe the crystal structure were made at 500 K using a furnace to achieve temperatures higher than ambient levels. Six 10 minute scans were made for each sample at this temperature.

Single crystal X-ray diffraction experiments were performed at Warwick on an Oxford Diffraction Gemini R diffractometer. The Gemini R is a 4-axis goniometer equipped with dual wavelength (Cu/Mo) fine focus X-ray sources. The detector is a Ruby CCD area detector, which allows for extremely fast data collection of the entire Ewald sphere [109]. Measurements at temperatures between 77-400 K are possible

using a liquid nitrogen cryosystem. The use of the molybdenum source meant the fluorescence of the cobalt was not present, meaning the quality of the data was much improved from the powder X-ray diffraction measurements. A single crystal fragment < 1 mm^3 of $Y_{0.15}Sr_{0.85}CoO_{3-\delta}$ was mounted on a glass fibre attached to a goniometer head.

Finally, single crystal neutron diffraction measurements were made on the four-circle diffractometer D10, the layout of which is shown in figure 5.5. The incident wavelength is either 2.36 Å using a PG-monochromator and filter or 1.26 Å using a Cu-monochromator. The diffraction peaks are measured using an 80 x 80 mm^2 area detector or a single He^3 detector which allows improved statistics. The offset C-shaped Eulerian cradle accommodates a cryostat with a temperature range from 1.6 K to 450 K [110].

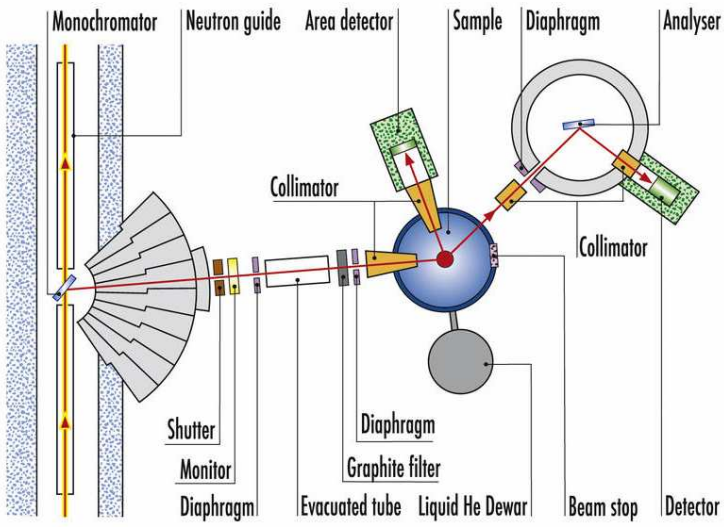

Figure 5.5: The layout of the four-circle single crystal diffractometer D10 with offset C-shaped Eulerian cradle and optional energy analyser. Taken from reference [110].

A section was cut from the boule of the O_2-annealed $Y_{0.15}Sr_{0.85}CoO_{3-\delta}$ single crystal and oriented using the OrientExpress neutron Laue. The sample was mounted on a pin and placed inside the Eulerian cradle cryostat allowing the instrument to access most of reciprocal space. The sample selected had a twin which was found to be randomly oriented, so should not have any significant impact on our measurements.

5.3.2 AD/OD and AD/OO Powder

The AD/OD and AD/OO phases of $Y_{1-x}Sr_xCoO_{3-\delta}$ were investigated using powder X-ray and neutron diffraction. The aim was to confirm the published structures, and assess the quality of the samples so that the magnetic structure of both compounds

could be characterised. The X-ray scans were 12 hrs and the neutron scans were 15 mins, but using an instrument with a much larger flux. The diffraction patterns recorded by both measurements are shown in figures 5.6 and 5.7 for the AD/OD and AD/OO compounds respectively. All the patterns were fitted with a calculated structural profile using the refinement program FULLPROF [111].

	AD/OD	AD/OO
Crystal System	Cubic	Orthorhombic
Space Group	$Pm\bar{3}m$	$Ima2$
a (Å)	3.8279(5)	15.712(2)
b (Å)	3.8279(5)	5.5027(9)
c (Å)	3.8279(5)	5.387(1)
Volume	56.09(3)	465.6(2)
Impurity AO/OO (%)	0.05596(5)	0.660(2)
Impurity CoO(%)	N/A	0.660(2)
χ^2	16.3	10.7
R_{Bragg}	0.25	3.50
R_p	6.61	9.63
R_{wp}	6.00	8.27

Table 5.3: Rietveld refinement details for the AD/OD and AD/OO forms of $Y_{1-x}Sr_xCoO_{3-\delta}$ measured using powder neutron diffraction at 500 K.

Both the diffraction patterns from the AD/OD powder were fitted using a cubic perovskite model, space group $Pm\bar{3}m$, as previously suggested, with the details of the refinement of the neutron diffraction data given in table 5.3 and the atom positions given in appendix A. The details of the fit to the X-ray data are not given because the noise due to the cobalt fluorescence gave an artificially good fit that was not representative of the goodness of fit of the model to the pattern, although the data could still clearly be fitted with the same model as the neutron diffraction data, as is shown in the first panel of figure 5.6.

The quality of the fit to the neutron data is also limited due to the fact that only four peaks corresponding to the AD/OD phase were fitted, and this accounts for the high value of χ^2. This is because the D1B instrument is optimised for the study of magnetic, not crystal structures. A small impurity phase was detected in the pattern, and this was indexed as being 0.06 % of the sample belonging to the AO/OO phase of the compound, whose presence was also indicated in the magnetisation measurements, discussed in section 6.1.1.

The simple perovskite structure of the AD/OD powder implies both the Y/Sr atoms and oxygen vacancies are randomly distributed through the lattice, and the single cobalt atom is situated in an oxygen octahedra, shown in figure 5.9(a). The oxygen content was fixed to be that determined using TGA, in this case $\delta = 0.30$, and

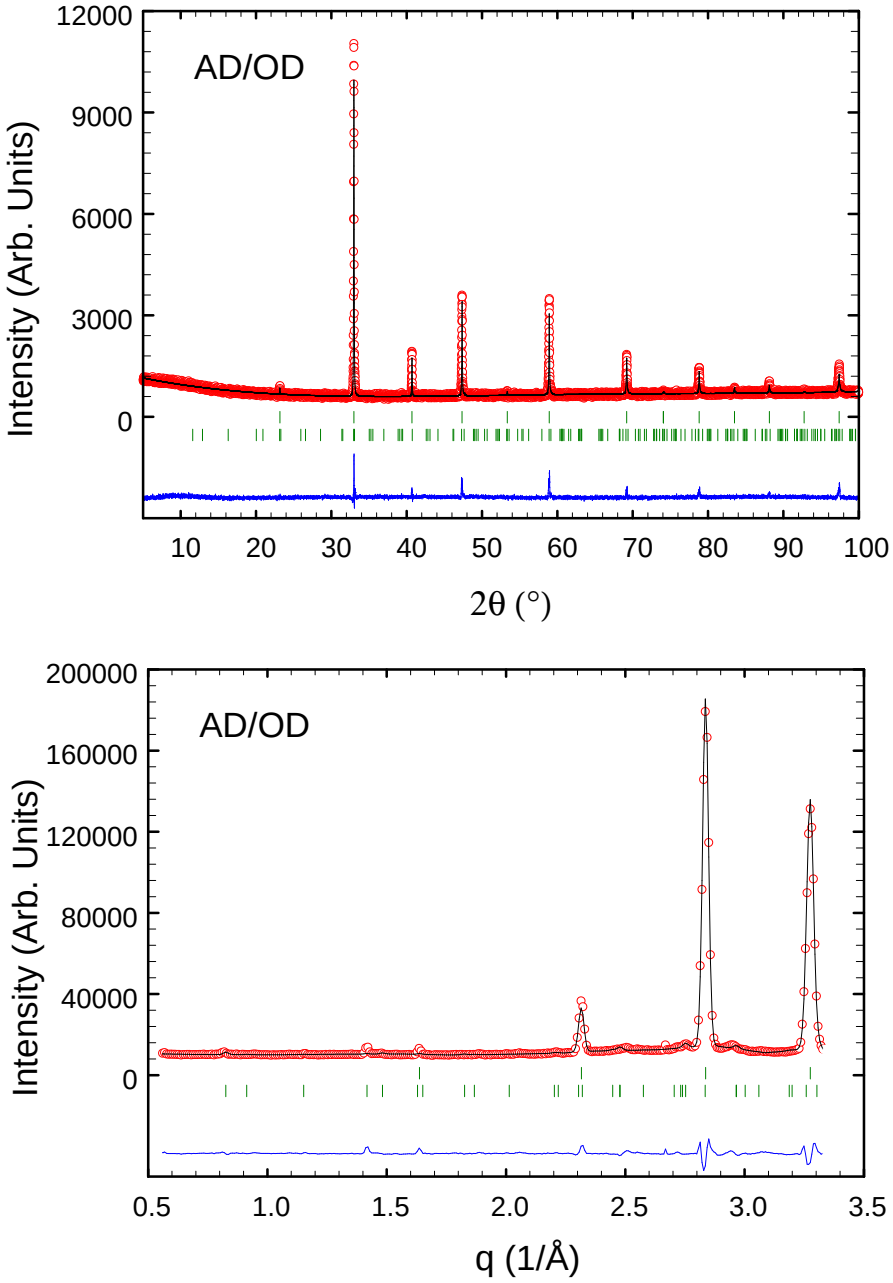

Figure 5.6: Powder diffraction patterns and calculated profiles for the AD/OD structural variant of $Y_{1-x}Sr_xCoO_{3-\delta}$. The upper panel shows the X-ray diffraction pattern taken at room temperature. The lower panel shows the neutron diffraction pattern, taken at a temperature of 500 K to eliminate any magnetic contribution.

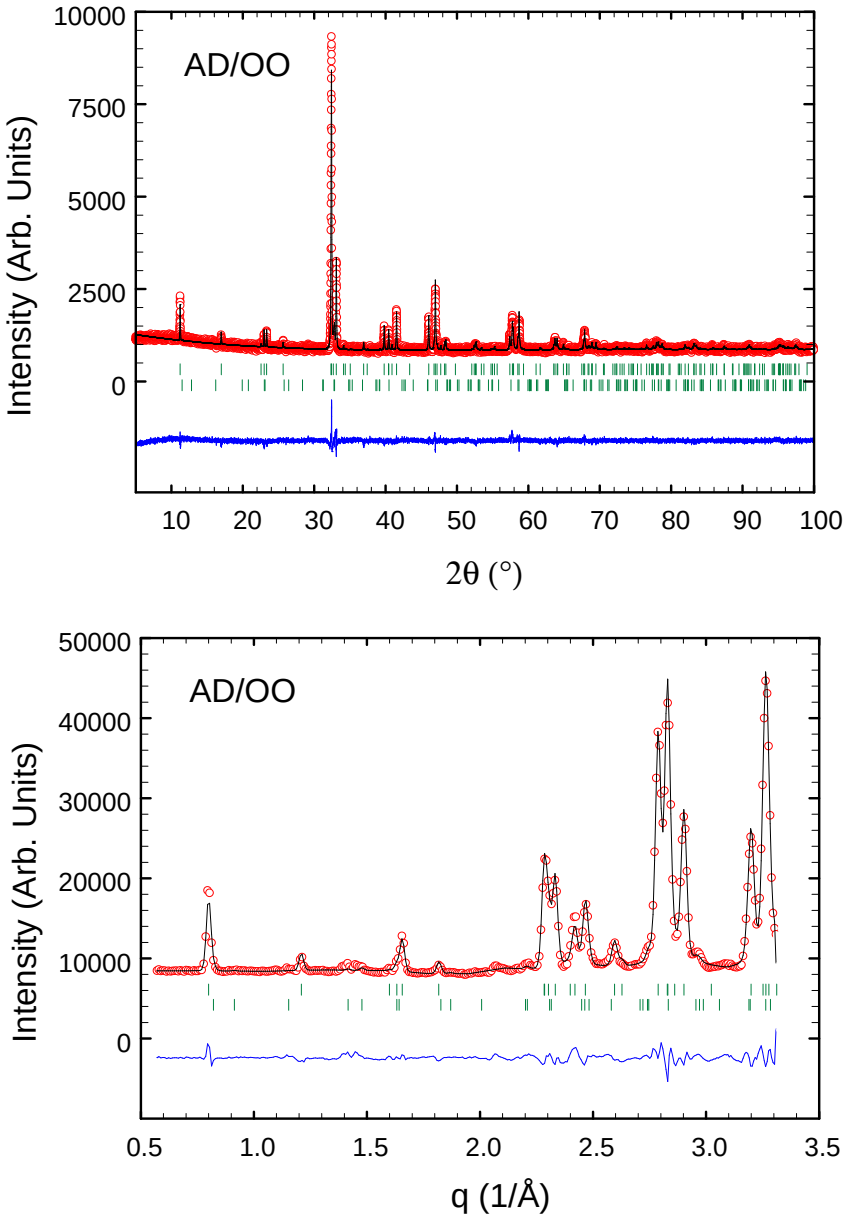

Figure 5.7: Powder diffraction patterns and calculated profiles for the AD/OO structural variant of $Y_{1-x}Sr_xCoO_{3-\delta}$. The upper panel shows the X-ray diffraction pattern taken at room temperature. The lower panel shows the neutron diffraction pattern, taken at a temperature of 500 K to eliminate any magnetic contribution.

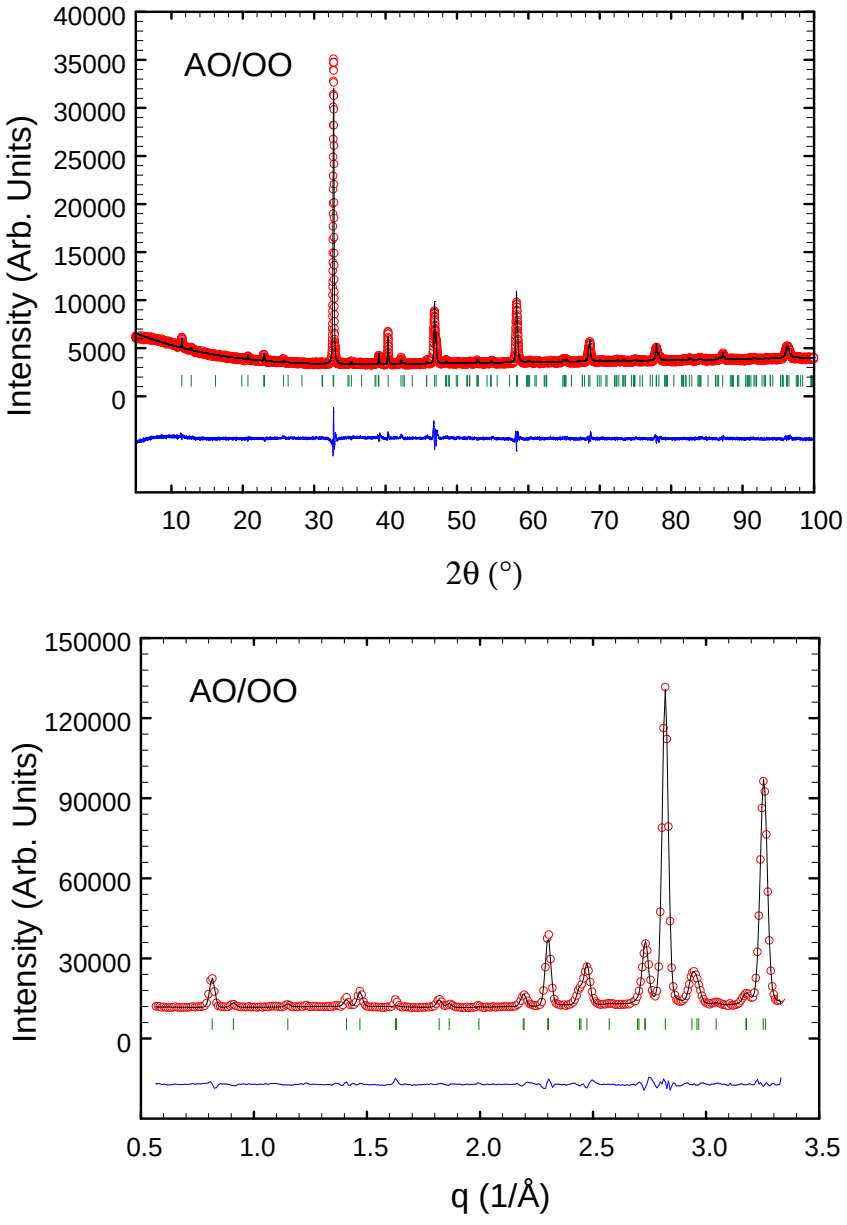

Figure 5.8: Powder diffraction patterns and calculated profiles for the AO/OO structural variant of $Y_{1-x}Sr_xCoO_{3-\delta}$. The upper panel shows the X-ray diffraction pattern taken at room temperature. The lower panel shows the neutron diffraction pattern, taken at a temperature of 500 K to eliminate any magnetic contribution.

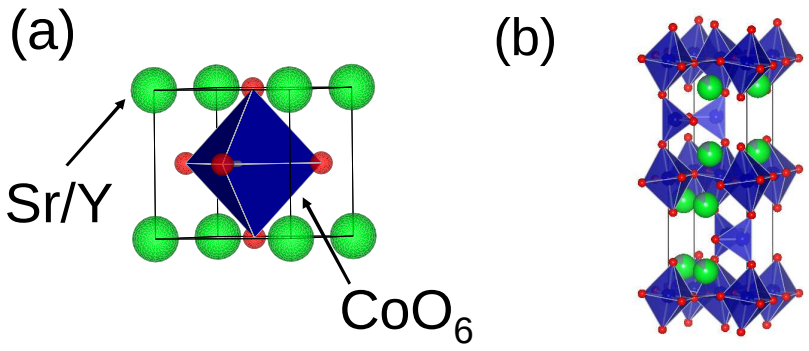

Figure 5.9: Crystal structures of the AD/OD (space group $Pm\bar{3}m$) and AD/OO (space group $Ibm2$) forms of $Y_{1-x}Sr_xCoO_{3-\delta}$ respectively [92]. Figure drawn using [113].

this fitted the diffraction pattern well. It should be noted that all the later structures discussed for the AD/OO and AO/OO structural variants of $Y_{1-x}Sr_xCoO_{3-\delta}$ are just distortions of this simple perovskite structure with lattice parameter 3.83 Å.

The X-ray and neutron diffraction patterns for the AD/OO phase are shown in figure 5.7. The AD/OO compound is oxygen deficient, with a value of $3-\delta$ of 2.5, whose brownmillerite [84] crystal structure was described by previous researchers [85]. The (2,0,0) peak of the crystal structure (space group $Ibm2$) is clearly identifiable at $2\theta = 11.2°$ in the X-ray diffraction pattern and at a q-spacing of 0.8 $Å^{-1}$ in the neutron diffraction pattern. This characteristic peak indicates oxygen vacancy ordering and means there are layers of corner-sharing cobalt octahedra, as in the simple perovskite structure, alternating with layers of cobalt tetrahedra and oxygen vacancies. This crystal structure is shown in figure 5.9(b).

Refinement of the structure of the AD/OO sample from the neutron diffraction data revealed a small AO/OO impurity, as with the AD/OD sample. The calculated atom positions from the refinement are given in appendix A. In this case, the percentage was slightly higher, but still only 0.66 % of the sample. For the AD/OO refinement, the χ^2 was lower than for the AD/OD sample, but the R_{Bragg} was higher. This reflects the fact that the fit to the data involves more peaks, so there is less uncertainty, but the pattern is more difficult to reproduce. However, considering the fit in figure 5.7 and the refinement parameters (table 5.3) the brownmillerite model (figure 5.7) seems to be appropriate, in agreement with previous results [85, 91, 92].

Figures 5.10 and 5.11 show the temperature dependence of the lattice parameters for AD/OD and AD/OO forms of $Y_{0.15}Sr_{0.85}CoO_{3-\delta}$ respectively. The lattice parameter of the AD/OO structure showing the largest expansion is the a lattice parameter of the brownmillerite unit cell. The expansion profile is very similar to that of the lattice parameter of the cubic AD/OD compound, with a change in the

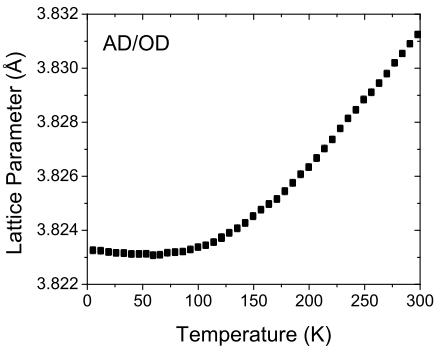

Figure 5.10: The temperature dependence of the lattice parameter for the cubic AD/OD form of $Y_{1-x}Sr_xCoO_{3-\delta}$.

rate of expansion between 100 and 150 K and linear expansion at higher temperatures. In contrast, the b and c lattice parameters of the brownmillerite structure contract as the temperature is increased. A change in the rate of expansion between 100 and 150 K was also observed for the b and c lattice parameters. Translating this to the change in volume as a function of temperature, there is a ~ 0.4 % increase in volume of the AD/OO unit cell between 10 and 300 K.

5.3.3 AO/OO Powder

The AO/OO phase was also studied using X-ray and neutron diffraction. To improve the statistics of the X-ray scans, the measurement was made over a timescale of 55 hrs, with the other parameters the same as for the AD/OD and AD/OO structures. However, the cobalt fluorescence is still present in the CuK_α range, again limiting the quality of the data. Neutron diffraction measurements were also made on D1B, but it must be noted that this instrument is optimised for magnetism as opposed to structural studies. Therefore we used models based on published structures to analyse the data as opposed to trying to solve the structure $ab-initio$.

The crystal structure of $Y_{1-x}Sr_xCoO_{3-\delta}$ was originally reported to be space group $I4/mmm$ with a 7.62 x 7.62 x 15.31 Å unit cell [83]. Although these initial powder diffraction measurements showed no evidence of an orthorhombic distortion, another study was made in 2009 [25] using the same space group but with a split site for the 8i(x,0,0) Wyckoff position, which is partially occupied with oxygen. Splitting a crystallographic site directly implies the true crystallographic symmetry is lower than $I4/mmm$, giving reason to investigate space groups with lower crystal symmetry. [83]. Electron microscopy measurements also suggested the existence of a superstructure with lower symmetry than the tetragonal $I4/mmm$ space group. A peak with index (0.25,0.25,0) was observed using synchrotron X-ray diffraction on the isostructural compound $Er_{0.78}Sr_{0.22}CoO_{2.63}$ [89] and the same small peak at $\sim 8^\circ$ was identified more recently in X-ray diffraction [92], implying a larger superstructure than the $I4/mmm$ tetragonal structure utilised by most researchers.

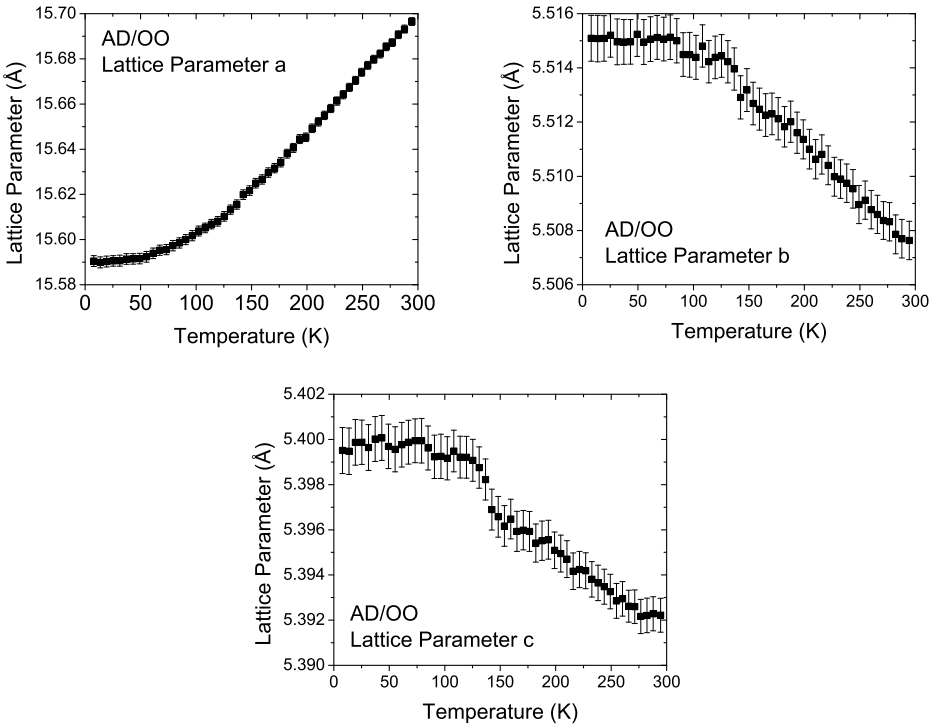

Figure 5.11: The temperature dependence of the a, b and c lattice parameters for the brownmillerite AD/OO form of $Y_{1-x}Sr_xCoO_{3-\delta}$. The size of the error bars is due to the systematic errors involved in refining the data, as the random errors in the data are small.

The electron diffraction suggested a ($2\sqrt{2}a_p$ x $4a_p$ x $2\sqrt{2}a_p$) supercell, where a_p is the simple perovskite cell, although it was suggested this was a local structure present in some crystallites. This modulated structure was initially proposed to be space group $C1c1$ or $Cmcm$ [87] based on the presence of a c glide perpendicular to the b axis. This was later revised to give an orthorhombic $Cmma$ space group in the solid solution range $0.750 \leq x \leq 0.850$ $Y_{1-x}Sr_xCoO_{3-\delta}$, outside of this range only peaks corresponding to the $I4/mmm$ space group were observed [21]. More recently, it was suggested that at a temperature of around 360 K there is a transition from an orthorhombic to monoclinic unit cell with space group $A2/m$ [89]. The temperature dependence of the crystal structure of $Y_{1-x}Sr_xCoO_{3-\delta}$ will be discussed later in section 5.3.5 on structural transitions.

Initially, the powder diffraction data for the AO/OO compound was refined in this $I4/mmm$ space group (details given in appendix A). The fit was good for both the neutron and the X-ray diffraction data, both of which are shown in figure 5.8. The type of oxygen vacancy ordering reported for the $I4/mmm$ structure of $Y_{1-x}Sr_xCoO_{3-\delta}$ was unreported prior to 2003. As with the AD/OO brownmillerite crystal structure, fully oxygenated and oxygen deficient layers alternate along the unique axis of the tetragonal unit cell. The fully oxygenated layers contain tilted CoO_6 octahedra. In the oxygen deficient layers, there is one extra oxygen atom per layer compared to the brownmillerite structure, with all the cobalt atoms sitting in oxygen tetrahedra. This implies charge ordering, as the Co^{3+} and Co^{4+} form a regular arrangement in the lattice. This unit cell is illustrated in figure 5.12. There is no scattering contrast between Sr^{2+} and Y^{3+} using either X-rays or neutrons, so the positions of the yttrium ions were fixed according to those in the literature [83].

A comparison of the diffraction patterns for the three variants of the com-

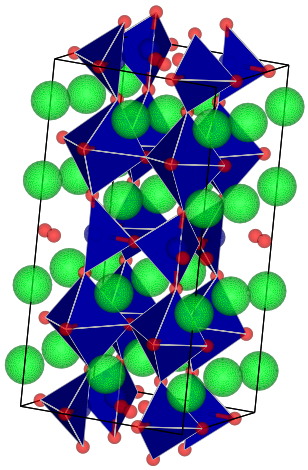

Figure 5.12: Crystal structure of the AO/OO (space group $I4/mmm$) form of $Y_{1-x}Sr_xCoO_{3-\delta}$ [92]. The cobalt polyhedra are shown in blue and the A-site strontium and yttrium atoms are shown in green. The figure clearly shows that fully-oxygenated and oxygen deficient layers alternate along the c axis of the unit cell. Figure drawn using [113].

pound is interesting. The peak at $2\theta = 11.2°$ in the X-ray diffraction pattern and at a q-spacing of 0.8 $Å^{-1}$ in the neutron diffraction pattern of the AD/OO compound is also present for the AO/OO compound, clearly demonstrating this peak is related oxygen vacancy ordering. Comparing the diffraction patterns from the AO/OO and simple perovskite AD/OD materials, we can see they are similar, reflecting the fact the AO/OO crystal structure is a distorted perovskite. The most notable difference between the two structures is the addition of oxygen tilt peaks flanking the perovskite structural peaks in the AO/OO patterns. The $I4/mmm$ unit cell is equivalent to a doubling of the simple perovskite cell along the a and b axes and a quadrupling along the unique axis c ($2a_p$ x $2a_p$ x $4a_p$).

Space Group		I4/mmm	Cmma	A2/m
a (Å)	X-ray	7.749(1)	15.4271(3)	21.938(6)
	Neutron	7.728(1)	15.397(3)	21.815(6)*
b (Å)	X-ray	7.749(1)	10.9551(1)	10.950(3)
	Neutron	7.728(1)	10.944(3)	10.934(3)*
c (Å)	X-ray	15.428(3)	10.9646(3)	15.427(4)
	Neutron	15.410(3)	10.910(3)	15.385(3)*
Volume	X-ray	926.4(2)	1853.08(6)	3706(2)
	Neutron	920.3(2)	1838.4(6)	3670(2)*
Z		16	32	64
χ^2	X-ray	3.93	3.89	3.91
	Neutron	14.7	12.0	13.5*
R_{Bragg}	X-ray	24.1	23.2	26.4
	Neutron	1.29	1.88	1.83*
R_p	X-ray	66.6	59.6	58.9
	Neutron	6.79	6.47	6.25*
R_{wp}	X-ray	23.6	23.4	23.9
	Neutron	6.50	5.95	6.00*

Table 5.4: Refinement details for AO/OO $Y_{0.15}Sr_{0.85}CoO_{3-\delta}$ powder in the $I4/mmm$, $Cmma$ and $A2/m$ space groups. *Some parameters had to be fixed during the refinement in the $A2/m$ space group because the quantity of free parameters caused the refinement to become unstable.

No impurities were detected in the AO/OO powder samples, and hence in figure 5.8 there is a single set of Bragg positions indicated. The χ^2 value of 14.7 for the neutron refinement is comparable to the value for the AD/OO sample given in table 5.3. However, the R-factors for this refinement, given in table 5.4, are significantly improved compared to the AD/OD and AD/OO compounds. This suggests the model is a good fit to the data, and hence the conclusion that the structure of our sample can be fitted adequately with the parent $I4/mmm$ space group.

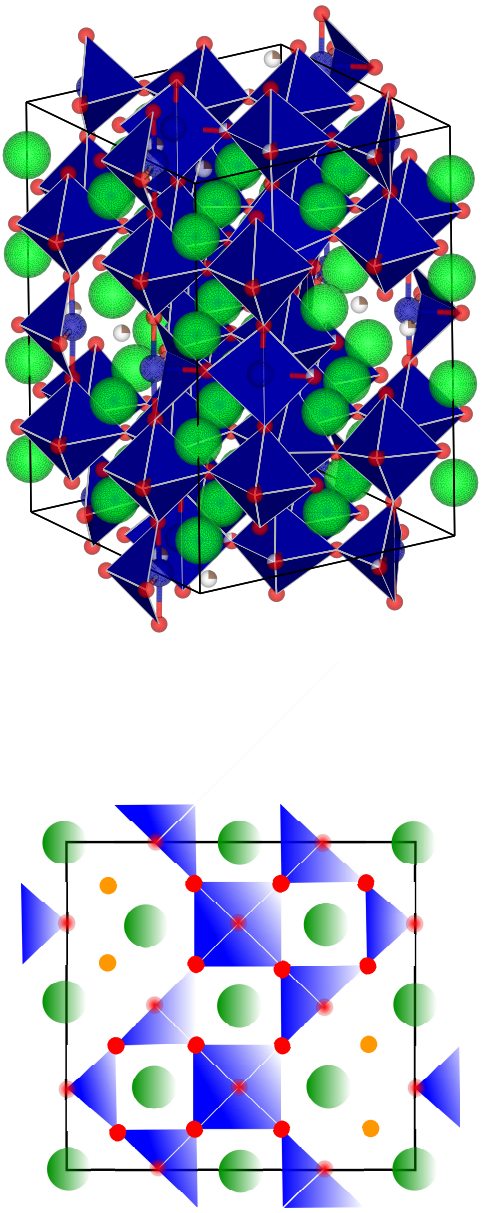

Figure 5.13: Orthorhombic crystal structure of AO/OO $Y_{1-x}Sr_xCoO_{3-\delta}$ with space group *Cmma*. The upper panel shows the three dimensional crystal structure with atom positions corresponding to those from the analysis of single crystal neutron diffraction data. The lower panel shows a schematic representation of the oxygen deficient layer in this structure, with the atoms in their ideal positions. The Y/Sr are shown in green, the cobalt polyhedra in blue, the oxygens in red and the oxygen vacancies in brown.

The AO/OO X-ray and powder neutron diffraction data were also refined in the $Cmma$ and $A2/m$ cells. These cells consist of a doubling and a quadrupling of the parent $I4/mmm$ unit cell respectively, and their respective lattice parameters, as refined from the neutron and X-ray diffraction data, are given in table 5.4. The translation matrix for moving from the $I4/mmm$ to the $Cmma$ space groups is:

$$M = \begin{pmatrix} 0 & 0 & 1 \\ 1 & 1 & 0 \\ -1 & 1 & 0 \end{pmatrix}$$

A centring translation of (0,+0.5,0) must also be applied to get the correct Wyckoff positions for the atoms. This means the unique axis c in the $I4/mmm$ space group is the a axis in the $Cmma$ space group.

As with the $I4/mmm$ space group, the $Cmma$ crystal structure, shown in figure 5.13, consists of alternating fully-oxygenated and oxygen deficient layers. In the fully-oxygenated layers all the cobalt species are in octahedral environments. However, in the oxygen deficient $CoO_{4+\delta}$ layers there are three different cobalt environments, octahedral, square pyramidal and tetrahedral, shown in the lower panel of the figure. These different environments form as a result of the ordering of the oxygen vacancies in zig-zag stripes in the bc plane.

Increasing the number of free parameters will always improve the refinement, with small improvements with the refinements in the lower symmetry space groups in table 5.4 as would be expected. Generally, the χ^2 values for each of the three space groups in table 5.4 are comparable, with the best values obtained for the $Cmma$ space group.

In this section, X-ray and neutron diffraction measurements on polycrystalline samples of $Y_{0.15}Sr_{0.85}CoO_{3-\delta}$ have been described. It has been shown that the data collected can all be fitted satisfactorily with published models for the crystal structure. However, there is some debate about the exact crystal structure of $Y_{1-x}Sr_xCoO_{3-\delta}$ and we have made single crystal diffraction measurements in the hope of shedding some light on this issue

5.3.4 Single Crystals

Prior to the work described in this thesis, diffraction measurements had never been performed on single crystals of any $Y_{1-x}Sr_xCoO_{3-\delta}$ compound. It was therefore important to carry out a general survey of the diffraction peaks as well as evaluating the changes in the structure as a function of temperature. Figure 5.14 shows unwarped images of the $(0kl)$, $(h0l)$ and $(hk0)$ planes of the $I4/mmm$ crystal structures, as measured using single crystal X-ray diffraction at room temperature, described in section 5.3.1. The shape of the peaks, with a tail directed away from

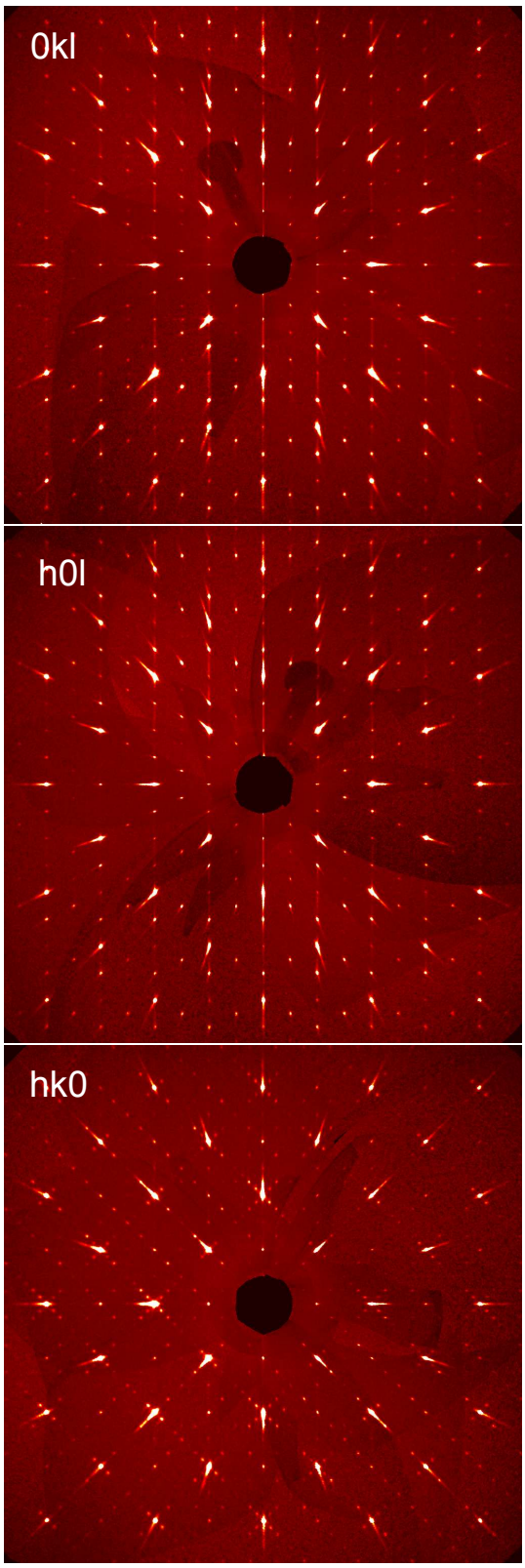

Figure 5.14: Single crystal X-ray diffraction data for $Y_{0.15}Sr_{0.85}CoO_{3-\delta}$ collected on an Oxford Diffraction Gemini R diffractometer at room temperature. The unwarped planes shown are $0kl$, $h0l$ and $hk0$ planes in the parent $I4/mmm$ structure.

the centre of the image, is a characteristic of the measurement. Closer inspection of one of these peaks shows the shape is a Maxwell-Bolzmann distribution due to the Bremsstrahlung continuum convolved with the positions of the K_α and K_β lines of the molybdenum source. The use of a molybdenum rather than a copper source meant the fluorescence which hampered the powder X-ray diffraction measurements was not an issue here.

Various qualitative conclusions can be drawn from the data in figure 5.14. The largest peaks correspond to those of the cubic perovskite base structure, at a lattice spacing of 3.84 Å. Along the c axis (the top and bottom panels), this cubic structure is 4-times modulated, in agreement with the 15.4 Å lattice parameter along this axis in the $I4/mmm$, $Cmma$ and $A2/m$ space groups. There is also clear diffuse scattering along this axis, indicating some structural disorder. This diffuse scattering is weak, many times weaker than the main structural peaks, and hence we would not expect to observe it in powder data. Diffuse scattering will usually serve to reduce the accuracy of any refinement of this data and lead to an anomalously high agreement factor. In a system such as this, the diffuse scattering may indicate that any proposed structure is an average of the true z positions of the atoms.

The diffraction data taken in the ab plane of the $I4/mmm$ crystal structure is shown in the central panel of figure 5.14. Careful study of this figure shows that the cubic perovskite structure is 8-times modulated along both the a and b axes. This would potentially indicate a lattice parameter of up to 30.8 Å, which is extremely large. The image confirms using single crystal measurements the existence of a complex superstructure postulated by several researchers from powder diffraction measurements.

The possibility of twinning in our single crystals was considered, as twinning is known to be a problem in tetragonal and orthorhombic systems when the system has formed from one with higher symmetry, which commonly happens in perovskite systems such as this when the sample cools, see section 2.3.2. The most common form of twinning in this case is merohedral twinning, where the system has a symmetry element which is not a symmetry element of the space group but that is a symmetry element of the crystal system. However, by comparing the intensities of equivalent peaks no clear sign of twinning was observed, and although models incorporating merohedral twinning were tested no improvement in the quality of the refinement was observed.

Attempts were made to solve this structure $ab-initio$ using the $GRAL$ applet of the Oxford Diffraction $CrysAlisPro$ software and the $SIR-92$ solution and $Shelx97$ refinement program. However, the challenges involved with such a solution: this data set contains modulation, diffuse scattering and the potential for twinning, meant that we were unable to solve the structure using this method.

Expert analysis may make finding such a solution possible but is beyond the scope of this work, which is motivated by the magnetic order rather than crystallographic properties of $Y_{1-x}Sr_xCoO_{3-\delta}$.

Parameter	X-rays	Neutrons
a (Å)	15.3981	N/A
b (Å)	10.9525	N/A
c (Å)	10.9165	N/A
R_p	0.0818	13.3
R_{wp}	0.0796	15.8
χ^2	1.888	6.97
λ	0.7107	1.26
Temperature (K)	300	420

Table 5.5: Refinement details for single crystals of AO/OO $Y_{0.15}Sr_{0.85}CoO_{3-\delta}$ in the *Cmma* space group. The lattice parameters for the neutron diffraction refinement are not given as this refinement is done on the basis of matching the intensities of set peaks, without considering their positions.

As a complete structural solution is unavailable, we should consider how the previously proposed $I4/mmm$, $Cmma$ and $A2/m$ structures fit with the observed diffraction pattern in figure 5.14 to enable quantitative analysis of this data. The tetragonal $I4/mmm$ parent structure only involves a doubling of the simple perovskite structure in the *ab* plane, so accounts for little of this complex superstructure. Therefore, the fit of this data to the previously proposed [21] $Cmma$ space group was tested. A comparison of the observed and calculated intensities of the peaks measured at a wavelength of 1.26 Å is shown in figure 5.15. Although this space group clearly does not account for all the peaks shown in figure 5.14, as it only involves a 4-fold modulation in the *ab* plane rather than the 8-fold one observed, it accounts for all bar a single set of peaks which appear nearest to the large perovskite peaks.

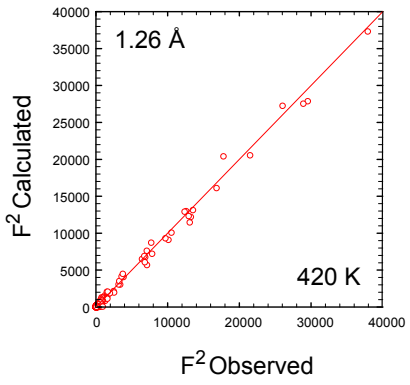

Figure 5.15: Comparison of the observed and calculated squares of the intensities of the diffraction peaks measured with an incident wavelength of 1.26 Å at 420 K on the single crystal diffractometer D10. The extent to which the peaks lie on the plotted $x = y$ line gives a visual measure of the quality of the fit to the $Cmma$ space group used for the fit.

The lattice parameters and fit details for the X-ray and neutron refinements in the $Cmma$ space group are given in table 5.5. The lattice parameters for the

Atom	Site	x	y	z	B	Occ.
Sr1	8a	0.36971(4)	0.5	0	0.0103(1)	1.0
		0.3704(6)	0.5	0	1.52(8)	1.0
Sr2	8a	0.35576(3)	0.25	0.25644(4)	0.0128(1)	0.4
		0.3649(4)	0.25	0.250(1)	1.31(6)	0.4
Y1	8a	0.35576(3)	0.25	0.25644(4)	0.0128(1)	0.6
		0.3649(4)	0.25	0.250(1)	1.31(6)	0.6
Sr3	8a	0.37662(3)	0.25	0.74186(4)	0.0166(1)	1.0
		0.3748(4)	0.25	0.7502(7)	1.15(6)	1.0
Sr4	8a	0.36709(4)	0.5	0.5	0.0118(1)	1.0
		0.3726(4)	0.5	0.5	0.51(5)	1.0
Co1	8a	0	0.00214(6)	0.25557(6)	0.0148(2)	1.0
		0	0.001(2)	0.250(2)	1.4(2)	1.0
Co2	4a	0.5	0.25	-0.00949(8)	0.0116(2)	1.0
		0.5	0.25	0.007(6)	3.5(7)	1.0
Co3	4a	0.25	0.25	0	0.0077(2)	1.0
		0.25	0.25	0	1.7(4)	1.0
Co4	4a	0.25	0.25	0.5	0.0076(2)	1.0
		0.25	0.25	0.5	0.2(2)	1.0
Co5	8a	0.25	0.5	0.24885(5)	0.0070(1)	1.0
		0.25	0.5	0.250(2)	1.0(1)	1.0
Co6	4a	0.5	0.25	0.49390(8)	0.0123(2)	1.0
		0.5	0.25	0.501(2)	0.0(2)	1.0
O1	16a	0.2392(2)	0.37340(3)	0.12660(2)	0.0156(6)	1.0
		0.2479(5)	0.3671(4)	0.1316(4)	0.83(4)	1.0
O2	16a	0.2430(2)	0.37340(3)	0.37360(2)	0.0147(6)	1.0
		0.2339(4)	0.3820(6)	0.3810(6)	1.66(7)	1.0
O3	8a	0.5	0.369(3)	0.136(2)	0.005(8)	0.10(1)
		0.5	0.394(3)	0.104(3)	1.8(5)	0.24(4)
O4	8a	0	0.1130(4)	0.1176(3)	0.023(1)	1.0
		0	0.132(1)	0.124(1)	2.1(1)	1.0
O5	8a	0.5	0.310(1)	0.3268(9)	0.050(4)	0.43(1)
		0.5	0.378(2)	0.376(2)	2.6(2)	0.70(4)
O6	8a	0.5	0.3855(4)	0.60790(3)	0.022(1)	1.0
		0.5	0.3947(7)	0.6073(8)	1.5(1)	1.0
O7	8a	0.3882(3)	0.25	0.0401(3)	0.0269(9)	1.0
		0.3750(6)	0.25	0.003(1)	1.04(8)	1.0
O8	8a	0.3757(3)	0.25	0.4813(3)	0.0223(9)	1.0
		0.385(2)	0.25	0.464(1)	3.7(2)	1.0
O9	16a	0.3835(2)	0.4699(3)	0.2504(2)	0.0273(6)	1.0
		0.3772(6)	0.4818(5)	0.2499(2)	2.8(1)	1.0

Table 5.6: Table of Wyckoff positions for single crystal $Y_{0.15}Sr_{0.85}CoO_{3-\delta}$ refined in the *Cmma* space group. The upper values are those from the refinement of the single crystal X-ray diffraction data taken at a temperature of 300 K. The lower values are those from the refinement of the single crystal neutron diffraction data taken at a temperature of 420 K. (see footnote 1 for the errors on the neutron data).

neutron diffraction refinement are not given as this refinement is done on the basis of matching the intensities of set peaks, without considering their positions. The refinements were also performed using different software, FULLPROF and *Shelx-97* for neutrons and X-rays respectively, so the R and χ^2 values should not be considered directly comparable. The X-ray refinement also included anisotropic thermal parameters, which further improved the refinement. The refined values generally agree with the structure proposed in reference [21]. The refined Wyckoff positions, given in table 5.6, of the partially occupied O3 and O5 sites are quite different, and this could be for one of several reasons. Either the difficulty in refining the positions of vacancies and sites with low occupancy have resulted in an error or there is some shift in the positions of these atoms at the structural transition at 370 K.[1]

Refining in a twinned $A2/m$ space group was considered, particularly as a version of this structure twinned in the *ab* plane would account would account for all the observed peaks. However, no evidence of twinning was found in the diffraction data, and such a structure was too complex to use without prior knowledge of some parameters, as too many free parameters tended to cause the refinement to become unstable. Quantitative analysis of the magnetic structure of $Y_{1-x}Sr_xCoO_{3-\delta}$ will therefore be done by using either the tetragonal $I4/mmm$ parent structure or the orthorhombic $Cmma$ structure, and the implications of using a simplified crystallographic structure for the interpretation of the magnetic data will need to be considered.

5.3.5 Structural Transitions

Previous work has established there are at least three structural phase transitions in the AO/OO phase of $Y_{1-x}Sr_xCoO_{3-\delta}$ as a function of temperature at ∼509, ∼360 [89] and ∼300 K [92]. The measurements described above were made at temperatures of 420 K for the neutron diffraction and 300 K for the X-ray diffraction. These are both below the first phase transition, which is believed to be from an $I4/mmm$ unit cell to a lower symmetry phase [89], hence the observation of a complex orthorhombic or monoclinic superstructure which could not be fully solved. This phase transition is generally acknowledged to be due to oxygen vacancy ordering [89]. This first structural phase transition will not be discussed any further, as this study has involved no structural measurements at temperatures above 509 K.

[1]The large number of free parameters in the $Cmma$ structure caused the refinement of the neutron data in FULLPROF to be unstable in some cases. For this reason, not all the parameters were refined simultaneously. This causes a problem when generating the errors on the final values. Therefore, after the final refinement cycle, the errors were generated by refining each final value individually, discarding any changes in the atom positions (which were generally negligible) before the next value was refined.

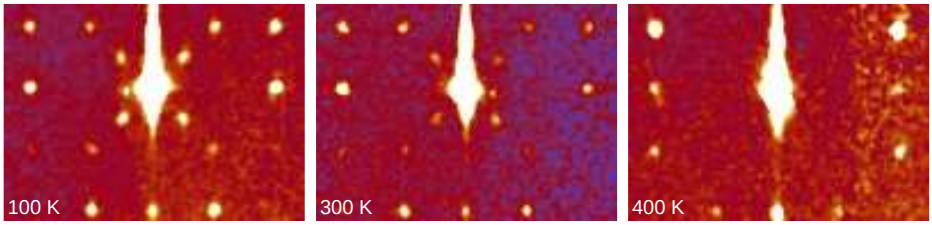

Figure 5.16: The $(4, 0, 0)$ peak in the $I4/mmm$ space group of AO/OO $Y_{1-x}Sr_xCoO_{3-\delta}$ measured using single crystal X-ray diffraction at 400, 300 and 100 K. Additional peaks appear at positions corresponding to $(3.5, 0.5, 0)$ and $(3.75, 0.25, 0)$ as the crystal is cooled.

The critical temperature of the second structural transition is a matter of some debate, and this debate is significant as it serves to establish whether the structural and magnetic transition coincide. This second structural transition is believed to be first order [89, 45]. Synchrotron X-ray diffraction gave a transition temperature of 360 K [89], powder neutron diffraction measurements suggested $T_c = 330$ K [24] and resonant X-ray scattering experiments gave a transition temperature of 390 K [45]. It should be noted these measurements were all made on different samples, the latter of which was a single crystal, and so it is conceivable the differences in oxygen content have affected the T_c. Our single crystal has been measured at three different temperatures using single crystal X-ray diffraction equipped with a cryostream, described in section 5.3.1. The $(4, 0, 0)$ peak at each of these temperatures is shown in figure 5.16. As the temperature is reduced, additional peaks appear at positions corresponding to $(3.5, 0.5, 0)$ and $(3.75, 0.25, 0)$ in the $I4/mmm$ space group. Peaks also appear at the appropriate symmetry equivalent positions to these. The peaks are strongest at the lowest temperature and appear at a temperature between 300 and 400 K, in keeping with the transition temperatures quoted by other groups. The presence of these peaks implies the formation of a monoclinic supercell at low temperatures. The precise temperature of this structural phase transition will be investigated further in section 6.3.2.

This second structural phase transition has been attributed to orbital ordering, described in section 2.1.3. Figure 5.17 has been taken from a recent resonant X-ray diffraction study on $Y_{1-x}Sr_xCoO_{3-\delta}$. It shows the proposed orbital ordering in the fully-oxygenated CoO_6 layers. These measurements immediately imply the existence of the IS state in $Y_{1-x}Sr_xCoO_{3-\delta}$, as neither the HS or LS spin states are e_g orbitally degenerate [45]. The structure proposed consists of $d_{x^2-y^2}$ and $d_{y^2-z^2}$ e_g orbitals of the IS Co^{3+} alternately arranged and separated by HS Co^{3+} spheres, a 'zig-zags and spheres' ordering [112]. The measurement of this type of antiferromagnetic orbital ordering in $Y_{1-x}Sr_xCoO_{3-\delta}$ was the first experimental observation of this kind of behaviour in any material [112].

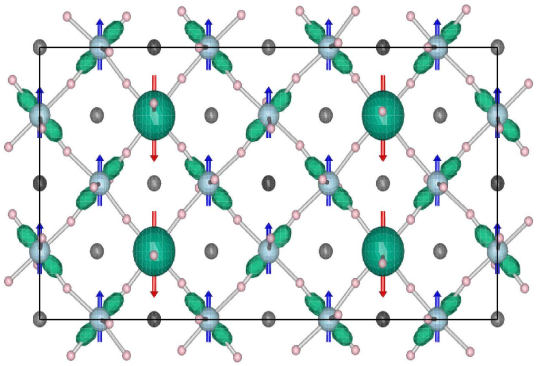

Figure 5.17: The proposed orbital ordering in the fully-oxygenated CoO_6 layers of $Y_{1-x}Sr_xCoO_{3-\delta}$. The structure proposed consists of $d_{x^2-y^2}$ and $d_{y^2-z^2}$ e_g orbitals of the IS Co^{3+} are alternately arranged and separated by HS Co^{3+} spheres, a 'zig-zags and spheres' ordering [112]. Figure taken from reference [45].

The third structural phase transition in $Y_{1-x}Sr_xCoO_{3-\delta}$ occurs at a temperature of ∼280 K [24]. Although a structural change at this temperature has been indicated by previous research, little has been established about its nature. Both the transition at ∼370 K and this one at ∼280 K were investigated by measuring the changes in the lattice parameters as a function of temperature. Changes in the lattice parameter at 370 K were observed using the triple-axis spectrometer 2T1 described in section 6.4.1 (not shown), and these changes were most prominent along the a direction of the $I4/mmm$ unit cell. The lattice parameters of the $I4/mmm$ unit cell as function of temperature measured using neutron diffraction are shown in figure 5.18. The trend agrees with that observed previously [25], and both a and c decrease as the temperature is reduced, as would be expected.

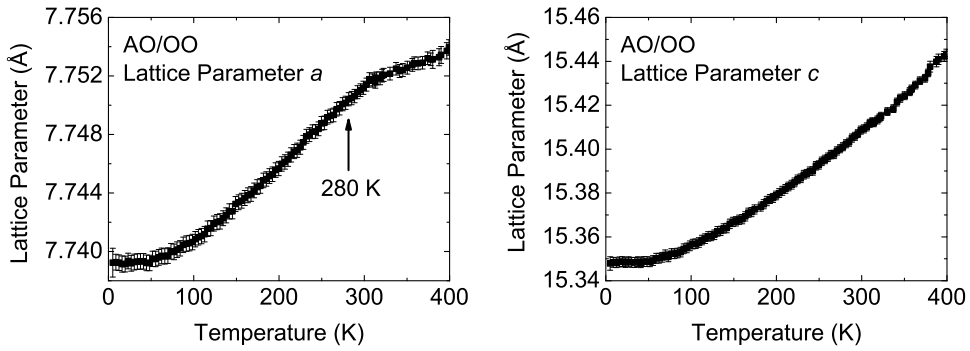

Figure 5.18: Temperature dependence of the lattice parameters a and c of the AO/OO form of $Y_{1-x}Sr_xCoO_{3-\delta}$ refined in the $I4/mmm$ space group.

At a temperature around 280 K to 300 K, the isotropic thermal expansion observed at low temperatures becomes more anisotropic, and there is a notable change in slope of the a lattice parameter as a function of temperature. The same measurements of the lattice parameters as a function of temperature were also made in the $Cmma$ space group. Figure 5.19 shows the temperature dependence of a, b and c lattice parameters as a function of temperature, and the same change in slope at ∼280 K described above was observed for the c lattice parameter, although there

are large errors on the measurement.

The transition at 280 K is believed to be of the displacive type. This is because the transition temperature is believed to be too low for a superstructure reconstruction [24]. Previous work [25] also suggested that many of the Co-O bond angles do not change with temperature, which means tilting of the oxygen polyhedra may not be responsible for this structural transition. This structural change also coincides with a change in the magnetic behaviour, discussed in the next chapter, and the relationship between the two has not yet been established.

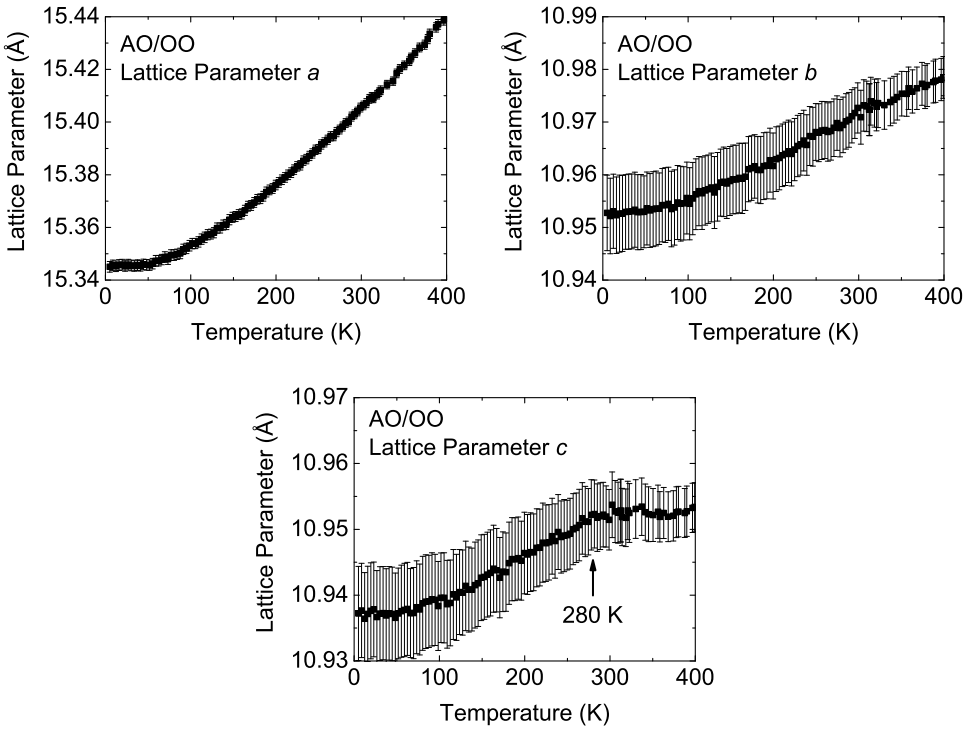

Figure 5.19: Temperature dependence of the lattice parameters a, b and c of the AO/OO form of $Y_{1-x}Sr_xCoO_{3-\delta}$ refined in the *Cmma* space group. The size of the error bars is due to the systematic errors involved in refining the data, as the random errors in the data are small.

5.4 Discussion

High quality single crystals of the A-site and oxygen vacancy ordered variant of the yttrium-doped strontium cobaltates $Y_{1-x}Sr_xCoO_{3-\delta}$ ($0.7 \leq x \leq 0.95$) have been produced using the floating zone technique. The yttrium and oxygen contents of these crystals have been evaluated using EDAX and TGA respectively and a single crystal with chemical formula $Y_{0.15}Sr_{0.85}CoO_{2.63}$ has been used for a detailed study. Powder samples of A-site and oxygen vacancy disordered (AD/OD), A-site

disordered and oxygen vacancy ordered (AD/OO) and A-site and oxygen vacancy ordered (AO/OO) forms of $Y_{0.15}Sr_{0.85}CoO_{3-\delta}$ were also produced using a standard solid state synthesis technique.

The crystal structures of both the $Y_{0.15}Sr_{0.85}CoO_{3-\delta}$ powders and single crystals were studied using X-ray and neutron diffraction. Although a full structural solution for the A-site and oxygen vacancy ordered variant of $Y_{1-x}Sr_xCoO_{3-\delta}$ was not found, the structure was investigated and evidence of a complex superstructure with an 8-fold modulation of the basic perovskite cell in the ab plane was recorded. Diffuse scattering along the unique axis (c axis of the $I4/mmm$ space group) of the unit cell was also observed suggesting some structural disorder along that axis. The crystal structure of AO/OO $Y_{0.15}Sr_{0.85}CoO_{3-\delta}$ was refined satisfactorily in each of the $I4/mmm$, $Cmma$ and $A2/m$ space groups, in agreement with the results of previous investigations. Transmission electron microscopy and combined X-ray, neutron and electron studies will be necessary to solve the exceptionally complex superstructure of this material.

Evidence of structural transitions at 370 K and 280 K was also observed using single crystal X-ray diffraction data and by studying the thermal expansion profile of the lattice parameters. The first of these transitions involves at least a doubling of the unit cell and a transition to a lower symmetry structure. This transition has been ascribed to orbital ordering of Co^{3+} ions in the intermediate spin state. The second of these is likely to be a displacive type structural phase transition. Both of these phase transitions appear to be linked to the magnetic behaviour of $Y_{1-x}Sr_xCoO_{3-\delta}$ which will be discussed in the next chapter.

Chapter 6

$Y_{1-x}Sr_xCoO_{3-\delta}$: Magnetism

The magnetic ordering in $Y_{1-x}Sr_xCoO_{3-\delta}$ has been of interest to researchers because of an observed room-temperature ferromagnetic signal [22] and magnetic behaviour heavily dependent on oxygen content [11]. The work undertaken utilised magnetisation, specific heat, powder neutron diffraction, single crystal neutron diffraction and neutron spectroscopy to study the magnetic behaviour of $Y_{1-x}Sr_xCoO_{3-\delta}$. The $Y_{0.15}Sr_{0.85}CoO_{3-\delta}$ compound was studied in all cases for consistency and because of the availability of single crystals of this composition. The aim of these measurements was to characterise the magnetic behaviour of $Y_{1-x}Sr_xCoO_{3-\delta}$ and determine the magnetic structure in zero field.

6.1 Characterisation Measurements

6.1.1 dc-Susceptibility of Powder

The dc-susceptibility of the powder samples of the three possible structural variants of $Y_{1-x}Sr_xCoO_{3-\delta}$, AD/OD, AD/OO and AO/OO, was measured as a function of temperature using a Quantum Design SQuID MPMS. The samples (masses between 36 and 69 mg) were placed in gel capsules and then put inside a plastic sample straw. The samples had the compositions $Y_{0.15}Sr_{0.85}CoO_{2.70}$, $Y_{0.15}Sr_{0.85}CoO_{2.53}$ and $Y_{0.15}Sr_{0.85}CoO_{2.50}$ respectively. All the measurements were carried out in applied magnetic fields of 0.1 and 1 T. The resulting six curves are shown in figure 6.1.

The magnetisation of the AD/OD compound shows evidence of two transitions as a function of temperature. The first transition on cooling is at 335 K and the second at 150 K, marked on panels (a) and (b) of figure 6.1. In higher fields (1 T) the change in the intensity of the magnetic signal at the first transition at 335 K is suppressed and the change in the intensity of the magnetic signal at the second transition at 150 K is enhanced. The transition at 150 K is believed to reflect the onset of ferromagnetic behaviour in this AD/OD compound. Comparing

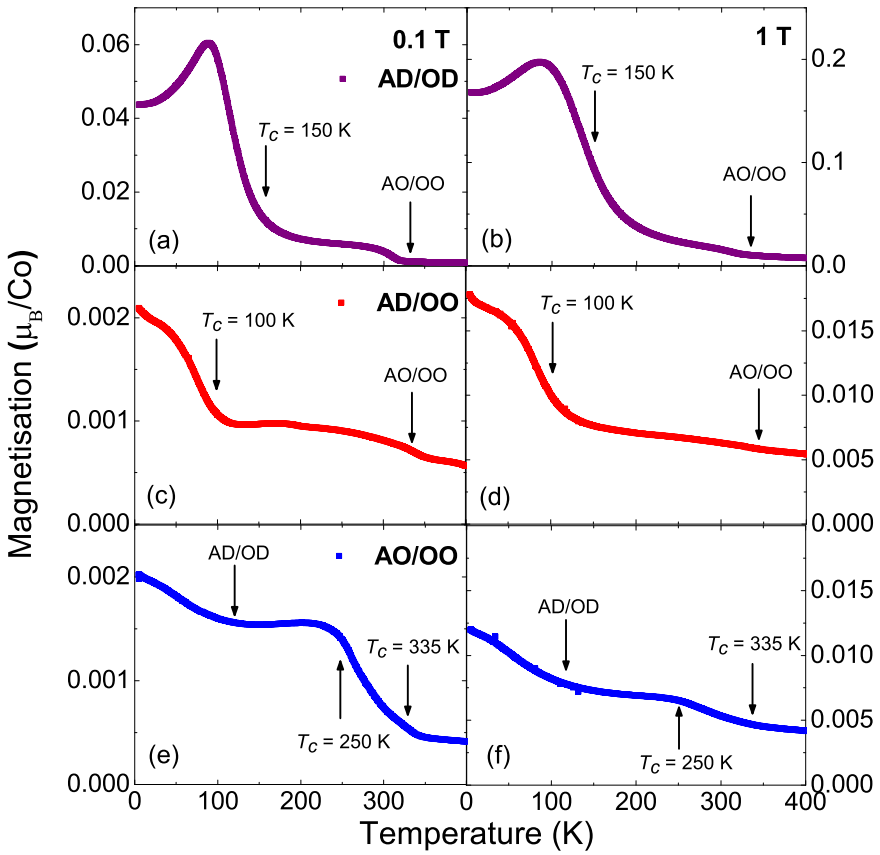

Figure 6.1: dc-magnetisation as a function of temperature as measured for AD/OD, AD/OO and AO/OO $Y_{0.15}Sr_{0.85}CoO_{3-\delta}$ samples. The measurements were made in applied magnetic fields of 0.1 (a, c and e) and 1 T (b, d and f) respectively. The transition temperatures for each of the samples and their suspected impurity phases are also marked.

with similar measurements made by other researchers, the recorded low temperature magnetisation agrees with the magnetisation of the lowest δ compound previously measured [92]. A similar ferromagnetic signal has been observed for other conventional perovskite cobaltates such as $La_{1-x}Sr_xCoO_3$ [57, 23, 92], and has been attributed to the double exchange interaction between neighbouring cobalt atoms with unequal valencies, which is the suggested mechanism in this AD/OD material.

At first glance, the magnetisation of the brownmillerite AD/OO form of $Y_{0.15}Sr_{0.85}CoO_{3-\delta}$ behaves similarly to the AD/OD compound, with two features which can be associated with magnetic transitions, one at 335 K and one at 100 K. However, the magnitude of the low temperature magnetisation is a factor of 20 lower than that measured for the AD/OD material. The transition temperature is comparable with the 130 K previously reported [91, 92] for the AD/OO material though lower than the 200 K that also been claimed [85]. The differences are credible considering the strong influence of oxygen content on the properties of the material (the AD/OO structure is only stable in the vicinity of $\delta = 0.5$). The origin of this weak ferromagnetic signal will be discussed in section 6.2.1, but the relative weakness of the signal means the bulk of the sample is unlikely to be ferromagnetically correlated.

The dc-magnetisation as a function of temperature of the sample of the AO/OO structural variant of $Y_{0.85}Sr_{0.15}CoO_{3-\delta}$ is shown in panels (e) and (f) of figure 6.1. The transition temperature of 335 K is in agreement with previously reported values [22, 92]. This is also means the transitions at 335 K for the AD/OD and AD/OO forms of the compound (panels (a) to (d)) are likely to be due to some AO/OO impurity phase. The quenching involved with the production of these structural variants of $Y_{0.85}Sr_{0.15}CoO_{3-\delta}$ means it is more likely impurity phases will be present in the samples than for samples formed without quenching. Conversely, an increase in the magnitude of the magnetisation of the AO/OO compound at lower temperatures indicates some phase fraction of disordered material is also present in this sample. A change in slope in the magnetisation is present at 250 K in the magnetisation of this AO/OO sample, and this is marked on panels (e) and (f) of figure 6.1. This cusp is present in the previous measurements done on this compound, and like the transition temperature, its position depends on the value of δ.

The magnetisation behaviour recorded for the AD/OD, AD/OO and AO/OO $Y_{0.85}Sr_{0.15}CoO_{3-\delta}$ powders agrees with that previously reported for polycrystalline samples of the $x = 0.75$ compound with similar values of δ [22, 91, 92]. However, very little is known about the magnetic properties of single crystals of any of the $Y_{1-x}Sr_xCoO_{3-\delta}$ series [94] and the subsequent sections aim to address this disparity.

6.1.2 dc-Susceptibility of Single Crystals

In order to measure the magnetic properties of single crystals of $Y_{0.15}Sr_{0.85}CoO_{3-\delta}$ small sections were cut from the boules using a low-speed diamond saw. Each boule was encased in wax before cutting to support the material, as the crystals were found to be quite brittle. In some instances the samples were aligned using the X-ray Laue method. dc-magnetisation measurements as a function of temperature were made between 5 and 400 K in applied magnetic fields of up to 1 T using a magnetometer. Samples with masses ∼100 mg were affixed to a polyether ether ketone (PEEK) plastic sample holder using GE varnish and then put inside a plastic sample straw for the the measurement.

Figure 6.2 shows the dc-susceptibility versus temperature measurements made on as-grown and O_2 annealed crystals of $Y_{0.15}Sr_{0.85}CoO_{3-\delta}$. All the single crystals discussed in this thesis were the AO/OO structural variant of $Y_{1-x}Sr_xCoO_{3-\delta}$. For the as-grown crystal the magnetic ordering temperature is around 350 K and the magnitude of the magnetisation at low temperatures is small, 0.0025 μ_B/Co. A broad peak at $\sim$ 100 K suggests that a small quantity of the AD/OD phase is present [92]. For the O_2-annealed crystal a much more apparent transition occurs at 370 K. The observed critical temperature for the transition is at the same as that previously reported for an $x = 0.75$ single crystal [94]. The magnitude of the dc-magnetisation at low temperatures is substantially less than would be expected if all the cobalt moments were ferromagnetically aligned, suggesting again that the measured magnetisation signal does not necessarily imply bulk ferromagnetism in the sample.

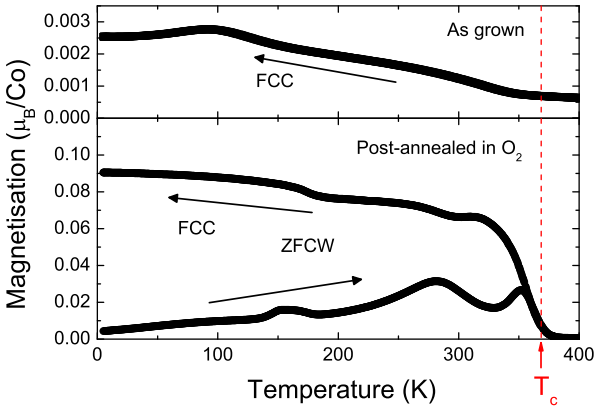

Figure 6.2: The temperature dependence of the zero-field cooled warming (ZFCW) and field-cooled cooling (FCC) dc-magnetisation of a single crystal of $Y_{0.15}Sr_{0.85}CoO_{3-\delta}$. The top panel shows the magnetisation for the as-grown crystal with a δ value of 0.41 and the bottom panel shows the magnetisation for the O_2-annealed crystal ($H \,||\, c$) with a δ value of 0.37. The measurements were made in an applied magnetic field μ_0H = 0.1 T.

A second transition in the magnetic behaviour is present at 280 K, which is most clear in the zero-field cooled measurement. This feature has been previously

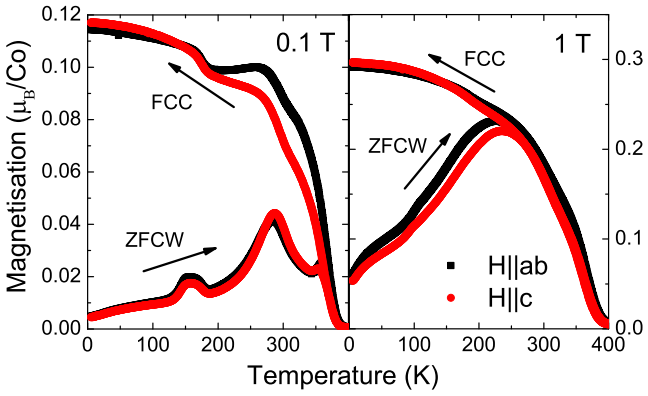

Figure 6.3: The temperature dependence of the zero-field cooled warming (ZFCW) and field-cooled cooling (FCC) dc-magnetisation of a crystal of $Y_{0.15}Sr_{0.85}CoO_{3-\delta}$ in applied magnetic fields of $\mu_0 H = 0.1$ (left panel) and 1 T (right panel) measured with $H \,||\, c$ and $H \,||\, ab$.

observed in the dc-magnetisation measurements on $Y_{1-x}Sr_xCoO_{3-\delta}$ powders, at 250 K in figure 6.1, and has been attributed to a smearing out of the ferromagnetic signal associated with the range of possible oxygen stoichiometries found in this material [92]. The magnetic response characteristic of the AD/OD material (a change in slope at ~ 150 K) is also visible in the data. This result suggests that the sample contains around 1% of the AD/OD phase. The increase in the transition temperature of the AD/OD minority phase (as compared to that seen in the as-grown sample) is consistent with an increase in the oxygen content of this phase due to the O_2-annealing. At low temperatures the magnetisation signal of the O_2-annealed sample is almost two orders of magnitude larger than for the as-grown sample, showing in the influence of oxygen content on the magnetic behaviour of $Y_{1-x}Sr_xCoO_{3-\delta}$. Substantial hysteresis is present between the field cooled and zero-field cooled measurements implying the presence of domains.

Figure 6.3 shows the same dc-magnetisation as a function of temperature measured with the crystal aligned parallel to the c axis of the $I4/mmm$ unit cell shown in figure 6.2. In addition, measurements were made with the crystal aligned parallel to the ab plane and in a 1 T applied magnetic field. The results indicate that the magnetisation is isotropic, as the same features appear with the similar magnitudes in both measurements. The slight difference in magnitudes between the measurements made with the sample aligned parallel to the c axis and parallel to the ab plane in a field of $\mu_0 H = 0.1$ T is attributed to the demagnetisation factor associated with the shape of the sample (which was closer to a cuboid than a sphere) rather than any anisotropy in the magnetic response of the sample. Anisotropy of the magnetic response of the sample might have been expected because of the layered crystal structure of the compound and the possibility of spin canting in the material. This interpretation agrees with the observed magnetisation in a $\mu_0 H = 1$ T applied magnetic field, which is almost perfectly isotropic.

6.1.3 ac-Susceptibility

The same MPMS system was used to carry out ac-susceptibility measurements on an O_2-annealed sample of single crystal aligned parallel to the c axis. As with the dc-susceptibility measurements the sample was mounted on plastic PEEK sample holder using GE varnish and put inside a non-magnetic straw. The sample had mass $m = 28.977$ mg. The measurements were made in zero external dc field, with a 0.0003 T (3 Oe) ac driving field at a frequency of 30 Hz. The results are shown in figure 6.4.

There are three clear features in the data, marked as $T_{c1} = 165$ K, $T_{c2} = 284$ K and $T_{c3} = 371$ K. These features imply reorientation of the magnetic moments at these temperatures, and their positions correlate with the temperatures of the three transitions observed in the equivalent dc-susceptibility data, shown in figure 6.2. This data gives us more exact positions for these transitions in temperature than the dc equivalent.

The feature at T_{c3} correlates with the transition to ferromagnetic behaviour observed in the dc-susceptibility at 370 K. The peak at T_{c1} has a similar character to the one at T_{c3}, with a sharp peak in both χ'_{ac} and χ''_{ac}. The peaks in χ''_{ac} indicate that the transitions at T_{c1} and T_{c3} are dissipative. In both cases, the peak in χ''_{ac} lags slightly behind that in χ'_{ac}. As discussed in the context of the dc-susceptibility measurements, we attribute the feature at T_{c1} to an A-site and oxygen vacancy disordered impurity in the sample. This interpretation is justified because because no evidence of a transition at this temperature has been observed either by other researchers or using the diffraction measurements detailed later in this chapter.

The ac-susceptibility data also contains a third feature at T_{c2}, identifiable as a cusp in the dc-susceptibility data at 280 K. The presence of this feature means there is either some reorientation or change in the magnitude of the moments at this temperature. The character of this peak in the ac-susceptibility is very different to the peaks at T_{c1} and T_{c3}; it is much broader, and the process that causes it is much less dissipative, as the peak in χ''_{ac} is relatively much smaller than the peaks in χ''_{ac} at T_{c1} and T_{c3}. The fact this feature has been seen by many other researchers and in many different samples suggests it is not associated with disorder or some impurity phase, but some intrinsic property of the material itself. This is reinforced by the presence of a structural change at this temperature, discussed in section 5.3.5. ac-susceptibility appears to be a good technique for studying this transition at T_{c2}, as it is much more clear than in the dc-measurements and has given new information about the dynamics of the potential spin reorientation process involved.

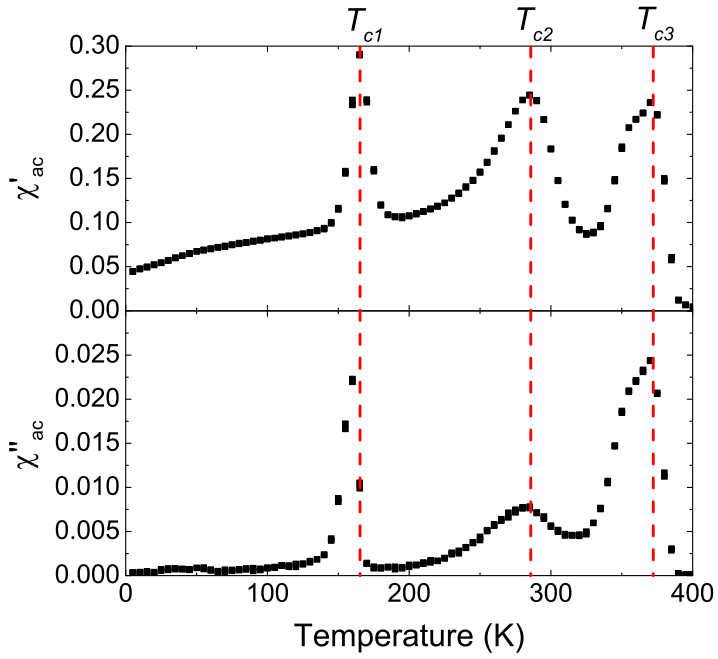

Figure 6.4: In-phase (χ'_{ac}) and out-of-phase (χ''_{ac}) components of the ac-susceptibility as a function of temperature measured in zero external dc-field with a 0.0003 T driving field with an alternating current frequency of 30 Hz. The sample was a single crystal of $Y_{0.15}Sr_{0.85}CoO_{3-\delta}$ aligned with the field parallel to the c axis. The positions of the three transitions observed are marked by dashed lines.

6.1.4 dc-Susceptibility above T_c

A furnace insert to the Quantum Design MPMS system was used to measure the dc-susceptibility of $Y_{0.15}Sr_{0.85}CoO_{3-\delta}$ single crystals at temperatures between 300 and 700 K. A 5.572 mg sample was put inside an alumina sample holder and measured in an applied magnetic field of $\mu_0 H = 0.1$ T. The sample was initially zero-field cooled and was measured both on zero-field cooled warming and on field cooled cooling, although we would expect both to be the same in the paramagnetic regime. This measurement was then repeated three more times without removing the sample. The mass of the sample after the measurement was 5.256 mg, so there was a $\sim$6 % mass loss. Assuming this mass loss is entirely due to the loss of oxygen from the sample, this gives an oxygen content of approximately $3 - \delta = 2.0$, compared to an oxygen content of $3 - \delta = 2.6$ before the measurement.

Figure 6.5 shows the inverse susceptibility $1/\chi$ of a single crystal of $Y_{0.15}Sr_{0.85}CoO_{3-\delta}$ as a function of temperature between 300 and 700 K. If we assume the sample is paramagnetic above T_c, then the data can be fitted with a straight line in this region. At the highest temperatures measured the data becomes quite noisy which is a feature of measurements using the furnace insert. The data between 450 and 550 K was fitted with a straight line with gradient 0.147 ± 0.001 K^{-1} and y-axis intercept 40.1 ± 0.5. Inspecting the data χ_0, the remnant diamagnetic susceptibility due to the sample holder or non-magnetic atoms in the sample, appears to be small and was assumed negligible in the analysis. The demagnetisation factor of the sample was also not considered. Accepting these approximations, and using equation 2.5, a Weiss temperature of -273 K is obtained, lower than the observed critical temperature. This difference between the critical and Weiss temperatures is typical for antiferromagnetic systems with complex magnetic interactions where next-nearest neighbour interactions need to be considered.

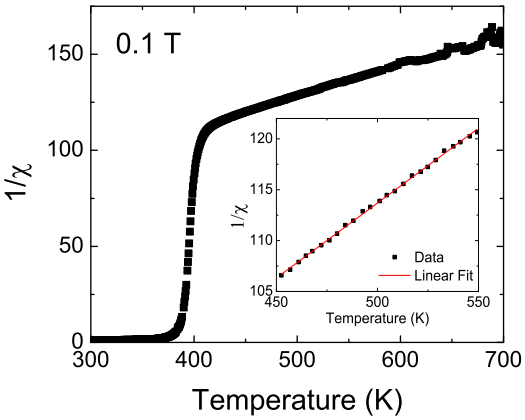

Figure 6.5: The temperature dependence of the inverse dc-susceptibility of a field-cooled crystal of $Y_{0.15}Sr_{0.85}CoO_{3-\delta}$ measured between 300 and 700 K in a $\mu_0 H = 0.1$ T applied magnetic field. Inset: Linear fit to the data between 450 and 550 K.

The gradient $1/C$ of the inverse susceptibility versus temperature in the

paramagnetic regime can be related to the effective magnetic moment μ of the sample using equation 6.1, where N_A is Avogadro's number.

$$C = \frac{\mu^2 \mu_B^2 N_A}{3k_B} \tag{6.1}$$

From the data in figure 6.5, we can therefore obtain an effective magnetic moment of $\mu = 2.33\ \mu_B/f.u.$ for $Y_{0.15}Sr_{0.85}CoO_{3-\delta}$. From our calculations of the cobalt valencies in section 5.2, it is believed that the valency of the cobalt ions in $Y_{0.15}Sr_{0.85}CoO_{3-\delta}$ is 3+. The expected magnetic moments for orbitally quenched Co^{3+} ions in the LS, IS and HS spin states are given in section 2.3.4, and the value of 2.33 is closest to the $\mu = 2.83\ \mu_B$ expected for IS Co^{3+}. In the first approximation, this calculation assumes a single valency and spin state for all the cobalt ions, it would therefore be expected that most of the cobalt ions in $Y_{0.15}Sr_{0.85}CoO_{3-\delta}$ would be in the intermediate spin state.

The measurement was repeated three more times, and each run changed the magnitude of the magnetisation at 300 K and the transition temperature. Heating the sample to 700 K served to increase the magnitude of the magnetisation at 300 K and increase the transition temperature up to a final value of 390 K. These measurements are shown in figure 6.6, where the data between 300 and 400 K is shown although the sample was heated to 700 K each time. The mass loss after the four runs suggests oxygen is lost by heating to 700 K, and the reduction in oxygen content causes the changes in the magnetisation and transition temperature. The repeated heating and cooling therefore acts to anneal the sample, although four runs was not found to saturate the transition temperature.

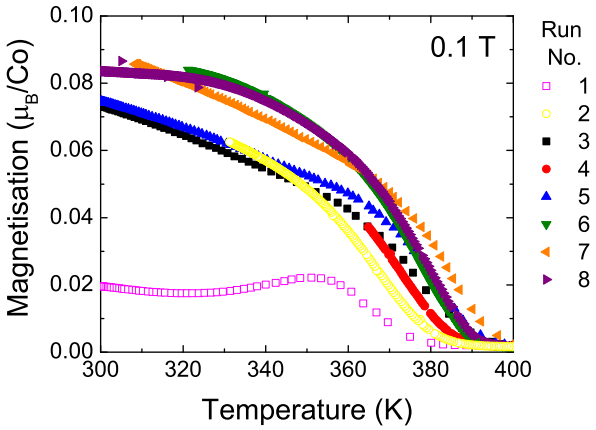

Figure 6.6: The change in the magnetisation between 300 and 400 K caused by heating $Y_{0.15}Sr_{0.85}CoO_{3-\delta}$ to 700 K in a 0.1 T applied magnetic field. The sample was initially zero-field cooled (pink) and then heated and cooled four times in total, giving the eight different runs shown.

6.1.5 Field Dependence of the Magnetisation

dc-magnetisation measurements as function of applied magnetic field were made in a 7 T Quantum Design SQuID MPMS. The sample was initially aligned with the field parallel to the c axis of the $I4/mmm$ unit cell and mounted on a plastic PEEK sample holder using GE varnish and put in a non-magnetic sample straw. The sample was then rotated so that the field was parallel to the ab plane and remeasured.

Figure 6.7 shows the dc-magnetisation as a function of applied magnetic field for the O_2-annealed crystal measured across the 370 K transition temperature. These $M(H)$ curves clearly reveal the ferromagnetic character of the magnetic transition seen at 370 K in the $M(T)$ data. As the temperature is reduced from 400 K to 270 K there is a rapid increase in the magnitude of magnetisation which is accompanied by the appearance of hysteresis in the $M(H)$ loops below 370 K, shown in figure 6.8. The coercive field is around 0.2 T at 270 K and the non-saturating component at high fields suggests an antiferromagnetic component to the magnetisation.

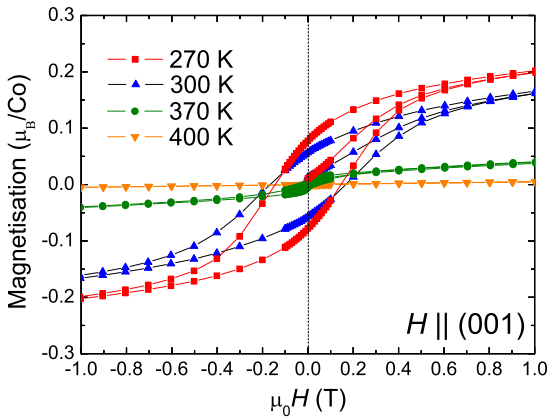

Figure 6.7: The field dependence of the dc-magnetisation of an O_2-annealed crystal of $Y_{0.15}Sr_{0.85}CoO_{3-\delta}$. The sample was warmed above T_c between runs.

Magnetisation measurements made on annealed single crystal samples with the magnetic field applied parallel and perpendicular to the c axis, shown in figure 6.8, reveal that the magnitude of the magnetisation at 7 T is $\sim 5\%$ higher for $H \,||\, c$, indicating a possible small net magnetic moment aligned along the c axis, although this may also be due to a sample shape effect. On the other hand, given the highly anisotropic crystal structure, the lack of anisotropy in the magnetic response of the materials again suggests that $Y_{0.15}Sr_{0.85}CoO_{3-\delta}$ is not a bulk ferromagnet.

The observation of an isotropic magnetic response should be considered in the context of the underlying mechanism for the measured ferromagnetic signal. The TGA measurements for the O_2-annealed crystal suggest the presence of a small amount of Co^{4+}, which would be expected if clustering were the mechanism behind the observed ferromagnetism [23]. An isotropic magnetisation profile would

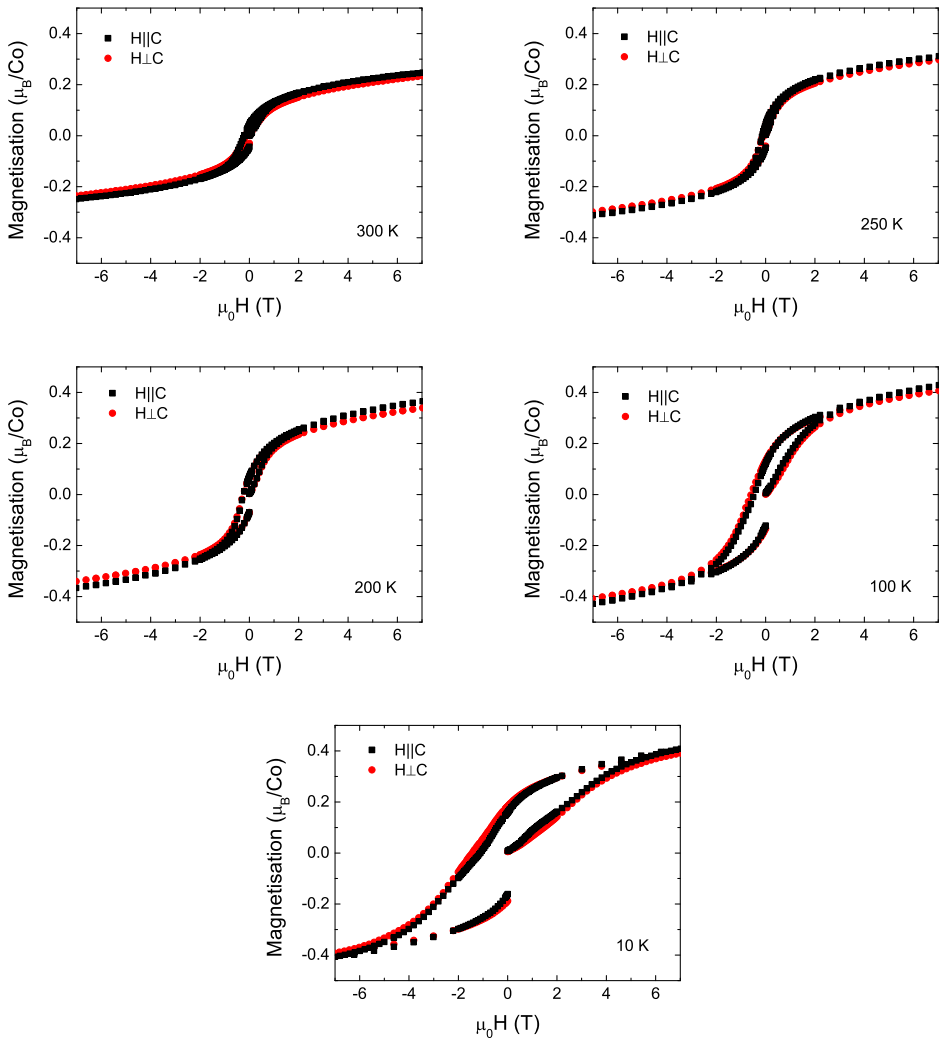

Figure 6.8: The field dependence of the dc-magnetisation of an O_2-annealed crystal of $Y_{0.15}Sr_{0.85}CoO_{3-\delta}$ at 300, 250, 200, 100 and 10 K. Measurements made parallel the c axis are shown in black and measurements made perpendicular to c are shown in red. The sample was warmed above T_c between runs.

be unlikely if spin canting was occurring in this compound, as the moments would generally be constrained to lie close to the direction of the overall antiferromagnetic order. More recent works [24, 45] have suggested the observed magnetisation signal is due to an overall ferrimagnetic ordering of the magnetic moments. On first consideration these ferrimagnetic moments might be expected to be constrained to lie close to the direction of the underlying antiferromagnetic order. However, in some cases such a constraint may not exist, and the remnant ferromagnetic signal due to spin canting or ferrimagnetism may be free to orientate with the applied field, which is likely to be the case here, explaining the isotropic magnetisation measurements.

6.1.6 Specific Heat

Specific heat measurements were performed on the O_2-annealed crystal using a two-tau relaxation method in a Quantum Design Physical Properties Measurement System (PPMS). The heat capacity of the empty sample stage, together with the Apiezon H grease used to attached the sample to the stage, was subtracted from the measured signal to give the sample heat capacity.

Figure 6.9 shows the temperature dependence of the specific heat capacity, $C(T)$, of the O_2-annealed $Y_{0.15}Sr_{0.85}CoO_{3-\delta}$ crystal and the non-magnetic perovskite $LaGaO_3$ that was used to estimate the lattice contribution to the heat capacity. A mass correction was found to give no improvement to the data. The heat capacity of the $Y_{0.15}Sr_{0.85}CoO_{3-\delta}$ contains only one significant feature corresponding to a bulk transition at $T_c = 370$ K. This means that the entropy associated with the features seen at 150 K and 280 K in the $M(T)$ data is small and may be linked with either spin reorientations within an ordered state, or to some magnetic ordering that occurs in a very small volume fraction of material. The extreme sensitivity of the magnetic properties of $Y_{0.15}Sr_{0.85}CoO_{3-\delta}$ to both oxygen disorder and oxygen concentration has led previous researchers to conclude the latter is more likely [92]. The total magnetic entropy released between 3 and 420 K [114] is 11.8 J mol^{-1}K^{-2} which is $\sim$ 88% of the $R\ln(2S+1) = 13.4$ J mol^{-1}K^{-2} expected for a Co^{3+} ion with a fully quenched orbital moment, $S = 2$ (R is the gas constant).

The low temperature ($T \leq 12$ K) data, shown in figure 6.9, can be fitted using the Debye model, as described in equation 2.13. This gives a $\gamma = 0.90$ mJ mol^{-1}K^{-2}, a rather low value that is consistent with previous reports on transition metal oxides that are close to the boundary between an insulating antiferromagnetic and a metallic ferromagnet state [115, 116, 117]. Using β we calculate the Debye temperature $\theta_D = \left(\frac{12}{5}\pi^4 pR/\beta\right)^{1/3}$ where p is the number of atoms in each molecule giving $\theta_D = 391$ K, a result that is compatible with the data at higher temperatures. Adding contributions that vary as T^n with $n = 3/2$ or 2 does not improve the quality of the fits suggesting that any magnetic spin-wave contribution to C varies as T^3,

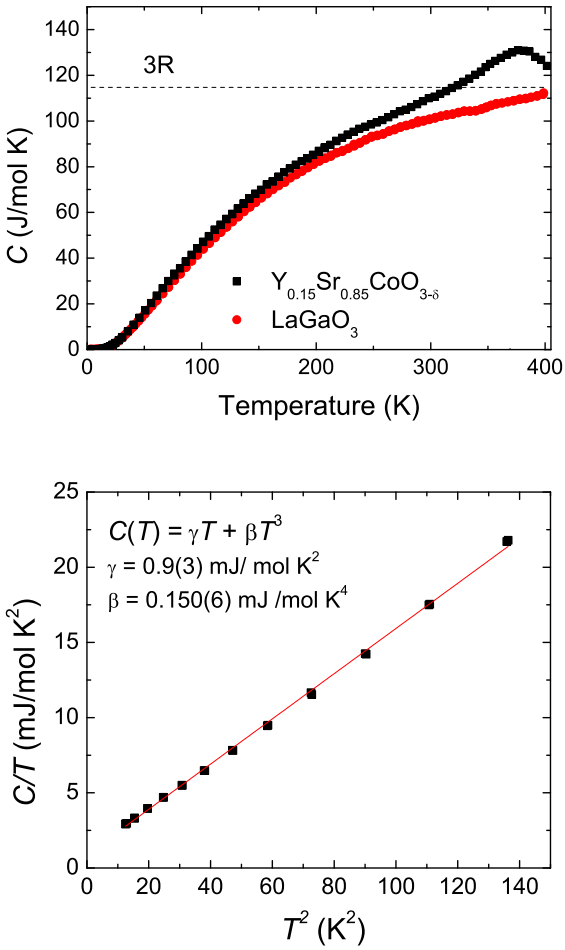

Figure 6.9: Upper panel: Temperature dependence of the specific heat of a single crystal of O_2-annealed $Y_{0.15}Sr_{0.85}CoO_{3-\delta}$. $LaGaO_3$, a non-magnetic perovskite, was also measured and is shown to indicate the lattice contribution to the recorded signal. The horizontal line indicates the value of 3R per atom for $Y_{0.15}Sr_{0.85}CoO_{3-\delta}$. Lower panel: C/T vs T^2 for the low temperature specific heat ($2 < T < 10$ K) of a single crystal of O_2-annealed $Y_{0.15}Sr_{0.85}CoO_{3-\delta}$. The fit is to a model consisting of the electronic (γT) and the lattice (βT^3) contributions to the specific heat, which appears to be a good description of this low temperature data.

a behaviour that is typical for a bulk antiferrromagnet and consistent with the arguments presented earlier.

6.2 Powder Neutron Diffraction

6.2.1 AD/OD and AD/OO Powder Measurements

Powder neutron diffraction measurements were carried out on the D1B instrument at the ILL on the AD/OD, AD/OO and AO/OO structural variants of $Y_{0.15}Sr_{0.85}CoO_{3-\delta}$. The experimental details are outlined in section 5.3.1. First we discuss the two disordered forms of the compound. Measurements were made between 8 and 300 K, with an additional measurement at 500 K for each of the forms of $Y_{0.85}Sr_{0.15}CoO_{3-\delta}$.

The diffraction pattern from the AD/OD form of $Y_{0.15}Sr_{0.85}CoO_{3-\delta}$ at 500 K was shown in figure 5.6 of chapter 5. The diffraction pattern looks identical to this at 8 K. On closer inspection there is a small shift in position between the patterns collected at 145 and 158 K, coinciding with the transition temperature of 150 K obtained from the susceptibility data, figure 6.1. No antiferromagnetic diffraction peaks were observed at any temperature for this AD/OD structural variant, indicating either a non-magnetic sample or a magnetic configuration which contributes to the peaks in such a way that it is not easily detectable, such as a ferromagnetic ordering that contributes equally to all the Bragg peaks. The latter of these explanations fits with the magnetisation measurements and confirms previous assertions [91, 92] that the AD/OD form of $Y_{1-x}Sr_xCoO_{3-\delta}$ is a bulk ferromagnet.

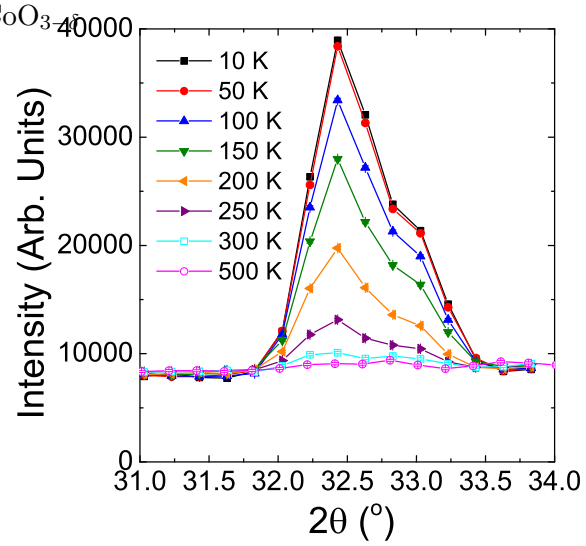

Figure 6.10: The (-1,0,1)/(-1,2,1) and (-1,1,2)/(1,-1,0) magnetic Bragg peaks (left and right respectively) of the AD/OO structural variant of $Y_{0.15}Sr_{0.85}CoO_{3-\delta}$ measured on the neutron diffractometer D1B at temperatures between 10 and 500 K.

A powdered sample of the brownmillerite AD/OO form of $Y_{0.15}Sr_{0.85}CoO_{3-\delta}$ was also studied using D1B. In this case, we observed quite different results to the AD/OD version. Figure 6.11 shows the refined low temperature (8 K) neutron diffraction data and the associated magnetic structure of the AD/OO structural

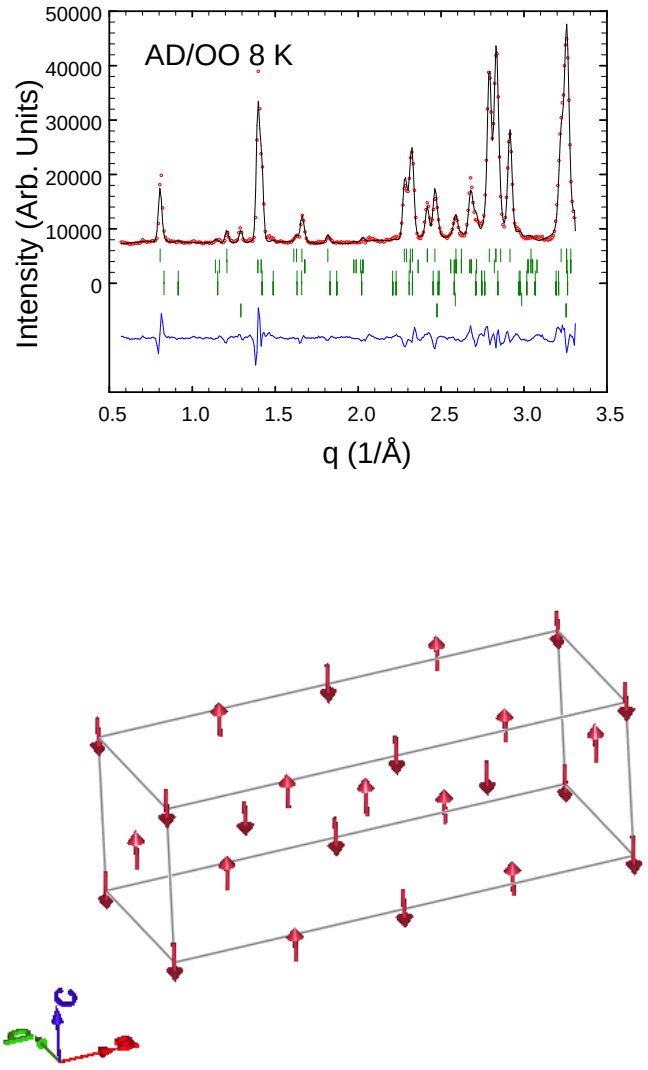

Figure 6.11: The powder neutron diffraction pattern, calculated profile and refined magnetic structure for the AD/OO phase of $Y_{0.85}Sr_{0.15}CoO_{3-\delta}$ at 8 K. The upper panel shows the measured profile (red), calculated profile (black), difference (blue) and peak positions for the six components of the refinement (peak positions in green). There were structural and magnetic components for the AD/OO $Y_{0.15}Sr_{0.85}CoO_{3-\delta}$ phase and each of the AO/OO $Y_{0.15}Sr_{0.85}CoO_{3-\delta}$ and CoO impurity phases implying six contributions to the diffraction pattern. The R-factors for the refinement were $R_p = 13.5$ and $R_{wp} = 13.9$. The magnetic R-factor for the AD/OO phase was 5.92. The lower panel shows the refined G-type magnetic structure of the material.

variant of $Y_{1-x}Sr_xCoO_{3-\delta}$. The data and calculated pattern are shown in red and black respectively, with the difference shown in blue. The refinement involve six different phases, with their peak positions marked in green. The top two sets of peak position markers denote the structural and magnetic peaks for the AD/OO phase, and the lower four mark the structural and magnetic peaks of the AO/OO and CoO impurity phases.

As explained in section 5.3.2, measurements of AD/OO $Y_{0.85}Sr_{0.15}CoO_{3-\delta}$ were also made as a function of temperature using a furnace and a cryostat. Figure 6.10 shows the temperature dependence of a double magnetic peak in the diffraction pattern at a 2θ value of 32.5°. This pair of magnetic peaks do not appear on top of a known structural peak, indicating the propagation vector is not (0,0,0). This also implies bulk antiferromagnetism in the powder. Additional magnetic Bragg peaks are also observable at 26.4, 39.3 and 55.3°. These peaks could all be indexed with propagation vector (1,1,1) and the same magnetic structure fitted the data as proposed for brownmillerite $SrCoO_{2.5}$ [85], shown in the lower panel of figure 6.11. The moments on both cobalt sites are oriented along the c axis of the unit cell defined in section 5.3.2. Additionally, the (1,1,1) propagation vector implies moments sited with a (1/2,1/2,1/2) translation from each other are antiferromagnetically coupled. As shown in figure 5.9, CoO_4 tetrahedra and CoO_6 octahedra alternate along the a axis of the unit cell and these layers are antiferromagnetically coupled with each other, forming a G-type antiferromagnetic structure. This means the two magnetic Bragg peaks shown in figure 6.10 can be indexed as the (-1,0,1)/(-1,2,1) and (-1,1,2)/(1,-1,0) peaks respectively.

The two cobalt sites were not constrained to have equal moments in the refinement, allowing for an overall ferrimagnetic ordering. Instead, the scale factors of the structural and magnetic phases were constrained to be equal and the magnitudes of the moments on the two sites were allowed to vary. The refined moments as a function of temperature between 0 and 300 K are shown in figure 6.12. Both moments have similar values across the temperature range measured, decreasing in value at higher temperatures, as might be expected. The uncertainty in the size of the magnetic moment on the two sites is large compared to the fluctuations. This suggests some systematic error in determining the moment magnitudes, and indeed there were not enough strong magnetic peaks in the diffraction pattern recorded to determine the sizes of these moments unambiguously.

At low temperatures, the refined moment on the Co1 site (figure 6.12) is slightly higher than the moment on the Co2 site, even accounting for the error bars, and this observation of unequal moments agrees with other recent measurements on the compound [85]. The error bars for the two refined moments begin to overlap around 80 K and continue to overlap up to 300 K, which means above this temper-

ature we were not able to ascertain whether the moments on the Co1 and Co2 sites were equal or not. Neither of the refined moments become zero within the 0-300 K temperature range, and systematic data was not taken above this temperature, so a Néel temperature was not ascertained absolutely. However, inspecting figure 6.10, the magnetic intensity appears to be gone by 500 K. Plotting the integrated intensity of the magnetic Bragg peaks in figure 6.10 (not shown), the trend suggests T_N is not much above 300 K. Previous measurements on $SrCoO_{2.5}$ found T_N was 537 K [85], and the difference may be due to the yttrium-doping of our sample.

This analysis leaves the weak ferromagnetic signal observed in the magnetisation data, shown in figure 6.1, somewhat unexplained. Other researchers have attributed it to an AO/OO or AD/OD impurity phase, both of which are known to have a ferromagnetic component to the magnetisation [85] or a transition to ferrimagnetism accompanying charge ordering [91], which seems unlikely given that we have found no evidence of a transition in the neutron diffraction data at the 100 K T_c suggested by the magnetisation.

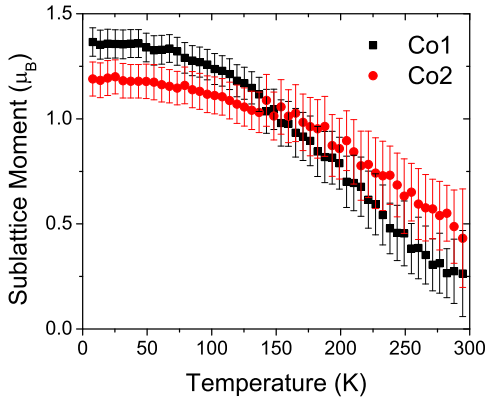

Figure 6.12: The refined magnitudes of the magnetic moments on the Co1 and Co2 lattice sites in the AD/OO $Y_{1-x}Sr_xCoO_{3-\delta}$ crystal structure as a function of temperature.

6.2.2 AO/OO Powder Measurements

The magnetic structure of the AO/OO form of $Y_{1-x}Sr_xCoO_{3-\delta}$ was also studied using powder neutron diffraction. The diffraction pattern from this sample recorded at 5 K on D1B is shown in the top panel of figure 6.13. The crystal structure of this variant of the compound was discussed in section 5.3.3, and the 500 K powder data has been fitted with structures with $I4/mmm$, $Cmma$ and $A2/m$ space groups. The data shown in figure 6.13 has been fitted with a structural model in the $I4/mmm$ space group. A large contribution to the (1,1,2) peak at $q = 1.41$ Å^{-1} is clearly present, and a contribution to the (1,1,6)/(3,1,2) peak at $q = 2.71$ Å^{-1} is also noticeable. All the observed magnetic reflections lay in positions occupied by nuclear peaks, implying the magnetic structure is commensurate.

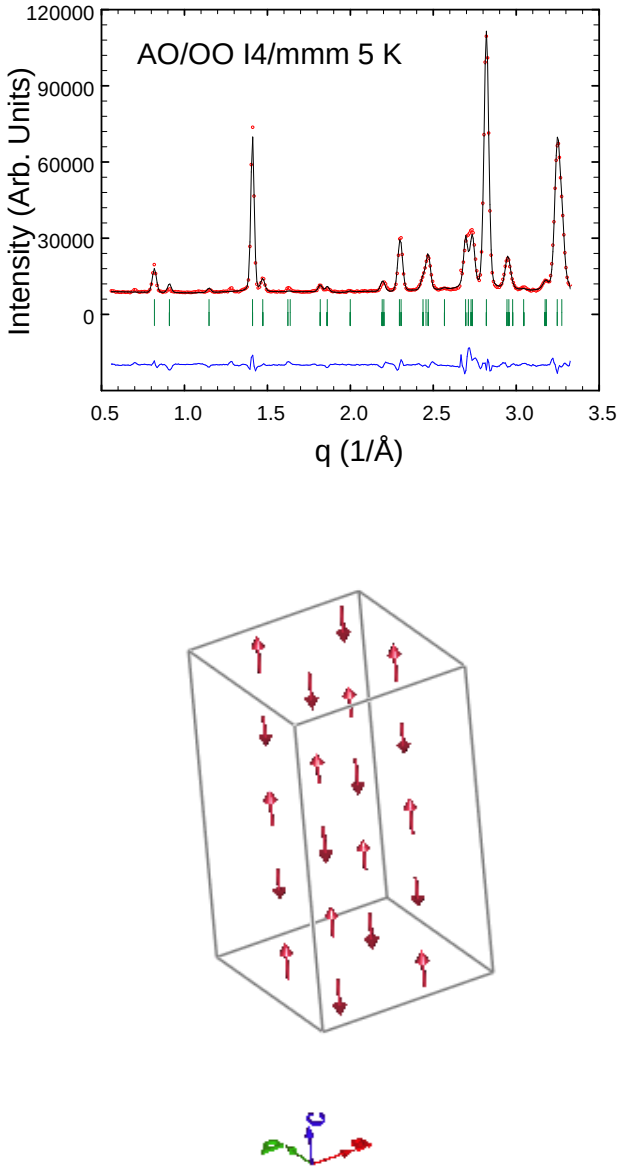

Figure 6.13: The powder neutron diffraction pattern, calculated profile and refined magnetic structure for the AO/OO phase of $Y_{1-x}Sr_xCoO_{3-\delta}$ at 5 K in the $I4/mmm$ unit cell. The upper panel shows the measured profile (red), calculated profile (black), difference (blue) and peak positions for the two components of the refinement (green), structural and magnetic. The R-factors for the refinement were $R_p = 10.2$ and $R_{wp} = 10.9$. The magnetic R-factor for the AD/OO phase was 2.53. The lower panel shows the refined magnetic structure of the material in this space group.

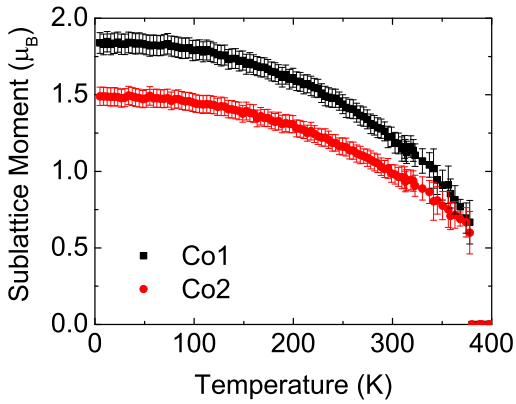

Figure 6.14: The refined magnitudes of the magnetic moments on the Co1 and Co2 lattice sites in the $I4/mmm$ crystal structure of AO/OO $Y_{1-x}Sr_xCoO_{3-\delta}$ as a function of temperature.

The main contribution to the magnetic ordering in $Y_{1-x}Sr_xCoO_{3-\delta}$ is antiferromagnetic. This is known from magnetisation measurements, shown in figures 6.7 and 6.8, which show a large non-saturating component, and neutron diffraction [23]. The antiferromagnetism appears to be G-type, and this means neighbouring magnetic moments are aligned antiparallel to one another. For the refinement, the moments were taken to be aligned along the c axis of the $I4/mmm$ unit cell. Including a contribution to the moment in either of the other directions did not improve the refinement, and all previous measurements of this compound have come to the same conclusion. Based on these observations, the refined magnetic structure which best fits the observed data is given in the lower panel of figure 6.13. This structure is in agreement with that described in reference [25].

Neutron diffraction measurements were made as a function of temperature from 5 K, scan shown in figure 6.13, to 500 K. Comparing the diffraction patterns at different temperatures, and the intensity of the main magnetic peak two important points must be noted. Firstly, there is still a substantial magnetic contribution to the intensity of the diffraction patterns above the 335 K transition temperature observed in the magnetisation (section 6.1.1). This is a further demonstration that observed ferromagnetic signal in the magnetisation in AO/OO $Y_{1-x}Sr_xCoO_{3-\delta}$ is not representative of the bulk magnetic state of the material, which is antiferromagnetic. Secondly, there is a change in the intensity of the two largest structural Bragg peaks, the (2,2,4) and the (4,0,0), at around 280 K. This is quite clear when all the diffraction patterns are plotted together (not shown). This is the same temperature at which a change in the thermal expansion of the lattice parameter was detected, section 5.3.5.

The presence of a magnetic contribution to the (1,1,0) Bragg peak implies the moments on the two different cobalt sites in the $I4/mmm$ crystal structure are different. The refinements of the neutron diffraction data as a function of temperature meant the thermal evolution of the moments on these two different cobalt

sites could be quantified. The results of this analysis are shown in figure 6.14. The refined values for the magnetic moments were 1.84 and 1.49 μ_B respectively at 5 K. The difference between the magnitudes of the moments on the two sites is reduced as the temperature is increased.

The transition temperature from the refinement was found to be just above the 370 K previously obtained from magnetisation measurements on single crystals [94]. Less oxidised forms of $Y_{1-x}Sr_xCoO_{3-\delta}$ are known to have higher transition temperatures than more oxidised forms [25], and this temperature is higher than reported by other groups on more oxidised powders, as would be expected. It was found necessary to fit the nuclear and magnetic contributions to the diffraction profile using different values for the same peak width parameters. This is because the widths of the two components were found to vary differently with temperature, with the width of the nuclear component having no temperature dependence and the width of the magnetic component having some temperature dependence, shown in figure 6.15. A change the width at around 280 K is observable. Below this temperature, the width appears to be resolution limited, however, above this temperature the magnetic correlations appear to be of finite spatial extent and cause peak broadening. This broadening effect may be due to domains, but the change in behaviour at 280 K may also be linked to the suspected structural and magnetic transitions at this temperature discussed in sections 5.3.5 and 6.1.

The process of refining the magnetic structure to fit the observed neutron diffraction pattern was also carried out using the *Cmma* structural space group. In this space group there are six separate cobalt sites, three in the CoO_6 and three in the $CoO_{4+\delta}$ layers. Those in the CoO_6 layers are all in octahedral environments. However, those in the $CoO_{4+\delta}$ layers sit in three different environments; octahedral Co2, square pyramidal Co6 and tetrahedral Co1 (for labels see table 5.6). In agreement with the refinement in the $I4/mmm$ cell, the moments were fixed to point parallel to the a axis and arranged in a G-type antiferromagnetic lattice. The mo-

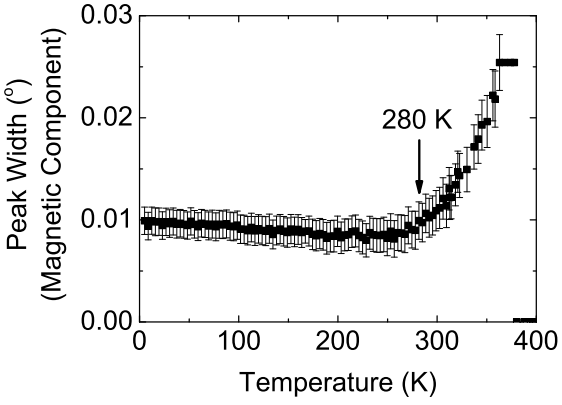

Figure 6.15: The refined width of the magnetic contribution to the neutron diffraction profile of AO/OO $Y_{0.15}Sr_{0.85}CoO_{3-\delta}$ as a function of temperature. A change the width at around 280 K is observable.

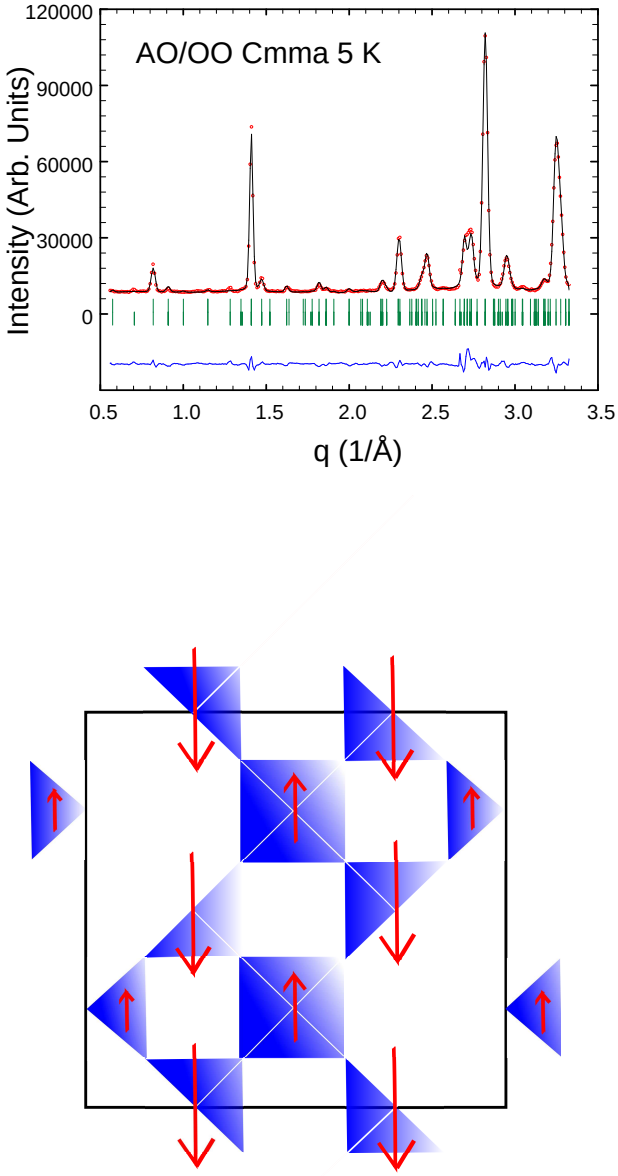

Figure 6.16: The powder neutron diffraction pattern, calculated profile and refined magnetic structure for the AO/OO phase of $Y_{1-x}Sr_xCoO_{3-\delta}$ at 5 K in the *Cmma* unit cell. The upper panel shows the measured profile (red), calculated profile (black), difference (blue) and peak positions for the two components of the refinement (green), structural and magnetic. The R-factors for the refinement were $R_p = 9.24$ and $R_{wp} = 9.72$. The magnetic R-factor for the AD/OO phase was 3.14. The lower panel shows cobalt environments of the oxygen deficient layer in the *Cmma* crystal structure of $Y_{0.15}Sr_{0.85}CoO_{3-\delta}$, as shown in figure 5.13. The refined magnetic structure of the material in this space group at 5 K is also represented, where the red arrows denote the sizes of the magnetic moments on each site.

ments in the CoO_6 layers were also fixed at the values found from the refinement of the moments in the smaller unit cell. This was justified as the moments of the cobalts on the three sites are all in the same oxygen environment, and are therefore believed to have similar magnitudes [24].

The diffraction pattern at 5 K was refined in the *Cmma* space group and the moments on the Co1, Co2 and Co6 sites in the $CoO_{4+\delta}$ layers were found to be 2.8(2) μ_B, 0.9(1) μ_B and 1.4(1) μ_B respectively. The value for the Co6 moment is in agreement with the size of the moments in the CoO_6 layers in the same octahedral environment. The magnitudes of these moments were then refined as a function of temperature, shown in figure 6.17. Like the equivalent refinements of the AD/OO data, the errors were larger than the fluctuations associated with data. Again this reflects the uncertainty in the magnitudes of the moments *per se*, as the resolution of the data and number of magnetic Bragg peaks were not sufficient to achieve a perfect refinement with small errors.

The observed macroscopic magnetisation can be explained by the unequal size of the moments on the Co1, Co2 and Co6 sites, as the net magnetic ordering will be antiferrimagnetic. The peak in the zero field magnetisation below T_c can also be reproduced by taking the difference between the moments in the $CoO_{4+\delta}$ layers, supporting this interpretation. This also suggests there is no component from spin canting or clustering contributing to the observed ferromagnetism, and the ferromagnetic magnetisation signal is purely due to the ferrimagnetism of the sublattice moments.

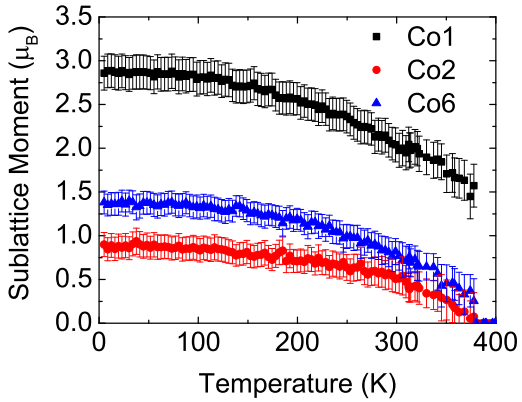

Figure 6.17: The refined magnitudes of the magnetic moments on the Co1, Co2 and Co6 lattice sites in the *Cmma* crystal structure of AO/OO $Y_{1-x}Sr_xCoO_{3-\delta}$ as a function of temperature.

The same analysis performed here was recently performed by another group on their powder neutron diffraction data [24]. Their sample was more oxidised than ours, and the magnitude of the moment on the Co2 site was found to be much larger. The dc-susceptibility of their sample were also an order of magnitude larger, so this difference is probably due to the different oxidation levels of the samples. Their data also suggests an increase in the magnitude of the moment on the Co1

site at around 280 K which is less clear in our data due to the larger error bars. However, there may be some increase in the size of the moment on that site at that temperature, masked by the large error bars, and some change in the relative sizes of the moments is expected as there is a change in the macroscopic magnetisation at this temperature. The same variation in the width of the magnetic contribution to the diffraction pattern at temperatures down to 280 K shown in figure 6.15 was also observed when refining in the *Cmma* space group.

6.3 Single Crystal Neutron Diffraction

6.3.1 Experimental Details: Single Crystal Diffractometers D7 and D10

Neutron diffraction experiments were performed on the O_2-annealed single crystals described in section 5.1.2. Measurements were made on the single crystal neutron diffractometer D10 and the polarised neutron diffractometer D7, and the instrument and experimental details for the D10 experiment are described in section 5.3.1. The aims of both these experiments were to assess the position and temperature dependence of the magnetic Bragg peaks and diffuse scattering in $Y_{1-x}Sr_xCoO_{3-\delta}$ and further understand the magnetic structure of this compound. The D10 data presented in the following section was all collected by fitting the Bragg peaks with either a Gaussian, a Lorentizan or a combination of the two, and using that function to determine the integrated intensity.

Diffraction measurements were made on the polarised neutron diffractometer D7. *xyz* polarisation analysis was implemented on the instrument as described in section 3.4.4, and the instrument layout is shown in figure 6.18. The entire instrument can be moved with respect to the neutron guide to access three differ-

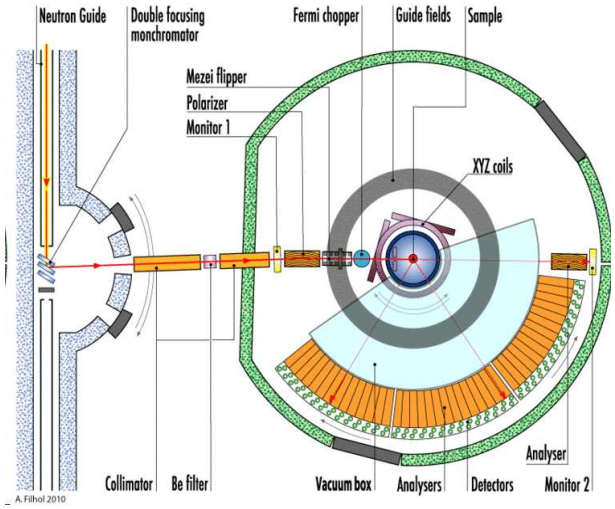

Figure 6.18: Layout of the polarised neutron diffractometer D7. Taken from reference [118].

ent incident wavelengths; $\lambda = 3.12$ Å, $\lambda = 4.86$ Å and $\lambda = 5.80$ Å, and for this experiment a $\lambda = 3.21$ Å incident wavelength was chosen. A cryofurnace with a temperature range of 1.5 to 550 K was mounted inside the instrument. A 6 mm diameter and 20 mm length single crystal, with a mass of 3.4 g, was aligned using the neutron Laue OrientExpress. The size of the spots on the neutron Laue were larger along the b axis of the $I4/mmm$ unit cell than along the a and c axes. The geometry of the experiment was such that we expect the spots to be larger when measuring large samples, and the b axis was along the longest axis of the crystal boule. The sample was wrapped in aluminium foil and screwed into an aluminium sample holder so it could be mounted in the cryofurnace.

Once the experiment was set up, it was necessary to measure three samples to calibrate the instrument. Vanadium is run as it is a purely incoherent, and therefore an isotropic, scatterer and allows for calibration of the detectors. Quartz (amorphous silica) is run as its scattering is entirely nuclear and means the finite polarisation of the incident beam can be corrected for. The empty sample holder must also be run to quantify its contribution to the background.

Initially the sample was oriented so that the $(h, k, 0)$ plane was measured. Scans as a function of sample angle were made with steps of 0.5° or 1° between scans. Complete 360° planes were measured at 400, 370 and 360 K. Quarter planes were measured at 260 and 10 K. The step sizes were either 0.5° or 1°. The sample was later rotated so the (h, h, l) plane was measured at 360, 370, 390 K, with quarter planes measured at 360 and 390 K and a three-quarter plane measured at 370 K. Temperatures around 370 K were chosen because 370 K was found to be T_c from the dc and ac-susceptibility data.

In all the figures shown below, powder diffraction rings are visible in the scattering. These rings are from a combination of two sources. Firstly, although the empty sample holder was measured independently and subtracted from the data, this subtraction is unlikely to be perfect, and some aluminium contribution may well be present. We would expect aluminium powder lines at q-positions of approximately 2.7 and 3.1 Å, and there are powder lines present at these points. Secondly, as mentioned in section 5.1.2, the $Y_{1-x}Sr_xCoO_{3-\delta}$ crystals form with a thin polycrystalline coating which cannot easily be removed due to the brittleness of the sample. This means there was a small amount of $Y_{0.15}Sr_{0.85}CoO_{3-\delta}$ powder in the beam when the measurement was made, accounting for the rest of the powder lines, including those present in the magnetic channel.

6.3.2 Behaviour below T_c

The nuclear and magnetic components of the scattering from the $(h, k, 0)$ plane of the $I4/mmm$ unit cell at 370 K, 260 K and 15 K are shown in figure 6.19. The top

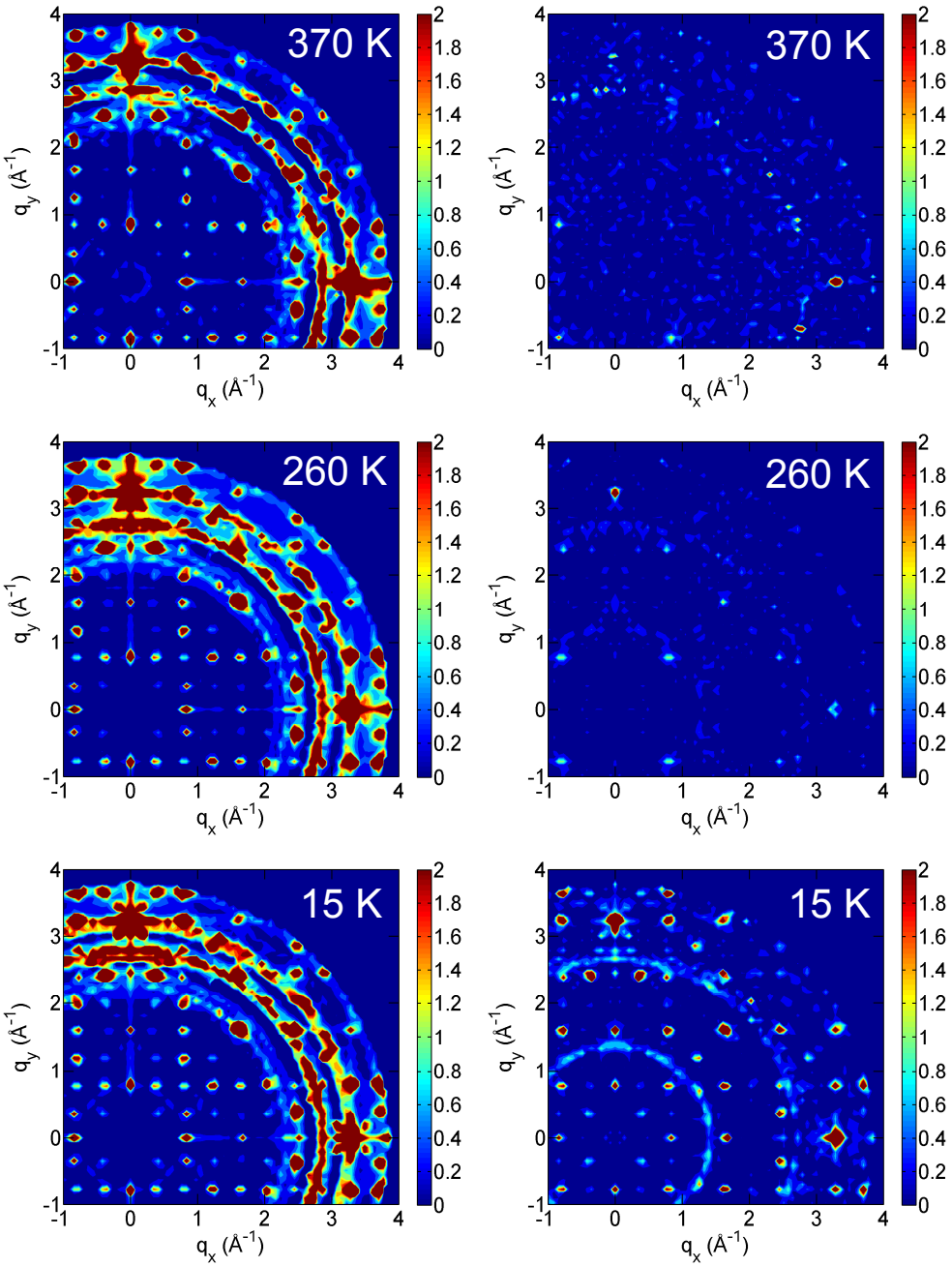

Figure 6.19: The $(h, k, 0)$ scattering plane in the $I4/mmm$ space group of $Y_{0.15}Sr_{0.85}CoO_{3-\delta}$ measured at temperatures of 370, 260 and 15 K respectively as recorded on the polarised neutron diffractometer D7. The left and right hand panels at each temperature show the nuclear and magnetic components of the scattering respectively.

left panel shows the nuclear scattering at 370 K, which as stated above is T_c from the magnetisation data. The largest peaks in the diffraction pattern, at $q_x = 3.25$ $q_y = 0$ and $q_x = 0$ $q_y = 3.25$ are the $(4, 0, 0)$ and $(0, 4, 0)$ and these are intersected by the aluminium powder lines from the sample holder. There is also clear evidence of the complex superstructure discussed in section 5.3. There are well-defined peaks at positions $q_x = 0.81$ $q_y = 0.41$, $q_x = 0.41$ $q_y = 2.43$ and $q_x = 0.41$ $q_y = 0.81$, with (h, k, l) indices $(1, 0.5, 0)$, $(0.5, 3, 0)$ and $(0.5, 1, 0)$ respectively in the $I4/mmm$ unit cell. This implies a unit cell at least double the 7.7 x 7.7 x 15.4 Å unit cell of the $I4/mmm$ space group in the ab plane, and there maybe additional superstructure peaks obscured by the aluminium powder lines.

The magnetic component of the scattering at 370 K is shown in the top right hand panel of figure 6.19. There are very few features in this figure, which is to be expected as 370 K is T_c for the compound. The strongest peak visible is the $(4, 0, 0)$, which is a large structural peak, and its presence, as well as the presence of the aluminium powder lines, implies the beam is slightly depolarised at this temperature, suggesting the presence of a ferromagnetic component to the magnetic order. The other peaks visible in this diffraction pattern are the $(1, 1, 0)$ and its equivalent positions, which are known to be magnetic peaks. As they are magnetic peaks, they will have more intensity in the magnetic channel than the nuclear one which is why they appear stronger in the right hand panel than the left hand one.

The degree of depolarisation increases when the temperature is reduced because the ferromagnetic contribution to the measured signal becomes greater. This means the polarisation analysis is incomplete and the separation into nuclear and magnetic components must be treated with some care. In particular, the strongest nuclear peaks will partially 'bleed through' into the calculated magnetic pattern. However, by comparing the intensity of particular peaks in both channels it is generally possible to determine if a particular peak is purely nuclear or has a magnetic component. In the patterns recorded at 260 and 15 K, additional peaks not obvious at 370 K are visible at q-positions $q_x = 0.41$ $q_y = 0.41$ and equivalents. At 15 K, these peaks are stronger in the magnetic than the nuclear channel, suggesting they are antiferromagnetic in origin. These peaks are also present at 260 K, but are much weaker than at 15 K.

On cooling below 370 K, peaks also appear surrounding the $(4, 0, 0)$ and $(0, 4, 0)$ structural peaks at positions corresponding to $(3.75, 0.25, 0)$ and equivalents in the $I4/mmm$ unit cell. These peaks are more intense in the structural than the magnetic channel, implying they are structural rather than magnetic in origin. They are in fact the same $(0.25, 0.25, 0)$ (and equivalent) peaks observed using single crystal X-ray diffraction shown in figures 5.14 and 5.16. These $(0.25, 0.25, 0)$ peaks

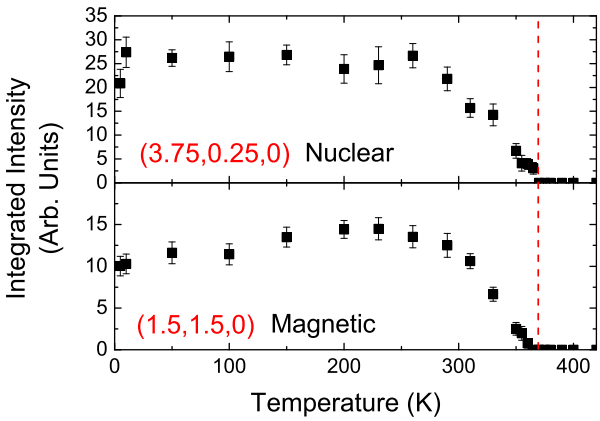

Figure 6.20: The integrated intensities of the $(3.75, 0.25, 0)$ and $(1.5, 1.5, 0)$ Bragg peaks in the $I4/mmm$ space group of $Y_{0.15}Sr_{0.85}CoO_{3-\delta}$ as a function of temperature as measured on the single crystal neutron diffractometer D10. T_c is marked with a red dashed line.

also appear to be present but weaker at 260 K. There is some small suggestion of diffuse scattering in the nuclear channel at all three temperatures along the $(h, 0, 0)$ and $(0, k, l)$ directions.

It was not practical to measure the temperature dependence of the peaks appearing below T_c on D7 because of the lack of q-resolution, however the temperature dependence of the peaks could be measured on the single crystal neutron diffractometer D10. Figure 6.20 shows the integrated intensity of the $(3.75, 0.25, 0)$ and $(1.5, 1.5, 0)$ peaks as a function of temperature between 400 K and the 2 K base temperature of the cryostat (the $(1.5, 1.5, 0)$ peak is an equivalent to the $(0.5, 0.5, 0)$ peak). Both peaks were fitted with Gaussian profiles, as they were too weak to be fitted with more complex functions. Although neither peak has a large integrated intensity, the measurement clearly shows both peaks appear at a temperature of 370 K. The polarisation analysis available on D7 described above showed that the $(3.75, 0.25, 0)$ and $(1.5, 1.5, 0)$ peaks are structural and magnetic respectively. These measurements therefore show that both a structural and a magnetic transition occur close to 370 K in this compound, and the transitions are most likely to coincide.

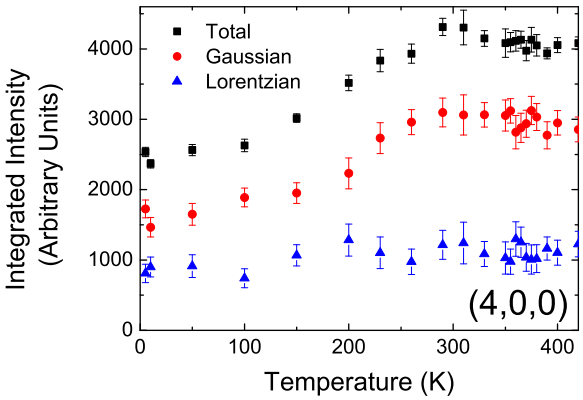

Figure 6.21: The integrated intensity of the $(4, 0, 0)$ peak in the $I4/mmm$ space group of $Y_{0.15}Sr_{0.85}CoO_{3-\delta}$ as a function of temperature as measured on the single crystal neutron diffractometer D10. The peak was fitted with two components, a Gaussian and a Lorentzian with widths of 0.13° and 0.25° respectively.

The influence of the two transitions on each other cannot be determined without further study of similar compounds with different doping levels and transition temperatures. Resonant X-ray scattering has suggested the ferrimagnetism is brought on by the orbital ordering of the IS cobalt ions, which would fit with our observation of coincident structural and magnetic transitions [45].

The temperature dependence of the strong nuclear peak $(4, 0, 0)$ in the $I4/mmm$ unit cell was also measured on D10. The peak was fitted with two components, a close to resolution limited Gaussian and a Lorentzian with a width of 0.25°, implying some finite length correlations in the material. The centres of the two peaks were fixed to coincide. Fitting the peak in this way also accounts for any change in the peak position as a function of temperature due to lattice expansion. The total integrated intensity of the peak would be expected to persist or slightly increase as the temperature was decreased, but as figure 6.21 shows, it decreases in intensity with temperature. In fact, between 300 and 100 K the total integrated intensity reduces by over a third. We take this to be further evidence of a structural transition at 280 K in $Y_{1-x}Sr_xCoO_{3-\delta}$. The presence of a structural transition at 280 K was discussed in section 5.3.5, as a feature was also observed in the lattice parameter data along the b and c axes at this temperature.

The temperature dependence of the integrated intensity of several other peaks was measured on D10, and the results for the $(0, 0, 8)$ and $(1, 1, 2)$ peaks in the $I4/mmm$ unit cell are shown in figure 6.22. The $(0, 0, 8)$ is a large structural peak akin to the $(4, 0, 0)$. The same drop in intensity observed for the $(4, 0, 0)$ peak is observed for this peak. The temperature at which this feature occurs is judged to be 280 K, the same temperature a currently unexplained feature occurs in the magnetisation. More information is required to identify the source of this change in intensity, which most likely requires a better structural model for the compound than the one currently available to fully resolve. As the $(0, 0, 8)$ and $(4, 0, 0)$ are nuclear peaks it might be expected that the change is due to some structural modulation, and the powder diffraction measurements discussed in section 5.3.5 suggest there is a displacive-type structural transition at this temperature. On the other hand, any ferromagnetic component to the magnetic order will contribute to all the Bragg peaks, so may also be responsible, but the magnitude of the change suggests it is due to a structural transition.

The largest magnetic peak for the AO/OO form of $Y_{0.15}Sr_{0.85}CoO_{3-\delta}$ is the $(1, 1, 2)$ in the $I4/mmm$ unit cell. This peak was also measured using the single crystal neutron diffractometer D10, shown in figure 6.22. Like the nuclear peaks, it was also fitted with two components, a Gaussian with width 0.30° and a Lorentzian with width 0.69°. Both components follow the expected trend for a magnetic peak as function of temperature below T_c. Unlike the equivalent powder data, shown in

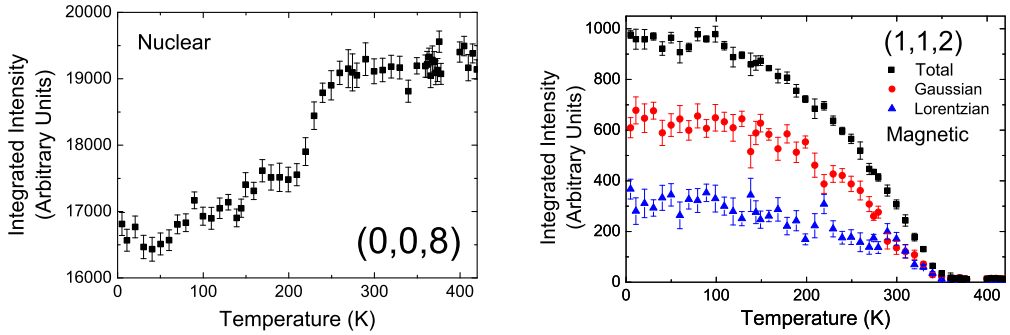

Figure 6.22: The integrated intensities of the nuclear $(0, 0, 8)$ and magnetic $(1, 1, 2)$ peaks in the $I4/mmm$ space group of $Y_{0.15}Sr_{0.85}CoO_{3-\delta}$ as a function of temperature as measured on the single crystal neutron diffractometer D10.

figure 6.15, the width was not found to change with temperature. This may be due to the direction or resolution of the scan, or it may be the variation in width seen in powder is due to some strain or domain effect not found in single crystals.

6.3.3 Behaviour above T_c

Measurements were also made in the (h, h, l) scattering plane at temperatures above the 370 K T_c with the polarised neutron diffractometer D7 to look for evidence of magnetic clustering or phase separation that may be responsible for the observed room-temperature ferromagnetic signal. Measurements were made above T_c because the beam became depolarised below the transition temperature due to the presence of a ferromagnetic component to the magnetic ordering. The nuclear and magnetic components of the scattering at 390, 370 and 360 K are shown in figure 6.23. The strongest peaks are at $q_x = 0$ $q_y = 3.28$ and $q_x = -2.24$ $q_y = 1.68$, and can be indexed by $(0, 0, 8)$ and $(2, 2, 4)$ in the 7.7 x 7.7 x 15.4 Å $I4/mmm$ space group. There are no clear changes in the intensity of structural peaks between the three temperatures measured.

The magnetic components of the scattering in the (h, h, l) plane at 390, 370 and 360 K are shown in the right hand panels of figure 6.23. Commensurate diffuse scattering was observed at all three temperatures, and the figures are shown on a logarithmic scale to make this clear. The diffuse scattering is most intense around a peak at a q-position of $q_x = -1.20$ $q_y = 0.83$. This corresponds to the position of the $(1, 1, 2)$ peak, which is known to be the strongest magnetic peak. At 370 K diffuse scattering is also present around a q-position of $q_x = -1.20$ $q_y = 2.49$, which corresponds to the $(1, 1, 6)$ peak, known to also be magnetic. This diffuse scattering becomes stronger as the sample is cooled from 390 to 360 K and only appears in the magnetic channel.

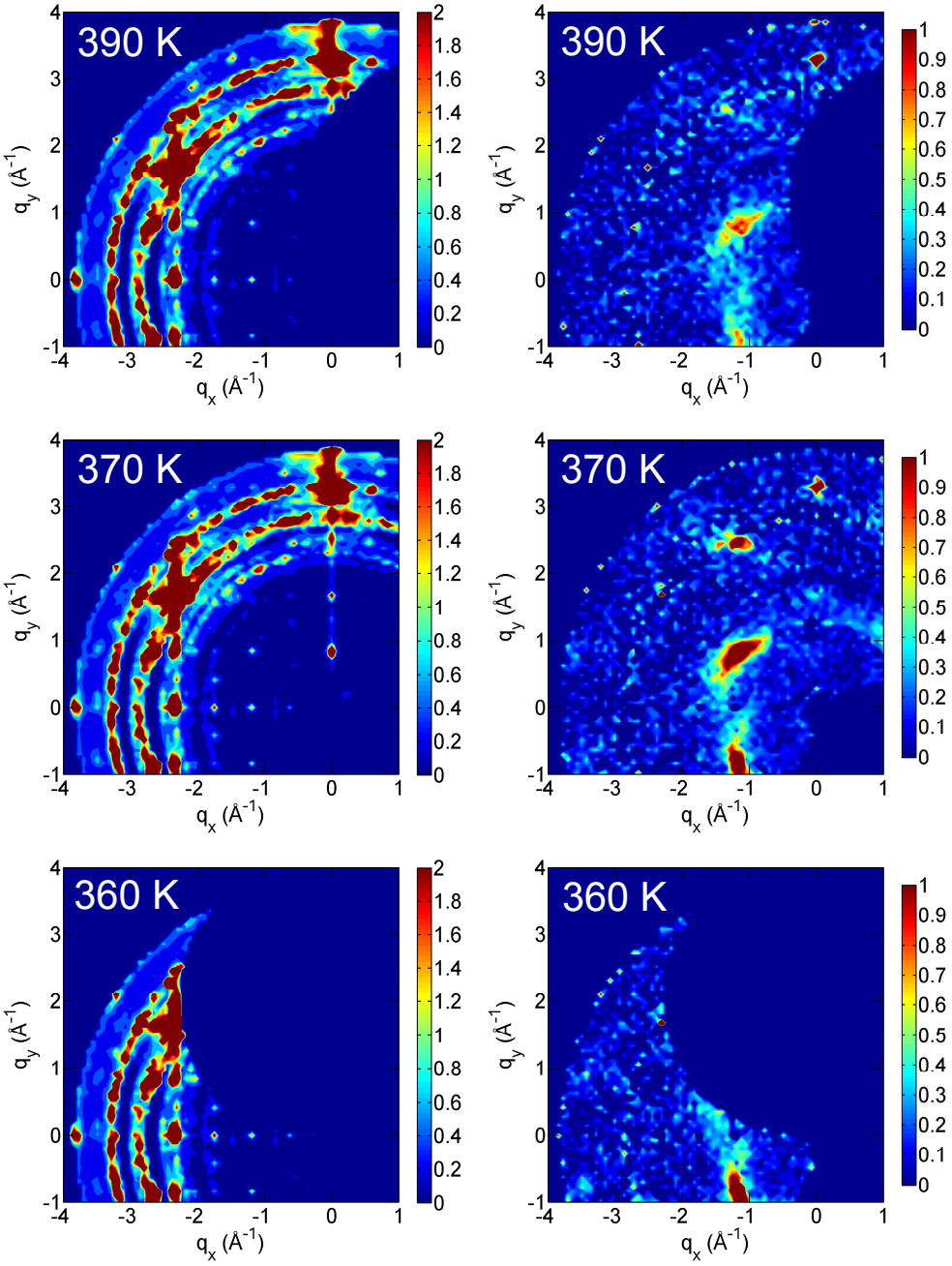

Figure 6.23: The (h, h, l) scattering plane in the $I4/mmm$ space group of $Y_{0.15}Sr_{0.85}CoO_{3-\delta}$ measured on the polarised neutron diffractometer D7 at temperatures of 390, 370 and 360 K respectively. Spiral features suggesting a Lorentzian inelastic component are observed. The left hand panels show the structural component of the scattering and the right hand panels show the magnetic scattering. The right hand figures have been plotted on a logarithmic scale to emphasise the magnetic diffuse scattering.

Previous work on chromium [119, 120] identified similar spiral features to the ones in figure 6.23 in the magnetic channel of a polarised neutron scattering measurement. They attributed these spiral features to magnetic, commensurate diffuse scattering localised in an arc around the magnetic $(1, 1, 2)$ lattice position which has a broad, Lorentzian energy distribution. The transformation of the data from the coordinates in measurement space to the reciprocal q-space used in the analysis of the D7 data assumes pure elastic scattering. This means inelastic scattering events are shifted from their original position in q-space, and become smeared out in a spiral pattern such as those observed here. The scattering events with the most energy are generally shifted by the greatest amount. In our single crystal AO/OO $Y_{0.15}Sr_{0.85}CoO_{3-\delta}$ sample, commensurate diffuse scattering due to magnetic inelastic scattering was only observed in the (h, h, l) plane and not the other plane measured, the $(h, k, 0)$ plane, implying anisotropic magnetic fluctuations not previously reported.

6.3.4 Magnetic Structure

Although it was not possible to refine the magnetic structure of the $Y_{1-x}Sr_xCoO_{3-\delta}$ single crystals from the D7 data as a complete data set was not collected, such an analysis is possible on D10, as the 4-circle diffractometer means a nearly complete data set can be collected from a single crystal sample. Data was collected at three temperatures, 420, 300 and 2 K, in the $I4/mmm$ space group. However, after analysing the powder diffraction data, section 6.2.2, it was shown that more information could be gleaned about the magnetic behaviour of $Y_{1-x}Sr_xCoO_{3-\delta}$ by refining in the $Cmma$ space group, so the data was transformed using the matrix given in chapter 5. The equivalent isotropic thermal parameters for the same species were constrained to be equivalent during the refinements.

The data at 420 K is purely nuclear and a description of the refined structure at this temperature was given in section 5.3.4. The data at 300 K was then refined including a magnetic contribution and according to the model described in section 6.2.2. The results for the moments on the different cobalt sites are given in table 6.1. The oxygen content of the single crystals was higher than the powders, so the small differences in moment magnitudes compared to the powders are not unexpected. Unfortunately, the errors on the refinement are somewhat higher that would be hoped, and that is because of the dominance of the nuclear contribution to the scattering compared to the magnetic intensity. For example, the largest nuclear peak in the refinement was the (0,4,4) with 59598 counts, but the largest magnetic peak was the (2,2,0) with 2033 counts (peaks given in the $Cmma$ cell). This means that because the model we have for the nuclear contribution is imperfect, a good refinement for the magnetic contribution was difficult to achieve.

Environment	Coordination	Site	420 K	300 K	2 K
Pyramidal	5	Co1	0	1.9(2)	2.5(2)
Tetrahedral	4	Co2	0	1.0(2)	1.0(2)
Octahedral	6	Co6	0	1.2(5)	1.1(4)
R-Factor			8.10	6.78	9.88
χ^2			13.7	15.9	30.8

Table 6.1: The magnetic moments in different environments and the goodness of fit parameters for the refinement of $Y_{0.15}Sr_{0.85}CoO_{3-\delta}$ single crystal neutron diffraction data taken on D10 at temperatures of 420, 300 and 2 K. The units for the magnetic moments are μ_B.

During the refinement, the biggest effect on χ^2 when refining the data at 300 and 2 K was not the magnetism but the oxygen positions. All the oxygens were found to shift their positions between 420 K and 300 K, across the structural transition that appears to coincide with T_c. The largest shifts in position between the measurements at these temperatures were along the c axis of the $Cmma$ unit cell for the O3 and O9 oxygen positions. The shifts were of more that 1% of the size of the unit cell. Between 300 and 2 K, across the structural transition at 280 K, the largest shift is in the position of the O7 atom along the a axis. Again, between these two temperatures, the largest effect on χ^2 was the change in the oxygen positions rather than the change in the magnetism of $Y_{0.15}Sr_{0.85}CoO_{3-\delta}$. This is why the χ^2 is so high for the refinement at 2 K.

Despite the difficulties with refining the single crystal magnetic data, a difference within error was recorded for the square pyramidal cobalt site between the refinements at 300 and 2 K. This supports what was seen from the powder refinement, and suggests there may be some change in the behaviour of the moment on this site around 280 K, either as a result of the structural transition or *via* some other mechanism such as a spin state transition.

6.4 Inelastic Neutron Spectroscopy

6.4.1 Experimental Details: 2T1 Neutron Spectrometer

The same 3.4 g AO/OO $Y_{0.15}Sr_{0.85}CoO_{3-\delta}$ single crystal used on D7 was used for inelastic neutron spectroscopy measurements on the triple-axis instrument 2T1 at the Orphee reactor neutron source at LLB. The aim was to characterise the dispersion relation for the compound and to assess the general features of the excitation spectrum. The experiment was intended to be a broad survey of the magnetic excitations along several high symmetry directions. Additionally, we wished to assess

what information inelastic scattering can contribute to an overall picture of the magnetic interactions in AO/OO $Y_{0.15}Sr_{0.85}CoO_{3-\delta}$.

2T1 is a thermal neutron triple-axis spectrometer built to study inelastic scattering from condensed matter systems. The layout of the instrument is shown in figure 6.24. Thermal neutrons from the reactor source are incident on a PG or Cu monochromator and are collimated before they arrive at the sample. The sample orientation table is used to move the sample so that different parts of reciprocal space can be accessed. A PG 002 analyser is used to select the final energy of the neutrons which are then recorded by the detector [121].

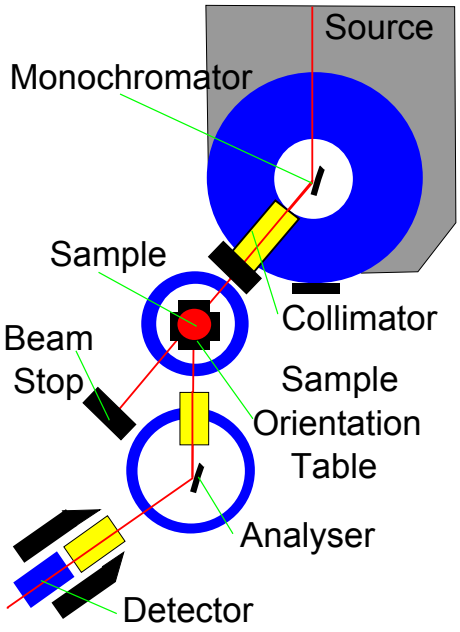

Figure 6.24: Layout of the thermal neutron triple-axis spectrometer 2T1. Adapted from reference [121].

The single crystal sample was strapped to an aluminium grating attached to the sample mount using aluminium wire. The G43 spectrometer was used to align the sample on its mount so that the c axis was vertical. A cryofurnace with a temperature range of 4 to 500 K was used for the experiment. Measurements were made in one of two modes. Either scans at a constant energy transfer were made by varying the direction of k_i and k_f or scans as a function of energy transfer were made by keeping k_i constant and therefore maintaining a constant q. An example of a q scan made around the $(1,1,2)$ lattice position along the ab direction in the crystal at a constant energy transfer of 12.4 meV is shown in figure 6.25. The q-scans were then fitted with pairs of symmetric peaks, as expected for dispersive behaviour, using the

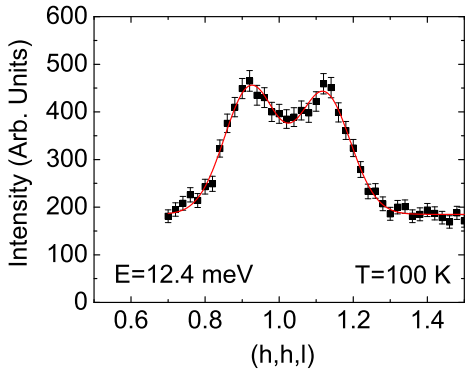

Figure 6.25: Scan along the $(h,h,2)$ direction across the $(1,1,2)$ peak in the $I4/mmm$ space group of $Y_{0.15}Sr_{0.85}CoO_{3-\delta}$ measured at 100 K at an energy transfer of 12.4 meV on the the triple-axis spectrometer 2T1. The red line is the fit to the data.

software $afitv$ available at LLB. The background, intensity, FWHM, q position, and asymmetry parameters for the peaks were all fitted, with the background, q-position and FWHM initially fixed to sensible values to achieve a good fit, before allowing all the parameters to vary.

6.4.2 Dispersion along the ab direction

A series of q-scans of the two strongest magnetic peaks, the $(1, 1, 2)$ and the $(1, 1, 6)$, were made at a temperature of 100 K with fixed values for the energy transfer. At each new temperature selected, the (0,0,6), (2,2,0) and (1,1,2) peaks were remeasured to check the alignment of the crystal had been maintained. The scans at constant energy transfer were chosen as transition metal oxide systems similar to $Y_{1-x}Sr_xCoO_{3-\delta}$ are known to have steep dispersion 'chimneys', where the inelastic features vary strongly in energy over a small q-range. The temperature of 100 K was chosen as the intensity of the magnetic peaks has been shown to remain constant below this temperature, illustrated in figure 6.22. For the $(1, 1, 2)$ peak, $(h, h, 2)$ scans were made at energy transfers of 4.1, 6.2, 8.3, 10.3 and 12.4 meV between h values of 0.5 and 1.5. For the $(1, 1, 6)$ peak higher energy transfers could be accessed, and $(h, h, 6)$ scans were made at energy transfers of 4.1, 8.2, 12.4, 16.5, 20.7, 24.8, 28.9, 33.0 and 37.2 meV between h values of 0.5 and 1.5.

Figures 6.26 and 6.27 show the dispersion along the ab direction around the $(1, 1, 2)$ and $(1, 1, 6)$ magnetic peaks respectively. The top panel of each figure shows the raw data in the form of scans at constant energy transfer. The central panel shows the same data displayed as a contour plot, with all points with a value greater than 1000 included in a single contour. The lower panel shows the values for q obtained by fitting the data to a dispersion as described above. The presence of a dispersive component is clear in both figures. Figure 6.26 shows the dispersion between 4 and 12 meV, where there is one clear dispersive branch, and the fits suggest there maybe a second. The data taken across a greater energy transfer range, displayed in figure 6.27, shows the same clear dispersion at lower energy transfers, with a concentration of intensity centred around an energy transfer of 20 meV where the mode becomes dispersive. The scans at energy transfers above this, such as the 33 meV scan, show evidence of dispersive behaviour, suggesting the presence of another inelastic mode with an energy gap at the zone centre.

Up to three excitation branches have been observed in the ab plane. We suggest these are likely to be magnon branches as they are at relatively high energies and we expect strong spin waves in this cobaltate system, but measurements above T_c are necessary to confirm this (section 6.4.4). In section 2.5.2, the dependence of ω on q for ferromagnets ($\omega \propto q^2$) and antiferromagnets ($\omega \propto q$) at q-positions near the zone centre was set out. For ferrimagnets, as we believe $Y_{1-x}Sr_xCoO_{3-\delta}$

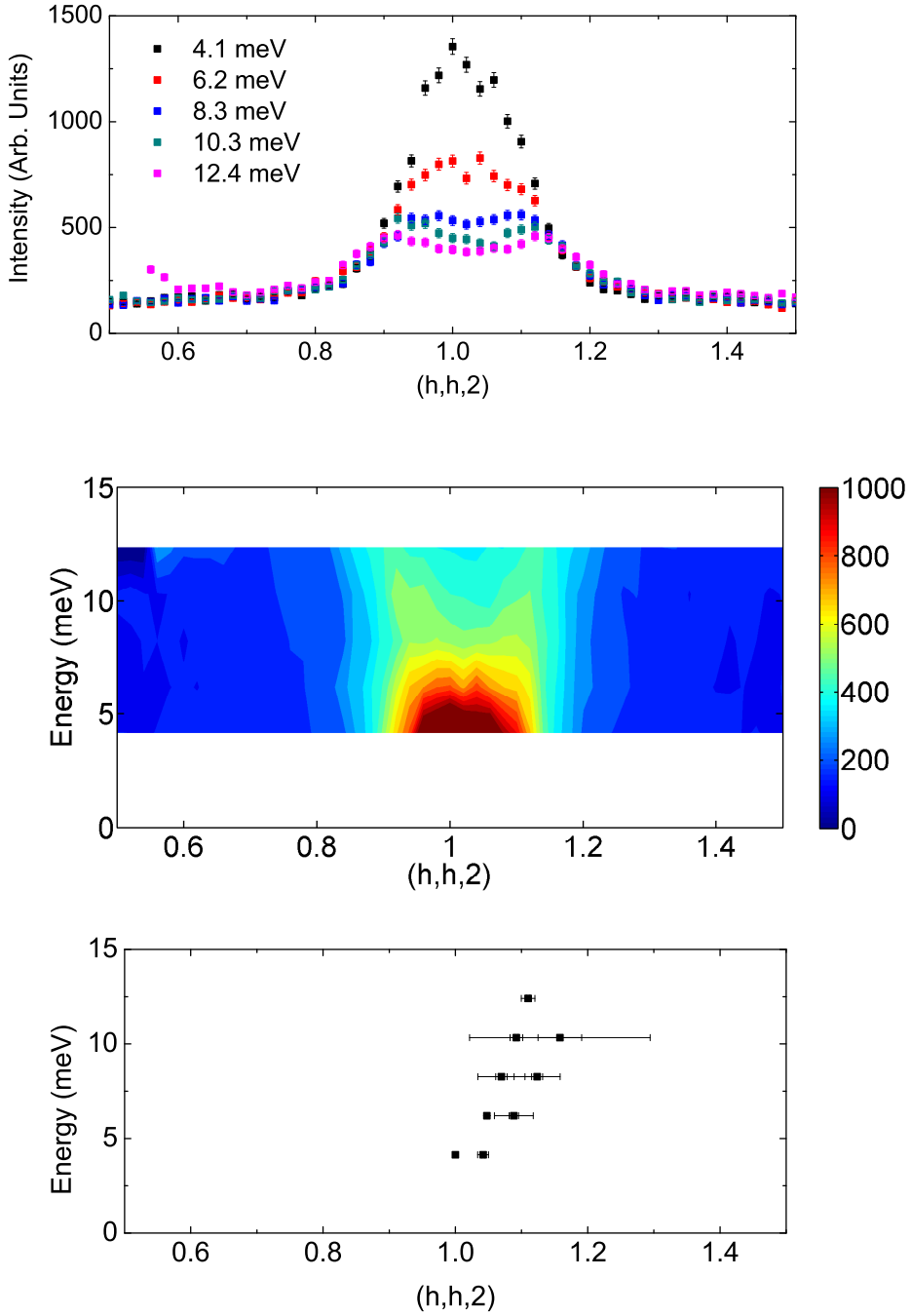

Figure 6.26: Scans along the $(h, h, 2)$ direction across the $(1, 1, 2)$ peak in the $I4/mmm$ space group of $Y_{0.15}Sr_{0.85}CoO_{3-\delta}$ measured at 100 K at energy transfers up to 16.5 meV on the the triple-axis spectrometer 2T1. The top panel shows the raw data, the central panel shows the same data plotted as a contour plot and the lower panel shows the q-positions obtained from fitting the data with a dispersion.

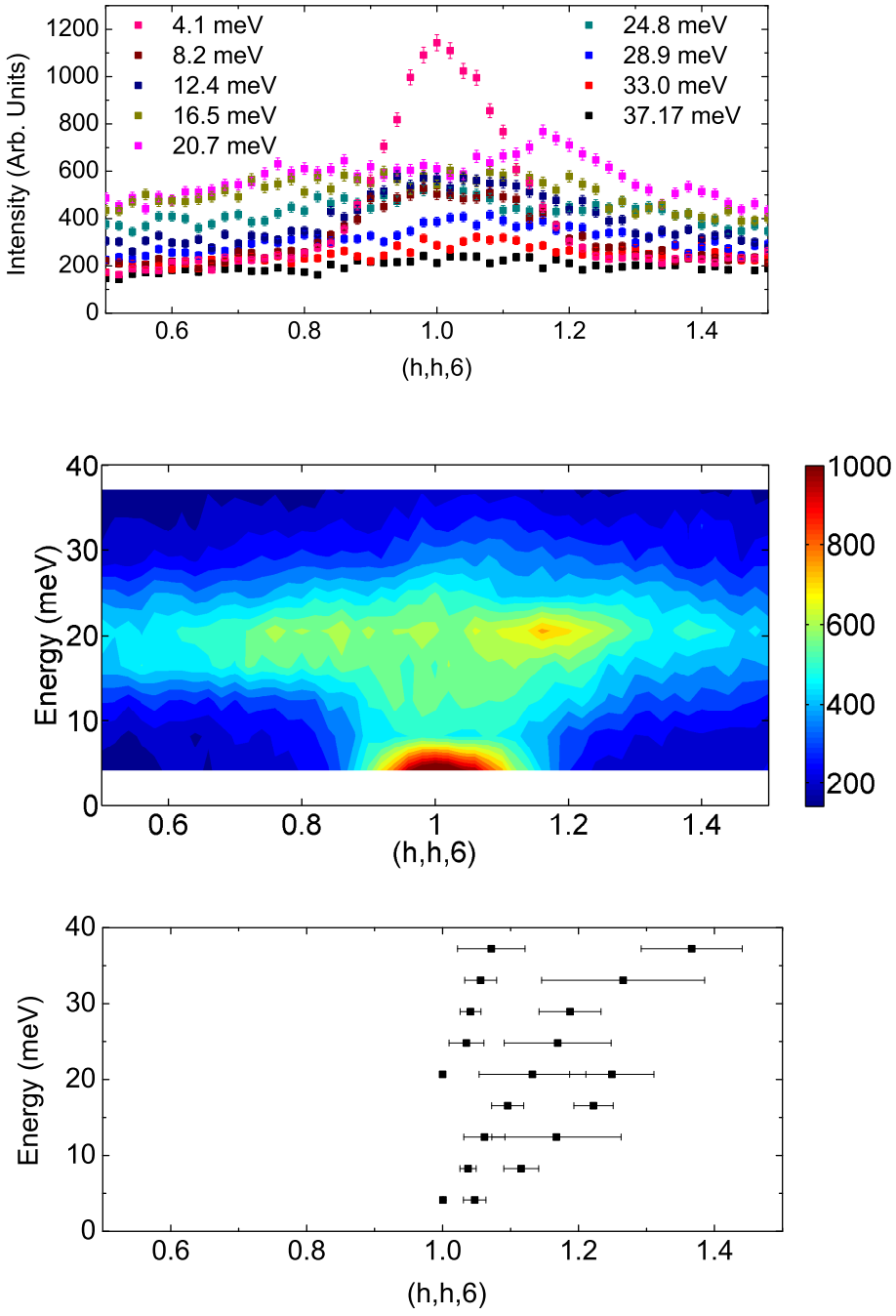

Figure 6.27: Scans along the $(h, h, 6)$ direction across the $(1, 1, 6)$ peak in the $I4/mmm$ space group of $Y_{0.15}Sr_{0.85}CoO_{3-\delta}$ measured at 100 K at energy transfers up to 37.2 meV on the the triple-axis spectrometer 2T1. The top panel shows the raw data, the central panel shows the same data plotted as a contour plot and the lower panel shows the q-positions obtained from fitting the data with a dispersion.

to be, a q-dependence of $\omega \propto q^2$ is to be expected. However, the dispersion for a ferrimagnet with an anisotropic crystal structure and at least three different cobalt moments, as is the case in our system, will be more more complex than this, and is beyond the scope of this experimental thesis, but suffice to say many magnon modes would be expected in the excitation spectrum.

All the inelastic measurements presented thus far were made at 100 K, but some attempt was also made to study the temperature dependence of the dispersion. In figure 6.28, the q-scan with energy transfer 28.9 meV shown in the top panel of figure 6.27 is plotted as a function of temperature. Within the error bar, there is limited difference between the different scans made below 300 K, they all show a dispersion peak centred on the $(1, 1, 6)$ position. The 350 K scan is also similar, but with a corresponding drop in intensity at the centre of the peak and an increase in intensity towards the edge of the scan. This is most likely due to the greater thermal fluctuations at this temperature causing a increased phonon contribution to recorded intensity.

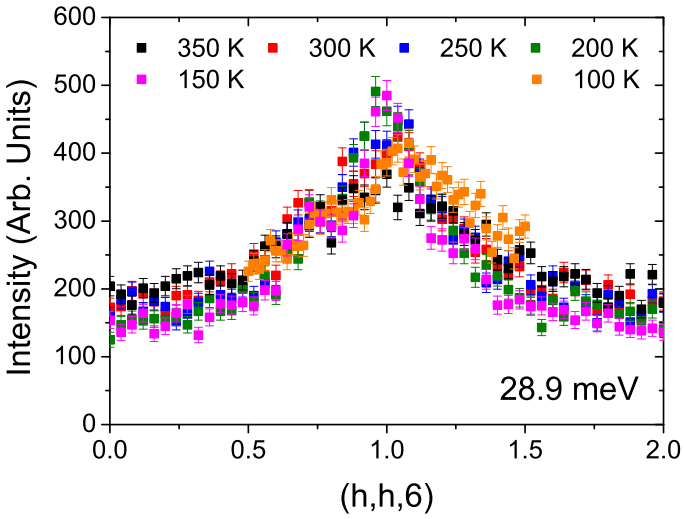

Figure 6.28: Scans along the $(h, h, 6)$ direction across the $(1, 1, 6)$ peak in the $I4/mmm$ space group of $Y_{0.15}Sr_{0.85}CoO_{3-\delta}$ measured at temperatures between 100 and 350 K at an energy transfer of 28.9 meV on the triple-axis spectrometer 2T1. The dispersion shows limited temperature dependence across this range.

6.4.3 Dispersion along the c direction

$Y_{1-x}Sr_xCoO_{3-\delta}$ has an anisotropic structure and the dispersion may be different along the different crystallographic axes. The dispersion along the $(1, 1, l)$ direction at 100 K is shown in figures 6.29 and 6.30 for the excitations around the $(1, 1, 2)$

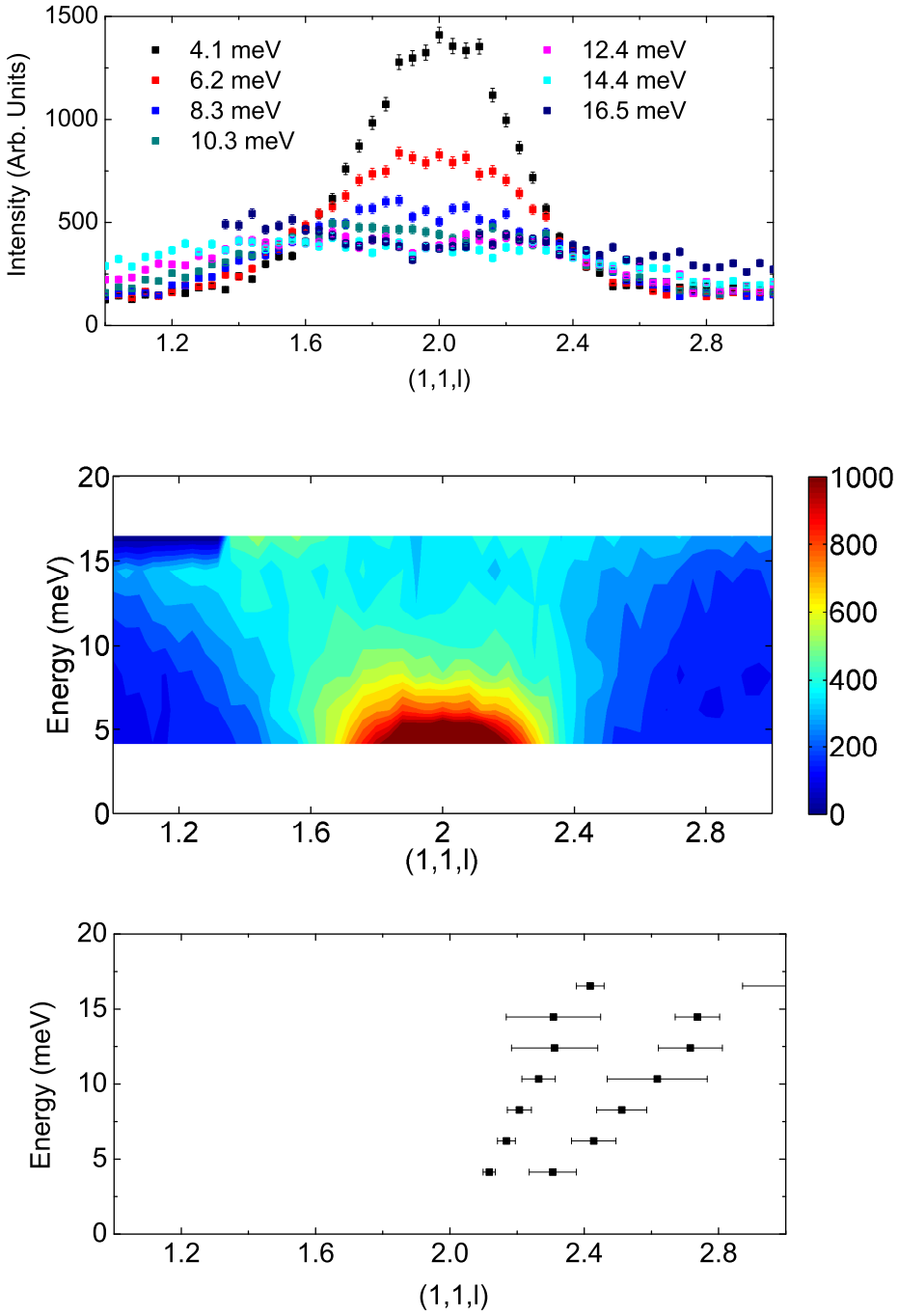

Figure 6.29: Scans along the $(1, 1, l)$ direction across the $(1, 1, 2)$ peak in the $I4/mmm$ space group of $Y_{0.15}Sr_{0.85}CoO_{3-\delta}$ measured at 100 K at energy transfers up to 16.5 meV on the the triple-axis spectrometer 2T1. The top panel shows the raw data, the central panel shows the same data plotted as a contour plot and the lower panel shows the q-positions obtained from fitting the data with a dispersion.

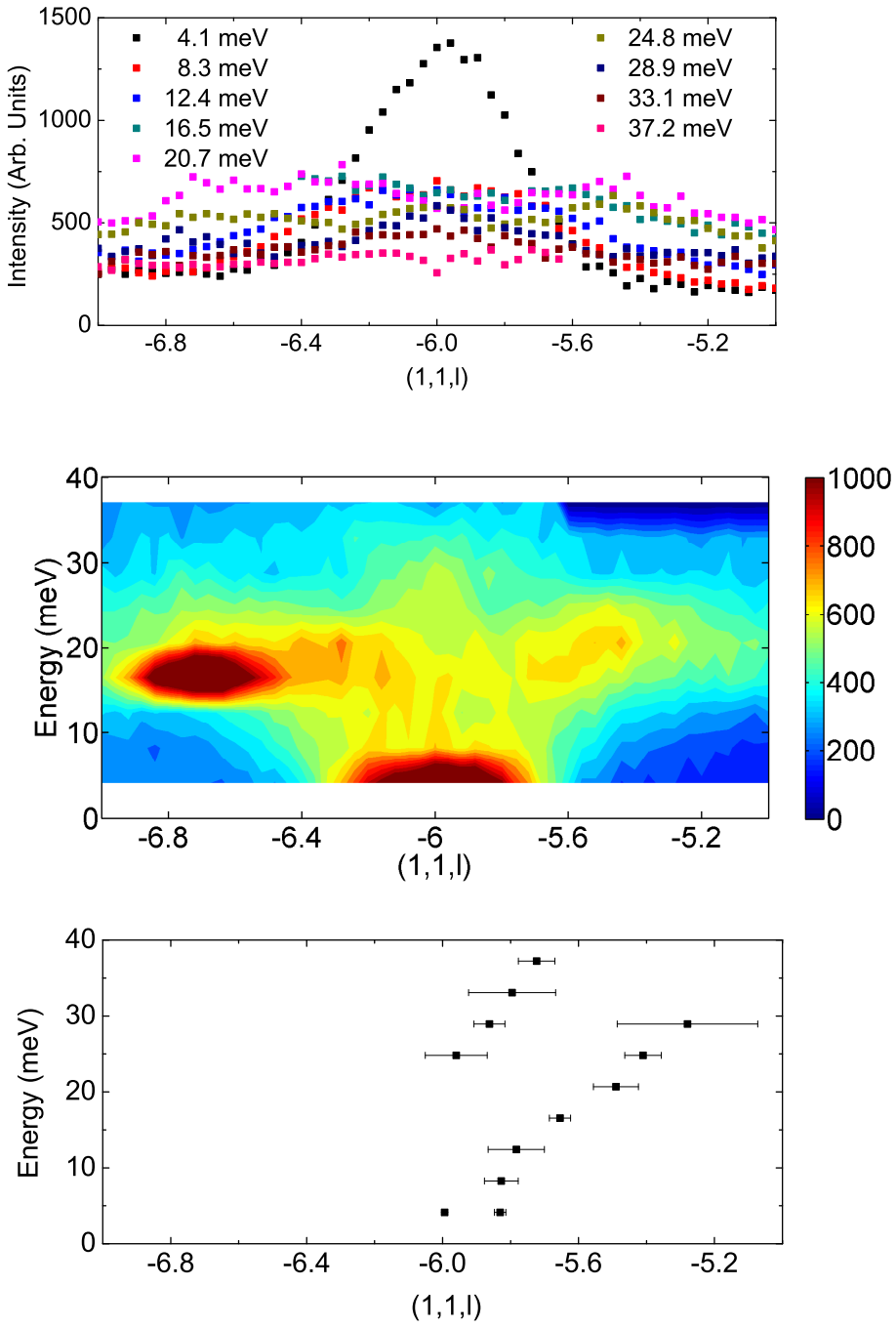

Figure 6.30: Scans along the $(1, 1, l)$ direction across the $(1, 1, 6)$ peak in the $I4/mmm$ space group of $Y_{0.15}Sr_{0.85}CoO_{3-\delta}$ measured at 100 K at energy transfers up to 37.2 meV on the the triple-axis spectrometer 2T1. The top panel shows the raw data, the central panel shows the same data plotted as a contour plot and the lower panel shows the q-positions obtained from fitting the data with a dispersion. The intense feature at $q = -6.7$ Å^{-1}, $E = 18$ meV is a spurion.

and $(1, 1, -6)$ peaks respectively. For the $(1, 1, 2)$ peak, $(1, 1, l)$ scans were made at energy transfers of 4.1, 6.2, 8.3, 10.3, 12.4, 14.4 and 16.5 meV between l values of 1 and 2. In figure 6.29, at least two dispersion modes are visible, and the q-positions obtained from fitting the scans with a dispersion corroborate this interpretation. As with the scans made along the *ab* direction, by measuring the dispersion around the $(1, 1, -6)$ magnetic peak higher energy transfers could be accessed. At least two, most likely magnon, branches are present at energy transfers between 4.1 and 37.2 meV. There is a concentration of intensity around 20 meV, as with the scans along the *ab* direction, where at least one excitation mode becomes dispersive.

Aside from the concentration of intensity around the Bragg peak, there is a second peak in intensity at an h value of -6.7 and an energy transfer of 18 meV. This is a parasitic signal commonly known as a spurion. Spurious signals can appear as a result of many processes, but this particular spurion is caused by a harmonic which satisfies the Bragg condition (equation 3.5) at that particular value of q. Or to express it another way, an additional elastic signal is recorded $\mathbf{Q}= nk_i - mk_f$ where n and m are integers. A larger spurion was present in the $(1, 1, l)$ measurement around the $(1, 1, 6)$ peak, hence the data presented in figure 6.30 was taken around the $(1, 1, -6)$ position.

In the measurement along the $(1, 1, l)$ direction shown in figure 6.30, the presence of a dispersive component at energy transfers higher than 15 meV is more obvious than the measurement in the $(h, h, 6)$ direction. This higher energy transfer mode is gapped at the $(1, 1, 6)$ position, suggesting anisotropy. A cold neutron spectrometer experiment would be necessary to probe this gap, and the potential for addition modes at low energy transfers, in more detail.

The temperature dependence of one of the constant energy transfer scans made along the $(1, 1, l)$ direction was also studied, and the results are shown in figure 6.31. A lower energy transfer scan of 12.4 meV was chosen compared to the comparable measurement along the $(h, h, 6)$ direction. There is a more obvious temperature variation at this value for the energy transfer, with the highest intensity excitations at 350 K and a steady decrease in intensity at temperatures below this. This is because as the sample is cooled below ordering temperature the magnetic fluctuations reduce and the magnetic ground state is approached. These measurements also show that significant excitation intensity is present at 390 K, above the magnetic transition temperature of the compound, and this will be further discussed in the next section.

6.4.4 Correlations above T_c

The ferrimagnetic transition temperature T_c for $Y_{0.15}Sr_{0.85}CoO_{3-\delta}$ is 370 K. Q-scans were made between 350 and 440 K, crossing this transition, along the $(h, h, 6)$

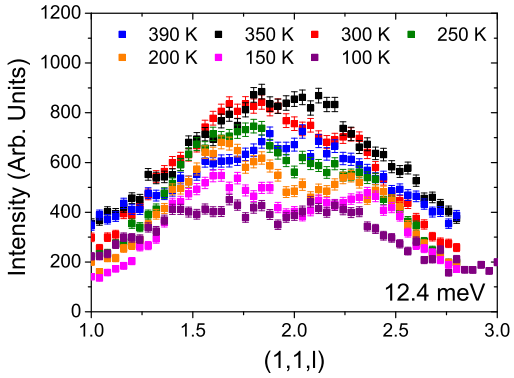

Figure 6.31: Scans along the $(1,1,l)$ direction across the $(1,1,2)$ peak in the $I4/mmm$ space group of $Y_{0.15}Sr_{0.85}CoO_{3-\delta}$ measured at temperatures between 100 and 390 K at an energy transfer of 12.4 meV on the triple-axis spectrometer 2T1.

and $(1,1,l)$ directions at up to five different energy transfers; 4.1, 12.4, 20.7, 28.9 and 37.2 meV on the triple-axis spectrometer 2T1. Some scans were made along $(-h,h,6)$ and $(-1,1,l)$ to avoid spurion signals. These scans are shown in figure 6.32. At the lowest energy transfer measured, 4.1 meV, there is a strong temperature dependence along both axes as the transition temperature is crossed, with the scans at 410 and 440 K having comparable intensities, and the scans at all temperatures along both axes showing evidence of dynamic magnetic correlations. At 12.4 meV, there is still a distinct temperature dependence of the correlations across the transition along the c axis of the $I4/mmm$ unit cell, but this is less clear along the other direction measured. These magnetic fluctuations have become negligible by an energy transfer of 28.9 meV along the $(1,1,l)$ axis, but there is still some evidence of correlations at an energy transfer of 37.2 meV in the scans along $(h,h,6)$ direction, although neither show any temperature dependence. Due to limitations on the equipment used, we were unable to probe temperatures above 440 K and establish a temperature at which these correlations disappear.

These measurements provide two key pieces of information about the magnetic correlations in $Y_{0.15}Sr_{0.85}CoO_{3-\delta}$. The dynamic magnetic correlations in $Y_{0.15}Sr_{0.85}CoO_{3-\delta}$ persist for a substantial temperature interval above T_c. Additionally, these correlations above T_c have a 2D character, evidenced by the fact that the peaks along the ab direction are significantly sharper than those along the c axis, implying longer-range fluctuations along this direction. This observation should be related to the measurements made at 390, 370 and 360 K on the polarised neutron diffractometer D7 shown in figure 6.23. Apparent magnetic diffuse scattering corresponding to an integrated inelastic contribution is obvious in the (h,h,l) scattering plane at T_c but not in the $(h,k,0)$ plane.

To try and understand this behaviour it should be considered in the context of similar systems. The perovskite $LaMnO_3$ is a antiferromagnet with a Néel temperature $T_N = 139.5$ K. The behaviour of the magnetic moments in this system, which are aligned along the b axis, does not fit with a 3D Heisenberg antiferro-

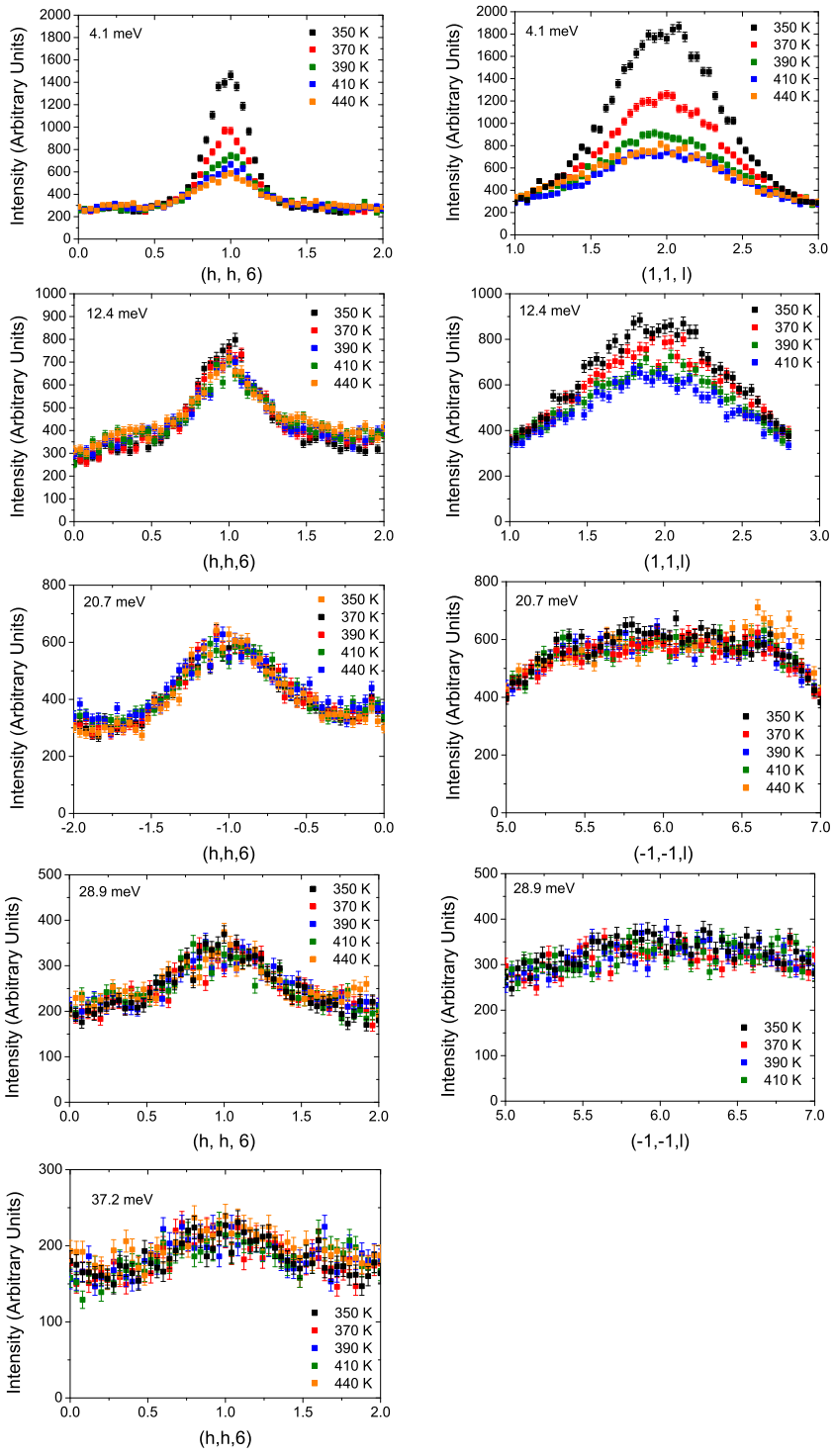

Figure 6.32: Scans along the $(h, h, 6)$ (left) and $(1, 1, l)$ (right) directions of the $(1, 1, 6)/(-1, -1, 6)$ and $(1, 1, 2)/(-1, -1, 2)$ peaks in the $I4/mmm$ space group of $Y_{0.15}Sr_{0.85}CoO_{3-\delta}$ respectively at energy transfers of 4.1, 12.4, 20.7, 28.9 and 37.2 meV. Scans have been made between 350 and 440 K on the triple-axis spectrometer 2T1.

magnet, but is instead a layered antiferromagnet. The correlations are ferromagnetic in the ab plane and antiferromagnetic along c, and the value of the ferromagnetic exchange integral is larger than the antiferromagnetic exchange integral [122]. Measurements on the doped manganite, $La_{1.2}Sr_{1.8}Mn_2O_7$ have also identified long-lived antiferromagnetic clusters above T_c, which on first glance are not dissimilar to those described here [123]. The weak ferromagnetic signal in $La_{1.2}Sr_{1.8}Mn_2O_7$ is attributed to a canted ferromagnetic component rather than the ferrimagnetism in $Y_{1-x}Sr_xCoO_{3-\delta}$ [124]. However, the principle that at the critical temperature dynamically ordered planes order against each other to achieve 3D static magnetic ordering is a plausible scenario for both materials. The presence of 2D fluctuations in $Y_{1-x}Sr_xCoO_{3-\delta}$ would be significant as it would mean it is magnetically ordered only in the planes above T_c, before 3D magnetic ordering onsets at T_c.

Scans in energy transfer at constant positions in reciprocal space were also made to probe the correlations above T_c in $Y_{0.15}Sr_{0.85}CoO_{3-\delta}$. These are shown in figure 6.33. Scans were made at the $(-1,-1,6)$, $(-2,-2,6)$ and $(-1,-1,7)$ Bragg positions at temperatures of 350, 370, 390 and 410 K. There is an increase in quasi-elastic scattering below T_c but the dispersive component between 10 and 20 meV shown earlier in figures 6.26, 6.27, 6.29 and 6.30 is clearly observable at all temperatures. The presence of inelastic modes with energy gaps is reinforced by peaks at $\sim$15 and $\sim$20 meV in the $(-1,-1,6)$ scan. The increased intensity of the $(-1,-1,7)$ scan compared to the $(-2,-2,6)$ at energy transfers up to 30 meV suggests anisotropy in the magnetic correlations, as already discussed.

6.5 Discussion

The magnetic behaviour of $Y_{0.15}Sr_{0.85}CoO_{3-\delta}$ powder and single crystals has been investigated. The simple perovskite AD/OD sample was found to be ferromagnetic with a T_c of 150 K by both magnetisation and neutron diffraction. However, the neutron diffraction measurements on the brownmillerite AD/OO and AO/OO structural variants showed the susceptibility measurements do not necessarily reflect the full story of the magnetic order in the bulk of the material. The magnetisation signal measured from the AD/OD sample was found to be due to ferromagnetic ordering of the cobalt moments. In contrast, the magnetisation signal measured from the AD/OO sample is believed to be due to a ferromagnetic impurity phase in an otherwise antiferromagnetic system.

A ferromagnetic-like magnetisation signal from single crystals of the AO/OO structural variant of $Y_{1-x}Sr_xCoO_{3-\delta}$ was also recorded below the transition temperature of 370 K, and was also found to be isotropic. This has been shown to coincide with the temperature at which a structural transition was observed, and it

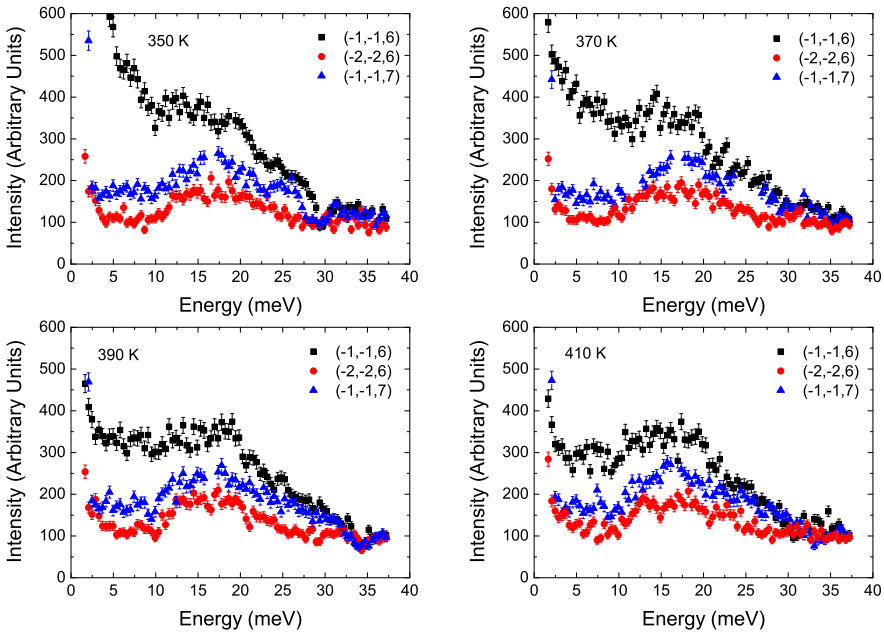

Figure 6.33: Scans of the $(-1,-1,6)$, $(-2,-2,6)$ and $(-1,-1,-7)$ peaks in the $I4/mmm$ space group of $Y_{0.15}Sr_{0.85}CoO_{3-\delta}$ as a function of energy transfer made on the triple-axis spectrometer 2T1. T_c is 370 K, and measurements have been made at 350, 370, 390 K and 410 K.

has been suggested that the antiferrimagnetism below 370 K in $Y_{1-x}Sr_xCoO_{3-\delta}$ is brought on by orbital ordering of the IS cobalt atoms [45]. The second change in the magnetic behaviour of $Y_{1-x}Sr_xCoO_{3-\delta}$ as a function of temperature, evident from the susceptibility measurements, is at 280 K. This change also seems to be accompanied by a displacive-type structural phase transition. The width of the magnetic contribution to the powder diffraction also appears to become resolution limited at this temperature, which may indicate that this change in magnetic behaviour is associated with domains. Alternatively, some change in the magnitude of a fraction of the magnetic moments, such as a spin state transition, may be associated with the change in structure and magnetic behaviour at 280 K.

Diffuse and inelastic scattering measurements on $Y_{0.15}Sr_{0.85}CoO_{3-\delta}$ have shown that the inelastic spectrum has a minimum of two magnon branches along each axis, and probably many more, as might be expected in such a complex system. There are also gapped energy modes indicative of the magnetic anisotropy of the system. Quasi-elastic magnetic scattering was observed both below and significantly above T_c using both techniques. The results suggest that the magnetic fluctuations are 2D becoming 3D at T_c, although more detailed investigation is necessary to fully understand this behaviour.

Studying the magnetism in $Y_{0.15}Sr_{0.85}CoO_{3-\delta}$ has demonstrated the necessity of using microscopic probes such as neutron scattering for studying this com-

pound. The ferromagnetic signal, although isotropic from magnetisation measurements, is due to the unequal, and antiferromagnetically aligned, moments on different cobalt sites, and this remnant moment is nevertheless not constrained to lie in any particular direction accounting for the isotropic ferromagnetism. For further progress to be made, an improved structural model for $Y_{1-x}Sr_xCoO_{3-\delta}$ as a function of temperature is necessary so the magnetic structure can be accurately determined.

Part III

$Ca_3Co_2O_6$

Chapter 7

$Ca_3Co_2O_6$: Introduction

$Ca_3Co_2O_6$ is a quasi-1D magnetic material with Ising spins on a triangular lattice. This configuration has the potential for geometrical frustration and other interesting magnetic behaviour. Regularly-spaced steps in the magnetisation as a function of applied magnetic field have been ascribed to either a quantum tunnelling of the magnetisation or the evolution of metastable states. This literature review covers the work on $Ca_3Co_2O_6$ to date and identifies the outstanding issues which led to the experimental work described in chapters 8 and 9.

7.1 Crystal Structure

Interest in the compound $Ca_3Co_2O_6$ was ignited in 1996 when Fjellvåg *et al.* [28] solved the structure by refining neutron and X-ray powder diffraction data. They indexed the structure with the rhombohedral space group $R\bar{3}c$ (Z=6, hexagonal setting), where the lattice parameters are a = 9.0793 Å and c = 10.381 Å at room temperature. The cobalt atoms (Co) alternate between face-sharing CoO_6 octahedra (Co1) and CoO_6 trigonal prisms (Co2), forming chains running along the c axis, shown in figure 7.1. In the ab plane these chains form a triangular

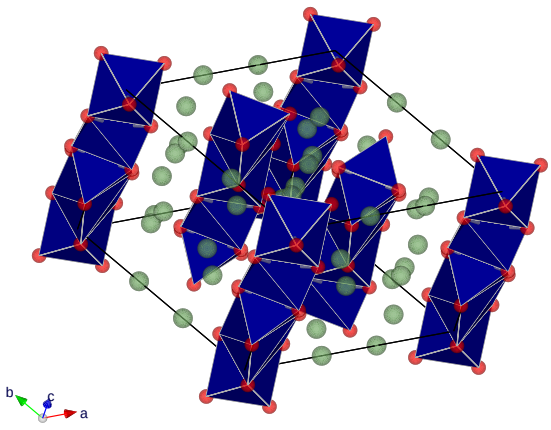

Figure 7.1: Crystal structure of $Ca_3Co_2O_6$. The chains of alternating CoO_6 octahedra and CoO_6 trigonal prisms are shown in blue with the oxygen atoms in red. The green spheres are the calcium atoms. In the ab plane the chains are arranged in a hexagonal lattice. Figure drawn using [113].

lattice, with calcium atoms separating the chains. The intrachain Co-Co separation is 2.59 Å whereas the interchain Co-Co separation is 5.24 Å. This means that $Ca_3Co_2O_6$ has a highly anisotropic crystal structure and can be characterised as a quasi-1D material.

7.2 Magnetic Structure

$Ca_3Co_2O_6$ has been found to magnetically order below 25 K, with an effective magnetic moment of 5.7 $\mu_B/f.u.$ in the paramagnetic regime [36]. The magnetic structure was refined as trivalent cobalt ions (Co^{3+}) whose spin state alternates, with high spin (HS) for the trigonal prisms, $S_{HS} = 3.00\ \mu_B/f.u.$, and low spin (LS) for the octahedra, $S_{LS} = 0.08\ \mu_B/f.u.$ [34, 35, 125, 126], with a large orbital contribution ($\sim 1.57\mu_B$) to the magnetic moment [127]. The cobalt moments on both sites are aligned along the c axis and ferromagnetic coupling dominates within the chains. Additional Bragg peaks (such as the (1,0,0) reflection) were observed below T_N indicating antiferromagnetic order, which is present between the chains in the ab plane [34].

The ferromagnetic intrachain interactions ($J_{FM} \sim 25$ K) in $Ca_3Co_2O_6$ are stronger than the antiferromagnetic interchain interactions ($J_{AFM} \sim 0.25$ K). The moments also appear to be constrained to exhibit Ising-like behaviour with an easy direction parallel to the chain direction. As the interactions between the Ising spins are antiferromagnetic on a triangular lattice in the ab plane, $Ca_3Co_2O_6$ is also a geometrically frustrated material (section 2.4.1). The geometrical frustration has led to the suggestion that $Ca_3Co_2O_6$ has a partially disordered antiferromagnetic structure, shown in figure 7.2. The model is used to describe a system where one of the three Ising spin chains in the unit cell will have spin up, one will have spin down, and the third will be incoherent [34, 39].

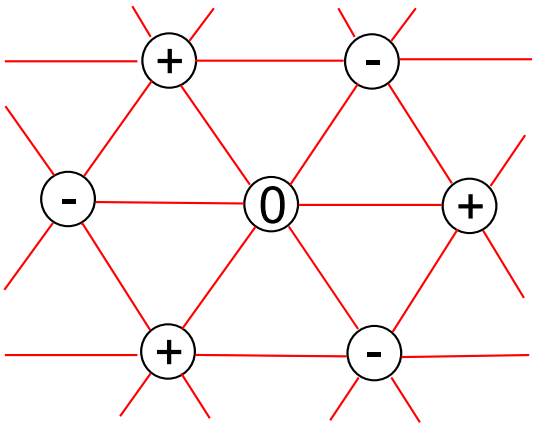

Figure 7.2: The partially disordered antiferromagnetic (PDA) structure on a hexagonal lattice. The circles represent the ferromagnetic spin chains. The plus and minus signs indicate the direction of the moment on each of the spin chains. The zero (0) indicates that the spin can be either plus or minus at random and is incoherent. Adapted from reference [128].

7.3 Behaviour in an Applied Magnetic Field

At temperatures below 5 K, steps in the magnetisation have been found to occur at applied magnetic fields of 0, 1.2, 2.4, 3.6 and 4.8 T respectively, shown in figure 7.3. Additional steps were claimed in fields of 6 and 7.2 T at temperatures below 2 K [37]. The relative magnitudes of these steps were cited as particularly interesting [129], as they appear to have relative magnitudes of $m = 1/4, 1/2, 1, 2,$ and 3, where $m = 1$ corresponds to the ferromagnetic ordering of a single chain and $m = 3$ corresponds to the ferromagnetic ordering of three chains on the same triangle and the maximum possible magnetisation. These steps can therefore be directly interpreted as reorientation of particular spin chains when a critical field is applied due to the geometrical frustration within the lattice. It has been claimed that next nearest neighbour interactions need to be considered to fully explain all of the steps [129].

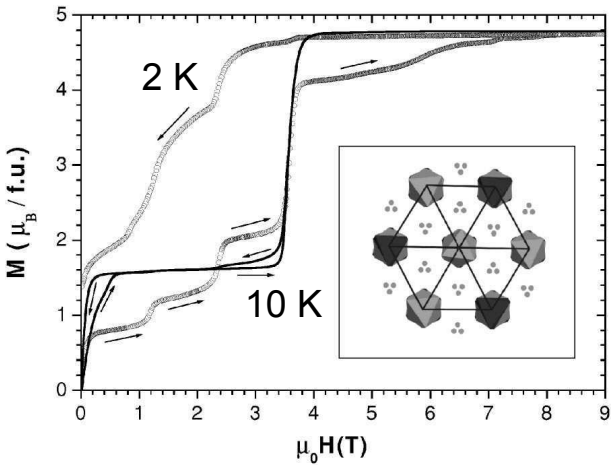

Figure 7.3: Hysteresis loops for $Ca_3Co_2O_6$ recorded at 2 and 10 K at a sweep rate of 0.1 T/min. The arrows indicate the direction of the field variation. The inset shows a projection of the crystal structure of $Ca_3Co_2O_6$ along the hexagonal c axis. The cobalt polyhedra are shown in dark and light grey and the small grey circles represent the Ca ions. Taken from reference [38].

On cooling from T_N, the hysteresis of the M-H loops increases around 12 K (T_{c2}), with substantial hysteresis at 2 K and evidence of spin-freezing (broadening of the magnetisation plateaux at low temperatures) [39]. Between T_N and T_{c2}, the M-H loops have two steps, the first step just above 0 T being the transition to a ferrimagnetic plateau with 1/3 of the saturation magnetisation and the second step being to a value close to the saturation magnetisation ($M_{Sat} = 4.8\mu_B/f.u.$), suggested to indicate a transition into a purely ferromagnetic phase [34].

The magnetic and physical properties of $Ca_3Co_2O_6$; dc-magnetisation, ac-susceptibility and resistivity, are highly anisotropic in accordance with the anisotropic crystal and magnetic structures. It has been established that the powder magnetisation primarily reflects the c axis behaviour alone [130]. The single crystals used for these measurements were grown using a flux method [129] and were a few mm in length and needle-like.

7.4 Time Dependent Behaviour

Various measurements [38, 129, 131, 132, 133] have made it clear that the dynamics of the particular measurement affect the appearance of the low temperature steps in $Ca_3Co_2O_6$. At 4 K, the steps at 1.2 T and 2.4 T are clearly visible features in the magnetisation data with a sweep rate of 1 T/min, but as the sweep rate is decreased these features are progressively smoothed, and at 0.01 T/min they are completely absent [38]. This relaxation in the bulk magnetisation is most pronounced at low temperatures, and at temperatures of 10 K and above there is almost no relaxation observable. At temperatures between 2 and 10 K unusual relaxation effects occur, often over timescales as long as several thousand seconds. These effects are most obvious in fields close to the step at 2.4 T. At 4 K, there is a crossover in the relaxation behaviour at 2.4 T, with the magnetisation increasing with time when measured in fields below 2.4 T and magnetisation decreasing with time in fields above 2.4 T [38]. Initially the magnetisation at 2.4 T and 4 K increases with time, before starting to decrease after just over an hour.

The appearance of steps in the magnetisation, substantial magnetic hysteresis and very slow spin-relaxation time are characteristics that $Ca_3Co_2O_6$ shares with the so-called 'single molecule magnets', Mn_{12} and Fe_8 [134]. These single molecule magnets are systems in which resonant quantum tunnelling of the magnetisation (QTM) is found, and supply a special opportunity to study this quantum mechanical phenomenon. The similarities in behaviour between $Ca_3Co_2O_6$ and the single molecule magnets has led to the suggestion that $Ca_3Co_2O_6$ is the first example of QTM in a magnetic oxide [37].

Materials which exhibit quantum tunnelling have two or more degenerate ground states with a potential energy barrier between them. Where a magnetic field is applied, the degeneracy of these ground states is lifted and one state is stabilized with respect to the other. As the field increases, this state becomes resonant with other excited spin states and quantum tunnelling becomes possible [37]. The asymptotic behaviour of the relaxation time in $Ca_3Co_2O_6$, with an onset of about 7 K, agrees well with the behaviour of the single molecule magnets [133], but the field dependence of the relaxation shows different features. Unlike the single molecule magnets, $Ca_3Co_2O_6$ has steeper variations in the relaxation time and the positions of the peaks in the time dependence as a function of field do not vary with sweeping rate as would be expected for a quantum tunnelling process [37].

There is still some debate about the classification of $Ca_3Co_2O_6$ as a quantum tunnelling system [37, 135] and it was originally suggested that below 12 K, $Ca_3Co_2O_6$ is a spin glass [39], with spin freezing ($T_{SF} = 7$ K) at low temperatures. This would be as opposed to 12 K being a crossover temperature where spin relaxation time τ becomes temperature independent, crossing from standard Arrhenius

behaviour described in section 2.4.3 to a potential quantum regime akin to the quantum tunnelling of the magnetisation in the single molecule magnets described above [37, 133]. However, some studies [129, 133] have suggested this behaviour is closer to that expected for superparamagnetic clusters [136] or the evolution of metastable states [137]. The experimental work presented in the following two chapters is intended to further our understanding of these issues.

7.5 Recent Developments

Resonant X-ray scattering investigations have highlighted a small incommensuration in the magnetic order along the c axis of $Ca_3Co_2O_6$ in low fields. In zero field, the modulation of the magnetic order changes continuously between 5 K, where it has a periodicity of 1500 Å, and 23 K, where it has a periodicity of 700 Å [138]. These are both very long scale modulations, and imply a long wavelength spin density wave (SDW) propagating along the c axis. This gives a general propagation vector of $\mathbf{k} = (0, 0, 1.01)$ for the antiferromagnetic spin density wave in $Ca_3Co_2O_6$ in zero field at temperatures below T_N. Recent thermal conductivity measurements [139] suggest an exchange-mediated heat transfer which is incompatible with the Ising model, and supports the helical exchange pathway implied by the spin density wave.

Neutron diffraction measurements have shown that the long-range magnetic order in $Ca_3Co_2O_6$ coexists with a short-range magnetic ordering with a correlation length of ∼180 Å in the ab plane. It was previously known that there was anomalous dip in the intensity of the Bragg peaks corresponding to long-range antiferromagnetic order at low temperatures [140]. The maximum intensity of these peaks was found at the temperature 18 K. It has been suggested that this drop in intensity is due to an increase in the fraction of material exhibiting this short-range order, however more recent results suggest some intensity is still unaccounted for [141].

7.6 Theoretical Work

Electronic structure calculations considering possible intrachain ferromagnetic and antiferromagnetic hopping events have shown that the origin of the ferromagnetic coupling along the chains is direct Co-Co orbital overlap between magnetic and non-magnetic cobalt ions with $J_1 \sim 25$ K. For the antiferromagnetic interchain coupling the exchange is via two oxygen sites, super-superexchange coupling $J_{AFM} \sim 0.25$ K [142]. By assuming these two exchange interactions between nearest and next nearest neighbours are different ($J_{AFM} = J_2 + J_3$) a helical exchange pathway is formed which serves to stabilise the SDW state [144]. This is shown in figure 7.4. The overlap of the oxygen $2p$ orbital is very small, so the nearest neighbour exchange

term J_2 is weaker than the next nearest neighbour exchange term J_3.

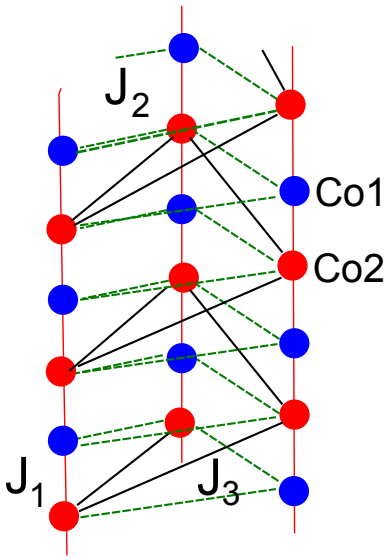

Figure 7.4: Exchange interactions in $Ca_3Co_2O_6$. The Co1 CoO_6 octahedra are shown in red and Co2 CoO_6 trigonal prisms are shown in blue. The J_1 ferromagnetic intrachain interactions are shown in red, the J_2 nearest neighbour antiferromagnetic interchain interactions are shown in dashed green and the J_3 next-nearest neighbour antiferromagnetic interchain interactions are shown in black. Adapted from [144, 145].

Magnetisation plateaux are expected in Heisenberg antiferromagnetic chains when $N_c(S - m)$ is an integer, where N_c is the number of sites in the magnetic unit cell, S is the spin quantum number and m the average magnetisation per spin [142, 143]. The location in field of the steps in the magnetisation observed in $Ca_3Co_2O_6$ agrees with this criterion and several researchers have attempted to reproduce the observed behaviour by theoretical considerations. The plateaux have been explained using entropy arguments focusing on the interchain magnetic order within a PDA honeycomb model [146]. In this model, there are a mixture of spin up, spin down and mixed spins sites forming a hexagonal lattice of spin up and spin down chains with a chain which can either be spin up or spin down at the centre. The steps correspond to the flipping of chains in particular configurations within the honeycomb, for example the step at $B = 0$ arises from the flipping of all the chains at the centre of the hexagons to align with the applied magnetic field [146, 147, 148]. Monte Carlo simulations have been used to assess the effect of these metastable states on the sweep rate dependence of the magnetisation and found reasonable agreement with experiment [137, 149, 150].

7.7 Discussion

In summary, $Ca_3Co_2O_6$ is a complex system with several competing magnetic interactions. Firstly the zero field magnetic structure consists of spin chains, with ferromagnetic interactions along the chains and antiferromagnetic interactions between the chains. These interactions give rise to a sinusoidally modulated SDW structure along the c axis generated by a helical exchange pathway in the ab plane.

Secondly, on application of a magnetic field $Ca_3Co_2O_6$ starts to display ferrimagnetic behaviour, then becoming ferromagnetic when the moment is saturated, with regularly-spaced steps appearing in the bulk magnetisation. Thirdly, the magnetic order has unusual time dependence at temperatures below 12 K. Fourthly, there is clear coexistence of long-range and short-range antiferromagnetic order in $Ca_3Co_2O_6$ at low temperatures. These four intriguing features of the magnetic behaviour of this material will be further explored in the following two chapters.

Chapter 8

$Ca_3Co_2O_6$: Temperature and Time Dependent Magnetic Behaviour

This chapter details experiments carried out on the neutron diffractometers GEM and D7 to study the time and temperature dependence of the different components of the magnetic order in $Ca_3Co_2O_6$. The aim of these experiments was to use neutron diffraction to understand the microscopic mechanisms behind the competition between short and long-range order and the slow relaxation of the magnetic order, frequency dependence of the ac-susceptibility and other time dependent behaviour observed in $Ca_3Co_2O_6$. All the work detailed in this chapter describes behaviour observed in zero applied magnetic field at temperatures below $T_N = 25$ K.

8.1 Magnetic Phases

8.1.1 Experimental Details: The GEM Neutron Diffractometer

The GEneral Materials (GEM) diffractometer [151] at the pulsed neutron source ISIS is a powder diffractometer with eight detector banks which cover the range of scattering angles between 1.2° and 171.4° designed to study a wide variety of different materials. The large number of detectors on GEM are engineered to give the highest possible count rate. The high reciprocal-space resolution of the instrument, with a best value of $\Delta Q/Q$ of 0.34 %, is made possible by having individual ZnS/^{6}Li scintillator detectors with an effective width of 5 mm and a relatively long moderator to sample distance of 17 m. The neutron flight path and sample tank are evacuated to prevent air scattering.

An experiment to study the time dependence of the magnetic order in $Ca_3Co_2O_6$ was carried out on GEM using 2.9 g polycrystalline sample. The sample was syn-

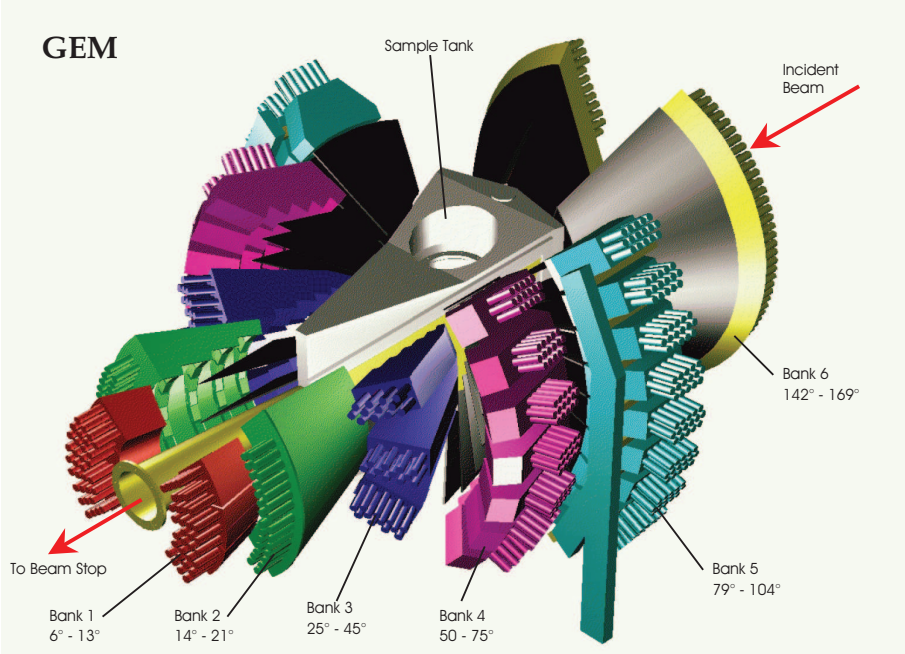

Figure 8.1: Layout of the powder diffractometer GEM at ISIS. The eight sets of detector banks are labelled in the figure [152].

thesized via a standard solid state reaction method [35, 39, 129] and pressed into a 32 mm rod. The magnetisation behaviour of the sample was checked and found to agree with that previous published by other researchers [39]. The sample was then inserted into a vanadium sample can and the can was packed with silica wool. The sample can was mounted in a standard 10 T cryomagnet with an aluminium window. Data were not collected in backscatter mode, so six detector banks were used for the experiment.

8.1.2 Magnetic Structure

The sample was installed at 300 K and then cooled to 35 K over a time period of several hours. A diffraction measurement was made at this temperature with a counting time of 1 hour 45 mins. The sample was then cooled to 2 K and a measurement was made with a counting time of 2 hrs. Later, when cooling using the same procedure, a further measurement was made at the intermediate temperature of 18 K with a counting time of 15 minutes.

The recorded neutron diffraction patterns were analysed by Rietveld refinement using the FULLPROF program [111]. A pattern collected above T_N (T= 35 K, shown in figure 8.2(a)) was refined using the known structural parameters of $Ca_3Co_2O_6$ (space group $R\bar{3}c$) and data from all six detector banks. A 0.08 % phase fraction of nonmagnetic CaO (space group $Fm\bar{3}m$) was found to be the only detectable impurity present, indicating the sample was of high quality. The final

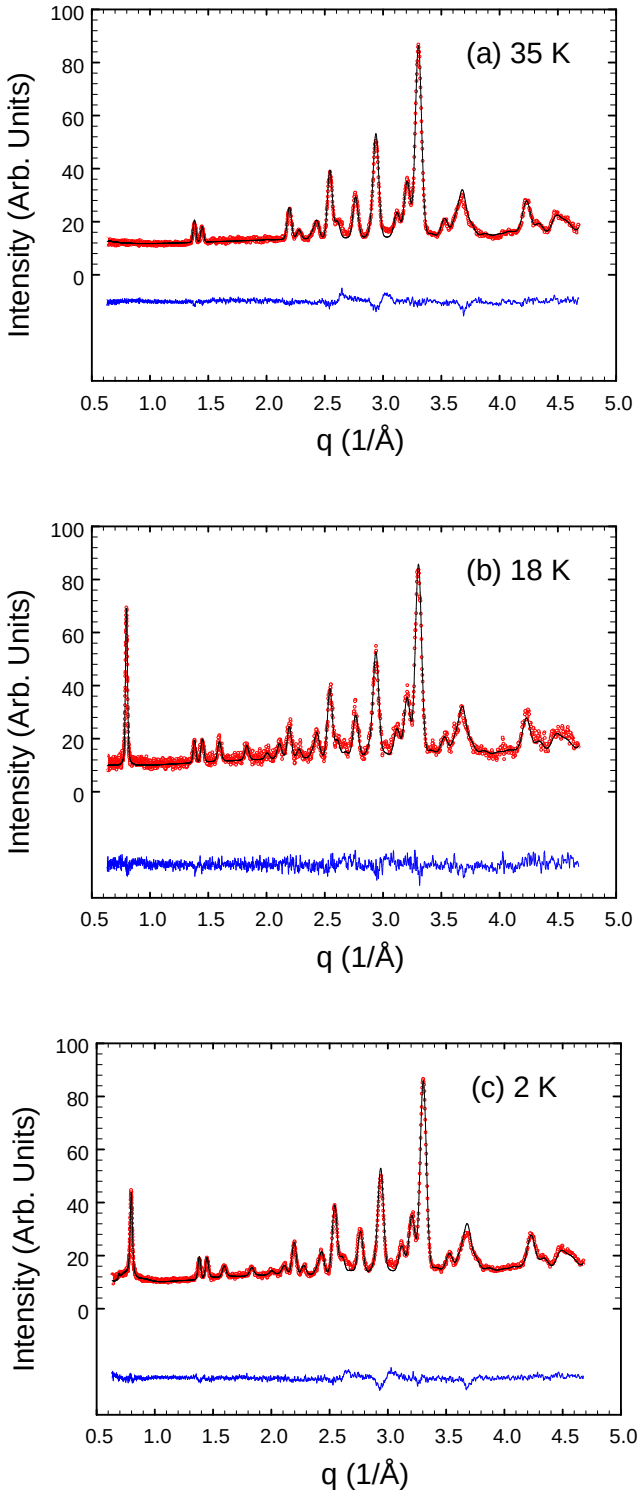

Figure 8.2: Raw diffraction data (red circles) and fits to the data (black lines) with difference plots (blue lines) made at temperatures of (a) 35 K (nuclear phase only $\chi^2 = 5.412$) (b) 18 K (nuclear and SDW phases $\chi^2 = 1.727$) (c) 2 K (SDW and short-range phases $\chi^2 = 3.317$). The data presented is from detector bank 2 of the powder diffractometer GEM.

atomic parameters and Wyckoff positions from the refinement are given in table 8.1.

Atom	Site	x	y	z	B	Occ.
Ca	18e	0.3688(3)	0	0.25	0.07(2)	1.0
Co1	6b	0	0	0	0.37(2)	1.0
Co2	6a	0	0	0.25	0.15(4)	1.0
O	36f	0.1762(3)	0.0245(2)	0.1144(3)	0.48(2)	1.0

Table 8.1: Table of atomic positions for $Ca_3Co_2O_6$ refined in the $R\bar{3}c$ space group. The lattice parameters were $a = b = 9.0733(1)$ Å and $c = 10.3830(3)$ Å, with $\alpha = 90°$, $\beta = 90°$ and $\gamma = 120°$. The data was collected at a temperature of 35 K.

When cooled below T_N, antiferromagnetic peaks appear in the diffraction pattern at q-values of 0.79, 1.59 and 1.82 $Å^{-1}$ (figure 8.2(b)). As established previously, these peaks correspond to an incommensurate antiferromagnetic phase and were fitted to a magnetic phase with propagation vector $k = (0, 0, 1.01)$. The success of this fit confirmed the presence of a spin density wave (SDW) structure along the c axis with period of 100 Å. The magnetic moment on the high spin Co2 site was refined to be 5.1 ± 0.1 μ_B directed along z, which includes a sizable orbital contribution. The magnetic moment on the Co1 site was fixed to be zero as it is well-established that it is in a non-magnetic low spin state. The analysis of the phase fractions discussed throughout this chapter is based on the assumption that the cobalt moment is saturated. This assumption is believed to be reasonable because of the low temperatures used, and is supported by the fact that the phase fractions for all our fits consistently summed to 1 [153].

The intensity of the peaks corresponding to the main antiferromagnetic phase have an unusual temperature dependence, decreasing in intensity as the temperature is reduced. This is clear when comparing figures 8.2(b) and 8.2(c), measured at 18 and 2 K respectively. The intensity of the three main antiferromagnetic Bragg peaks can be seen to have decreased noticeably. A broad peak is also visible to the low-q side of the main antiferromagnetic Bragg peak, extending down to a q-spacing of 0.69 $Å^{-1}$. This broad peak indicates short-range antiferromagnetic correlations which are not symmetrical about the main antiferromagnetic Bragg peak, unlike those previously identified [154]. It has previously been suggested that the loss in intensity of the peaks corresponding to the long-range antiferromagnetic phase is, at least in part, due to the an increase in the volume of material correlated on a shorter length scale [154]. However, it is clear that the short-range order observed here is not simply antiferromagnetic correlations on a finite length scale with the same propagation vector as the SDW phase, but something more complex.

8.1.3 Commensurate Antiferromagnetic Phase

Time dependent behaviour has previously been observed in laboratory measurements of $Ca_3Co_2O_6$ [133], including a time dependence in the magnetisation at temperatures below 10 K. The experiment described here was designed to study this time dependence using neutron diffraction. Firstly, the sample was warmed above T_N to remove any magnetic history. Then it was cooled slowly to 2 K, where it was allowed to thermalise for 15 minutes. The sample was then warmed to 8 K, where diffraction data was collected as a function of time. After some time, a distinct, sharp peak, not present when the sample was first warmed to 8 K, emerges at a q-value of 0.69 $Å^{-1}$, along with other smaller peaks at higher q-values. These peaks become sharper and more intense with time, shown in figure 8.3. This peak does not correspond to the SDW or the short-range magnetic phases and indicates a new type of long-range magnetic order has emerged as a function of time.

This new magnetic phase, hereafter referred to as the commensurate antiferromagnetic (CAFM) phase, was indexed with a propagation vector $k = (0.5, -0.5, 1)$ with respect to the hexagonal setting of the unit cell, which provided a good fit to the data. This propagation vector indicates a doubling of the unit cell in the a and b directions forming stripes of magnetic order in the ab plane.

The magnetic unit cells of the SDW and CAFM phases are shown in figure 8.4, along with the positions of the cobalt atoms in the equivalent structural unit cell. For all the phases, the moments along the chains are ferromagnetically aligned. For the SDW phase, the magnetic moment modulates between +M and -M along all the chains, so that at some points in the lattice the magnetic structure has the PDA structure shown in the figure with configuration $(\sqrt{3/2}M, -\sqrt{3/2}M, 0)$. At other lattice points however, the configuration is $(M, -M/2, -M/2)$. In contrast, the magnetic structure of the CAFM phase is believed to be commensurate.

The broad feature connecting the main magnetic peaks of the SDW and CAFM phases is indicative of short-range correlations. It is not symmetrical about either Bragg position, implying its propagation vector is not the same as either phase. We suggest that it is caused by defects in the ferromagnetic chains due to the helical exchange pathway of the antiferromagnetic superexchange interactions [144]. However, from this single feature it is not possible to determine the magnetic arrangement responsible for these short-range correlations.

The main magnetic peak of the CAFM stripe phase appears to be resolution limited. However, some of the smaller peaks, those indexed with $(h, -h, 0)$, are additionally broadened due to the finite correlation length of the phase. This broadening was found to indicate the magnetic domains of the stripe phase have a platelet shape along the stripe direction. The correlation length associated with this size broadening was found using the Scherrer equation $D = CK/S_z$, where C is

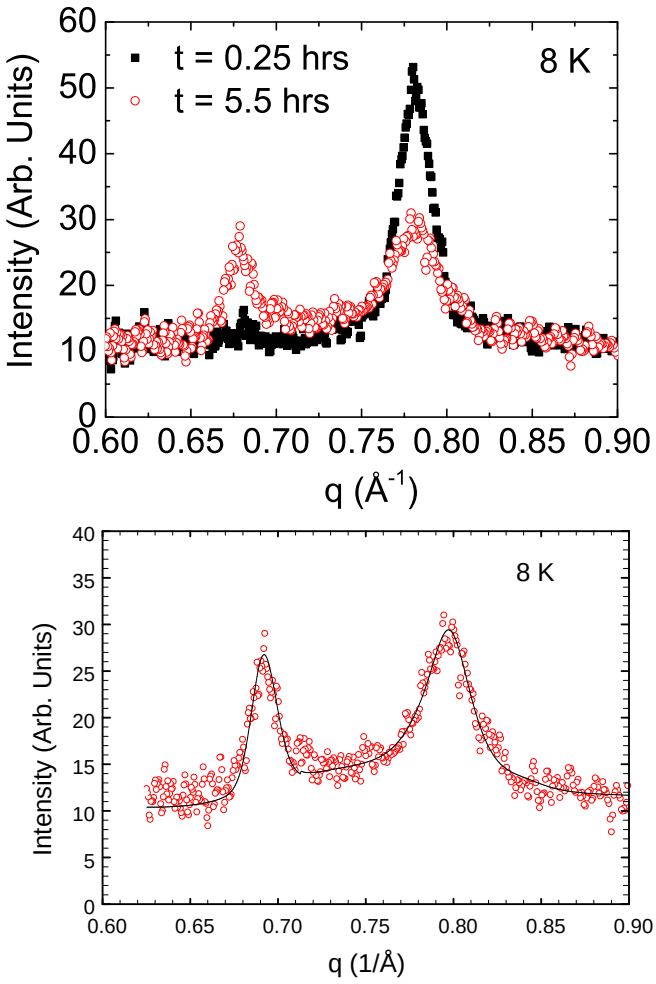

Figure 8.3: Upper panel: The main magnetic peaks of the SDW and CAFM phases in $Ca_3Co_2O_6$ measured on reaching 8 K (black squares) and after waiting for 5.5 hours at this temperature (red circles). Lower panel: The same data taken at 8 K after 5.5 hours (red circles) with the fit obtained using the model we propose shown in black.

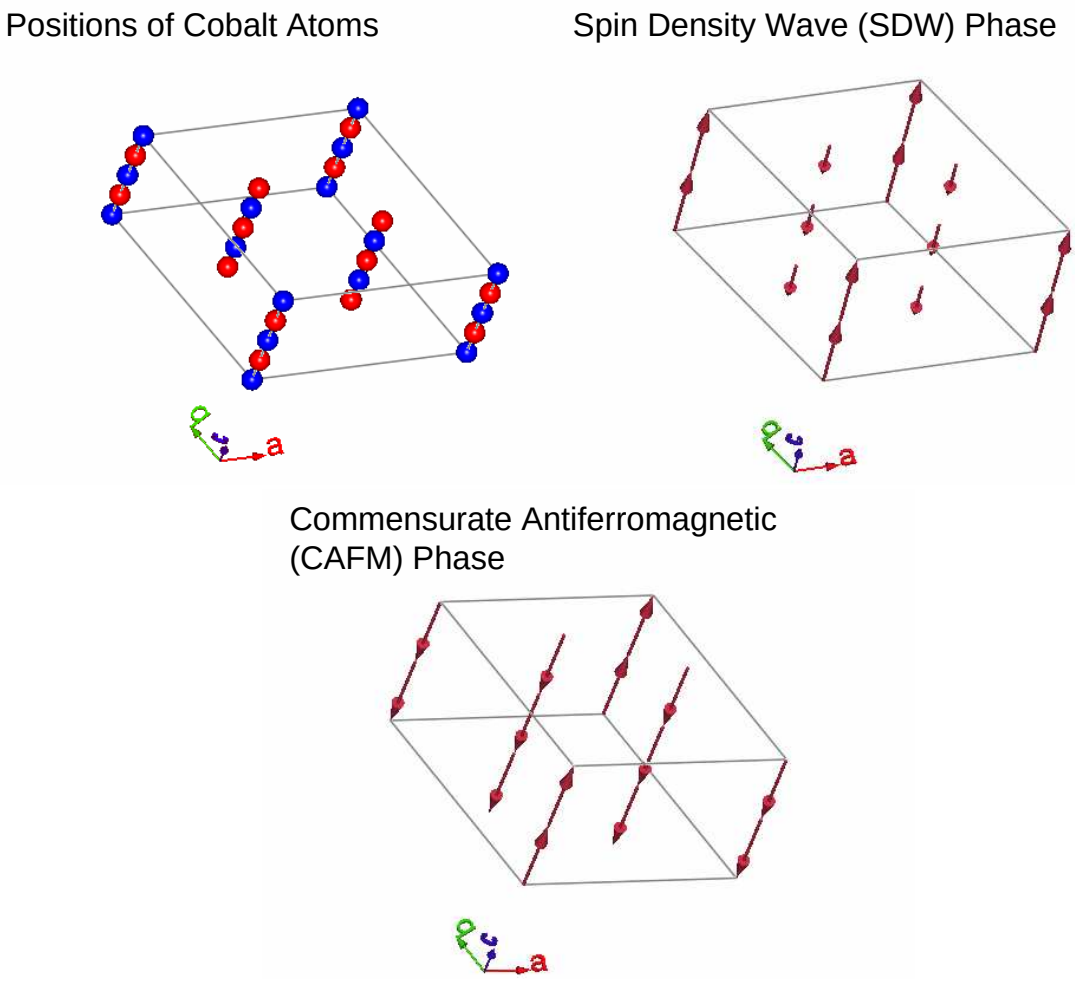

Figure 8.4: SDW and CAFM magnetic unit cells and the positions of the cobalt atoms in the structural unit cell. The top left panel shows the positions of the nonmagnetic Co1 (blue) and magnetic Co2 (red) cobalt atoms in the $Ca_3Co_2O_6$ unit cell. The PDA magnetic structure of the SDW phase is shown in the top right panel and the bottom panel shows the CAFM magnetic phase.

the diffractometer constant and K is the Scherrer constant (~ 0.9). The Lorentzian contribution to the anisotropy is of the form $S_z \cdot \cos\phi$, where S_z is the refined parameter and ϕ is the acute angle between the scattering vector and the stripe direction $[1, -1, 0]$. A refined S_z value of 10 gives a magnetic correlation length of around 100 Å along the stripe direction.

8.2 Time and Temperature Dependent Behaviour

8.2.1 Time Dependence

Time dependence in systems without inherent randomness or impurities is rare on an appreciable timescale to be measured by neutron diffraction. However, such a time dependence was recently observed in the compound $CeIr_3Si_2$, where there are two magnetic transitions within 1 K of each other. The time dependence was observed when the compound was rapidly cooled to a low temperature (2 K), leading to a time dependent lock-in transition between the incommensurate and commensurate magnetic phases [58]. $Ca_3Co_2O_6$ has also been reported to exhibit a time dependent lock-in transition in a low applied magnetic field [155]. However, neither of these reports involves a magnetic phase with an entirely different propagation vector such as the one discussed here.

In order to study the time dependence of the conversion of the SDW to the CAFM phase in $Ca_3Co_2O_6$, the sample was warmed above T_N and allowed to thermalise to erase the magnetic history. It was then thermalised again at 18 K and cooled rapidly to 2 K at a rate of approximately 2 K/min. It was then warmed to the required temperature. To evaluate the time dependent behaviour the data were binned into 15 minute intervals. The phase fractions of the different magnetic phases in $Ca_3Co_2O_6$ were evaluated at each 15 minute interval by refinement of the scale factors.

The time dependence of the data collected at 8 K is shown in the top panel of figure 8.5. The resulting curves for the SDW and CAFM phases were then fitted using stretched exponentials, defined in section 2.4.3, where the order parameter is the phase fraction (given as a percentage) of each of the magnetic phases. Using this method, the characteristic relaxation time τ was found to be 4.4 ± 0.9 hrs at 8 K. Equilibrium values of 28 ± 5 % and 24 ± 5 % were found for the SDW and CAFM phases respectively, showing that within error bar the equilibrium percentages of the two phases are equal. The phase fraction of the short-range component increases slightly in the first hour of measurement before reaching a relatively stable value of $\sim$35 %.

The time dependence of the magnetic phases in $Ca_3Co_2O_6$ was also measured at a temperature of 10 K, shown in the lower panel of figure 8.5. At this temperature

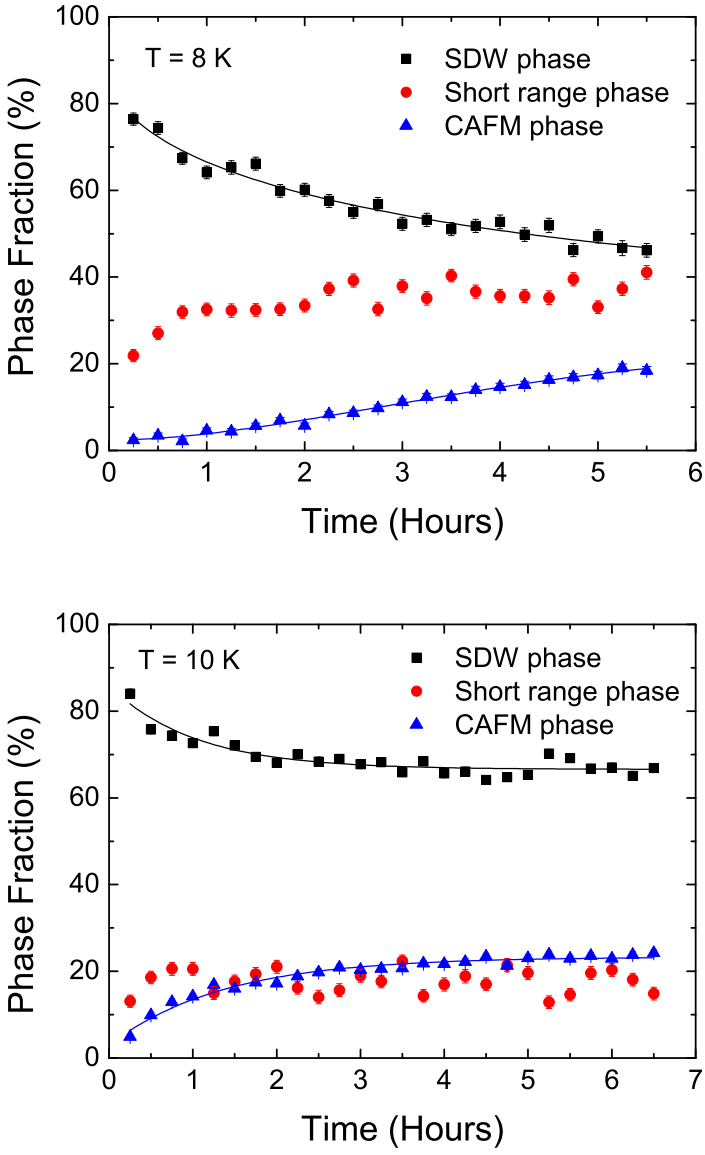

Figure 8.5: Time dependence of the phase fractions of the SDW, short-range and CAFM phases in $Ca_3Co_2O_6$ at 8 and 10 K. The data has been binned into 15 minute intervals, with the first measurement assigned a time of 15 minutes allowing for the fact that some time had passed before the measurement had started. The solid lines are fits to the data, described in the text.

the relaxation to equilibrium is faster than at 8 K, with a characteristic relaxation time of $\tau = 1.4 \pm 0.2$ hrs. However, at 10 K the equilibrium values of the SDW and CAFM phases are no longer comparable, and are 66.6 ± 0.6 % and 23.3 ± 0.4 % respectively. The phase fraction of the short-range component oscillates around a constant value of ∼17.4 %. It is the reduced number of short-range correlations that causes the equilibrium percentage for the SDW phase to be higher at this temperature. The diffraction patterns collected at 2 K with counting times up to 4 hours show no appreciable time dependence, and it is believed that the timescale for relaxation at this temperature is too long to feasibly measure using neutron diffraction.

8.2.2 Temperature Dependence

The time dependent evolution of the SDW to form the CAFM phase in $Ca_3Co_2O_6$ is reproducible. That is, if warmed above 12 K the peaks corresponding to the CAFM phase disappear and the peaks corresponding to the SDW phase increase in intensity and become resolution limited. The temperature dependence of the magnetic phases after the CAFM phase has been allowed to evolve at 8 K is shown in figure 8.6. The phase fraction of the CAFM phase appears to increase slightly from 15 % to 20 % between 8 and 10 K before decreasing rapidly above 10 K until it disappears at 13 K. The phase fraction of the short-range phase also decreases steadily as the temperature is increased from 8 to 13 K.

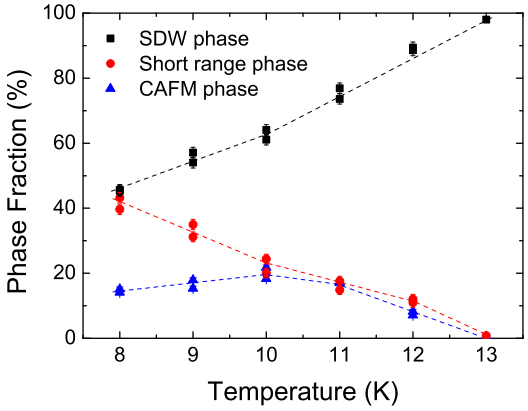

Figure 8.6: The temperature dependence of the phase fractions of the SDW, short-range and CAFM phases, after the CAFM phase has been allowed to reach equilibrium at 8 K. The dashed lines are guides to the eye.

The increased preference for the CAFM phase at the expense of the SDW phase as the temperature is decreased suggests the CAFM phase may well be the true magnetic ground state of $Ca_3Co_2O_6$. Calculations including next-neighbour super-superexchange interactions in the model for the magnetic behaviour of the compound have also shown that the CAFM phase has a lower exchange energy that the SDW phase [144], supporting this theory. Above 12 K we have shown that

the SDW phase is preferred and this is attributed to a difference in configurational entropy between the two phases. This is because the SDW phase has greater entropy, containing regions with nearly zero ordered moment, whereas in the CAFM phase every magnetic site is fully ordered. However, it is evident from the competition between the SDW and CAFM phases and the lack of a clear preference of the system towards one particular configuration as the temperature is reduced that the two phases are nearly degenerate. The incomplete nature of the magnetic transition between the two phases is attributed to defects and pinning centres such as domain walls which should have already established themselves at higher temperatures.

It has previously been noted [140, 141] that there is an anomalous dip in the intensity of the Bragg peaks corresponding to the SDW phase at temperatures below 18 K. Our measurements indicate a broadening of the peaks corresponding to the SDW phase as the temperature is reduced implying a corresponding reduction in the magnetic correlation length from 500 to 300 Å. Variations in widths of both the CAFM and SDW phases with changes in temperature implies that the interconversion process is due to an intergrowth of the magnetic phases rather than magnetic phase separation. It is believed that the peak broadening, coupled with the presence of short-range order and the emergence of the CAFM phase, fully explain the anomalous dip in intensity of the peaks belonging to the SDW which was previously not fully accounted for [141].

The measurements made on GEM also showed that it is possible to 'freeze in' the CAFM phase if the sample is rapidly cooled to 2 K after the phase has been allowed to evolve at a higher temperature such at 8 or 10 K. This history dependence will be further discussed in the next section.

8.3 History Dependent Behaviour

8.3.1 Experimental Details: The D7 Neutron Diffractometer

Measurements to study the short-range correlations and time dependence of the magnetic order were also made on the diffuse scattering polarised neutron diffractometer D7, described in section 6.3.1. As $Ca_3Co_2O_6$ is an antiferromagnet in zero field, complete polarisation analysis is possible for polycrystalline samples. A 3.6 g sample of $Ca_3Co_2O_6$ powder was enclosed in aluminium foil and then wrapped around a cylindrical aluminium insert. This was then placed inside an aluminium sample can 10 cm in length. The sample was installed in a standard orange cryostat and cooled to 35 K.

Standard vanadium, quartz and empty sample can measurements were made to calibrate the diffractometer at the two different wavelengths used for the experiment, $\lambda = 4.8$ Å and $\lambda = 3.2$ Å. The different normalised contributions to total

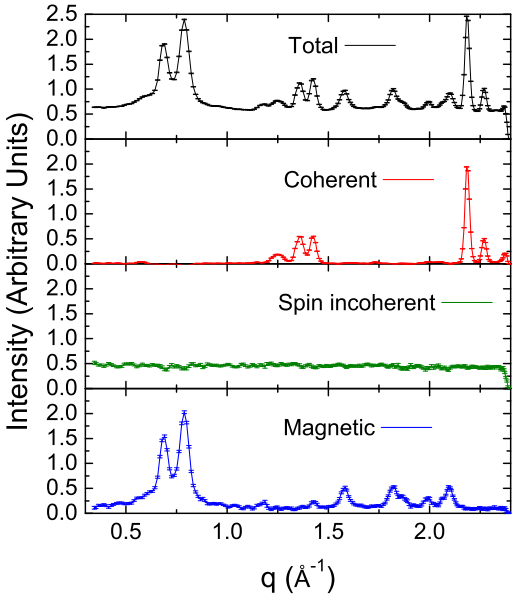

Figure 8.7: Normalised magnetic, spin incoherent and coherent (nuclear) contributions to the total scattering from $Ca_3Co_2O_6$ at 1.5 K as measured on the polarised neutron diffractometer D7.

scattering determined using the polarisation analysis on D7 are shown in figure 8.7.

The use of polarisation analysis to separate the nuclear and magnetic contributions to the total scattering showed that the CAFM phase is purely magnetic in origin, and the formation of this phase does not coincide with any structural change in the system.

8.3.2 Measurements at $\lambda = 4.8$ Å.

The sample was measured on cooling at temperatures of 30, 25, 20, 15, 10, 5 and 1.5 K, with counting times of 5 hrs per temperature. This meant the cooling rate was very slow, the equivalent of 1 K/hr if cooled continuously. These measurements made on slow cooling are shown in figure 8.8(a). Unlike the measurements made on GEM, the CAFM phase was immediately prominent in all the measurements at 10 K and below. This was attributed to the significantly longer measuring times and slower cooling rate involved in the experiment.

The slow cooled measurements were then compared with measurements made when the sample had been warmed above T_N to clear the magnetic history, then rapidly cooled to 1.5 K at the maximum cooling rate of the cryostat. The sample was then measured on warming for 4 hrs per temperature at 1.5, 5, 7.5, 10 and 15 K, shown in figure 8.8(b). The main magnetic peak of the CAFM phase, although clearly present, was much smaller at 1.5 K than when measured on slow cooling, and the measurements do not become equivalent until the sample is warmed up to 10 K.

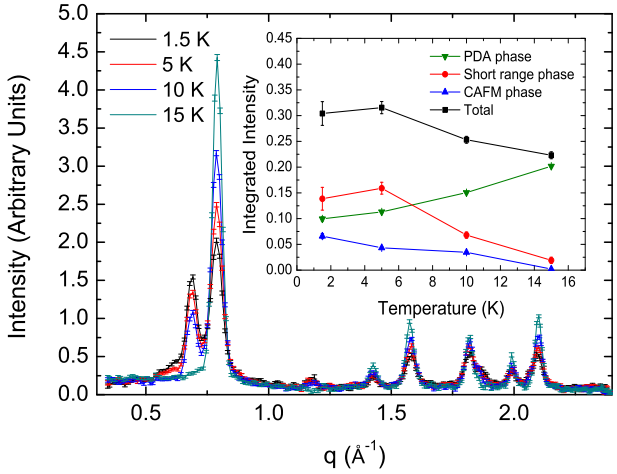

(a) Data collected on slow cooling, counting was for ∼5 hrs per temperature. Inset: Integrated intensity of the main magnetic peak as a function of temperature for the SDW, short-range and CAFM phases when slow cooled

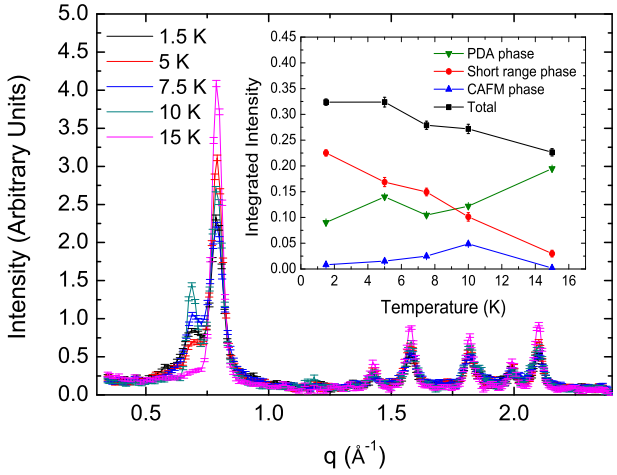

(b) Data collected on warming after rapid cooling to 1.5 K, counting was for ∼4 hrs per temperature. Inset: Integrated intensity of the main magnetic peak as a function of temperature for the SDW, short-range and CAFM phases after rapid cooling

Figure 8.8: Magnetic component of the scattering from a polycrystalline sample of $Ca_3Co_2O_6$ measured in diffraction mode on D7 with an incident wavelength of $\lambda = 4.8$ Å. The insets show the integrated intensities of the main peaks of each of the magnetic phases when slow and rapid cooled respectively. All the data has been normalised to the monitor and counting time, and the appropriate calibrations have been applied.

The main magnetic peaks of the SDW, short-range and CAFM phases have been fitted at each temperature and plotted as a function of temperature for both slow cooled and rapid cooled measurements, figures 8.8(a)(Inset) and 8.8(b)(Inset). This allows us to compare the behaviour of the two phases already discussed and the short-range order when rapid and slow cooled and so assess the contribution of the magnetic history of the sample to the magnetic order.

The fraction of short-range correlated material is far higher when rapid cooled, which is due to the fact it has not had time to form long-range order at a temperature when the energy barrier is equivalent to or less than the thermal energy of the spins. Interestingly, the relative intensities of the SDW phase when slow and rapid cooled to 1.5 K are similar, indicating that in this case the CAFM phase is forming at the expense of the short-range correlated material rather than the SDW phase. In both measurements, the fraction of material exhibiting short-range order changed between 5 and 10 K, and there were fewer short-range correlations at the higher temperature in both cases.

In the range 5 to 10 K the behaviour of the three magnetic phases is different when slow (5 hrs per temperature) and rapid (maximum rate of the cryostat) cooled. Once formed by slow cooling, the CAFM phase remains at a constant intensity. However, when rapid cooled to 1.5 K the fraction of material in the CAFM phase is very small, and then when the temperature is increased the fraction of CAFM material increases to a maximum around 10 K, as observed on GEM. The extra thermal energy available at this temperature compared to at 1.5 K means that part of the sample overcomes the energy barrier involved in forming the CAFM phase. This means that unlike the slow cooled phase, where the intensity of the peaks corresponding to the SDW phase steadily increases, there is a dip in the intensity of the peaks corresponding to the SDW phase at 7.5 K. This dip marks the point where the thermal energy available is greater than the energy barrier and the intensity of the peaks corresponding to the CAFM phase starts to increase.

The contrast in behaviour between the slow and rapid cooled measurements shows the importance of magnetic history to the study of $Ca_3Co_2O_6$. Although the dynamics are such that at intermediate temperatures (8-10 K) the CAFM phase will become apparent if left for a sufficiently long amount of time, if rapidly cooled from these temperatures its current magnetic state will become 'frozen in' as the dynamics of the system are too slow at low temperatures (2 K and below) for the relative phase fractions of the different magnetic phases to change with time.

The total scattering, defined as the sum of the areas of the main magnetic peaks of the SDW, CAFM and short-range correlated phases, follows a similar trend for both rapid and slow cooled measurements. That trend is an increase in peak intensity at temperatures between T_N and 5 K, at which point the combined in-

tensity of the three phases remains at a constant value. This is notable because it shows the presence of the CAFM and short-range correlated phases fully accounts for the drop in intensity of the SDW phase at low temperatures, giving a temperature dependence which is as we would expect for an antiferromagnetic material.

8.3.3 Measurements at $\lambda = 3.1$ Å.

Measurements were also made with an incident wavelength of $\lambda = 3.1$ Å. The shorter wavelength meant more peaks were visible in the diffraction pattern and therefore more peaks belonging to the metastable phase could be identified at higher values of q. As the sample was slow cooled in this incidence, the CAFM phase was clear at all temperatures below 10 K, reproducing the results at the longer wavelength.

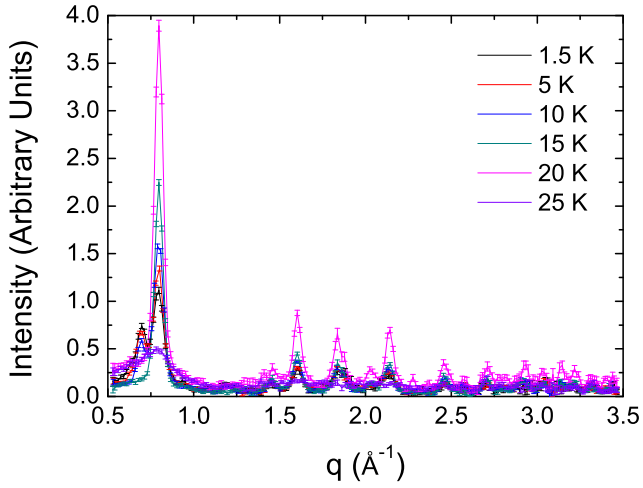

Figure 8.9: Magnetic component of the $Ca_3Co_2O_6$ data collected on the D7 polarised neutron diffractometer on slow cooling, counting was for ∼4 hrs per temperature. The incident neutron wavelength was 3.1 Å.

8.4 High Temperature Correlations

The specific heat data in zero field for $Ca_3Co_2O_6$ was measured by Hardy *et al.* and is shown in reference [132]. When the lattice component has been subtracted to give the magnetic contribution, there is a sharp lambda-like peak at T_N, which is as expected. There is also a broad maximum centered around 90 K, suggesting magnetic correlations exist above the transition temperature. Such a result would be expected in a 1D magnetic compound due to the development of magnetic correlations along the chains. This behaviour could also be due to a spin state transition but other measurements directly probing the spin states of the two cobalt sites [136]

suggest this possibility is unlikely.

These correlations were also observed on D7, and measurements were made at temperatures of 25, 30, 35, 50, 75 and 100 K (figure 8.10). At 25 K, there is a well-defined broad peak at low-q. This peak is still clearly visible in all the scans up to 75 K. By 100 K, it is much less distinct. This is a similar temperature to the maximum in the specific heat described earlier and shows the same short-range magnetic behaviour above T_N is present as suggested by the specific heat measurements. Attempts are now underway to model this behaviour using Monte-Carlo methods.

8.5 Discussion

Neutron diffraction measurements on polycrystalline $Ca_3Co_2O_6$ have shown for the first time that an unusual order-order transition between two different magnetic phases takes place in zero field over a time period of hours at temperatures between 8 and 12 K. The incommensurate SDW phase with propagation vector $k = (0, 0, 1.01)$, dominant at higher temperatures is intergrown with a commensurate antiferromagnetic (CAFM) phase with propagation vector $k = (0.5, -0.5, 1)$. This interconversion is never complete although measurements and calculations suggest this previously unreported CAFM phase is the true ground state of the system.

This magnetic transition is particularly notable because of the very slow time dynamics involved. It is well-established that the spins in $Ca_3Co_2O_6$ are Ising-like and $Ca_3Co_2O_6$ has a quasi-1D lattice, and as discussed in section 2.2.3, it is theoretically impossible for any magnetic transition to long-range order to occur in such a system as it involves flipping an infinite chain of spins. As $Ca_3Co_2O_6$ is not perfectly 1D, and the magnetic coupling is in fact helical [154], magnetic order is possible, but we can assume it has a high energy cost. In an analogy with the behaviour of the single molecule magnets, there is an Ising energy barrier which hampers reversal of an individual spin and causes the slow time dynamics.

The other time dependent magnetic behaviour observed in $Ca_3Co_2O_6$, the slow relation of the dc-magnetisation and frequency dependence of the ac-susceptibility, is likely to be part of same phenomenon discussed here. No reports currently exist of the other similar systems exhibiting the same kind of order-order transition, and this work is likely to either lead to the discovery of other materials that exhibit this behaviour or to establish that the unusual time dependent behaviour of $Ca_3Co_2O_6$ is in fact unique.

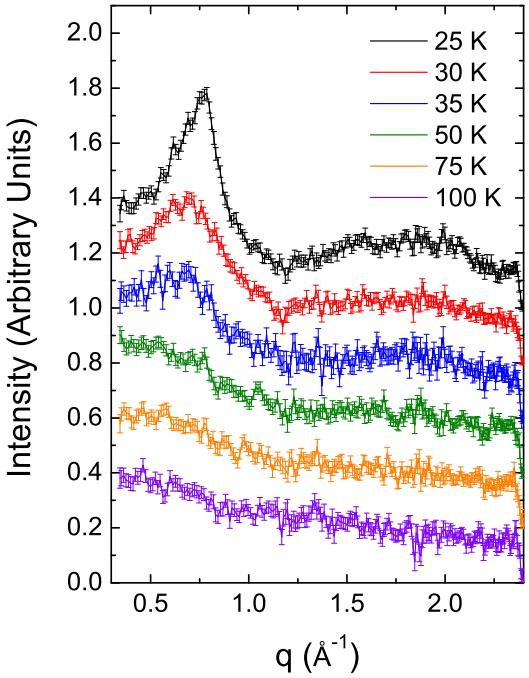

Figure 8.10: Magnetic component of the $Ca_3Co_2O_6$ powder data collected on D7 at temperatures above T_N on warming after rapid cooling to 1.5 K. Counting was for 4 hrs per temperature. The data has been offset by a value of 0.2 in intensity per temperature for the purposes clarity. The broad peak at low-q indicates short-range magnetic correlations.

Chapter 9

$Ca_3Co_2O_6$: The Effect of an Applied Magnetic Field

The effect of an applied field on the magnetic behaviour of $Ca_3Co_2O_6$ was studied using both single crystal and powder neutron diffraction. The regularly-spaced low temperature magnetisation steps were observed at the fields of 1.2, 2.4, 3.6 and 4.8 T for the first time using a microscopic probe. The ferrimagnetic order which emerges when a magnetic field is applied was probed by measuring the temperature and field dependence of the ferromagnetic and antiferromagnetic Bragg peaks associated with it. The effect of a magnetic field on the CAFM phase was also measured, and it was found that relatively large fields are necessary to stabilise the SDW phase at low temperatures once the CAFM phase has been allowed to form.

9.1 Magnetic Field Dependent Behaviour

9.1.1 Experimental Details: The GEM and D10 Neutron Diffractometers

During the same experiment on the GEM diffractometer described in section 8.1.1, measurements were made in an applied magnetic field. The same 2.9 g rod of $Ca_3Co_2O_6$ powder was used, with the vanadium sample can mounted in a 10 T vertical cryomagnet. The maximum applied magnetic field was 8 T, and the data collected in this field (detector bank 2) is shown in figure 9.1.

To study the field dependence of the magnetic behaviour of single crystals of $Ca_3Co_2O_6$, an 8 x 2 x 2 mm^3 crystal produced using a flux method was used. This crystal had been used for previous experiments, and its preparation is described in detail in reference [154]. The high quality of the crystal had previously been established using X-ray techniques and magnetic measurements. The sample was aligned by putting the crystal in slow drying glue and applying a strong magnetic

field. Due to the highly anisotropic magnetic response of $Ca_3Co_2O_6$, the crystal aligned with the c axis parallel to the direction of the applied field and the field was maintained until the glue dried and the sample was fixed in position.

The single crystal neutron diffraction measurements were carried out on the four-circle diffractometer D10 at the ILL, described in section 5.3.1. The incident wavelength used was 2.36 Å. The sample was mounted in a 6 T vertical cryomagnet, and was found to be aligned to within 1° of a magnetic field applied parallel to the c axis. The geometry of the cryomagnet limited the scattering to the $(hk0)$ plane. Measurements were made both with the standard configuration 2D 80 x 80 mm^2 area detector and with the vertically focusing pyrolytic graphite analyser and a single ^{3}He detector.

Data was collected on D10 in one of two different modes. Either by summing the intensity across a small region of the area detector containing the Bragg peak of interest while sweeping the field or temperature or by integrating scans through the peak (rocking curves varying the angle ω) at fixed values of field or temperature. All the data was normalised to the monitor time, which was 60 s/pt for sweeping mode and 20 s/pt for the ω scans.

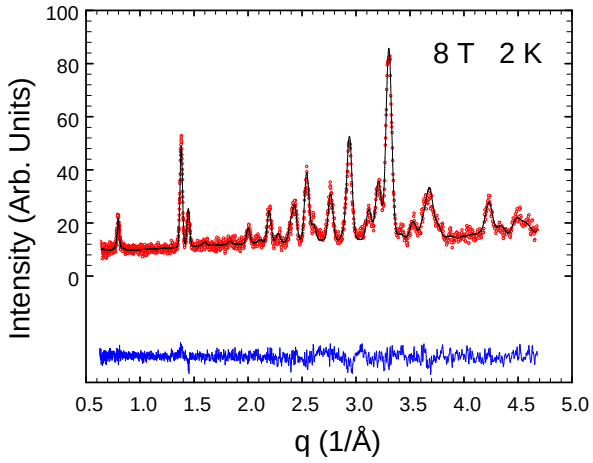

Figure 9.1: Raw data (red), refinement (black, discussed below) and difference (blue) plots of the $Ca_3Co_2O_6$ powder diffraction measurements made on GEM at a temperature of 1.5 K in an 8 T applied magnetic field. The ferromagnetic order can be clearly seen contributing to the Bragg peaks at 1.4 and 1.5 $Å^{-1}$.

9.1.2 Ferrimagnetic Behaviour

When a magnetic field is applied parallel to the c axis, $Ca_3Co_2O_6$ exhibits a slow lock-in transition from SDW to either antiferromagnetic or ferrimagnetic behaviour. The field position of this lock-in transition changes with temperature, but occurs at 0.4 T at 5 K. Early work on $Ca_3Co_2O_6$, based on powder neutron diffraction and

magnetisation measurements, suggested in the purely ferrimagnetic phase the magnetisation is equal to $M_{Sat}/3$. Theoretical descriptions of the purely ferrimagnetic phase consist of two thirds of the chains being spin up and one third being spin down [140]. The ferrimagnetic phase is commensurate, the lock-in transition marking the removal of any incommensuration associated with the SDW zero field state. Ferrimagnetic behaviour persists in magnetic fields up to 3.6 T, and at temperatures below 10 K additional steps in the magnetisation are present in the ferrimagnetic regime at 1.2 and 2.4 T.

In high magnetic fields, $Ca_3Co_2O_6$ enters a fully ferromagnetic phase [34] with a saturation magnetisation of $M_{Sat} \sim 4.8\mu_B/f.u.$ [37, 140]. From magnetisation measurements, the transition to a ferromagnetic phase occurs at 3.6 T at 10 K, but the moment is not fully saturated until $\sim$ 7 T at 2 K, although this is dependent on sweep rate [133]. The steps in the magnetisation suggest that at low temperatures there are magnetic fields where the magnetic structure does not correspond to either the SDW, ferrimagnetic or ferromagnetic structures described and adopts some intermediate antiferromagnetic or ferrimagnetic configuration [146].

In order to provide a framework to describe the magnetic field dependent behaviour of $Ca_3Co_2O_6$ a model has been developed by some of my research collaborators [156] which describes the ferrimagnetic phase as the sum of the ferromagnetic (M, M, M) and antiferromagnetic phases $(M, -M/2, -M/2)$, where the antiferromagnetic (AFM) phase is the SDW phase in zero field. Equation 9.1 gives the general description of $Ca_3Co_2O_6$ in an applied magnetic field specified by this model.

$$\mid a \mid (M, M, M) \; + \; \mid b \mid (M, -M/2, -M/2) \tag{9.1}$$

In this description, the mixing coefficients a and b have physical meanings, with a^2 = I(generic)/I(AFM) and b^2 = I(generic)/I(ferro). In the purely ferrimagnetic phase $\mid a \mid$ = M/M_{Sat} = 1/3 and $\mid b \mid$ = -4/3 and we have:

$$(-M, M, M) \; = \; 1/3 \; (M, M, M) \; - \; 4/3 \; (M, -M/2, -M/2) \tag{9.2}$$

By using this model, we therefore only need to fit the antiferromagnetic (including SDW and CAFM) and ferromagnetic phases in order to fully describe the behaviour of the system as a function of applied field. This is a convenient description for the data we have, as in powder neutron diffraction, peaks belonging to the ferrimagnetic phase appear in the same positions as the antiferromagnetic and ferromagnetic peaks.

Having established all this, it is clear that when $Ca_3Co_2O_6$ is measured in an applied magnetic field two kinds of peak will be observed corresponding to three or more magnetic phases; ferromagnetic, ferrimagnetic and antiferromagnetic.

It is not immediately obvious how to separate these phases, so the quantitative results we obtain will be presented in terms of the measured ferromagnetic and antiferromagnetic components. These will then later be qualitatively discussed in relation to the ferromagnetic, AFM and ferrimagnetic phases.

9.2 Ferromagnetic Bragg Peaks

9.2.1 Peak Shape

Both for the powder and single crystal samples, ferromagnetic peaks appear in field at positions on top of the nuclear peaks. For the single crystal, these peaks could adequately be fitted with a single Gaussian, and the (3,0,0) is shown in figure 9.2 as an example. The width of these peaks was considered to be limited by the resolution of the D10 instrument, with a typical FWHM of 0.35°. This implies that the ferromagnetic component of the ferrimagnetic phase is fully long-range ordered.

For all the ferromagnetic peaks, the nuclear component was measured in zero field and has been subtracted to give a purely ferromagnetic intensity. This analysis has been applied to the data shown in figures 9.3, 9.4 and 9.5.

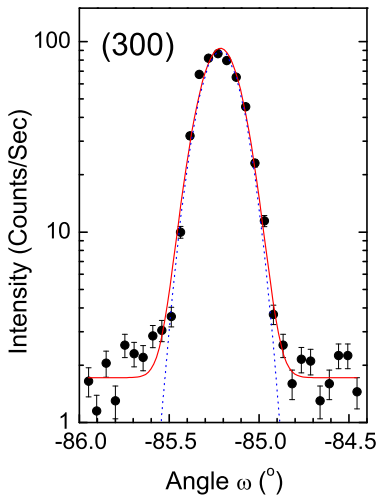

Figure 9.2: The lineshape of the ferromagnetic (3,0,0) peak measured at 2 K in zero field. The peak was fitted with a single Gaussian (blue line) and a flat background.

9.2.2 Field Dependent Magnetic Behaviour

Figure 9.3 shows the intensity of the ferromagnetic component of the (3,0,0) peak at 12 and 2 K. At 12 K, there is single step at 3.6 T marking the transition from ferrimagnetic to ferromagnetic behaviour, with little hysteresis between the measurements made with the field ramping up and the field ramping down. When cooled to 2 K a much larger hysteresis develops. This large hysteresis has previously been seen in magnetisation measurements [38]. Additional steps are distinguishable in the 2 K data, at 2.4 T and 4.8 T when the field is ramped up and steps in similar positions were also observed when the field was ramped down.

If the positions of the magnetic peaks in the (hkl) scattering plane change significantly as function of magnetic field then the method we have used of integrat-

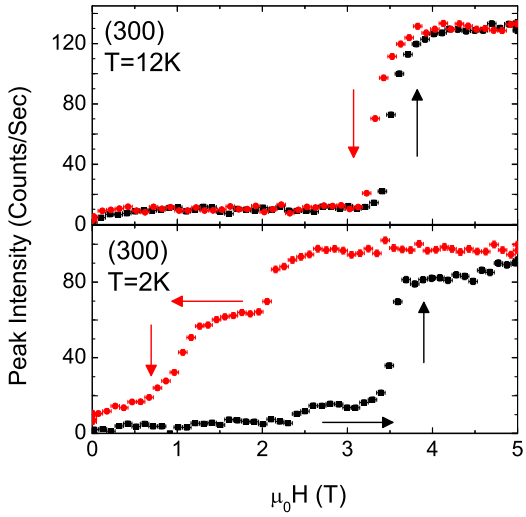

Figure 9.3: The intensity of the ferromagnetic (3,0,0) peak as a function of applied magnetic field at 12 K and 2 K. The nuclear component of the ferromagnetic peak (89 Counts/Sec) has been subtracted from both data sets. The ramp rate of magnetic field was 0.1 T/min.

ing over a constant area of the detector is not valid. In this case, integrating scans through the peak is a more accurate way of assessing the overall peak intensity. Figure 9.4 shows the results of integrating ω scans made as a function of magnetic field. One of the advantages of using this method is that the peak widths and peak positions as a function of magnetic field can also be measured. As the inset to figure 9.4 shows, the position of the centre of the ferromagnetic/nuclear peaks moves very little, with a small drift of less than 0.01° below 2.4 T becoming fixed above 2.4 T. Comparing to the measurements made using a constant detector area, the two methods of data collection are in good agreement with each other, justifying the use of the area detector and the sweeping method. This is important as the shape of the hysteresis curve in $Ca_3Co_2O_6$ is strongly dependent on measurement time and the sweeping method is a faster method of data collection than integrating the peak intensity at each point.

Figure 9.4 shows both the integrated ω scans made on D10 at 2 K and a magnetisation curve taken at the same temperature [156], with the positions of the steps marked by blue dashed lines. The equally-spaced steps in intensity of the ferromagnetic peak match well with those seen in magnetisation measurements, with clear steps observed at 2.4, 3.6 and 4.8 T, and a likely feature at 1.2 T. The observed increase in the intensity of the ferromagnetic peaks close to 0 T is relatively small. However, given the fact that the magnetic intensity of the ferromagnetic peaks is proportional to the magnetisation squared, equation 3.6, the agreement between the

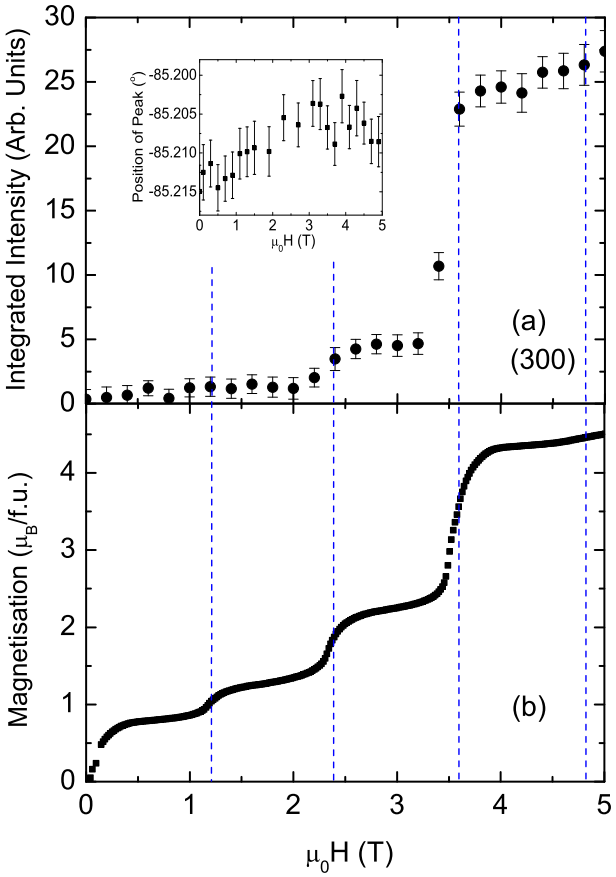

Figure 9.4: Panel (a) shows the integrated intensity of the ferromagnetic (3,0,0) peak at a temperature of 2 K as a function of applied magnetic field. These data were taken after zero field cooling. The nuclear component of the FM peak (equating to 24.9 in the units of integrated intensity used in the figure) has been subtracted. The inset to this figure shows the position of this nuclear/magnetic peak as a function of applied field. Panel (b) shows magnetisation data as a function of applied field for a single crystal of $Ca_3Co_2O_6$ aligned with the field along the c axis. These data are presented for comparison purposes and are not my own work [156]. The blue dashed lines indicate the positions of the magnetisation steps, and show that the positions of the steps, where they could be observed, are the same for both measurements.

neutron data and the magnetisation curve shown in figure 9.4 is quantitatively good.

9.2.3 Temperature and History Dependent Behaviour

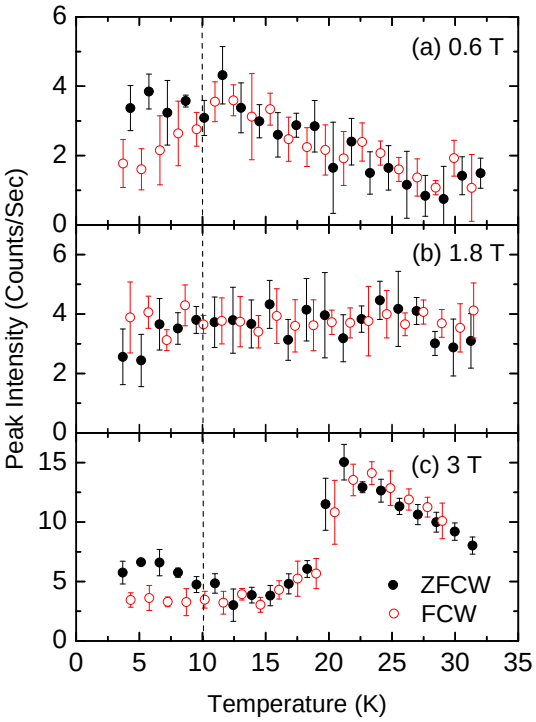

Figure 9.5: Temperature dependence of the intensity of the ferromagnetic (3,0,0) peak measured in three different fields, 0.6, 1.8 and 3 T. The data taken while warming the sample in field after zero field cooling (ZFCW) is shown in black and the red symbols show the data taken in field while increasing the temperature after field cooling (FCW). An irreversibility temperature is visible at around 10 K, where the intensities of the ZFCW and FCW measurements diverge, marked by a dashed line on the figure. The temperature ramp rate was 0.3 K/min.

The intensities of the ferromagnetic peaks were also measured in magnetic fields of 0.6, 1.8 and 3 T as a function of temperature. These fields were chosen as they are the mid-points on the plateaux seen in the bulk magnetisation curve. The results are shown in figure 9.5. In addition to the apparent transition to the paramagnetic state at 20 K in a magnetic field of 3 T (figure 9.5(c)) another notable feature is the presence of an irreversibility temperature around 10 K. Below this temperature there is a pronounced difference between the zero field cooled and field cooled data for the 0.6 and 3 T measurements, while in the intermediate field of 1.8 T the difference is very slight. There is also a crossover in the the zero field cooled and field cooled data at 1.8 T, as at this point the field cooled data has greater magnitude than the zero field cooled data at 2 K, whereas at 0.6 and 3 T the opposite is true. This observation should be linked to the magnetisation relaxation measurements [38], which revealed that at lower temperatures the magnetisation of $Ca_3Co_2O_6$ has a pronounced time dependence and that the magnetisation could relax up or down depending on the value of the applied field.

9.3 Antiferromagnetic Bragg Peaks

9.3.1 Peak Shape

The antiferromagnetic peaks, such as (1,0,0), can be best fitted with a combination of a Gaussian and a Lorentzian peak. The Gaussian (FWHM of 0.37°) is resolution limited, as were the ferromagnetic and nuclear peaks, while the Lorentzian component is indicative of the presence of magnetic disorder (figure 9.6(a)). This observation is in agreement with the previously reported coexistance of short-range magnetic correlations with the long-range magnetic order in zero field at 5 K [154]. The observed full width at half maximum (FWHM) of the Lorentzian component (typically 1.9°) allows us to estimate the magnetic correlation length using equation 9.3.

$$D(\text{Å}) = \frac{2\pi}{\text{FWHM(Å)}} \tag{9.3}$$

Using this formula, the magnetic correlation length was found to be $D = 250$ Å. This value is in reasonably good agreement with the previously reported values ($D = 180$ Å was obtained in ref [154]). It is possible that this small difference is due to the truncation of the data in the earlier measurement, where typically the

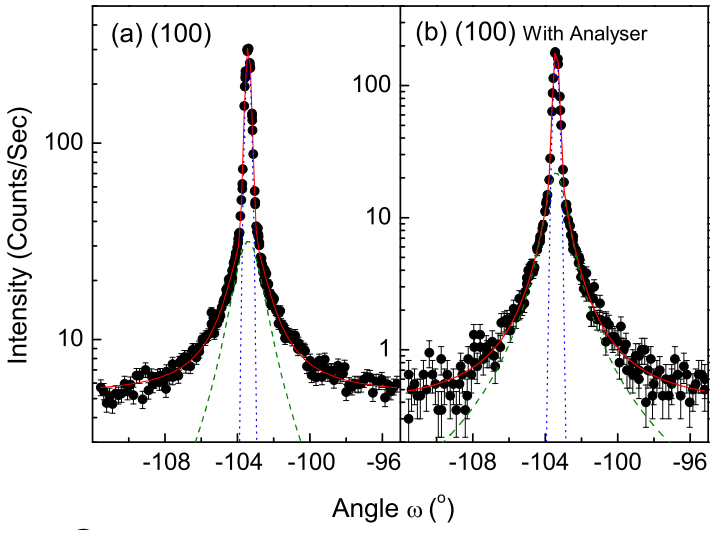

Figure 9.6: Examples of the lineshapes of the antiferromagnetic (1,0,0) peak measured at 2 K and in zero field. The profiles shown in panels (a) and (b) were obtained without and with the use of a vertically focusing PG analyser respectively. Solid lines are the fits consisting of two components, a main resolution limited Gaussian component (blue dotted line) and a broad Lorentzian component (green dashed line) as well as a flat background.

scans were much shorted than the 20° rocking curves shown in figure 9.6.

The (1,0,0) peak was also measured using the pyrolytic graphite energy analyser available on D10, with a typical peak profile shown in figure 9.6(b). Apart from a narrowing of the Gaussian component due to the improved resolution down to 0.34° and a significant reduction in the background (from 5.3 to 0.4 counts per second) the shape of the peak remained largely unchanged. The ratio of the areas of the Lorentzian to the Gaussian components of the peak measured with and without the analyser are 0.7 and 0.9 respectively. This observation might suggest that the magnetic disorder is at least partially dynamic in nature. However, to draw any firm conclusions regarding the presence of magnetic excitations in $Ca_3Co_2O_6$ and their influence on the short-range magnetic correlations, much more systematic measurements with greatly improved energy resolution are required.

9.3.2 Field Dependent Magnetic Behaviour

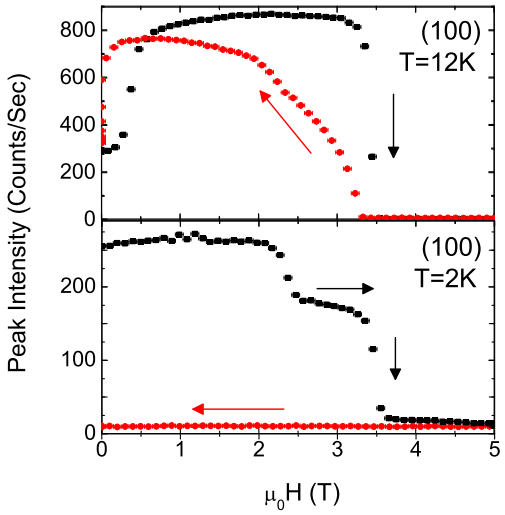

Figure 9.7: The intensity of the antiferromagnetic (1,0,0) peak as a function of applied magnetic field at 12 and 2 K. The ramp rate of magnetic field was 0.1 T/min.

Figure 9.7 shows that clear steps in the intensity of the antiferromagnetic peak were observed at 2.4 T and 3.6 T, and a possible feature was also seen at 1.2 T. At 2 K, there is a small but distinctly nonzero intensity for the antiferromagnetic reflection even above the transition at 3.6 T. This is because the field value is sufficient to fully polarise the system only at higher temperatures, while at 2 K a much higher field is required. Figure 9.8 also shows that the step-like behaviour is observed for both the Gaussian and the Lorentzian components of the antiferromagnetic peak. Therefore it has been shown that the application of a magnetic field affects both the long-range antiferromagnetic order and the short-range antiferromagnetic correlations in $Ca_3Co_2O_6$.

Figure 9.7 also shows that the steps at 1.2 and 2.4 T are not associated with a redistribution of intensity between the Gaussian and Lorentzian components, establishing that the degree of antiferromagnetic disorder does not change at these fields.

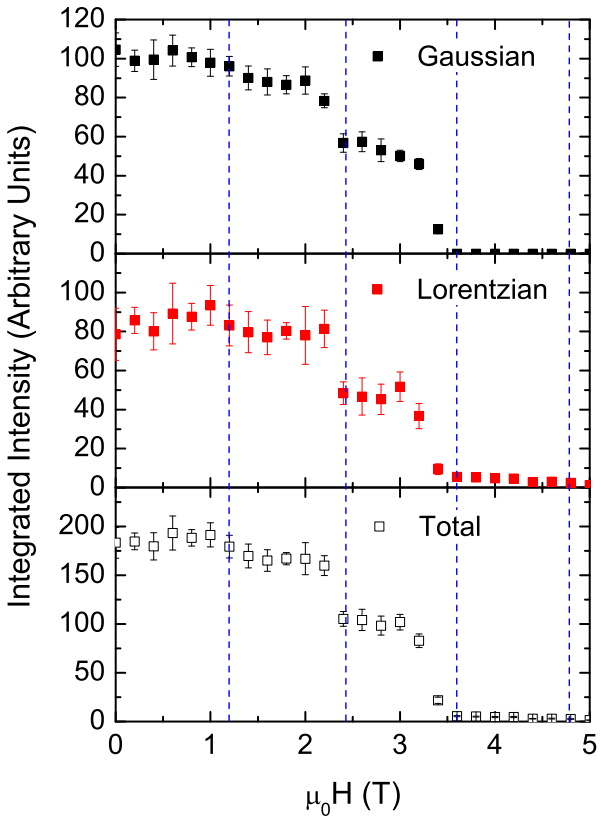

Figure 9.8: Integrated intensity of the antiferromagnetic (1,0,0) reflection split into Gaussian and Lorentzian components as a function of increasing applied magnetic field. The blue dashed lines are drawn at fields of 1.2, 2.4, 3.6 and 4.8 T to highlight the positions of the magnetisation steps. All the data were taken at a temperature of 2 K.

Significantly, the Lorentzian component of the antiferromagnetic peak continues to have some intensity above 3.6 T, commonly believed to be the critical field at which there is a transition to the ferromagnetic state. The widths of both components of the antiferromagnetic peak are found to be field independent until the transition at 3.6 T above which the width becomes resolution limited.

The most significant feature observed at base temperature is that the intensity of the antiferromagnetic reflection is very weak (nearly zero) for decreasing magnetic fields. Therefore at 2 K the zero-field cooled magnetic state of $Ca_3Co_2O_6$ is completely different from the magnetic state after the application and subsequent removal of an external magnetic field. This observation is only possible with a microscopic magnetic probe such as neutrons while all the previous bulk properties measurements have failed to note such a difference in the magnetic state after the application and removal of a magnetic field. In order to restore the intensity of the antiferromagnetic peaks the sample has to be warmed up to 30 K and then cooled in zero field.

Unlike the ferromagnetic peaks, the intensity of the (1,0,0) antiferromagnetic peak also shows significant hysteresis at 12 K in a wide range of applied fields (see figure 9.7). At this temperature there is also a rapid change in the intensity of the antiferromagnetic reflection near zero field for the data taken in both ascending and descending magnetic fields, while at 2 K the intensity of this peak does not change appreciably on the application of a magnetic field. The intensity curve for the antiferromagnetic reflection taken while decreasing the field at 12 K suggests a transition at 2.4 T, which in magnetisation measurements [38] is visible at temperatures up to 10 K [133].

9.3.3 Temperature and History Dependent Behaviour

Investigations in 2008 [154] suggested that the origin of the anomalous dip in the intensity of the antiferromagnetic peaks at low temperatures is due to an increase in the fraction of short-range correlated material at the expense of the fraction of long-range ordered material. We have repeated the zero field measurements reported in reference [154] in a field of 0.6 T, the results of which are shown in figure 9.9. For a zero field cooled sample at base temperature, the antiferromagnetic order has both Gaussian and Lorentzian components, indicating a range of correlation lengths. On warming, the intensity of both components initially increases. There is a sharp dip in the integrated intensity of the Gaussian component at 8 K, which coincides with a maximum in the integrated intensity of the Lorentzian component. Above this temperature the Gaussian component continues to grow while the Lorentzian component diminishes rapidly. The sharp decrease of the Gaussian component at 8 K indicates that some additional restructuring of the antiferromagnetic order is

taking place at this temperature.

For a field cooled sample the peak shape can be fitted with a single Gaussian indicating the short-range magnetic component is absent. At 2 K, the overall intensity of the field cooled data collected in 0.6 T is higher that the zero field cooled data at the same temperature. The total intensity of the antiferromagnetic (1,0,0) peak for the field cooled sample decreases monotonically as the temperature is increased and the zero field cooled and field cooled data sets crossover around 5 K before coming together again at temperatures close to T_N.

Similar measurements made in fields of 1.8 T and 3 T gave comparable results for the behaviour of the short-range and long-range components of the antiferromagnetic order in $Ca_3Co_2O_6$, and are also shown in figure 9.9.

9.4 Powder Measurements

9.4.1 Ferromagnetic Phase

All the measurements made on single crystals were made with the magnetic field directed along the c axis. It is generally acknowledged that the measured behaviour of $Ca_3Co_2O_6$ powder in a magnetic field also reflects the magnetic ordering along the c axis due to the Ising nature of the spins, and many of the same features as detailed in the previous two sections have been observed using powder diffraction.

As with the single crystal measurements, in an applied magnetic field ferromagnetic peaks appear on top of the nuclear peaks. This ferromagnetic component can be refined as a function of applied field and is shown in figure 9.10, along with the antiferromagnetic (AFM) and short-range antiferromagnetic phases, where the AFM phase is either commensurate or incommensurate depending on the applied field. These measurements were made at 2 K, and the commensurate antiferromagnetic (CAFM) phase has not been allowed to develop, meaning its contribution to the refinement was negligible. This figure should be compared to figures 9.3 and 9.4. Although not enough data points were collected to make the steps immediately apparent (this would be difficult anyway using powder diffraction without an extremely high density of points), the hysteresis loop associated with the ferromagnetic component is broad at this temperature, as observed with single crystals. There are large changes in intensity between 3 and 4 T on field increasing and between 2 and 3 T on field decreasing, which are likely to be associated with the stepped magnetic behaviour.

In contrast to the single crystal measurements there is a substantial difference between the zero-field cooled and field cooled measurements in fields of 5 T for all three components of the magnetic order. At this field strength the single crystal measurements show the moment to be saturated with a value $M_{Sat} = 5.1\ \mu_B/f.u.$

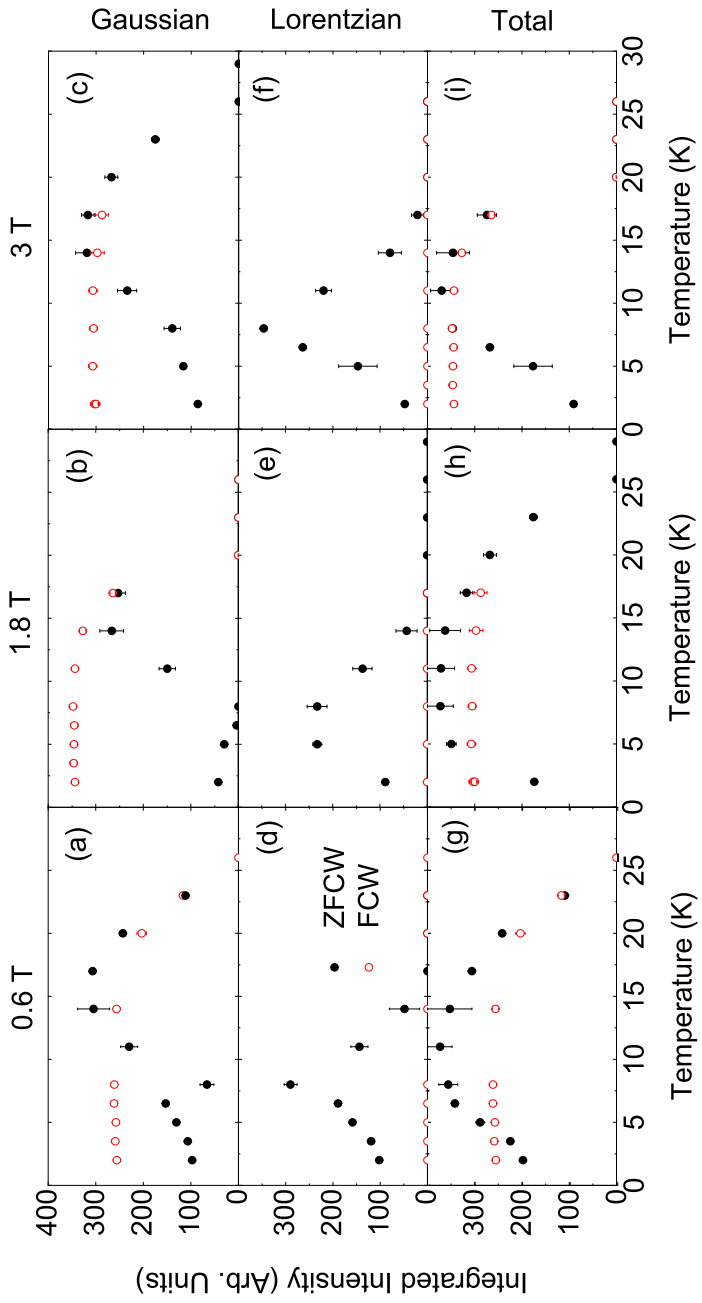

Figure 9.9: The temperature dependence of the Gaussian and the Lorentzian components as well as of the total integrated intensity of the antiferromagnetic (1,0,0) peak in fields of 0.6, 1.8 and 3 T. The black symbols show the data taken while warming the sample in field after zero field cooling (ZFCW) and the red symbols show the data taken in field while increasing the temperature after field cooling (FCW).

The fact the magnetic moment does not saturate at 2 K until fields nearly twice the saturation field at 10 K (3.6 T) was also observed in the equivalent magnetisation measurements [133]. The interactions in the *ab* plane of $Ca_3Co_2O_6$ are well known to be antiferromagnetic, which is likely to be the major contribution to the substantial antiferromagnetic intensity recorded in fields above 3.6 T.

The results displayed in figure 9.10 show that the overall ordering scheme is ferrimagnetic at 2 K in all but the lowest fields as there are both antiferromagnetic and ferromagnetic contributions to magnetic order across almost all of the measured range at this temperature. Considering the substantial hysteresis we measure for both the ferromagnetic and antiferromagnetic components, it implies the ferrimagnetic phase is hysteretic up to fields of around 7 T. These results and the results presented earlier in the chapter show that at these temperatures the steps at 0 and 3.6 T do not mark the transitions to ferrimagnetic and ferromagnetic behaviour respectively in powder or single crystals, as they do at 10 K and as had been suggested by some previous interpretations.

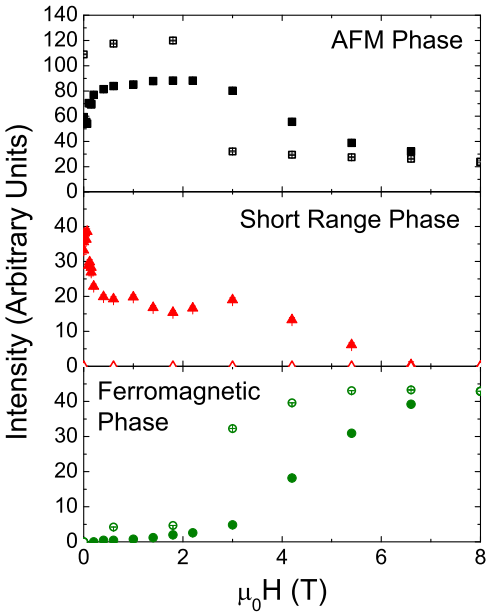

Figure 9.10: The refined intensity of the main magnetic phases in $Ca_3Co_2O_6$ powder as a function of applied magnetic field. The data was all taken at a temperature of 2 K. The closed symbols show the data taken on zero field cooled warming and the open symbols show the data taken on field cooled cooling.

9.4.2 Antiferromagnetic Phase

The refined intensities of the AFM and short-range phases are also shown in the figure. The behaviour of both components matches that observed in single crystals across the majority of the field range measured. However, at the lowest fields there is a clear difference. The step at 0 T seen in the magnetisation measurements, while clearly absent in the single crystal data (figure 9.8), is seen in the AFM component of the powder diffraction refinement. This sharp increase in intensity of the AFM phase is matched by an equivalent reduction in the fraction of material exhibiting short-range order. This provides evidence that the origin of the first step at 0 T is not the same as the rest of the steps in $Ca_3Co_2O_6$. We suggest this step

is due to a fraction of the magnetically disordered material becoming long-range ordered on the application of a magnetic field. Furthermore, the fact this is only observed in the powder data suggests this ordering may well be associated with the presence of magnetic domains.

Refinement of the powder data means the effect of a magnetic field on the spin density wave in $Ca_3Co_2O_6$ can also be measured, though neutron diffraction is not the most precise technique for doing so as the results are limited by the resolution of the GEM instrument. The results of the analysis are shown in figure 9.11. They suggest the incommensuration is still present in low fields, becoming completely commensurate in fields above 2 T at a temperature of 2 K. This lock-in transition from SDW to commensurate antiferromagnetic behaviour is know to vary with temperature, and has been studied in further detail by other researchers using resonant X-ray scattering [157].

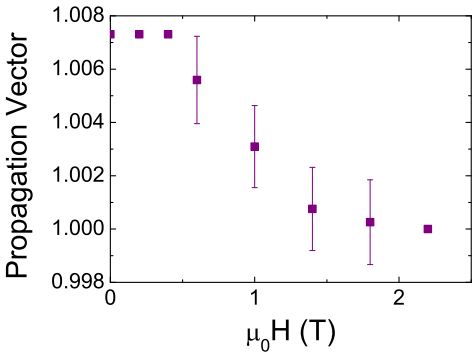

Figure 9.11: The incommensuration along the c axis in $Ca_3Co_2O_6$ as a function of applied magnetic field. The data was collected at a temperature of 2 K by refining powder neutron diffraction data.

9.4.3 Commensurate Antiferromagnetic Phase

The effect of the application of a magnetic field on the time dependent commensurate antiferromagnetic (CAFM) phase has also been studied. Figure 9.12 shows intensity of the AFM, short-range and ferromagnetic phases as function of magnetic field at four different temperatures, 10, 8, 5 and 1.5 K. To collect this data, the sample was cooled to 2 K, allowing the AFM phase to form, and thermalised for 10 minutes. In each case the sample was then warmed to 10 K and held for 2 hours to allow the CAFM phase to develop before quenching to the required temperature, a procedure which meant the CAFM phase could be 'frozen in' before a magnetic field was applied.

The measurements made at 1.5 K, which were made with a 1 hour counting time per field, show a different behaviour to the data taken at 5, 8 and 10 K. At the higher temperatures, the CAFM phase is reduced in intensity on the application of a magnetic field, causing a consequent increase in the AFM phase. At 1.5 K however, both the AFM and CAFM phases gradually reduce in intensity as the field

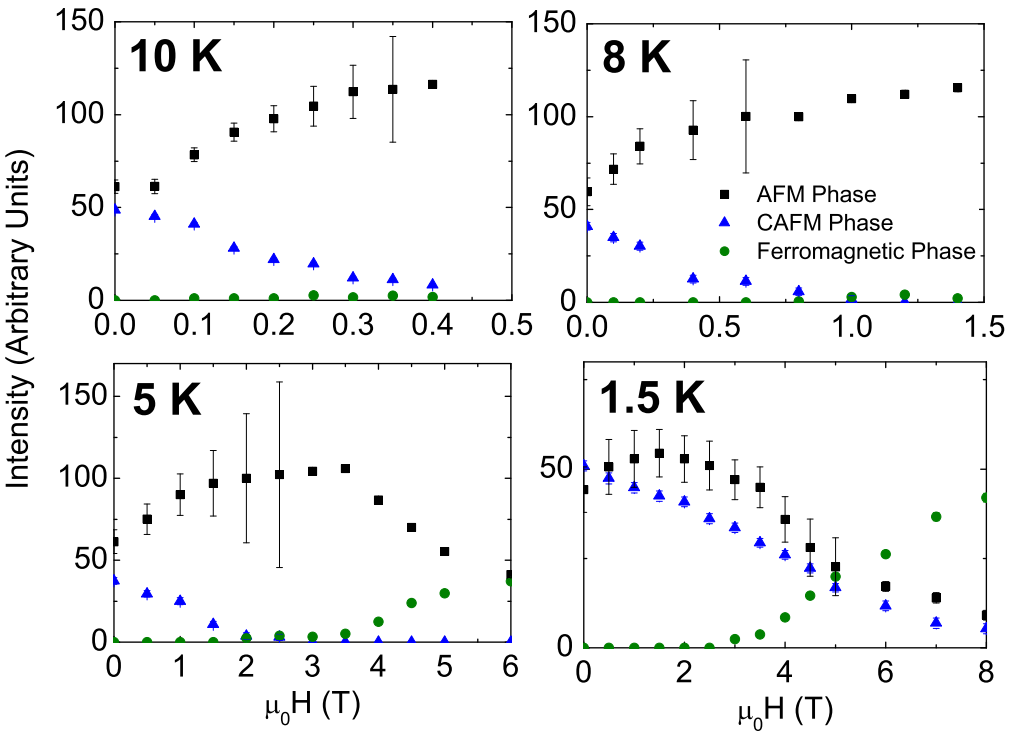

Figure 9.12: The refined intensity of the magnetic phases in $Ca_3Co_2O_6$ powder as a function of applied magnetic field. The measurements were made after the CAFM phase had been allowed to form for 2 hours at 10 K and quenched to the required temperature.

is increased, and this is balanced by an increase in the ferromagnetic phase above 3 T. At 8 T, both the AFM and CAFM phases still have some remaining intensity at 1.5 K. This increased robustness can be explained due to the slower spin dynamics at low temperatures, and gives valuable information towards a H-T phase diagram for $Ca_3Co_2O_6$.

9.5 Discussion

The stepped magnetisation behaviour in $Ca_3Co_2O_6$ has sparked intense interest from researchers in this material. Our neutron scattering study on single crystals has measured these steps for the first time using a microscopic probe and detailed measurements have been made of the field and temperature dependence of the magnetic order. The discovery of an additional antiferromagnetic ordering scheme (the CAFM phase) implies the origin of these steps in the magnetisation must be reassessed to include this behaviour and favours an interpretation in terms of an evolution of metastable states to a quantum tunnelling of the magnetisation. Measurement of the CAFM phase in single crystals is necessary to assess whether the stepped magnetic order can be observed for this phase, and to study its role in their development.

The magnetic behaviour of $Ca_3Co_2O_6$ powder as a function of applied magnetic field has also been studied. The results suggest the presence of domains in zero field and have shown that the high temperature AFM phase is stablised by a magnetic field. However at 1.5 K, the CAFM phase is surprisingly robust, and decreases in line with the AFM phase as the amount of ferromagnetic order increases, supporting the interpretation that this is the true magnetic ground state of the compound.

Part IV

Conclusions

Chapter 10

Conclusions

The cobaltates $Y_{1-x}Sr_xCoO_{3-\delta}$ and $Ca_3Co_2O_6$ are both compounds which exhibit complex magnetic behaviour and where the crystal structure strongly influences the magnetic ordering. Both materials are bulk antiferromagnets, with $Y_{1-x}Sr_xCoO_{3-\delta}$ displaying a weak ferromagnetic-like magnetisation signal due to the unequal sizes of the magnetic moments on different sites and $Ca_3Co_2O_6$ becoming ferrimagnetic on the application of a magnetic field. In zero field, $Ca_3Co_2O_6$ has a spin density wave structure and coexistent long-range and short-range magnetic order. By explaining the observed magnetic behaviour in these compounds a broader understanding of physics of this whole class of materials should be achieved, potentially assisting in the development of their applications in solid state devices. Furthermore, it is hoped studying these materials will lead to the development of new physics to explain the phenomena observed. This thesis has detailed measurements of the structural and magnetic properties of these two compounds and their magnetic behaviour as a function of temperature and applied magnetic field.

Prior to the start of the work described in this thesis, only a single brief report existed on either the growth or properties of single crystals of $Y_{1-x}Sr_xCoO_{3-\delta}$. This led us to develop a method of growing single crystals of $Y_{1-x}Sr_xCoO_{3-\delta}$ ($0.7 \leq x \leq 0.95$) using floating zone technique, and the ratio of the atoms on the A-site of the perovskite crystal structure and the oxygen content δ were characterised using EDAX and TGA respectively. A single crystal with chemical formula $Y_{0.15}Sr_{0.85}CoO_{2.63}$ was subjected to a detailed study using X-ray and neutron scattering. Structurally ordered, disordered and partially-ordered powders of $Y_{0.15}Sr_{0.85}CoO_{3-\delta}$ were also studied to obtain a more complete picture of the structural and magnetic behaviour of this compound, and neutron diffraction showed that the different crystal structures of the three powders leads to three very different magnetic ordering schemes.

The X-ray and neutron diffraction measurements on $Y_{0.15}Sr_{0.85}CoO_{3-\delta}$ single crystals have identified a complex superstructure with peaks at $(0.25, 0.25, 0)$

and symmetry equivalent positions in the $I4/mmm$ parent structure indicating a 8-times modulation in the ab plane at low temperatures. This superstructure could not be solved $ab-initio$, but has been refined in both the $I4/mmm$ and $Cmma$ unit cells, showing the results agree with previous interpretations. Evidence of structural transitions at 370 K, involving a doubling of the unit cell in the ab plane due to orbital ordering, and at 280 K, which appears to be a displacive-type structural transition, has also been observed. The diffraction measurements also indicate that in $Y_{0.15}Sr_{0.85}CoO_{3-\delta}$ single crystals the structural and magnetic transitions at 370 K coincide, in contrast to published data on polycrystalline samples [24]. This supports the conclusion drawn from recent resonant X-ray scattering work [45] that the ferrimagnetic ordering in $Y_{1-x}Sr_xCoO_{3-\delta}$ is instigated by the orbital ordering of the orbitally degenerate intermediate-spin cobalt ions.

The magnetic ordering in $Y_{1-x}Sr_xCoO_{3-\delta}$ has been shown to be ferrimagnetic, with moments of different magnitudes on the four, five and six-fold coordinated cobalt sites. However, the macroscopic magnetisation has been found to be isotropic, with the remnant ferromagnetic moment not constrained to any particular lattice direction. Antiferromagnetic Bragg peaks appear below T_c at positions symmetric with $(0.5, 0.5, 0)$ in the $I4/mmm$ unit cell. There is also a transition in the magnetic behaviour associated with the structural transition at 280 K, evident from the dc and ac-susceptibility measurements, whose origin is unclear. Powder diffraction measurements suggest this may be due to domain effects above this temperature, but equally a change in the magnetic moment on one of the cobalt sites such as a spin state transition would account for the coexistance of a structural transition and the observed change in the magnetisation. Above the transition at 370 K, polarised and inelastic neutron scattering measurements found evidence of anisotropic magnetic fluctuations. The structural and magnetic behaviour of $Y_{0.15}Sr_{0.85}CoO_{3-\delta}$ single crystals as a function of temperature is summarised in figure 10.1.

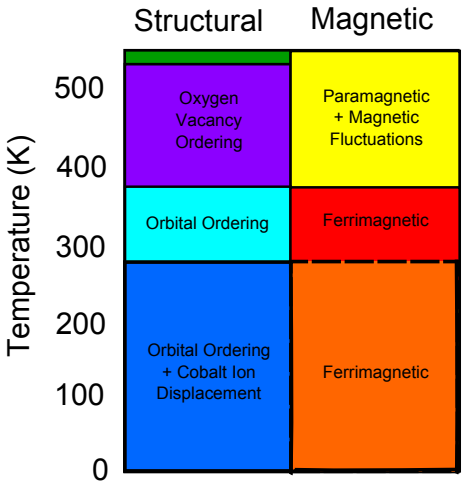

Figure 10.1: The structural and magnetic behaviour of $Y_{0.15}Sr_{0.85}CoO_{3-\delta}$ single crystals as a function of temperature.

$Y_{1-x}Sr_xCoO_{3-\delta}$ is a member of a class of doped strontium cobaltates $Ln_{1-x}Sr_xCoO_{3-\delta}$ (Ln = Y, Ho, Er, Ce, Eu, Gd, and Dy), many of which are known to have the same weak ferromagnetic-like signal in the magnetisation observed for $Y_{1-x}Sr_xCoO_{3-\delta}$.

It is quite possible that the source of the ferromagnetic signal in some of these materials is the same underlying ferrimagnetic ordering of the cobalt moments found in $Y_{1-x}Sr_xCoO_{3-\delta}$, although further investigation is required. Certainly, the behaviour of $Y_{1-x}Sr_xCoO_{3-\delta}$ seems quite different to that of the well-studied compound $La_{1-x}Sr_xCoO_{3-\delta}$ which is an intrinsically phase-separated material with ferromagnetic clusters in an antiferromagnetic matrix.

$Ca_3Co_2O_6$ is a low-dimensional material consisting of ferromagnetic spin-chains along the c axis of the unit cell which are antiferromagnetically coupled in the ab plane. In zero magnetic field, the magnetic structure of $Ca_3Co_2O_6$ is incommensurate with propagation vector $(0, 0, 1.01)$, implying a spin density wave (SDW) propagating along the c axis of the unit cell. The interactions in the ab plane are geometrically frustrated, so a complex magnetic ground state is expected. Neutron diffraction measurements detailed in this thesis have shown the different interactions in this system result in a time dependent magnetic transition from one ordered antiferromagnetic state to another with a different propagation vector, determined to be $(0.5, -0.5, 1)$. Entropy and exchange energy calculations [144] have suggested this new magnetic state is the true ground magnetic state of the material. This time dependent magnetic transition occurs over a timescale of hours and is never complete.

Neutron diffraction was also used to measure the magnetic order in $Ca_3Co_2O_6$ as a function of applied magnetic field. Regularly-spaced steps in the intensity of both the ferromagnetic and antiferromagnetic Bragg peaks were observed for the first time in this material using a microscopic probe. The stepped magnetisation as a function of applied field was also observed for the short-range component of the magnetic order. It is likely that these steps in the magnetisation of $Ca_3Co_2O_6$ are related to the time dependent antiferromagnetic behaviour. Prior to this research, the steps had been discussed in terms of either a quantum tunnelling of the magnetisation or the evolution of metastable states. The observation of such a metastable state favours the latter interpretation.

The measurements presented in this thesis of the magnetic behaviour of $Ca_3Co_2O_6$ as a function of applied magnetic field are summarised in the form of a magnetic phase diagram in figure 10.2. The red data points indicate the temperature of the magnetic transition to antiferromagnetic behaviour, T_N, in different fields. The blue data points indicate the magnetic field at which the SDW antiferromagnetic state is stabilised at the expense of the time dependent antiferromagnetic phase. The orange data points indicate the position of the lock-in transition from incommensurate to commensurate antiferromagnetic behaviour; these measurements were made by other researchers and are not described in this thesis [157]. The magnetisation steps as a function of applied magnetic field are also marked on the figure

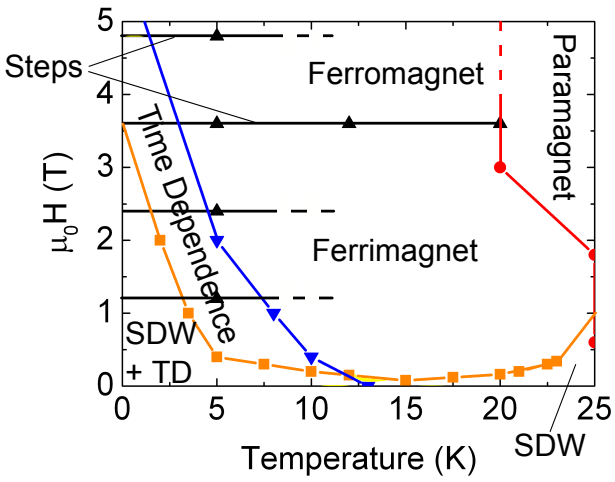

Figure 10.2: Magnetic phase diagram for the compound $Ca_3Co_2O_6$. The data points indicate transitions established from measurements described in this thesis [157]. The steps in the magnetisation as a function of applied magnetic field are marked by lines at low temperatures.

with black data points.

The magnetic properties of $Ca_3Co_2O_6$ should be compared to similar systems. There are relatively few examples of systems of 1D spin chains on a triangular lattice. The most important examples are those belonging to the same A'$_3$ABO$_6$ (A$'$ = Ca, A = Co and B = Co, Ni, Ru, Ir or Rh) class of materials or the ABX$_3$ (A = Cs or Rb, B = Co and X = Cl or Br) family of hexagonal magnets [158]. It has been suggested that the compounds $Ca_3Co_2O_6$ and Ca_3CoRhO_6 have similar phase diagrams [132]. For example, like early reports on $Ca_3Co_2O_6$, it has been suggested Ca_3CoRhO_6 also has a region of glassy behaviour at temperatures well below T_N. Recent work has also suggested $Sr_3Co_2O_6$ is an isostructural compound to $Ca_3Co_2O_6$, and this material also exhibits stepped magnetisation behaviour as a function of applied magnetic field which shows remarkable agreement with that observed in $Ca_3Co_2O_6$ [159]. It is likely the mechanism for this behaviour is the similar in both materials, and further investigation is required in this area.

The presence of charge, orbital and spin state degrees of freedom in the cobaltates means they often display complex phases diagrams containing several magnetic phases. $Y_{1-x}Sr_xCoO_{3-\delta}$ and $Ca_3Co_2O_6$ are good examples of this, with oxygen vacancy and orbital ordering in $Y_{1-x}Sr_xCoO_{3-\delta}$ leading to a complex ferrimagnetic state and geometrical frustration in $Ca_3Co_2O_6$ leading to unusual time dependent magnetic behaviour. In order to further our understanding of the magnetic order in $Y_{1-x}Sr_xCoO_{3-\delta}$ the crystal structure in the low-temperature state now needs to be solved so that a more accurate magnetic structure can be obtained. Further research

is also needed into the nature of the magnetic transition at 280 K to acquire a more complete understanding of the magnetic behaviour of this material.

Following the discovery of a time dependent magnetic transition in polycrystalline samples of $Ca_3Co_2O_6$ it desirable to carry out similar measurements of single crystals of $Ca_3Co_2O_6$ to understand this behaviour in more detail. It is hoped that such measurements will establish a comprehensive magnetic phase diagram for this compound. Finally, the discovery of a magnetic order-order transition in $Ca_3Co_2O_6$ is likely to lead to researchers searching for similar behaviour in other low-dimensional materials.

Appendix A

Refined Wyckoff positions of the $Y_{0.15}Sr_{0.85}CoO_{3-\delta}$ powders

Tables A.1, A.2 and A.3 give details of the refined crystal structures of the AD/OD, AD/OO and AO/OO forms of $Y_{0.15}Sr_{0.85}CoO_{3-\delta}$. They are based on the structural models of a simple perovskite, brownmillerite [85] and the oxygen vacancy ordered form of $Y_{1-x}Sr_xCoO_{3-\delta}$ [83] for the AD/OD, AD/OO and AO/OO compounds respectively.

Atom	Site	x	y	z	B	Occ.
Sr1	1a	0	0	0	0.5(2)	0.85
Y1	1a	0	0	0	0.5(2)	0.15
Co1	1b	0.5	0.5	0.5	0.5(2)	1.0
O1	3c	0.5	0	0.5	0.5(2)	0.9(1)

Table A.1: Refined structural parameters for AD/OD $Y_{0.15}Sr_{0.85}CoO_{3-\delta}$ powder in space group $Pm\bar{3}m$.

Atom	Site	x	y	z	B	Occ.
Sr1	8c	0.1099(7)	0.013(6)	0.53(6)	0.7(3)	0.85
Y1	8c	0.1099(7)	0.013(6)	0.53(6)	0.7(3)	0.15
Co1	4a	0	0	0	0.7(3)	1.0
Co2	4b	0.25	0.910(4)	-0.01(4)	0.7(3)	1.0
O1	8c	0.994(1)	0.25(1)	0.27(5)	0.7(3)	1.0
O2	8c	0.1416(6)	0.032(6)	0.04(7)	0.7(3)	1.0
O3	4b	0.25	0.88(2)	0.64(5)	0.7(3)	0.5

Table A.2: Refined structural parameters for AD/OO $Y_{0.15}Sr_{0.85}CoO_{3-\delta}$ powder in space group $Ima2$.

Atom	Site	x	y	z	B	Occ.
Sr1	4e	0	0	0.879(1)	1.735(6)	0.85
Y1	4e	0	0	0.879(1)	1.735(6)	0.15
Sr2	8g	0	0.5	0.868(1)	1.023(6)	1.0
Sr3	4e	0	0	0.348(1)	0.420(6)	1.0
Co1	8h	0.748(2)	0.748(2)	0	3(1)	1.0
Co2	8f	0.25	0.25	0.25	1(1)	1.0
O1	16n	0	0.231(1)	0.2414(7)	1.9(2)	1.0
O2	16m	0.2842(7)	0.2842(7)	0.1119(4)	1.9(2)	1.0
O3	8i	0	0.724(2)	0	1.9(2)	1.0
O4	8j	0.42(2)	0.5	0	1.9(2)	0.09(1)

Table A.3: Refined structural parameters for AO/OO $Y_{0.15}Sr_{0.85}CoO_{3-\delta}$ powder in space group $I4/mmm$.

Bibliography

[1] N. N. Greenwood and A. Earnshaw, *Pergamon Press* **Chemistry of the Elements** P1290-1294 (1984).

[2] K. Briggs, *Allen Lane* **A Dictionary of Fairies** P254 (1984).

[3] M. P. Crosland, *Heinemann* **Historical Studies in the Language of Chemistry** P110 (1962).

[4] Image taken by PHGCOM (Own work, photographed at British Museum) via Wikimedia Commons

[5] K. Mizushimaa, P. C. Jones, P. J. Wiseman and J. B. Goodenough, *Materials Research Bulletin* **15** (1980) 783.

[6] N. B. Ivanova, S. G. Ovchinnikov, M. M. Korshunov, I. M. Eremin and N. V. Kazak, *Physics-Uspekhi* **52** (2009) 789.

[7] J. Shi, R. Yan, Y. Zhu and X. Zhang, *Talanta* **6** (2003) 157.

[8] H. D. Bhatt, R. Vedula, S. B. Desu and G. C. Fralick, *Thin Solid Films* **350** (1999) 249.

[9] K. Takada, H. Sakurai, E. Takayama-Muromachi, F. Izumi, R. A. Dllanlan and T. Sasaki, *Nature* **422** (2003) 53.

[10] H. Mizoguchi, T. Kuroda, T. Kamiya and H. Hosono, *Phys. Rev. Lett.* **106** (2011) 237001.

[11] A. Maignan, S. Hebert, V. Caignaert, V. Pralong and D. Pelloquin, *J. Solid State Chem.* **178** (2005) 868.

[12] G. Briceno, H. Chang, X. Sun, P.G. Schultz and X. -D. Xiang, *Science* **270** (1995) 273.

[13] J. G. Bednorz and K. A. Muller, *Z. Phys. B-Condensed Matter* **64** (1986) 189.

[14] M. K. Wu, J. R. Ashburn, C. J. Torng, P. H. Hor, R. L. Meng, L. Gao, Z. J. Huang, Y. Q. Wang and C. W. Chu, *Phys. Rev. Lett.* **58** (1987) 908.

[15] K. Asai, P. Gehring, H. Chou and G. Shirane, *Phys. Rev. B* **40** (1989) 10983.

[16] K. Asai, O. Yokokura, N. Nishimora, H. Chou. J. M. Tanquada, G. Shirane, S. Higuchi, Y. Okajima and K. Kohn, *Phys. Rev. B* **40** (1989) 10983.

[17] M. Zhuang, W. Y. Zhang and N. B. Ming, *Phys. Rev. B* **57** (1998) 10705.

[18] K. Asai, A. Yoneda, O. Yokokura, J. M. Tranquada and G. Shirane, *J. Phys. Soc. Japan* **67** (1998) 290.

[19] Y. Tokura and Y. Tomioka, *J. Magnetism and Magnetic Materials* **200** (1999) 1.

[20] D. Phelan, D. Louca, S. Rosenkranz, S. -H. Lee, Y. Qiu, P. J. Chupas, R. Osborn, H. Zheng, J. F. Mitchell, J. R. D. Copley, J. L. Sarrao and Y. Moritomo, *Phys. Rev. Lett.* **96** (2006) 027201.

[21] M. James, M. Andeev, P. Barnes, L. Morales, K. Wallwork and R. L. Withers, *J. Solid State Chem.* **180** (2007) 2233.

[22] W. Kobayashi, S. Ishiwata, I. Terasaki, M. Takano, I. Grigoraviciute, H. Yamauchi and M. Karppinen, *Phys. Rev. B* **72** (2005) 104408.

[23] D. J. Goossens, K. F. Wilson, M. James, A. J. Studer and X. L. Wang, *Phys. Rev. B* **69** (2004) 134411.

[24] D. D. Khalyavin, L. C. Chapon, E. Suard, J. E. Parker, S. P. Thompson, A. A. Yaremchenko and V. V. Kharton, *Phys. Rev. B* **83** (2011) 140403(R).

[25] D. V. Sheptyakov, V. Yu. Pomjakushin, O. A. Drozhzhin, S. Ya. Istomin, E. V. Antipov, I. A. Bobrikov and A. M. Balagurov, *Phys. Rev. B* **80** (2009) 024409.

[26] J. Zaanen and O. Gunnarsson, *Phys. Rev. B* **40** (1989) 7391.

[27] Y. Maeno, H. Hashimoto, K. Yoshida, S. Nishizaki, T. Fujita, J. G. Bednorz and F. Lichtenberg, *Nature* **372** (1994) 532.

[28] H. Fjellvåg, E. Gulbrandsen, S. Aasland, A. Olsen, and B.C. Hauback, *J. Solid State Chem.* **124** (1996) 190.

[29] H. Wu, Z. Hu, D. I. Khomskii and L. H. Tjeng, *Phys. Rev. B* **75** (2007) 245118.

[30] J. Sugiyama, G. D. Morris, H. Nozaki, Y. Ikedo, P. L. Russo, S. L. Stubbs, J. H. Brewer, E. J. Ansaldo, C. Martine, S. Hebert and A. Maignan, *Physica B* **404** (2009) 603.

[31] A. Jain, S. Singh and S. M. Yusuf, *Phys. Rev. B* **74** (2006) 174419.

[32] V. Kiryukhin, S. Lee, W. Ratcliff II, Q. Huang, H. T. Yi, Y. J. Choi and S. -W. Cheong, *Phys. Rev. Lett.* **102** (2009) 187202.

[33] H. Wu, T. Burnus, Z. Hu, C. Martin, A. Maignan, J. C. Cezar, A. Tanaka, N. B. Brookes, D. I. Khomskii and L. H. Tjeng, *Phys. Rev. Lett.* **102** (2009) 026404.

[34] S. Aasland, H. Fjellvåg, and B. Hauback, *Solid State Comm.* **101** (1997) 187.

[35] H. Kageyama, K. Yoshimura, K. Kosuge, M. Azuma, M. Takano, H. Mitamura, and T. Goto, *J. Phys. Soc. Japan* 66 1997 3996.

[36] H. Kageyama, K. Yoshimuru, K. Kosuge, X. Xu, and S. Kawano, *J. Phys. Soc Japan* **67** (1998) 357.

[37] A. Maignan, V. Hardy, S. Hébert, M. Drillon, M.R. Lees, O. Petrenko, D. McK. Paul, and D. Khomskii, *J. Mater. Chem.* **14** (2004) 1231.

[38] V. Hardy, M.R. Lees, O.A. Petrenko, D. McK. Paul, D. Flahaut, S. Hébert, and A. Maignan, *Phys. Rev. B* **70** (2004) 064424.

[39] H. Kageyama, K. Yoshimuru, K. Kosuge, H. Mitamura, and T. Goto, *J. Phys. Soc. Japan* **66** (1997) 1607.

[40] E. Dagotto, *Science* **309** (2005) 257.

[41] Image taken from faculty.uml.edu/ndeluca/84.334/topics/topic6.htm

[42] S. Blundell, *Oxford University Press* **Magnetism in Condensed Matter** (2001).

[43] F. Duan and J. Guojun, *World Scientific* **Introduction to Condensed Matter Physics: Vol. 1** (2005).

[44] P. D. Hatton, S. B. Wilkins, T. A. W. Beale, T. Johal, D. Prabhakaran and A. T. Boothroyd, *J. of Superconductivity: Inc. Novel Mag.* **18** (2005) 387.

[45] H. Nakao, T. Murata, D. Bizen, Y. Murakami, K. Ohoyama, K. Yamada, S. Ishiwata, W. Kobayashi and I. Terasaki, *J. Phys. Soc. Japan* **80** (2011) 023711.

[46] C. Kittel, *John Wiley and Sons* **Introduction to Solid State Physics** (2005).

[47] M. T. Dove, *Oxford University Press* **Structure and Dynamics** (2003).

[48] D. S. Keeble, *Ph.D Thesis* Warwick University (2010).

[49] C. Giacovazzo, H. L. Monaco, D. Viterbo, F. Scordari, G. Gill, G. Zanotti and M. Catti, *Oxford Science Publications* **Fundamentals of Crystallography** (1992).

[50] T. Kimura, T. Goto, H. Shintani, K. Ishizaka, T. Arima and Y. Tokura, *Nature* **426** (2003) 55.

[51] A. S. Wills, *Physica B* **276** (2000) 680.

[52] A. M. Glazer, *Acta Crystallogr. A* **31** (1975) 756.

[53] R. H. Mitchell, *Almaz Press* **Perovskites: Modern and Ancient** (2002).

[54] Y. Kobayashi, N. Fujiwara, S. Murata, K. Asai and H. Yasuoka, *Phys. Rev. B* **62** (2000) 410.

[55] M. F. Collins and O. A. Petrenko, *Can. J. Phys.* **75** (1997) 605.

[56] L. Balents, *Nature* **464** (2010) 199.

[57] J. Wu and C. Leighton, *Phys. Rev. B* **67** (2003) 174408.

[58] K. Motoya, Y. Muro, and T. Takabatake, *J. Phys. Conf. Ser.* **200** (2010) 032048.

[59] S. J. Crowe, *Ph.D Thesis* Warwick University (2005).

[60] M. Karppinen, M. Matvejeff, K. Salomaki and H. Yamauchi, *J. Mater. Chem.* **12** (2002) 1761.

[61] K. Conder, E. Pomjakushina, A. Soldatov and E. Mitberg, *Mater Res. Bull.* **40** (2005) 257.

[62] M. McElfresh, *Quantum Design* **Fundamentals of Magnetism and Magnetic Measurements Featuring Quantum Design's Magnetic Property Measurement System** (1994).

[63] D. Martien, *Quantum Design* **Introduction to AC Susceptibility** (2002).

[64] *Quantum Design* **Physical Property Measurement System: Hardware Manual** (2000).

[65] *Quantum Design* **Physical Property Measurement System: Heat Capacity Option User's Manual** (2000).

[66] E. S. R. Gopal, *Heywood Books* **Specific Heats at Low Temperatures** (1966).

[67] B. T. M. Willis and C. J. Carlile, *Oxford University Press* **Experimental Neutron Scattering** (2009).

[68] G. L. Squires, *Dover Publications* **Introduction to the theory of thermal neutron scattering** (1996).

[69] www.neutron.ethz.ch/research/resources/formfactor.

[70] J. R. Stewart, P. P. Deen, K. H. Andersen, H. Schober, J. -F. Barthelemy, J. M. Hillier, A. P. Murani, T. Hayes and B. Lindenau, *J. Appl. Cryst.* **42** (2009) 69.

[71] R. Caciuffo, D. Rinaldi, G. Barucca, J. Mira, J. Rivas, M. A. Senaris-Rodriguez, P. G. Radaelli, D. Fiorani and J. B. Goodenough, *Phys. Rev. B* **59** (1999) 1068.

[72] M. Itoh, I. Natori, S. Kubota and K. Motoya, *J. Phys. Soc. Japan* **63** (1994) 1486.

[73] M. A. Senaris-Rodriguez and J. B. Goodenough, *J. Solid State Chem.* **118** (1995) 323.

[74] A. Nakatsuka, A. Yoshiasa, N. Nakayama, T. Mizota and H. Takei, *Acta. Cryst. C* **60** (2004) i59.

[75] H. Watanabe, *J. Phys. Soc. Japan* **12** (1957) 515.

[76] H. Taguchi, M. Shimada and M. Koizumi, *J. Solid State Chem.* **29** (1979) 221.

[77] C. Zener, *Phys. Rev.* **82** (1951) 403.

[78] R. H. Potze, G. A. Sawatzky and M. Abbate, *Phys. Rev. B* **51** (1995) 11501.

[79] H. Watanabe, Y. Yamaguchi, H. Oda and H. Takei, *J. Magnetism and Magnetic Materials* **15** (1980) 521.

[80] H. Takei, H. Oda, H. Watanabe, I. Shindo, *J. Mater. Sci.* **60** (1978) 519.

[81] S. Kawasaki, M. Takano and Y. Takeda, *J. Solid State Chem.* **121** (1996) 174.

[82] M. James, D. Cassidy, K. F. Wilson, J. Horvat and R. L. Withers, *Solid State Sciences* **6** (2004) 655.

[83] S. Ya. Istomin, J. Grins, G. Svensson, O. A. Drozhzhin, V. L. Kozhevnikov and E. V. Antipov, *Chem. Mater.* **15** (2003) 4012.

[84] A. A. Colville and S. Geller, *Acta. Cryst.* **B27** (1971) 2311.

[85] A. Munoz, C. de la Calle, J. A. Alonso, P. M. Botta, V. Pardo, D. Baldomir and J. Rivas, *Phys. Rev. B* **78** (2008) 054404.

[86] M. James, D. Cassidy, D. J. Goossens and R. L. Withers, *J. Solid State Chem.* **177** (2004) 1886.

[87] R. L. Withers, M. James and D. J. Goossens, *J. Solid State Chem.* **174** (2003) 198.

[88] M. James, L. Morales, K. Wallwork, M. Avdeev, R. L. Withers and D. J. Goossens, *Physica B* **385** (2006) 199.

[89] S. Ishiwata, W. Kobayashi, I. Terasaki, K. Kato and M. Takata, *Phys. Rev. B* **75** (2007) 220406(R).

[90] I. O. Troyanchuk, D. V. Karpinsky, V. M. Dobryanskii, A. N. Chobot, G. M. Chobot and A. P. Sazonov, *J. Exp. and Theo. Phys.* **108** (2009) 428.

[91] S. Fukushima, T. Sato, D. Akahoshi and H. Kuwahara, *J. Appl. Phys.* **103** (2008) 07F705.

[92] S. Fukashima, T. Sato, D. Akahoshi and H. Kuwahara, *J. Phys. Soc. Japan* **78** (2009) 064706.

[93] G. Maris, Y. Ren, V. Volotchaev, C. Zobel, T. Lorenz, and T. T. M. Palstra, *Phys. Rev. B* **67** (2003) 224423.

[94] W. Kobayashi and I. Terasaki, *AIP Conference Proceedings* **850** (2006) 1223.

[95] N. O. Golosova, D. P. Kozlenko, L. S. Dubrovinsky, O. A. Drozhzhin, S. Ya. Istomin and B. N. Savenko, *Phys. Rev. B* **79** (2009) 104431.

[96] S. Yoshida, W. Kobayashi, T. Nakano, I. Terasaki, K. Matsubayashi, Y. Uwatoko, I. Grigoraviciute, M. Karppinen and H. Yamauchi, *J. Phys. Soc. Japan* **78** (2009) 094711.

[97] S. Kimura, Y. Maeda, T. Kashiwagi, H. Yamaguchi, M. Hagiwara, S. Yoshida, I. Terasaki and K. Kindo, *Phys. Rev. B* **78** (2008) 180403(R).

[98] S. Balamurugan, K. Yamaura, A. Asthana, A. Ubaldini, Y. Matsui and E. Takayama-Muromachi, *J. Appl. Phys.* **103** (2008) 07B903.

[99] D. J. Goossens, K. F. Wilson and M. James, *J. Phys. Chem. Solids* **66** (2005) 169.

[100] A. Hassen, A. I. Ali, B. J. Kim, Y. S. Wu, S. H. Park and Bog G. Kim, *J. Appl. Phys.* **102** (2007) 123905.

[101] A. Maignan, B. Raveau, S. Hebert, V. Pralong, V. Caignaert and D. Pelloquin, *J. Phys. Condes. Mat.* **18** (2006) 4305.

[102] K. H. Kim, T. Qian and Bog G. Kim, *J. Appl. Phys.* **102** (2007) 033910.

[103] Y. F. Zhang, S. Sasaki, O. Yanagisawa and M. Izumia, *J. Magnetism and Magnetic Materials* **310** (2007) 1002.

[104] S. Streule, M. Medarde, A. Podlesnyak, E. Pomjakushina, K. Conder, S. Kazakov, J. Karpinski and J. Mesot, *Phys. Rev. B* **73** (2006) 024423.

[105] D. Rupasov, A. Chroneos, D. Parfitt, J. A. Kilner, R. W. Grimes, S. Ya. Istomin and E. V. Antipov, *Phys. Rev. B* **79** (2009) 172102.

[106] K. Zhang, R. Ran, L. Ge, Z. Shao, W. Jin and N. Xu, *J. Alloys Compd.* **474** (2009) 477.

[107] C. L. Fleck, G. Balakrishnan and M. R. Lees, *J. Mater. Chem.* **21** (2011) 1212.

[108] B. Ouladdiaf, J. Archer, G. J. McIntyre, A. W. Hewat, D. Brau and S. York, *Physica B* **385** (2006) 1052.

[109] www2.warwick.ac.uk/fac/sci/physics/research/condensedmatt/x-ray/.

[110] www.ill.eu.

[111] J. Rodriguez-Carvajal, *Physica B* **192** (1993) 55.

[112] T. Katsufuji, *J. Phys. Soc. Japan Online - News and Comments* (Feb 10, 2011).

[113] K. Momma and F. Izumi, *J. Appl. Crystallogr.* **41** (2008) 653.

[114] The heat capacity data for $Y_{0.15}Sr_{0.85}CoO_{3-\delta}$ between 400 and 420 K was extrapolated from the measurements below 400 K in order to calculate the point of intersection with the $LaGaO_3$ data.

[115] B. F. Woodfield, M. L. Wilson, and J. M. Byers, *Phys. Rev. Lett.* **78** (1997) 3201.

[116] M. R. Lees, O. A. Petrenko, G. Balakrishnan, and D. McK. Paul, *Phys. Rev. B* **59** (1999) 1298.

[117] C. He, S. Eisenberg, C. Jan, H. Zheng, J. F. Mitchell, and C. Leighton, *Phys. Rev. B* **80** (2009) 214411.

[118] Image taken from www.ill.eu/instruments-support/instruments-groups/instruments/d7/.

[119] B. H. Grier, G. Shirane and S. A. Werner, *Phys. Rev. B* **31** (1985) 2892.

[120] Th. Zieske, D. Hohlwein and W. Prandl, *Physica B* **241** (2008) 628.

[121] Image adapted from www-llb.cea.fr/fr-en/spectros-llb.pdf.

[122] F. Moussa, M. Hennion, J. Rodriguez-Carvajal, H. Moudden, L. Pinsard and A. Revcolevschi, *Phys. Rev. B* **54** (1996) 15149.

[123] T. G. Perring, G. Aeppli, Y. Moritomo and Y. Tokura, *Phys. Rev. Lett.* **78** (1997) 3197.

[124] R. Osborn, S. Rosenkranz, D. N. Argyriou, L. Vasiliu-Doloc, J. W. Lynn, S. K. Sinha, K. E. Gray and S. D. Bader, *Phys. Rev. Lett.* **81** (1998) 3964.

[125] T. Burnus, Z. Hu, M.W. Haverkort, J.C. Cezar, D. Flahaut, V. Hardy, A. Maignan, N.B. Brookes, A. Tanaka, H.H. Hsieh, H.-J. Lin, C.T. Chen, and L.H. Tjeng, *Phys. Rev. B* **74** (2006) 245111.

[126] K. Takubo, T. Mizokawa, S. Hirata, J.-Y. Son, A. Fujimori, D. Topwal, D.D. Sarma, S. Rayaprol, and E.V. Sampathkumaran, *Phys. Rev. B* **71** (2005) 073406.

[127] H. Wu, M.W. Haverkort, Z. Hu, D.I. Khomskii and L.H. Tjeng, *Phys. Rev. Lett.* **95** (2005) 186401.

[128] S. Niitaka, K. Yoshimura, K. Kosuge, M. Nishi and K. Kakurai, *Phys. Rev. Lett.* **87** (2001) 177202.

[129] A. Maignan, C. Michel, A.C. Masset, C. Martin, and B. Raveau, *Eur. Phys. J. B* **15** (2000) 657.

[130] V. Hardy, D. Flahaut, R. Frésard and A. Maignan, *J. Phys. Condes. Mat.* **19** (2007) 145229.

[131] B. Raquet, M.N. Baibich, J.M. Broto, H. Rakoto, S. Lambert, and A. Maignan, *Phys. Rev. B* **65** (2002) 104442.

[132] V. Hardy, S. Lambert, M.R. Lees, and D. McK. Paul, *Phys. Rev. B* **68** (2003) 014424.

[133] V. Hardy, D. Flahaut, M.R. Lees and O.A. Petrenko, *Phys. Rev. B* **70** (2004) 214439.

[134] R. Sessoli and D. Gatteschi, *Angew. Chem. Int. Ed.* **42** (2003) 268.

[135] S. Rayaprol, K. Sengupta, and E.V. Sampathkumaran, *Solid State Commun.* **128** (2003) 79.

[136] E.V. Sampathkumaran, N. Fujiwara, S. Rayaprol, P.K. Madhu, and Y. Uwatoko, *Phys. Rev. B* **70** (2004) 014437.

[137] R. Soto, G. Martinez, M.N. Baibich, J.M. Florez, and P. Vargas, *Phys. Rev. B* **79** (2009) 184422.

[138] S. Agrestini, C. Mazzoli, A. Bombardi, and M.R. Lees, *Phys. Rev. B* **77** (2008) 140403.

[139] J.-G. Cheng, J.-S. Zhou, and J. B. Goodenough, *Phys. Rev. B* **79** (2009) 184414.

[140] O.A. Petrenko, J. Wooldridge, M.R. Lees, P. Manuel, and V. Hardy, *Eur. Phys. J. B* **47** (2005) 79.

[141] C. L. Fleck, M. R. Lees, S. Agrestini, G. J. McIntyre and O. A. Petrenko, *Europhys. Lett.* **90** (2010) 67006.

[142] R. Frésard, C. Laschinger, T. Kopp, and V. Eyert, *Phys. Rev. B* **69** (2003) 140405.

[143] M. H. Qin, K. F. Wang and J. M. Liu, *Phys. Rev. B* **79** (2009) 172405.

[144] L.C. Chapon, *Phys. Rev. B* **80** (2009) 172405.

[145] Y. Zhao, S. S. Gong, W. Li and G. Su, *Appl. Phys. lett.* **96** (2010) 162503.

[146] Y.B. Kudasov, *Phys. Rev. Lett.* **96** (2006) 027212.

[147] Y.B. Kudasov, *Europhys. Lett.* **78** (2007) 57005.

[148] Y.B. Kudasov, A. S. Korshunov, V. N. Pavlov, and D. A. Maslov, *Phys. Rev. B* **78** (2008) 132407.

[149] X.Y. Yao, S. Dong, and J.-M. Liu, *Phys. Rev. B* **73** (2006) 212415.

[150] X.Y. Yao, S. Dong, H. Yu and J.-M. Liu, *Phys. Rev. B* **74** (2006) 134421.

[151] A.C. Hannon, *Nuclear Instruments and Methods in Physics Research A* **551** (2005) 88.

[152] Image taken from wwwisis2.isis.rl.ac.uk/disordered/gem/gem.

[153] S. Agrestini, C. L. Fleck, L. C. Chapon, C. Mazzoli, A. Bombardi, M. R. Lees and O. A. Petrenko, *Phys. Rev. Lett.* **106** (2011) 197204.

[154] S. Agrestini, L.C. Chapon, A. Daoud-Aladine, J. Schefer, A. Gukasov, C. Mazzoli, M.R. Lees, and O.A. Petrenko, *Phys. Rev. Lett.* **101** (2008) 097207.

[155] T. Moyoshi, R. Takahashi and K. Motoya, *J. Phys: Conf. Series* **273** (2011) 012125.

[156] Measurements made and model developed by S. Agrestini.

[157] Measurements made by S. Agrestini, C. Mazzoli and A. Bombardi on the beamline ID20 at the ESRF, April 2009, Unpublished.

[158] K.E. Stitzer, J. Darriet and H.-C. Zur Loye, *Curr. Opin. Solid State Mater. Sci.* **5** (2001) 535.

[159] X. X. Wang, J. J. Li, Y. G. Shi, Y. Tsujimoto, Y. F. Guo, S. B. Zhang, Y. Matsushita, M. Tanaka, Y. Katsuya, K. Kobayashi, K. Yamaura and E. Takayama-Muromachi, *Phys. Rev. B* **83** (2011) 100410(R).